

University of Louisville

ThinkIR: The University of Louisville's Institutional Repository

Electronic Theses and Dissertations

8-2006

Near room temperature self-assembly of nanostructures by reaction of gallium with metal thin films.

Mehdi M. Yazdanpanah 1975-
University of Louisville

Follow this and additional works at: <https://ir.library.louisville.edu/etd>

Recommended Citation

Yazdanpanah, Mehdi M. 1975-, "Near room temperature self-assembly of nanostructures by reaction of gallium with metal thin films." (2006). *Electronic Theses and Dissertations*. Paper 1622.
<https://doi.org/10.18297/etd/1622>

This Doctoral Dissertation is brought to you for free and open access by ThinkIR: The University of Louisville's Institutional Repository. It has been accepted for inclusion in Electronic Theses and Dissertations by an authorized administrator of ThinkIR: The University of Louisville's Institutional Repository. This title appears here courtesy of the author, who has retained all other copyrights. For more information, please contact thinkir@louisville.edu.

NEAR ROOM TEMPERATURE SELF-ASSEMBLY OF NANOSTRUCTURES
BY REACTION OF GALLIUM WITH METAL THIN FILMS

By

Mehdi M. Yazdanpanah
B.Sc., Sharif University of Technology, 1998
M.S., Beheshti University, 2001

A Dissertation
Submitted to the Faculty of the
Graduate School of the University of Louisville
in partial Fulfillment of the Requirements
for the Degree of

Doctor of Philosophy

Department of Electrical and Computer Engineering
University of Louisville
Louisville, Kentucky, 40292

August 2006

NEAR ROOM TEMPERATURE SELF-ASSEMBLY OF NANOSTRUCTURES
BY REACTION OF GALLIUM WITH METAL THIN FILMS

By

Mehdi M. Yazdanpanah
B.Sc., Sharif University of Technology, Tehran, Iran, 1998
M.S., Beheshti University, Tehran, Iran, 2001

A Dissertation Approved on

July 28, 2006

By the following Dissertation Committee:

Robert W. Cohn (Dissertation Director)

Bruce W. Alphenaar

Kevin Walsh,

Gamini Sumanasekera,

Steven A. Harfenist

DEDICATION

I dedicate this dissertation to

My Parents

Mr. Mohammad Hossein Yazdanpanah and Mrs. Baygom Rezaie

For their lifetime support and encouragement.

ACKNOWLEDGMENTS

This dissertation would not have been finished without the help, support, and encouragement from several persons.

My supervisor, Professor **Robert W. Cohn** deserves very special thanks not only for his professional and financial support on this dissertation but also for inspiring and encouraging me to a deeper understanding, and his invaluable comments from the beginning of this work to the end. His calm attitude during these years of study and research provided me a very appropriate situation to enjoy my work.

I am very grateful to Dr. Steven Harfenist a member of my committee for training me on equipment in the lab, and for several useful discussions concerning this dissertation. Other members of my committee Dr. Bruce Alphenaar, Dr. Kevin Walsh and Dr. Gamini Sumanasekara deserve special thanks for the qualifier exams, and their time and patience for reviewing this work.

I am very grateful to everyone who has read parts of the manuscript, especially, Martin D. Williams, Kimchau N. Nguyen, and Dustin T. McKnight. I would like to specially thank, Romaneh Jalilian, Abdelilah Safir, Timilehin A. Olaleye, Santosh Paba, and Dr. Todd Hastings (University of Kentucky) who have shared their data in this work. I also thank Dr. Shi-Yu Wu, Dr. Frank Zamborini and Dr. Shudun Liu for several useful discussions. Also thanks to members of the Microfabrication facility, Mark Crain, Usha

Gowrishetty, Mike Martin, Julia Aebersold, Josef Lake, Rekha Pai and Tommy Roussel for special training on different equipment and helping me in device fabrication.

Finally I wish to express my special gratitude to my parents, my mother in-law, my grandmother, my brothers, and my sister for their emotional support. My wife, **Romaneh** deserves my deepest appreciation. We had several useful discussions about every single chapter of this dissertation. Besides that, she relieved me of many responsibilities at home during this period of time and was the greatest source of encouragement and inspiration.

ABSTRACT

NEAR ROOM TEMPERATURE SELF-ASSEMBLY OF NANOSTRUCTURES BY REACTION OF GALLIUM WITH METAL THIN FILMS

Mehdi M. Yazdanpanah

July 28, 2006

Liquid gallium (Ga) spontaneously alloys with thin films of metals such as Ag, Au, Pt, Al, and Cu at near or even below room temperature resulting in rapid self-assembly of nanostructures. In this dissertation, studies of the formation of these nanostructures are reported together with application of the processes towards device fabrication.

Ag₂Ga needles, CoGa₃ rods, and Ga₆Pt plates self-assemble at room temperature at the interface of Ga and thin films of Ag, Co, and Pt. The Ag₂Ga needles orient nearly vertical to the interface which suggests that an individual needle can be directed to grow in a desired direction by drawing a silver-coated surface from the Ga droplet. Needles from 25 nm to microns in diameter and up to 33 microns long were grown by this method. Needle-tipped cantilevers have been used to perform atomic force microscopy (AFM) and voltage lithography. Mechanical properties of the Ag₂Ga needles are measured during bending, buckling, yielding, and AC electric excitation of vibrational modes.

The rates of reactive spreading of Ga through thin films of Au and Ag from room temperature to 200 °C are measured. A model of the reduction in spreading rate of Au-Ga over time describes the reduction in area for inter granular flow as the Ga₂Au crystallites precipitates and grow together. Ga spreading on Au microelectrodes is used to perform

time-resolved measurement of changes in the contact resistance of multiwall carbon nanotubes.

Networks of Au-Ga nanowires form when a liquid Ga drop spreads and reacts on 10- to 100- nm-thick Au thin film at temperatures between 310 °C and 400 °C. Au suspended nanowires were fabricated by etching these networks in HCl followed by anisotropic etching of the Si substrate. Suspended nanowires as long as 6 μm and as narrow as 35 nm diameters have been produced.

Superporous Au and Pt thin films with feature size as small as 5 nm are formed after HCl etching of metal thin films that have been reacted with gallium. Superporous Pt formed on a set of microelectrodes was evaluated for electrochemical sensing. These electrodes showed a 6 fold improvement in its limit of detection for H_2O_2 over the non-porous Pt electrodes.

TABLE OF CONTENTS

	Page
ACKNOWLEDGMENTS.....	iv
ABSTRACT.....	vi
LIST OF TABLES.....	xiv
LIST OF FIGURES.....	xv
 CHAPTERS	
PART I INTRODUCTION AND BACKGROUND.....	1
1 INTRODUCTION.....	2
1.1 Defining self-assembly.....	3
1.2 The physical basis for self-assembly.....	4
1.3 Self-Assembly represented by phase diagrams.....	5
1.4 Deviation from the phase diagrams due to non equilibrium kinetics.....	5
1.5 Deviation from the phase diagram: Spatial and size effects.....	6
1.6 Introduction to the metal alloy systems studied.....	7
2 OBSERVATIONS THAT MOTIVATE THE STUDY.....	9
2.1 General background on gallium.....	9
2.2 Spontaneous growth of ordered phase binary alloys.....	11
2.3 Identification of likely alloys from Ga-M phase diagrams.....	18
2.4 Self-Assembly over distance: Spreading fronts.....	20
PART II FUNDAMENTAL SELF-ASSEMBLY PROCESSES.....	23
3 REACTIVE SPREADING OF GA: PLANAR SPREADING.....	24

3.1	Overview of experimental methods.....	27
3.2	Visual description of spreading.....	29
3.3	Geometry and topography of samples.....	32
3.4	Crystallography and composition analysis.....	35
3.4.1	Examination of crosssection of the reacted film.....	35
3.4.2	Material Analysis of Ga-M films.....	37
3.5	Spreading rates	43
3.6	Temperature dependence of Ga diffusion through Au.....	49
3.7	Model of the time dependent front velocity of reactive spreading of Ga on Au ₅₃	
3.7.1	Parameters for model.....	56
4	REACTIVE SPREADING OF GA: NON-PLANAR SPREADING.....	62
4.1	Sample preparation.....	62
4.2	Experimental results.....	63
4.2.1	SEM observation.....	63
4.2.2	AFM dimensional measurements.....	66
4.2.3	Effect of film thickness in non-planar spreading.....	67
4.2.4	Effect of temperature range and reaction time.....	68
4.2.5	Observations of non-planar spreading under an optical microscope.....	69
4.2.6	Composition analysis.....	70
4.3	Discussion of nanostructure formations in non-planar spreading.....	74
5	SELECTIVE GROWTH OF INDIVIDUAL Ag ₂ Ga NANONEEDLES.....	76
5.1	Introduction.....	76

5.2	Non-selective formation of Ag-Ga needles.....	78
5.2.1	Experimental procedures.....	78
5.2.2	Experimental results.....	79
5.3	Selective growth of single needles.....	86
5.3.1	Experimental procedures.....	86
5.3.2	Results of selective growth of needles by the pulling technique.....	87
5.4	Discussion of the growth process.....	94
5.4.1	Nucleation.....	94
5.4.2	Lengthening and tapering.....	98
PART III APPLIED PROCESSES.....		100
6	SUSPENSION OF GOLD NANOWIRE NETWORK.....	101
6.1	Sample preparation.....	102
6.2	Results.....	103
7	POROUS MATERIALS MADE BY CHEMICAL MODIFICATION OF SELF-ASSEMBLED GA-M ALLOY NANOSTRUCTURES.....	105
7.1	Formation of superporous Au.....	106
7.1.1	Sample preparation.....	106
7.1.2	The resulting superporous Au.....	106
7.1.3	Characterization of the dealloying step.....	109
7.2	Formation of superporous crystals of Pt.....	111
7.2.1	Sample preparation.....	111
7.2.2	Results of superporous Pt formation.....	111
7.2.3	Material composition and structure.....	112
7.3	Discussion.....	113

7.3.1	Chemistry of the etching (oxidation) process.....	113
7.3.2	Estimate of the porosity.....	114
7.3.3	Possible theory for pore formation during dealloying.....	115
PART IV APPLICATIONS.....		118
8	MECHANICAL PROPERTIES OF Ag ₂ Ga NEEDLES.....	119
8.1	Introduction.....	119
8.2	General background on the mechanical systems studied	121
8.3	Overview of the experimental procedures.....	125
8.3.1	Electrostatic deflection of needles	126
8.3.2	AFM force microscopy	126
8.3.3	Visual observation of deflection	126
8.4	Measurement of <i>E</i> and <i>Q</i> by electrostatic deflection	127
8.4.1	Experimental procedure	127
8.4.2	Experimental results and discussion	129
8.5	Spring constant of cantilevered needles by force microscopy	131
8.5.1	Mechanics of the double cantilever system	133
8.5.2	Experimental details	137
8.5.3	Results and discussion.....	138
8.6	Measurement of vdW force between Ag ₂ Ga and Si.....	140
8.6.1	Theory.....	140
8.6.2	Results.....	143
8.7	Frictional properties of Ag ₂ Ga needles.....	145
8.7.1	Mechanical model.....	145

8.7.2	Experimental details.....	148
8.7.3	Results.....	149
8.8	Buckling in long needles.....	151
8.8.1	Modification of the buckling in semi-vertical needles	151
8.8.2	Experimental detail.....	152
8.8.3	Results and discussion.....	152
8.9	Summary of results obtained from elastic deformation experiments.....	156
8.10	Potential application of freestanding needles as a mass balance.....	157
8.11	Plastic deformation.....	159
8.11.1	Plastic deformation during the bending.....	159
8.11.2	Plastic deformation during the collision.....	161
9	AFM PROFILING AND NANOLITHOGRAPHY WITH NEEDLE-TIPPED CANTILEVERS.....	164
9.1	Non-contact AFM topography with needle-tipped cantilevers.....	165
9.1.1	Experimental details.....	165
9.1.2	AFM topography results.....	166
9.2	Durability of needle-tipped cantilevers in contact and non-contact modes.....	167
9.2.1	Experimental Details.....	167
9.2.2	Results of durability testing of needle-tipped cantilevers.....	168
9.3	Nanolithography with needle-tipped cantilevers on polymer substrates.....	169
9.3.1	Experimental details.....	169
9.3.2	Results of lithography on PMMA	170
9.4	Voltage nanolithography results on silicon substrates.....	172
9.4.1	Experimental details.....	172

9.4.2	Results.....	173
9.5	Advantage of using needle-tipped cantilevers for AFM lithography.....	175
10	GALLIUM SPREADING TO STUDY CONTACT RESISTANCE OF CARBON NANOTUBES.....	177
10.1	Introduction.....	177
10.2	Experimental Details.....	178
10.3	Results and discussion.....	180
11	ELECTROCHEMICAL SENSING WITH SUPERPOROUS Pt.....	185
11.1	Sample preparation.....	185
11.2	Setup for evaluation sensing performance.....	188
11.3	Sensing performance.....	188
12	PATTERNING OF GALLIUM.....	190
12.1	Texturing of gallium.....	191
12.2	Dip pen nanolithography with Ga.....	194
12.3	Nanoimprint lithography (NIL) with Ga	196
PART V	CONCLUSIONS AND FUTURE PLANS.....	199
13	CONCLUSIONS AND FUTURE PLANS.....	200
	REFERENCES.....	202
	BIBLIOGRAPHY OF THE UNREFERENCED ARTICLES.....	211
	APPENDIX A.....	216
	CURRICULUM VITAE.....	217

LIST OF TABLES

Table	Page
2.1 Physical constant of Gallium at different temperatures.....	10
2.2 Prediction and measurement of intermediate phase formation at room temperature in several Ga-M systems.....	19
3.1 List of the instruments and their application for this study.....	28
3.2 Transition width for various Au film thicknesses.....	42
3.3 Transition width for various Ag film thicknesses.....	43
3.4 Activation energies for various Au film thicknesses and temperature ranges.....	52
3.5 Activation energies for various Ag film thicknesses and temperature.....	53
3.6 Experimental value used for the model.....	57
3.7 Value resulting from the best fits to the model of reactive spreading of Ga on Au.....	59
4.1 EDS composition analysis of non-planar spreading reaction.....	71
8.1 List of the key equations and definitions of the constants used in Chapter 8.....	120
8.2 The mechanical parameters of needles and cantilevers of Sample 1 before and after the adding the needles.....	138
8.3 Mechanical parameters of Sample 2	149
8.4 Measured spring constant of the needle-cantilever system at locations 1 to 4.....	151
8.5 Needle spring constant and Young's modulus, Quality factor and Hamaker constant.....	157
9.1 List of the needle-tipped cantilever used for AFM topography and lithography.....	165
11.1 Limit of detection and sensitivity of the microelectrodes before and after porosity treatment.....	189

LIST OF FIGURES

Figure	Page
2.1 Crystals that form at the interface between a Ga droplet and a metal foil	12
2.2 Binary phase diagrams that illustrate two types of intermediate phases.	14
2.3 Binary phase diagram for Ga-Pt	15
2.4 Ag-Ga binary phase diagram.....	16
2.5 Ga-Au binary phase diagram.....	17
2.6 Self-assembly over distance.	21
3.1 Schematic drawing of Ga spreading on a Au film.	25
3.2 Ga spreading on Au.	30
3.3 Ga spreading on patterned Au of thickness (a) 50 nm, (b) 110 nm and (c) 287 nm.....	31
3.4 Backscattered SEM images of Ga spreading layer	32
3.5 The height of the reacted film as a function of metal film thickness.....	33
3.6 SEM images of Ga-Au crosssection. The thicknesses of the Au films before reactive spreading are (a) 110, (b) 330 and (c) 421 nm	36
3.7 Crosssection SEM images of Ga-Ag taken with In-lens secondary detector.....	37
3.8 XRD of Ga-Au film before and after cooling the sample well below the Ga melting point.	38
3.9 TEM images of an AuGa ₂ grain in Ga-rich liquid.	39
3.10 Composition changes from the Ga reservoir to the front on Au thin films.	41
3.11 X- ray diffraction pattern of Ga-Ag. The spectrum corresponds to the ordered intermetallic ξ' phase of Ag ₂ Ga	43
3.12 Ga front (a) position and (b) velocity as a function of time for 50 nm, 114 nm and 308 nm thick Au films	45

3.13	Ga front (a) position and (b) velocity on Ag thin films as a function of time.....	46
3.14	The velocity of the spreading front for (a) Au and (b) Ag films as a function of film thickness	47
3.15	Temperature dependence of front velocity on Au thin films of 35 nm thickness.....	48
3.16	Ga diffusion constant at the early stage of the spreading process as a function of temperature	50
3.17	Time-dependent velocity of fronts on 125 nm thick patterned Au lines.....	58
3.18	Ga diffusion constant as a function of temperature on 125 nm Au.	60
4.1	Pattern due to non-planar spreading of Ga on a 35 nm Au thin film at 360 °C for 5 min.....	64
4.2	Oblique view of the boundary between Zone 3 and Zone 4 taken at 45° sample tilt.....	65
4.3	SE detector SEM image of a nanowire network and islands formed on a 5 μm wide Au line.	66
4.4	Typical dimensions observed after Ga spreading at 370 °C on a 10 nm Au thin film.....	67
4.5	Time-lapse optical images of Ga spreading over a 35 nm Au thin film, after a 100 μm diameter Ga droplet is placed on the Au surface at 350 °C.	70
4.6	Composition of different zones of a typical sample. Compositions listed are Ga:Au or Cr:Ga:Au.....	73
4.7	SEM images of the islands, located at the boundary between Zones 2 and 3.	73
4.8	Schematic of the formation of the Au-Ga nanowire network.	75
5.1	Schematic showing a method for pulling nanoneedles from a gallium droplet.....	77
5.2	Patterning Ag ₂ Ga nanoneedles. (a).....	79
5.3	Nanoneedles formed by Ga reacting with Ag thin films.....	80
5.4	Dependence of needle (a) diameter and (b) quantity as a function of Ag film thickness.....	81
5.5	Selective removal of excess Ga.....	82
5.6	Region of Ag foil after reaction with Ga.	83

5.7	Time-lapse SEM images of needle formation inside a Ga droplet.....	84
5.8	Measurements of the composition and structure of the Ga-Ag needles.....	85
5.9	Time-lapse images of freestanding needle fabrication inside the SEM.....	88
5.10	Nanoneedles formed on AFM tips by the pulling technique.....	89
5.11	SEM images of two selectively grown needles by AFM manipulation.....	90
5.12	Needle fabrication on a tipless cantilever.	90
5.13	Needles of custom orientation and length.	92
5.14	Time-lapse SEM images of the formation of the meniscus and a nanoneedle at an oblique orientation to the AFM tip.	93
5.15	Nucleation and growth	96
5.16	Proposed model of the nucleation of the needles.	98
6.1	Au-Ga structures (a) before and (b) after etching.	101
6.2	Close-ups of suspended nanowires from Figure 6.1b.	103
7.1	SEM images of Au-Ga alloy film (a) before and (b) after the etching step using Recipe 1.	107
7.2	Superporous Au, made from (a) 30 nm and (b) 150 nm Au thin films.....	108
7.3	SE detector SEM images of both sides of the porous film.....	108
7.4	Superporous Au prepared by Recipe #2.	109
7.5	The effect of HCl etching on porosity and Au purity.	110
7.6	Alloying of Pt with Ga, followed by dealloying.	112
8.1	Mechanical elements used to model bending and buckling of the nanoneedles....	121
8.2	AC voltage excitation of a nanoneedle.....	128
8.3	Histogram of Young's modulus of 21 nanoneedles.	130
8.4	Deflection as a function of frequency of a needle around its fundamental mode.....	130
8.5	Schematic of F-D experiment with an AFM cantilever.	132

8.6	Schematic of the two cantilever system that consists of needle attached to the side of an AFM tip.	134
8.7	SEM image of a nearly-parallel grown nanoneedle on the side an AFM cantilever.....	137
8.8	F-D curve of the needle-cantilever system (Sample 1).....	139
8.9	van der Waal force between the tip of a needle positioned close to a planar substrate.	141
8.10	Comparison of theory of vdW snap-down [equation (8.29)] with measured value of snap-down.	144
8.11	Free body diagram of a rigid rod sliding during (a) extension and (b) retraction of an actuator.....	146
8.12	SEM images of Sample 2 (a) before and (b) after breaking off the needle.....	149
8.13	F-D response of a cantilever (a) after and (b) before breaking off the needle	150
8.14	Time-lapse SEM images of Sample 3 during compression and release. The cross-hatching is added to make the surface easier to see	153
8.15	F-D curves of Sample 3 for a (a) 160 nm, (b) 500 nm, and (c) 1100 nm piezo extension range. The straight lines in (c) are the slopes at Location 8 and 11.....	155
8.16	SEM images of elastic and plastic deformation of a long needle.	160
8.17	Sharpening of a needle by electrostatic deflection.....	162
9.1	Images for evaluating the resolution of the needle-tipped cantilever (Tip 1) (Images taken by S. Harfenist)	166
9.2	Time-lapse non-contact mode AFM topography with a needle-tipped cantilever.....	168
9.3	Time-lapse contact mode AFM topography images with the same needle-tipped cantilever as used for Figure 9.2.....	169
9.4	Voltage nanolithography results of PMMA with needle-tipped and conventional AFM tips.....	171
9.5	Voltage lithography results on silicon using Ag ₂ Ga nanoneedles.	173
9.6	Close-up view of voltage lithography results from the 7 V region of Figure 9.5...174	

9.7	SEM images of the end of a Ag ₂ Ga needle-tipped AFM probe (a) before and (b) after 20 min of voltage nanolithography with continuous application of 150 pA of current.....	175
10.1	Apparatus for observing contact resistance changes in a CNT.....	179
10.2	Zero bias differential conductance of MWNTs at 320 °K as the front spreads along the Au electrodes.....	181
10.3	Temperature and bias dependence of a single channel nanotube before and after Ga spreading.	182
10.4	Differential conductance of a Ga-contacted MWNT as a function of bias at 175 K.....	184
11.1	A micrograph of a ceramic microelectrode array (Quanteon, L.C.C., Denver CO).....	186
11.2	Images of the transformation of a Pt microelectrode into a superporous film.	187
12.1	Array of gallium dots pulled with AFM from a liquid Ga bath. Maximum height is about 1.4 μm.	192
12.2	F-D curves for (a) extension into and (b) retraction from Ga.....	193
12.3	Line of gallium written from an AFM tip to a silicon substrate.	195
12.4	Lines of gallium written from an AFM tip to a gold-coated silicon substrate.....	196
12.5	Nanoimprinting lithography (NIL) of Ga at 85 °C using a PMMA mold.....	197

PART I

INTRODUCTION AND BACKGROUND

CHAPTER 1

INTRODUCTION

This dissertation explores the self-assembly of nanostructures due to interactions between specific metals at and near room temperature. Most relevant to the physical basis for the study are concepts from materials science, in general, and from metallurgy, in particular. For decades metallurgists have observed nanostructures that form during the solidification of metals and metal alloys, but unfortunately they refer to any small structures that are larger than atomic scale as *microstructure*.

Metallic nanostructures self-assemble through the evolution of material systems toward states of thermodynamic equilibrium. The difference between the free energy of the system in the initial and final states produces a force that drives the transformation of state. However, the system may also have to first climb an energy barrier before a spontaneous reaction can occur. A reaction can also go through several metastable states which each have excess free energy barriers that can stop the reaction before the thermodynamic minimum can be reached. As a result of the complex physics of metal systems there are numerous structures that can be realized. For instance, from a binary metal melt of iron and carbon, there are innumerable varieties of steel that can be produced through variations in cooling rates and the fraction of carbon to iron [1]. The numerous types of transformations from one nanostructure morphology to another are

found throughout the solidification process [2]. From the viewpoint of this dissertation, these processes can all be considered to be types of self-assembly.

When similar physical transformations take place in metal thin films, rather than in bulk, it becomes possible to incorporate the resulting nanostructures into microfabricated devices, which often use thin films as part of the fabrication process. It is specifically the possibilities of developing micro- and nano- devices that the studies of metal self-assembly are directed at in this dissertation. In the remainder of this introduction a general background on self-assembly is given together with an overview of the processes observed during this study.

1.1 Defining self-assembly

The term *self-assembly* describes the automatic and autonomous transformation from one state or configuration into another. Self-assembly is ubiquitous in nature, and can be observed in the formation of galaxies, in the evolution of geological formations and climate patterns, in the formation of bubbles and snowflakes, in the sedimentation of colloids, in chemical reactions, and in the process in which a fertilized egg together with the surrounding nutrients in the womb self-assembles into a baby. The term self-assembly is descriptive and qualitative, rather than physically precise. Nonetheless, it is an appealing and important concept for engineers and applied scientists, in that self-assembly offers the possibility of fabricating materials, structures, and devices with less effort and complexity than by traditional fabrication methods. This is especially appealing in the field of nanostructure fabrication, where with the continually decreasing feature sizes, the cost of traditional fabrication equipment (e.g. electron beam pattern

generators, focused ion beam tools, x-ray lithography, extreme UV lithography systems) is becoming increasingly costly. G. M. Whitesides [3-5] has been the strongest proponent of adapting self-assembly to replace complex and expensive tools with simpler and automatic processes from nature. In a broader context E. Drexler [6] presented an earlier vision of “bottom up” assembly starting from individual atoms and molecules. In contrast R. Feynman’s original description of nanofabrication [7], in which evolutionary refinement of accuracy and precision of the fabrication tools was envisioned, and which is now referred to as “top down” nanofabrication. The value of developing self-assembly for nanostructure fabrication is especially important in that it can enable many more researchers fast, economical and practical ways to perform research at the nanoscale. Furthermore, processes that self-assemble with adequate control, precision, and repeatability could potentially replace and reduce the manufacturing costs of current top down processes used in the fabrication of integrated circuits and other integrated devices [e.g. micro electro mechanical systems (MEMS), BioMEMS, Microflips, Lab-on-a-chip].

1.2 The physical basis for self-assembly

Self-assembly in metal and alloy systems is described by kinetics, or the evolution of a system toward a state of equilibrium. Excess free energy (ΔG) above equilibrium can be due to any number of physical or thermodynamical variables e.g. temperature, pressure, chemical composition in binary (or m-ary) systems, electrical potential or gravitational potential. Therefore if a system is initially in equilibrium, an instantaneous change in a thermodynamic variable causes the system to evolve toward a new state of equilibrium. Since the system has been removed from a state of equilibrium there is a change in free

energy which drives the reaction. Change in any variable can be associated with a “driving force” that pushes the system towards a state of equilibrium.

1.3 Self-Assembly represented by phase diagrams

A general map of transformations between states is represented by phase diagrams [8-10]. These show various states, or phases, of matter as a function of various state variables such as temperature, pressure or composition. A change in the values of the variables can change the state of the material. For instance, for a one component material (say, water) a reduction of temperature can induce the self-assembly of ice from liquid. It should be noted that the phase diagram only represents the states of matter in thermodynamic equilibrium. That is, the phase diagram is drawn under the assumption that the transformation between states is achieved by changing the state variables between the initial and final state at infinitesimally slow rates.

For a material to be in a certain phase (in thermodynamic equilibrium) that phase must also have a Gibbs free energy, G that is lower than the energy of any other phases. Therefore, in the ice phase on the phase diagram, the free energy of ice is lower than the free energy of liquid water, and in the liquid phase, ice has the higher free energy. At the boundaries of the phases (say, the ice-liquid boundary) the phases coexist and have equal free energies.

1.4 Deviation from the phase diagrams due to non equilibrium kinetics

Infinite variations from the equilibrium phase diagram are possible due to non equilibrium variation of the state variables which can result in a rich set of complex

morphologies [8-11]. One simple example that illustrates the differences between equilibrium transformations (thermodynamics) and non-equilibrium transformations (kinetics) is the carbon phase diagram for which the diamond phase exists at high temperature and pressure[12]. Diamond does not occur at standard temperature and pressure on the phase diagram. However, diamond exists (albeit, in a metastable state) at standard temperature and pressure due to a non-equilibrium return to ambient conditions. An example that illustrates the widely varying morphologies possible through kinetics is the infinite varieties of microstructure that are formed depending on the cooling rate applied to molten steel [13].

1.5 Deviation from the phase diagram: Spatial and size effects

The phase diagrams are drawn under the assumption that the material is homogeneous and infinite in extent. But boundaries and finite size are known to increase the free energy, which can provide additional driving forces for self-assembly. For example at a boundary between two infinite planes, the entropy of mixing drives diffusion [14]. For spherical and rounded surfaces, small radii of curvature can significantly increase free energy (referred to as the Gibbs-Thomson effect) and significantly affect the solubility of the nanostructure in the surrounding material [15].

The above discussion relating the concept of self-assembly to thermodynamics and kinetics provides a general framework and landscape for describing self-assembly in metal alloy systems. As appropriate to the particular material system described in the following chapters, specific physical models will be presented and related to the above general concepts.

1.6 Introduction to the metal alloy systems studied

This study on alloy self-assembly began during initial attempts to selectively wet and adhere gallium to silicon surfaces. While gallium was found to adhere well to gold, shortly thereafter it was observed that gallium spreads over gold thin films. The spreading was found not to be surface wetting, but instead it was determined that gallium reacts with the gold leaving behind a raised and roughened surface that could be considered to be corroded. On the basis of these initial reactions that were observed at ambient laboratory conditions, a number of related studies were begun on the reactions between several gallium-metal (Ga-M) systems that are reported herein. From the thermodynamic and kinetic framework outlined above, as it should apply to nanostructured alloy formation, it is clear that other binary (as well as m-ary) combinations of metals could also result in the self-assembly of nanostructures. The use of Ga, in particular, is of great interest because it reacts with a number of metals at room temperature, which simplifies the experimental requirements, as well as potential application. It is also of significant practical interest for microdevice fabrication, that while Ga melts within a few degrees of room temperature, it alloys to produce solid compounds that melt well above room temperature. These initial results motivated a study with these overall goals:

To identify self-assembly processes in the formation of metal alloy nanostructures.

To determine physical properties of the resulting materials and nanostructures.

To demonstrate potentially useful applications of metal alloy nanostructures.

Following these goals the dissertation is organized in 5 parts as follows:

- I. Introduction and Background
- II. The Fundamental Self-Assembly Processes
- III. Applied Self-Assembly Processes
- IV. Applications of the Self-Assembled Nanostructures
- V. Conclusions and Future Research Directions

CHAPTER 2

OBSERVATIONS THAT MOTIVATE THE STUDY

This chapter presents a number of fundamental observations about Ga-M alloy systems that point to the potential of these materials to self-assemble into useful nanostructures. These observations are taken both from the technical literature and from experiments performed by the author. Alloys that form at or near room temperature are of special interest and are the focus of most of in-depth studies in the subsequent chapters.

2.1 General background on gallium

It is first worth reviewing the key properties of gallium. Perhaps the most notable property of Ga is its low melting point (29.77 ± 0.01 °C) [16] together with its unusually high boiling point of 1983 °C [17] and hence, low vapor pressure at room temperature. These properties make gallium an important element for chemical vapor synthesis of nanomaterials [18].

Ga is a group III element of the periodic table with atomic number 31 and atomic weight 69.72. D.I. Mendeleev who is famous for creating the periodic table, predicted the existence of Ga four years before its discovery. P.E. Lecoq de Boishaudran observed the

first indication of the existence of this element and named it gallium in honor of France which in Latin is *Gallia* [19,20].

The atomic radius of Ga is 1.3 Å [21]. It crystallizes below its melting point in the rhombic (pseudotetragonal) system. Diatomic molecules (Ga_2) form a lattice structure with $a = 2.47$ Å [17] that leads to Ga expanding on freezing [22]. Ga_2 molecules are found in the molten state. Such coexistence of molecular and atomic structures in a liquid metal state is rare. High purity Ga, can be supercooled in the liquid phase down to -28 °C or 57.7 °C below its melting point [22]. Supercooled Ga can be quickly crystallized by the introduction of a seed such as a crystal of Ga. Even small shaking of supercooled droplets can induce crystallization of liquid Ga. Some Ga alloys have even lower melting points than pure Ga. For example a mixture of Ga:In:Zn:Sn of atomic percentage of 61:25:1:13 has a melting point of 3 °C [19]. Additional physical constants of Ga are listed in Table 2.1.

Table 2.1. Physical constants of Liquid Ga at different temperatures [17,23]

Temperature (°C)	Surface tension (mN/m)	Viscosity (cP)	Density, (g/cm ³)	Vapor pressure (mm Hg)	Specific Heat (cal/g deg)
29.8	766±17		5.90		
52.9		1.894			
97.9		1.612			
119					0.079
301		1.029			
500		0.8119			
771				10^{-5}	
1100		0.578	5.445		
1443				1.0	

2.2 Spontaneous growth of ordered phase binary alloys

Nanostructures readily form at the interface between two metals. If one of the metals is Ga, nanostructures can self-assemble even near room temperature. This is demonstrated by placing 2 μm to 1 mm diameter drops of Ga (99.9 % purity from Alfa Aesar), in contact with sputter deposited metal thin films or foils of Au (99.9 %), Ag (99.998 %), Pt (99.99 %), Pd (99.95 %), and Co (99.95 % purity) all from Alfa Aesar. The thin films are between 20 nm and 350 nm and the foils are between 25 μm and 125 μm in thickness. Ga is left in contact with the foil from 10 minutes to 24 hours. In some cases, the Ga is not completely reacted with the film. The excess Ga is removed by etching the sample in 1 N HCL at 60 $^{\circ}\text{C}$ for 5 to 10 minutes. Figure 2.1 shows the crystals that result from the reaction of Ga with different metal foils. Each material combination produces unique crystal morphologies and in each experiment, structures of nanoscale dimensions are formed.

Figure 2.1a and b show SEM images of Ag_2Ga crystalline needles that self-assembled at 200 $^{\circ}\text{C}$ and room temperature respectively. The larger diameter of the needles in Figure 2.1a than for the needles in Figure 2.1b appears to be related to the higher growth temperature [24]. Plates of Pt_6Ga self-assemble during the reaction of Ga with metal foil at 160 $^{\circ}\text{C}$ (Figure 2.1c) and room temperature (Figure 2.1d) again producing larger structures at the higher temperature. Crystal size as a function of temperature is often due to the temperature dependence of the diffusion constant [24].

Further examples of the formation of Ga-Pd crystals and Co-Ga nanorods are shown in Figure 2.1 e and f.

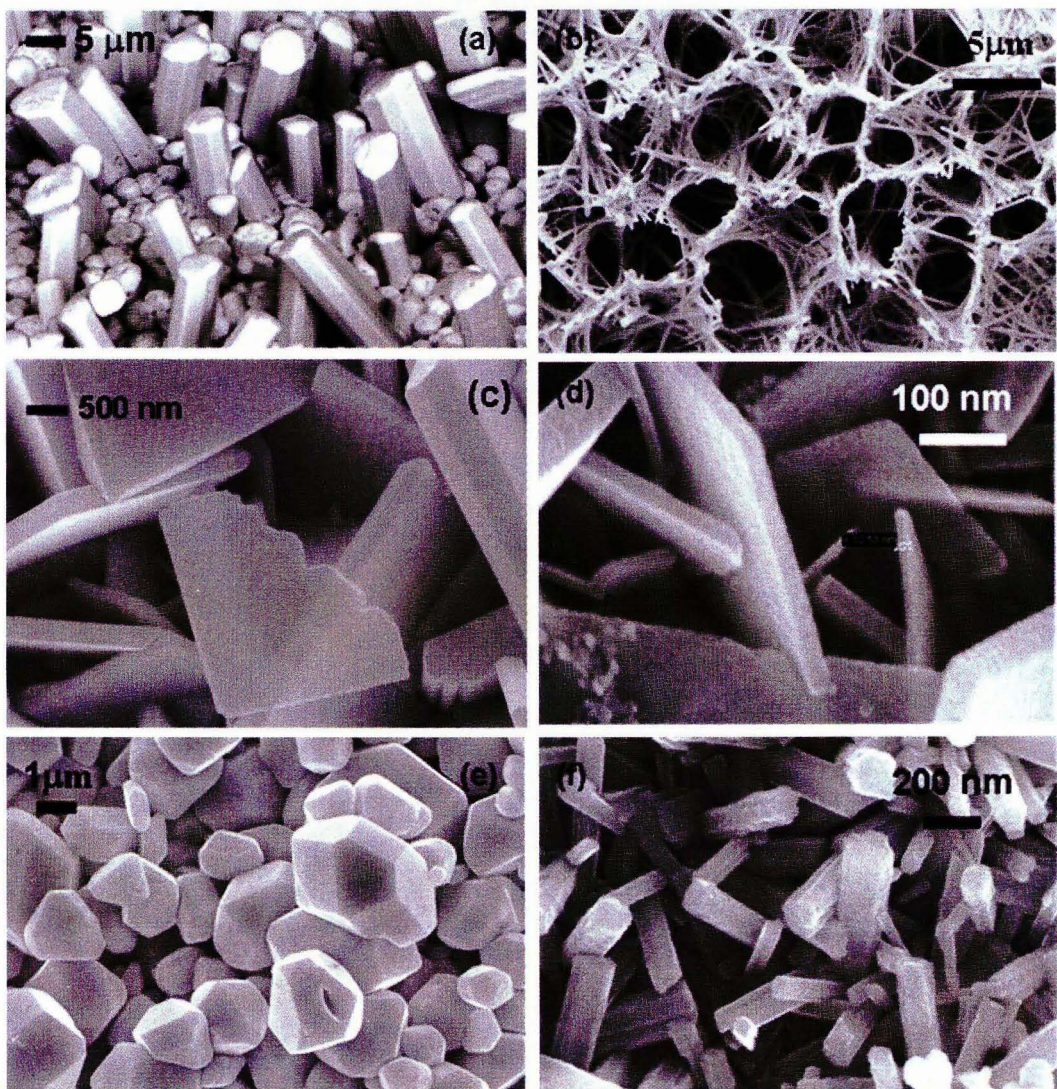


Figure 2.1. Crystals that form at the interface between a Ga droplet and a metal foil for foils of (a,b) Ag, (c,d) Pt, (e) Pd, and (f) Co. Crystals formed at 200° C in (a), at 160° C in (c) and at 25° C in (b), (d), (e), (f).

From examination of Ga-M phase diagrams, the crystallites in Figure 2.1 appear to be *ordered phases* (as will be explained below). The identification of some of the ordered phase alloys has been confirmed by X-ray diffraction (XRD), energy dispersive spectroscopy (EDS), selective area diffraction (SAD) and high resolution transmission electron microscopy (HRTEM), as will be reported in subsequent chapters.

Intermediate phases (some of which can be ordered phases) can be identified on binary phase diagrams. Figure 2.2 presents idealized drawings of portions of binary phase diagrams that show intermediate phases. Figure 2.2a shows a phase diagram that includes the line compound AB [25]. This ordered phase has a 1:1 composition of elements A and B. It should be noted that the phase diagram between the AB phase and pure B can be interpreted as a binary phase diagram of the compounds AB and element B. [26] The particular shape of this portion of the phase diagram in Figure 2.2a is very similar to that of a binary eutectic, in which the AB compound and β phase can simultaneously arise from the liquid phase (L) at the eutectic temperature (indicated by the horizontal *invariant* line at which L, AB and β are simultaneously in equilibrium.) [27]

Figure 2.2b presents a slightly modified version of Figure 2.2a. In this case a β phase is formed that has varying composition rather than forming a single line compound. This phase can also be an ordered phase, demonstrating long range crystalline ordering at the atomic level. In both Figure 2.2a and 2.2b the compound (at its highest melting point) melts directly into a liquid of the same composition. These phases are referred to as congruently melting solids [28]. Incongruently melting compounds produce liquid phases of differing compositions from the solid phase. An example of an incongruently melting solid is Ga_6Pt (see Figure 2.3) which converts to liquid and Ga_7Pt_3 above 563 K. Below the invariant line in Figure 2.2a, there are two intermixed solid phases of AB and β . There are also two two-phase regions above the eutectic temperature in which there is a phase of liquid and AB and a phase of liquid and β . The reason that the AB to B region can be considered as a phase diagram is related to the principle of interpretation of the

binary phase diagram. These two-phase regions can only be bounded by single phase regions. For example in Figure 2.2a, the single phases are AB and β . The fraction of the two single phases in a double phase region can be calculated by the tie-line construction or *lever rule*. This is shown in Figure 2.1c for the two phase region from Figure 2.1b. The two phase alloy has a fraction of concentration of constituent B of X_0 . It is composed of $l_1:l_2$ parts of γ and β phases, respectively. These proportions are identical to the lengths l_1 and l_2 indicated on the tie-line in Figure 2.2c for temperature T_0 . For example, the ratio of γ to β for an alloy of concentration X_0 of element B is

$$\frac{l_1}{l_2} = \frac{X_0 - X_\beta}{X_\gamma - X_0}$$

If the horizontal axis is plotted in atomic percent of B then the proportions are in atomic percent, and if the axis is in weight percent (wt. %), the proportions are in term of wight percentage. Additional features of binary phase diagrams are illustrated with examples taken from actual phase diagrams.

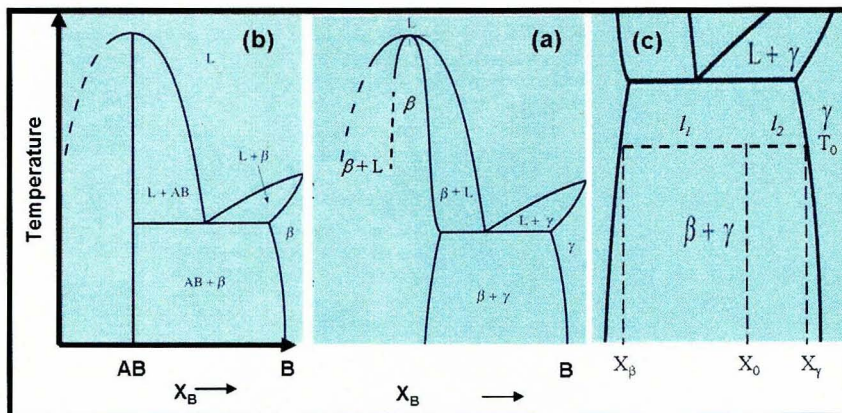


Figure 2.2. Binary phase diagrams that illustrate two types of intermediate phases. (a) A phase diagram that includes the line compound AB which is an ordered phase. (b) A phase diagram that has an intermediate phase that may be an ordered phase. (c) A close-up view of (b) that is used to explain the lever rule.

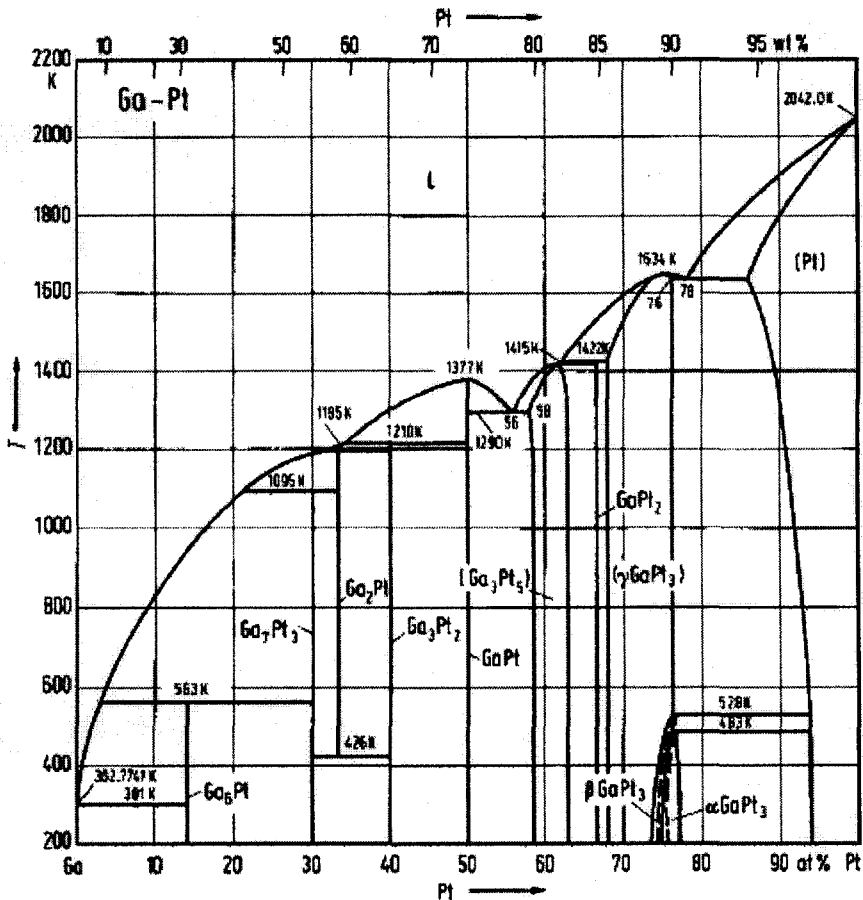


Figure 2.3. Binary phase diagram for Ga-Pt [26]

Figure 2.4 for Ag-Ga alloys shows the intermediate phases of ζ and ζ' that are respectively, disordered and ordered. To the left and right side of the ζ' peak at 27 at. % Ga there is a two-phase region on the left between 395-425 °C and on the right between 302-425 °C. Thus for compositions in these two phase regions there can be a combination of disordered and ordered phases, which can be calculated by the lever rule. Another important feature on this phase diagram is found at the 26° C invariant line. Note that the liquidus line intersects the invariant line at about 98 at. % Ga. This is the eutectic point for Ag-Ga. The second liquidus line is so close to 100 % that it is not

visible on this plot. Instead, the melting point for 100 % Ga is indicated on the diagram to make clear that this is a eutectic region of the phase diagram. Similarly, for Au-Ga (Figure 2.5) the eutectic point is almost 100 % Ga and the rightmost liquidus line that intersects the eutectic point and 100 % Ga is not visible on the diagram.

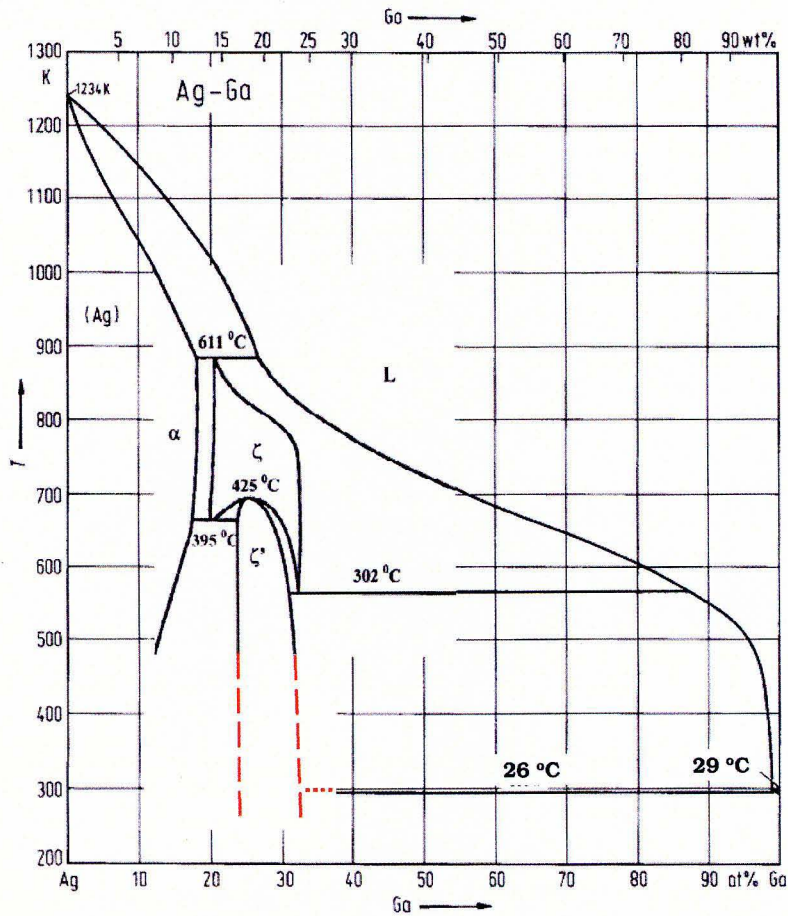


Figure 2.4. Ag-Ga binary phase diagram [26, 29]

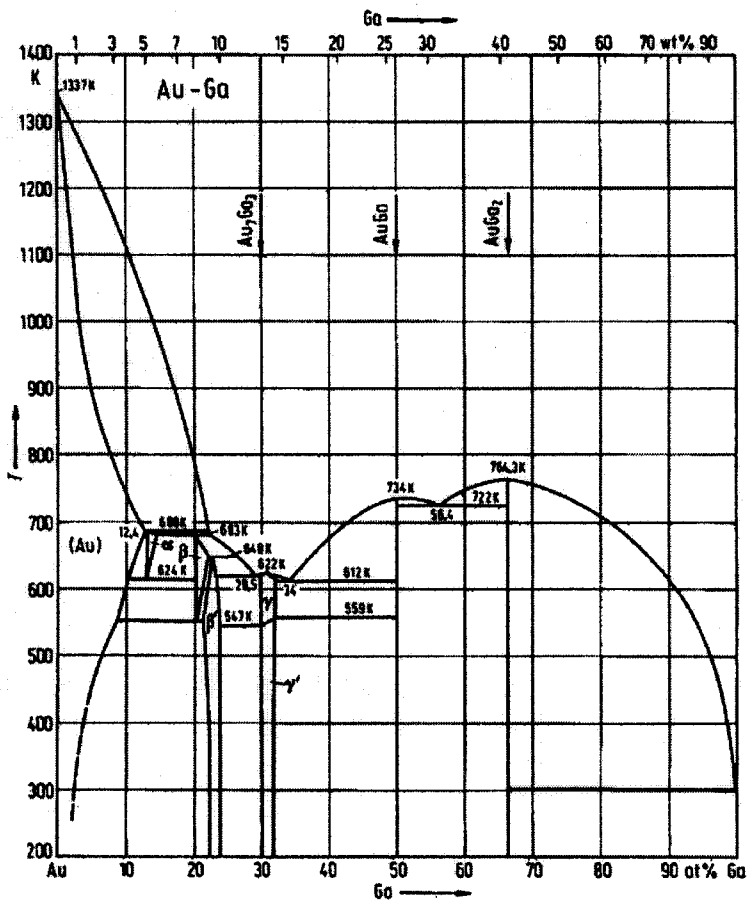


Figure 2.5. Ga-Au binary phase diagram [26]

For this dissertation the most significant feature on the phase diagrams in Figures 2.3-2.5 is the near room temperature invariant line that is formed between the intermediate phase and the Ga-rich phase. This horizontal line represents the lowest temperature at which a liquid phase for the alloy is found. The intermediate phases Ga_6Pt (in Figure 2.3), Ag_2Ga (in Figure 2.4) and $AuGa_2$ (in Figure 2.5) appear to be the ones that did form in the studies (e.g. in Figure 2.1) where Ga-M crystals resulted. It seems possible that this lowest temperature phase would be most likely to form, since liquid Ga is one of the compounds of this two phase region and it would be expected to diffuse more rapidly

at room temperature than other constituents on the phase diagram. However, this thermodynamic argument does not account for kinetics and thus, while empirically it appears that this hypothesis is true, it is possible that other phases could also form at room temperature.

2.3 Identification of likely alloys from Ga-M phase diagrams

As a further evaluation of the hypothesis that:

The lowest temperature liquid-solid invariant (which is usually a eutectic invariant corresponds to the ordered phase that will self-assemble.

a number of Ga-M phase diagrams were examined. The lowest temperature invariant line and the associated intermediate phase are reported in Table 2.2. Of the 31 phase diagrams examined 20 have an invariant line at temperature of 34 °C or lower. Of course, even if an alloy is shown on the phase diagram, it may not form in a reasonable time. To further study the reasonableness of the hypothesis, Ga drops were reacted at room temperature with a number of elemental metals by the procedure in Section 2.2. As reported in Table 2.2, a number of materials do form crystals. EDS analysis has been used to confirm the composition of some of these crystals, and available is reported in the Table 2.2. Ga-Al was also studied. It readily alloys with Ga, but rather than forming crystals it forms an amorphous alloy.

Also note that some of the metals do not react with Ga at room temperature, and in fact, the invariant temperature can be very high (e.g. Ga-Ti, Ga-W). These metals prove useful both as barrier materials to prevent the Ga reaction and as adhesion promoters that improve the wetting of Ga to substrates (e.g. Si and SiO₂ for which Ga barely wets.)

Table 2.2. Prediction and measurement of intermediate phase formation at room temperature in several Ga-M systems [26].

Element	Symbol	Characteristic from phase diagrams		Experimental observations by author	
		Ordered phase for the lowest temperature liquid Ga-ordered phase-invariant line	Temperature of the invariant line (°C)	Are Ga-M crystallites observed at room temperature?	Atomic ratios of observed crystallites by EDS (Ga:M)
Aluminum	Al	None	N/A	No	-
Cadmium	Cd	None	N/A		
Chromium	Cr	CrGa ₄	29.5	No	-
Copper	Cu	CuGa ₂	29	Yes	2:1
Cobalt	Co	CoGa ₃	30.5	Yes	1:2
Gold	Au	AuGa ₂	29	Yes	2:1
Hafnium	Hf	Ga ₃ Hf	29		
Indium	In	Ga _{14,2} In _{85,8}	15.3		
Iron	Fe	FeGa ₃	34		
Manganese	Mn	Ga ₆ Mn	29		
Molybdenum	Mo	GaMo ₃	1108		
Mercury	Hg	None	N/A		
Nickel	Ni	Ga ₄ Ni	29.2		
Niobium	Nb	Ga ₃ Nb	29.2		
Osmium	Os	*	*		
Palladium	Pd	Ga ₅ Pd	29	Yes	5:1
Platinum	Pt	Ga ₆ Pt	28	Yes	6:1
Rhenium	Re	None	N/A		
Rhodium	Rh	*	*		
Ruthenium	Ru	*	*		
Scandium	Sc	Ga ₃ Sc	29		
Silver	Ag	Ag ₂ Ga	28	Yes	1:2
Tantalum	Ta	**	**		
Tin	Sn	None	N/A		
Thallium	Tl	None	N/A		
Titanium	Ti	**	**	No	-
Vanadium	V	Ga ₄₁ V ₈	29.7		
Yttrium	Y	Ga ₂ Y	29.8		
Zinc	Zn	None	N/A		
Zirconium	Zr	Ga ₃ Zr	860		
Tungsten	W	Ga ₅ W ₂	2237	No	-

* No phase diagram exists. Ga₃Os, Ga₂Os, Ga₃Ru, Ga₂Ru, GaRu, Ga₃Rh, Ga₁₇Rh₁₀, GaRh, GaRh₂, are known ordered phases of Ga-Os, Ga-Ru and Ga-Rh respectively.

** Phase diagram is incomplete. Ga₃Ta, Ga₂Ta₃, Ga₃Ta₅, Ga₃Ti, Ga₂Ti, Ga₅Ti₃, GaTi, Ga₄Ti₅, Ga₃Ti₅, GaTi₃, are known ordered phases of Ga-Ta and Ga-Ti respectively.

The key experimental results reported in Table 2.2 can be summarized as follows. Thirty one Ga-M phase diagrams were examined. Twenty four of these systems have at least one intermediate phase. Seventeen of these diagrams have a two phase region of liquid and intermediate phase for which the Ga remains liquid near room temperature. Seven of these systems were experimentally studied by the author to see if crystals form at room temperature. Six of the seven did form crystals. There appear to be at least nine more materials that are expected to form ordered phases at room temperature. A general conclusion is that there are many potential self-assemblies possible with Ga-M systems, not to mention the additional reactions possible at room temperature using m-ary systems or other low melting temperature metals (e.g. In, Hg, Bi, Sn). Rather than complete this empirical study, the remaining chapters will focus on properties and applications of a few of the Ga-M reactions that have been initially reported in this chapter.

2.4 Self-Assembly over distance: Spreading fronts

The reactions indicated in Figure 2.1 need not be limited to the immediate vicinity of an interface, but can extend for considerable distances as a spreading front. Figure 2.6a shows an example of a nearly planar front from a drop of Ga (outside the field of view of the image) that is spreading across a thin film of Au at room temperature. Figure 2.6b presents a schematic of the cross section of the front. The action of continuous spreading can be viewed as a type of self-assembly. The reacted region is grainy in appearance compared to the Au. It is composed mostly of crystallites of AuGa_2 (Figure 2.6c and d) and a Ga-rich liquid that is found between the grains. Note that this front spreads by an alloying reaction rather than by wetting. For thicker films of Au, Ga does

spread by wetting, but the wetting front is preceded by the reaction front. Figure 2.6e shows cross section of the Ga spreading on Ag that is composed of Ag_2Ga crystals surrounded by Ga-rich liquid.

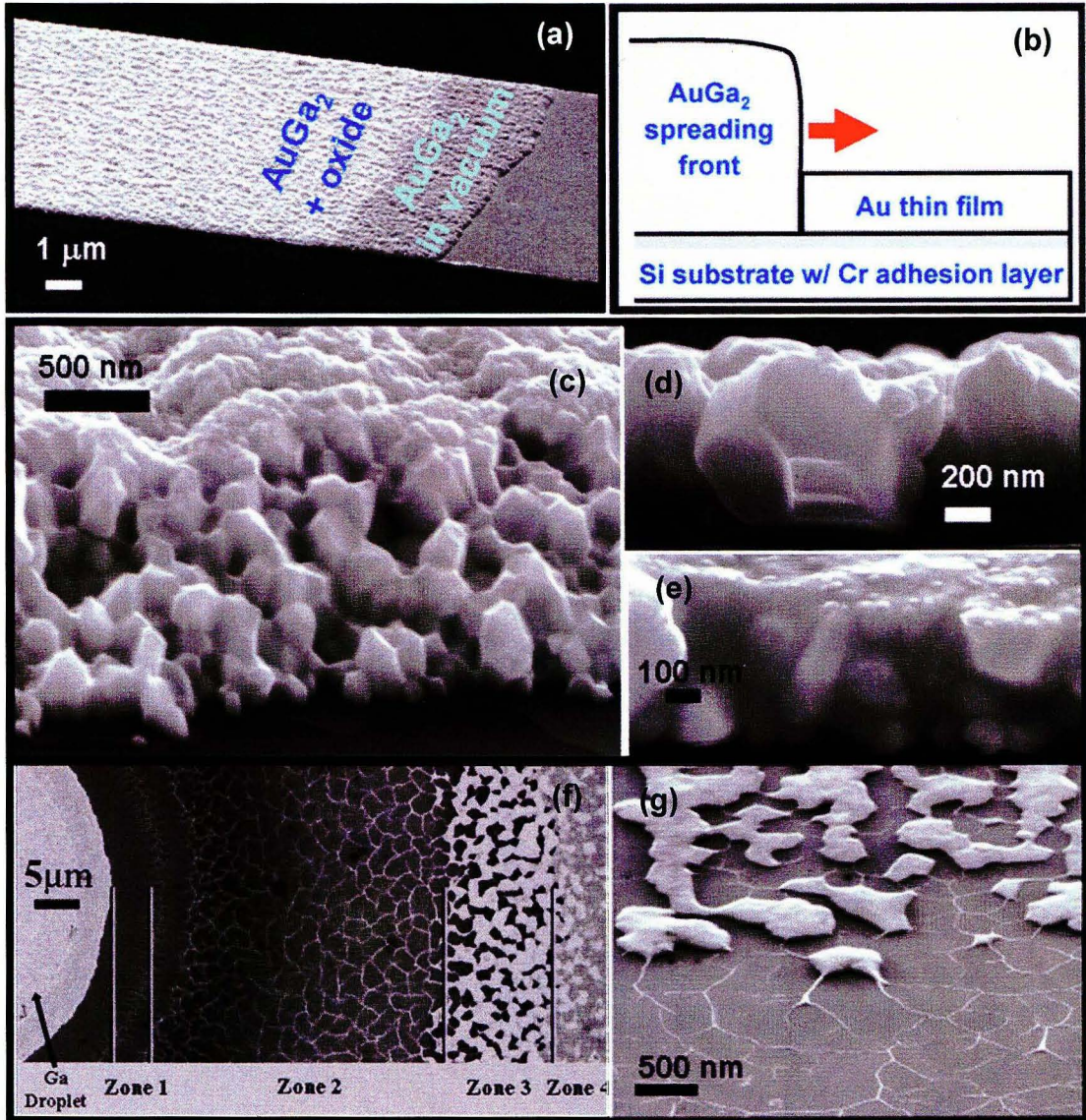


Figure 2.6. Self-assembly over distance. (a) A Ga-Au alloy planar front spreading at room temperature over Au. (b) A schematic of the front (side view). (c-e) Cross-section of the films after the passage of the spreading front that show the crystallites of (e and d) AuGa_2 , and (f) Ag_2Ga are surrounded by a Ga-rich liquid. (f,g) Nanostructured Au thin film due to non-planar spreading of Ga on Au thin film at 370°C .

Figures 2.6f and g show that the reactive spreading from a Ga droplet on a Au thin film can produce a variety of morphologies dependent on radial distance from the droplet [30]. This non-planar front of Ga spreading is observed at temperatures well above room temperature (between 310° C and 400 °C). Thus, reactive spreading through thin films appears well-matched to the processes used in microfabrication and planar lithography, and might offer some potentially interesting extensions to device fabrication.

This chapter has introduced several fundamental alloying reactions and their potential to serve as ways to obtain self-assembly of nanostructures. Detailed characterization of these processes will be reported in Part II.

PART II
FUNDAMENTAL SELF-ASSEMBLY PROCESSES

CHAPTER 3

REACTIVE SPREADING OF GALLIUM THROUGH THE METAL THIN FILM: PLANAR SPREADING

This chapter explores the interactions of liquid Ga with Au and Ag thin films near room temperature that results in formation of *reactive spreading fronts*. It was observed that when a drop of Ga is placed on a thin film of Au or Ag between 260 K and 470 K, a front spreads from the Ga through the film. This spreading is different from the regular mechanical spreading [31] of liquid over a flat surface which is referred to as *wetting*. Instead the Ga spreads through the metal film and reacts with it to produce Ga-M alloys.

Given the complexity of the spreading process, it is worth first presenting a qualitative description of the spreading process. Then qualitative images and quantitative measurements are presented that show that these descriptions are valid. Then time and temperature models of the spreading velocity are presented.

Figure 3.1 produces an overview of the main qualitative observation of Ga spreading on thin films of Au and Ag. Figure 3.1a shows the main features of reactive spreading from the source droplet. Au is dissolved from the film and then precipitates in crystals (which are found to be AuGa_2). The crystal in the droplet can grow to several microns in diameter. Depending on the film thickness the reaction front spreads with a velocity between ~ 0.1 and $7 \mu\text{m/hr}$ at room temperature.

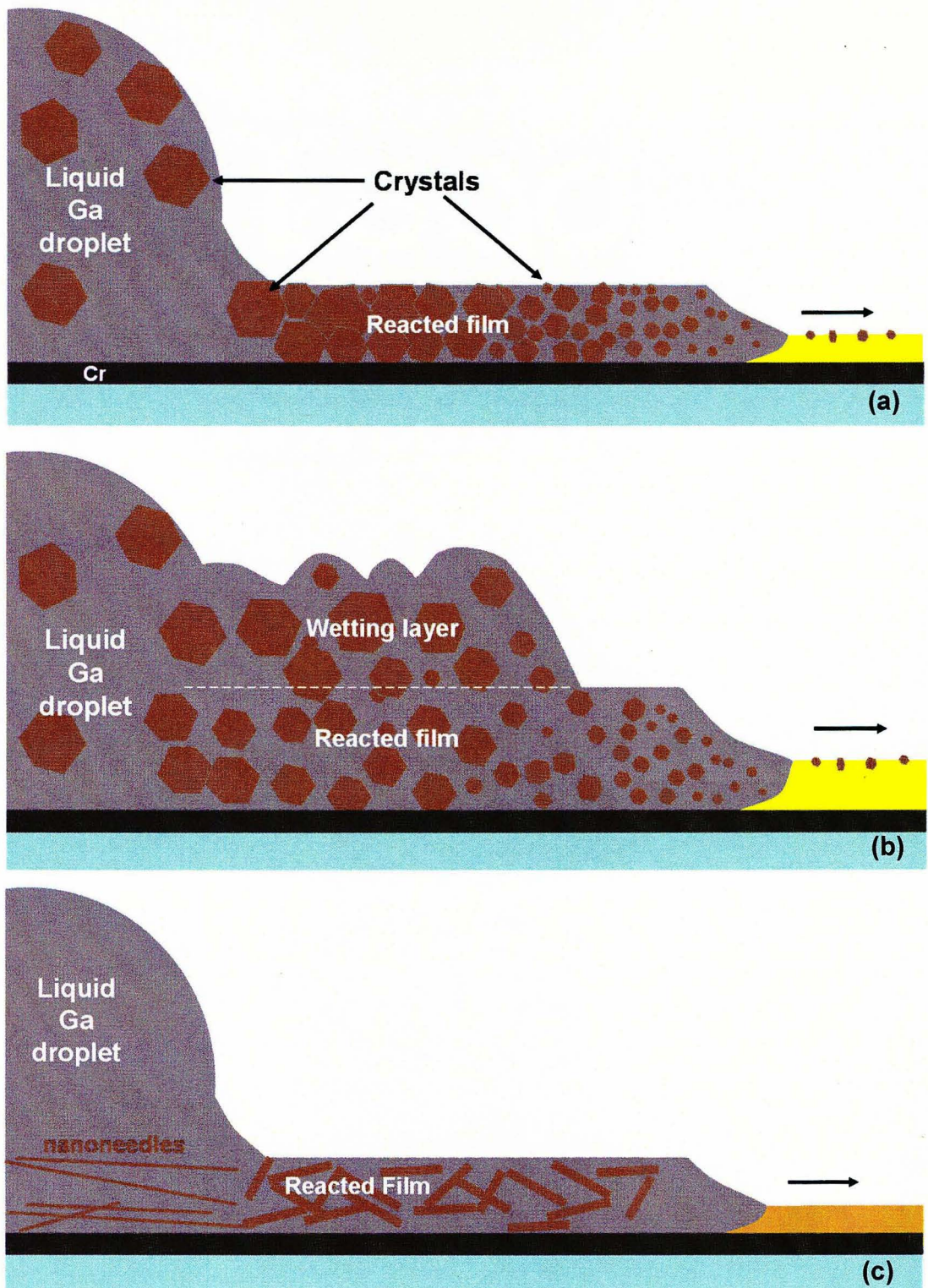


Figure 3.1. Schematic drawing of Ga spreading on a Au film (a) less than 150 nm, and (b) greater than 150 nm thick and (c) on Ag films at least as thick as 450 nm.

As the Ga spreads, it continues to dissolve the Au ahead of it and crystallites of diameters on the order of the film thickness precipitate from the liquid. The front is found to be 3.96 times thicker than Au film. The liquid Ga to AuGa₂ concentration found in the reacted films is consistent with the levels one would expect from the Au-Ga phase diagram. This is specifically seen in the thickness increases of the reaction front over that of the thin film. These thicknesses are consistent with all the Au being converted to the equilibrium value of liquid Ga and AuGa₂ phases at the location of the Ga front. However, this is not precisely true, because the crystals in the reacted layer continue to grow over time. This is also shown in that the crystallites closest to the droplet are larger and more closely packed than are the crystallites that are closer to the front. This suggests that while Ga diffuses forward rapidly, there is also a backward diffusion of Au, which is driven by the excess Ga in the droplet. Large crystals of AuGa₂ up to 10 μm diameter have been found in the droplet several months after the spreading appears to have stopped.

The velocity of the spreading front is observed to slow down over time. In typical solidification processes growth velocity decreases with time as $v(t) \propto t^{-1/2}$ because of diminishing quantities of liquid ahead of the front [32]. In the spreading processes observed in this study, the velocity also decreases over time. In this case, the velocity decreases due to the reduction in transport of Ga from behind the front to the front. It appears that as the crystallites grow together, they pinch off the flow of Ga from the droplet. While the front appears to stop, there is the possibility that dilute quantities of Ga diffuse into the Au without noticeably increasing the film thickness. This is noted in Chapter 4 experiments as discoloration of Au far beyond the front.

For Au films that exceed 150 nm in thickness, (Figure 3.1b) the front spreads with a nearly constant velocity over time. At these increased thicknesses the Ga wets the reacted layer. The wetting front does lag at a fixed but small distance behind the reaction front. The wetting front provides a source of Ga that bypasses the pinched-off channels between the crystallites. The wetting layer has a wavy appearance as would be expected for the thermally driven process known as Marangoni convection [33].

Ga reactions on Ag films are summarized in Figure 3.1c. For this system, spreading is only limited by the reaction rate. Even for Ag films as thick as 450 nm no wetting layer is observed. As long as Ga remains in the source droplet the velocity of the front is constant and the crystallites formed are rod-like and of random orientations. They never closely pack together, which leaves large channels for the transport of Ga. As a result, the front velocity remains constant with time.

Just ahead of the spreading front (in Figure 3.1a,b) small grains form. Apparently some Ga in the mostly Au film tends to nucleate small crystals. In Chapter 4 where spreading is reported for temperatures from 310 to 400 °C, more complex formations arise. At these temperatures the front becomes non-planar and large islands and other patches free of Au form ahead of the front.

3.1 Overview of experimental methods

Observations and evaluations of Ga spreading through thin films required several types of analysis to develop an understanding of the process. Electron microscopy, topography measurements of microscopic surfaces, composition analyses and

crystallographic structural analyses were performed using one or more instruments.

Table 3.1 summarizes the instruments and applications used in the study.

Table 3.1. List of the instruments and their application for this study.

Type	Model	Application	Specification
Scanning Electron Microscopy (SEM), Secondary electron detector	FE-SEM Supra 35	Imaging (contrast depends on height and conductivity)	2 nm resolution
SEM, Backscatter electron detector	FE-SEM Supra 35	Imaging (contrast depends on atomic number)	50 nm resolution
Transmission Electron microscopy (TEM)	JEOL 2000	High resolution Imaging	0.1 Å resolution
Atomic force microscopy (AFM)	M5 Park Scientific Instruments	Roughness and height measurements	1 Å resolution
Video/Optical microscopy	Wyko NT 2000	Movement of spreading front	500 nm resolution
Energy dispersive spectroscopy (EDS)	EDAX detector in SEM	Composition Analysis	1 at.%, 1 μm resolution
Crystallography	Rigaku D/max/B	Diffraction	0.005 degree

Unless stated otherwise in this chapter, all thin films of Au and Ag are prepared in a Technics sputtering system under the following conditions: A 10 nm Cr adhesion layer is sputtered using RF power of 300 W at 20 mbar operating pressure. Au and Ag are sputtered using DC power of 350 W at 20 mbar operating pressure. Au film of thickness between 20 and 400 nm and Ag films between 20 and 450 nm were prepared this way.

The placement of liquid Ga on the metal thin film is achieved by dipping a tungsten tip inside a Ga droplet. A small amount of Ga hangs from the tip. Dragging the Ga across

or touching the metal surface with the suspended Ga drop produces a liquid Ga line or droplet from 50 to 500 μm wide and from 5 to 50 μm thick.

Spreading front position and velocity is observed for up to 800 hours over a range of temperature between 260 K and 470 K. Occasionally samples up to 6 months old are examined; e.g., to observe long-term changes in crystal morphology.

3.2 Visual description of spreading

The sketches in Figure 3.1 are compared with SEM images. Due to the dramatic variations in scale sizes between the large Ga droplet, the great extent of spreading, and the small size of the crystallites, several images must be viewed to construct the conceptual model represented by Figure 3.1. Figures 3.2 to 3.4 show these features, starting with the Ga droplet in Figure 3.2. Figure 3.2a shows at an early time a Ga droplet on a 260 nm thick, unpatterned Au film. A grainy region is observed that extends about 100 microns beyond the base of the droplet. Ga continuously spreads until the droplet is drained of Ga. Figure 3.2b shows a smaller droplet of Ga on a different area of the same thin film after 3 days. The droplet is drained of Ga leaving behind a buckled film on the top of the reacted film. This film appears to be a gallium oxide (presumably Ga_2O_3 [17]). Also a wetting layer is seen on the top of reacted film.

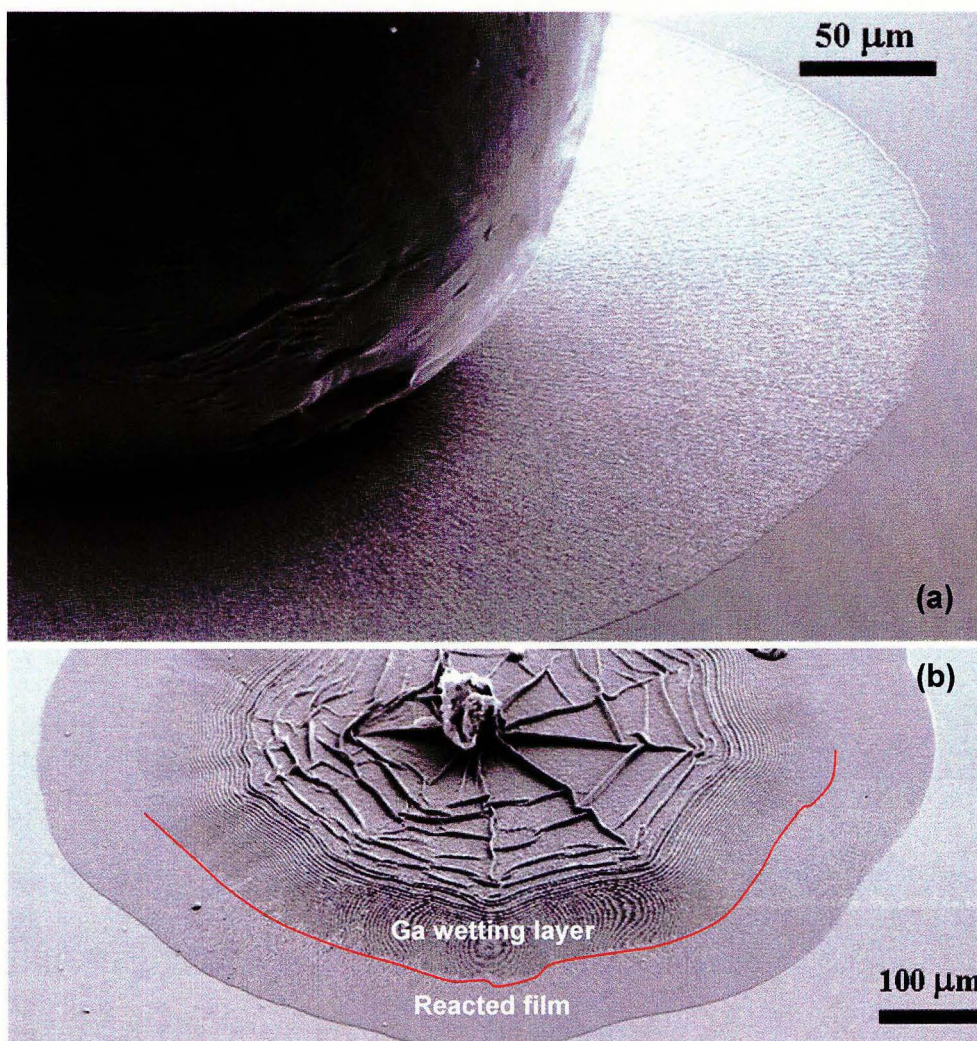


Figure 3.2. Ga spreading on Au. SEM image of Ga-Au front on a 260 nm thick Au after (a) a few hours from one droplet, and (b) after 3 days of spreading from another droplet.

Figure 3.3 shows fronts spreading on patterned Au lines of varying thickness. The fronts extend $\sim 100 \mu\text{m}$ past the Ga source. A spreading layer formed from a 50 nm thick Au layer is shown in Figure 3.3a. The material behind the front is grainy due to the growth of crystallites. The last 3 to 4 μm of the film are not as bright as the film further behind the front. This contrast difference results in differences in film conductivity. The darker region arises from one hour of spreading in the vacuum of the SEM. This is

evidence that the Ga at the surface is oxidized in air. For 110 nm film in Figure 3.3b the grains appear to be larger and in the 287 nm film in Figure 3.3c, an undulating wetting layer is observed.

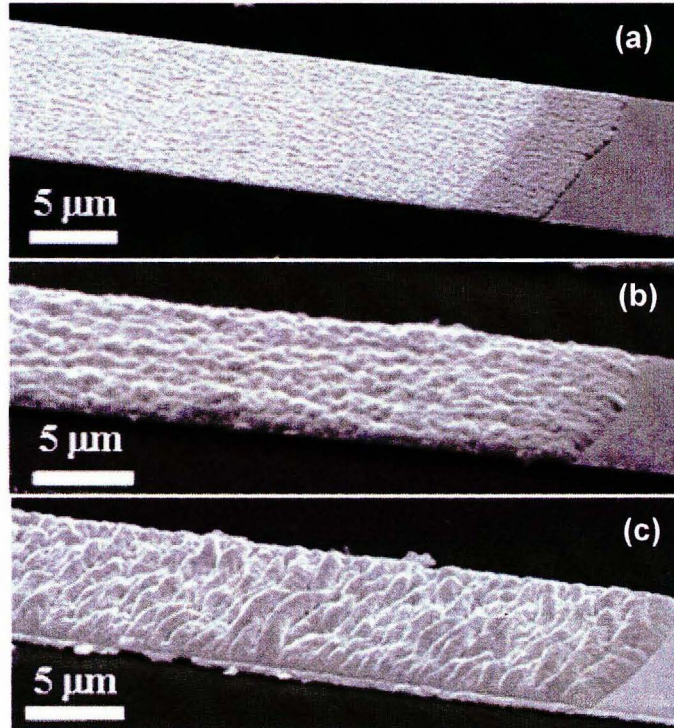


Figure 3.3. Ga spreading on patterned Au of thickness (a) 50 nm, (b) 110 nm and (c) 287 nm.

Backscatter SEM images of Ga-Au spreading layers formed at room temperature from 50 nm and 280 nm Au films are shown in Figure 3.4. The images of the Ga-Au crystals show up with higher contrast than the Ga [34]. In Figure 3.4a, well-separated domains of Au-Ga alloy (brighter regions) appear to be floating in the Ga-rich liquid (darker region) while in Figure 3.4b, the crystals are more densely packed and the Ga is barely visible.

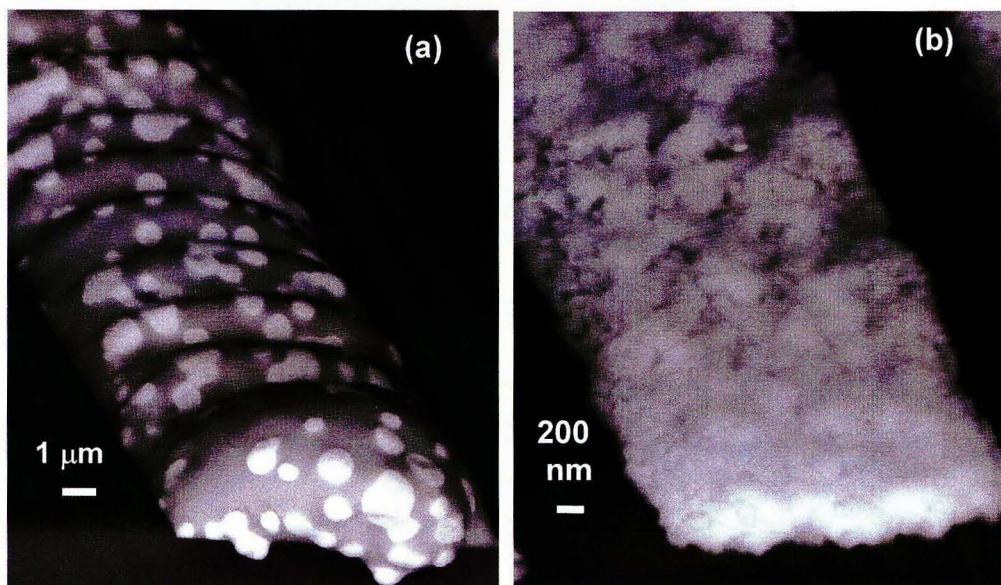


Figure 3.4. Backscattered SEM images of Ga spreading layer on (a) 280 nm and (b) 50 nm Au films that are cleaved normal to the direction of spreading. In (a) the Ga-Au crystals are well separated, compared to (b) where they are densely packed.

Reactive spreading of Ga on sputtered Ag films produces layers that appear less rough than reactively formed Ga-Au films of comparable thickness. No Ga wetting layer was observed for any Ag films between 20 nm and 450 nm thick.

3.3 Geometry and topography of samples

Figure 3.5a show a close-up of a spreading front that illustrates that the front is several times thicker than the thickness of the Au film. The graph in Figure 3.5b is derived from AFM measurements of the step height difference between the Au and the spreading front. The measurements show that the front is 3.96 times thicker than the original Au film for Au thicknesses up to 150 nm. For Au thicker than 150 nm the wetting layer is evident. The wetting layers up to 10 μm thick have been observed.

However, since the wetting front lags behind the reactive spreading front, the step height of the reactive front can still be measured. In Figure 3.5a For Ag the front height is 2.41 times higher than the thickness of the Ag film (Figure 3.5c).

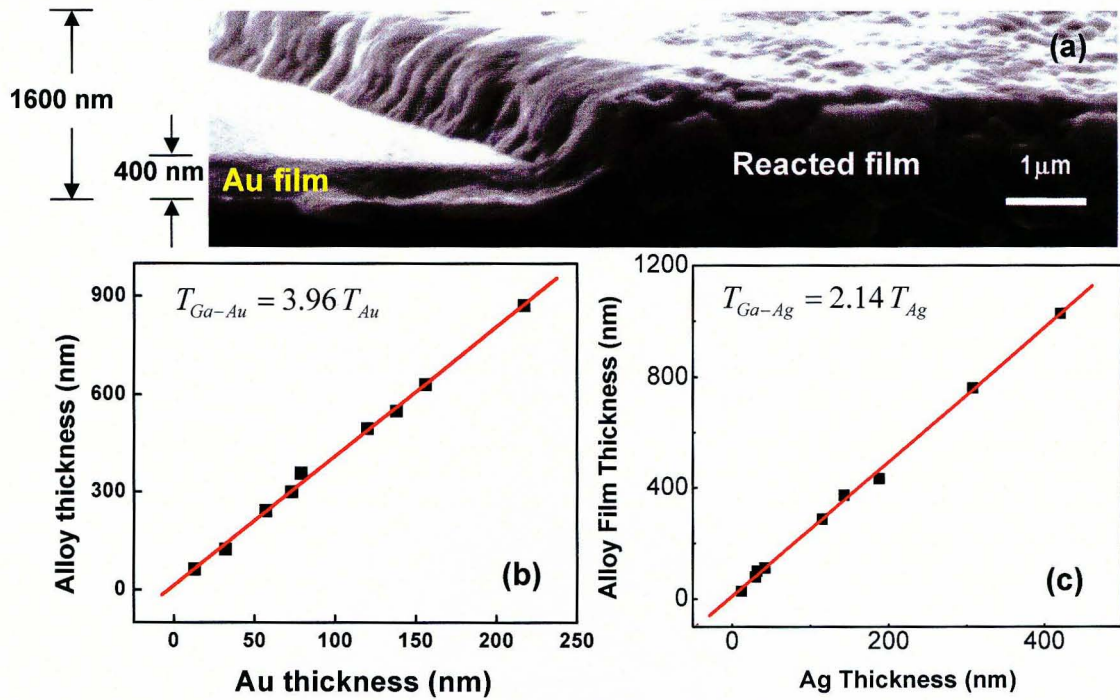


Figure 3.5. The height of the reacted film as a function of Metal film thickness. (a) SEM image of a Ga-Au spreading front. The thickness of the reacted film as a function of (b) Au and (c) Ag film thicknesses.

From difference in thicknesses between the metal film and the front one can estimate the volume between the crystal particles through which it is assumed most of the Ga-rich liquid flows. First, the atomic volume of the Au, Ga, and Ga_2Au is calculated. The atomic volume of an element or a compound is calculated as

$$\text{Atomic volume in cm}^3/\text{molecule} = \frac{\text{atomic weight in gm/mole}}{(\text{density in gm/cm}^3)(\text{Avogadro's number in molecule/mole})}$$

The densities of Ga and Au are 5.9 gm/cm^3 and 19.6 gm/cm^3 , respectively. The atomic weights of Ga and Au are 69.9 gm/mole and 196.9 gm/mole , respectively. Thus, the atomic volume of Ga is $1.96 \times 10^{-23} \text{ cm}^3$ and the atomic volume of Au is $1.69 \times 10^{-23} \text{ cm}^3$. Crystallography and composition analysis of the reacted film (Section 3.4) shows that the layer is made of crystalline AuGa_2 and Ga-rich liquid ($\sim 99\%$ Ga). The atomic volume of AuGa_2 has not been measured, but it can be roughly estimated. By adding the atomic volumes of Au and Ga_2 the atomic volume of the AuGa_2 crystals is $5.61 \times 10^{-23} \text{ cm}^3$. Dividing the atomic volume of AuGa_2 by atomic volume of Au, the occupied volume by AuGa_2 crystals in the spreading film is 3.31 times the volume of the Au film. Since the total volume of the layer is 3.96 times that of unreacted Au, the remaining liquid Ga is 0.65 times the volume of the Au film. The fractional volume of liquid that supports flow is then $0.65/3.96$ or 16 %.

The thickness of the fronts on sputtered Ag thin films was also measured as a function of the original Ag film thickness to be ~ 2.41 times greater than that of the Ag film (Figure 3.5c). The density of Ag is 10.5 gm/mole and the atomic weight of Ag is 107.8. Thus, the estimated atomic volume of Ag_2Ga crystals, assuming negligible density changes on formation of the ordered phase, is $1.70 \times 10^{-23} \text{ cm}^3$. A similar calculation shows that the volume fraction between the grains is 34 %. This shows that the grains are less densely packed during Ga-Ag spreading than during Ga-Au spreading.

Note that the roughness of the film after spreading depends on the thickness of the original Au film. In the thinner films, (i.e. 50 nm in Figure 3.3a), the peak-to-valley roughness (R_{pv}) of the film is $\sim 20 \text{ nm}$ R_{pv} . For thicker films, (i.e. 110 nm in Figure 3.3b) R_{pv} of the spreading layer is $\sim 100 \text{ nm}$ R_{pv} . Above 150 nm film thickness, the wetting

layer creates a thick wavy layer of Ga-rich liquid with roughness of 2 to 10 μm . However, the first few microns behind the fronts are thinner and more uniform than the wetting layer. The roughness value of this part of the film is ~ 200 nm R_{pv} .

3.4 Crystallography and composition analysis

3.4.1 Examination of crosssection of the reacted film

Reacted thin films are examined in crosssection. First, the samples are cooled in liquid nitrogen and then they are cleaved by fracturing the Si substrate normal to the direction of spreading. Figures 3.6 and 3.7 show the crystallites in Au and Ag films that form during the reactive spreading of Ga.

The Ga-Au reacted films are composed of nanometer to micrometer scale Ga-Au crystals within the film. Ga-rich liquid is found between the crystals and on the top surface. Comparing between particles on Figure 3.6a and b on which both were approximately 6 months old when sectioned, smaller particles are seen in the thinner film (Figure 3.1a), and larger particles are seen in the thicker film (Figure 3.6b). In both cases, the thickness of the crystals are nearly as thick as the reacted film.

Figure 3.6c is an SEM image of a crosssection of the reacted film formed on a 421 nm thick Au film. This sample was only one day old when sectioned. Since this film is even thicker than that in Figure 3.6a and b, the formation of larger particles is expected. However, the particles in Figure 3.6c are actually smaller than those in Figure 3.6b. Over time it appears that the smaller particles are absorbed into larger particles through the process known as Ostwald ripening [35].

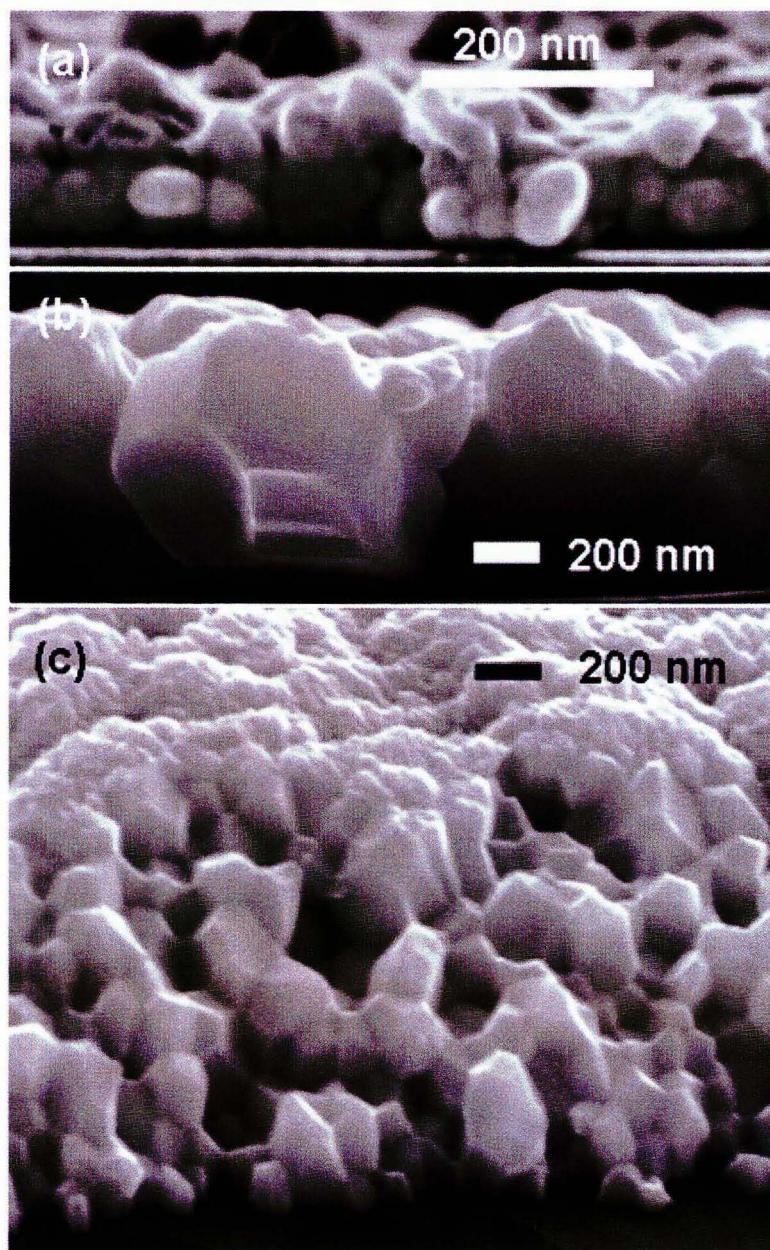


Figure 3.6. SEM images of Ga-Au crosssection. The thicknesses of the Au films before reactive spreading are (a) 110, (b) 330 and (c) 421 nm.

Figure 3.7 shows crosssections of Ga-Ag films after several days of reactive spreading. In all cases, the films have a nearly uniform texture on the nanometer scale

with crystals surrounded by Ga-rich liquid. Comparing the Ga-Au and Ga-Ag reacted films, the particles are more closely packed in Ga-Au than Ga-Ag.

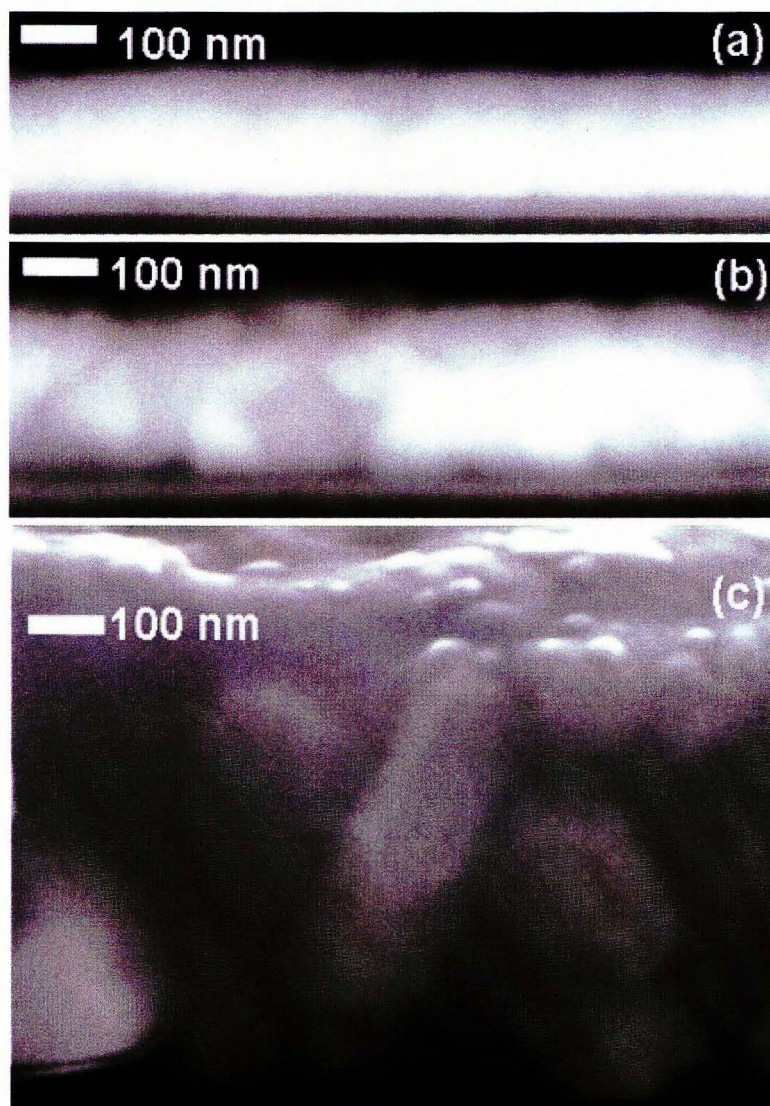


Figure 3.7. Crosssection SEM images of Ga-Ag taken with In-lens secondary detector. The thicknesses of the Ag films before reactive spreading are (a) 110, (b) 135 and (c) 250 nm.

3.4.2 Material Analysis of Ga-M films

EDS was performed to determine the concentration of Au and Ga behind the reaction front. EDS studies of Ga reacted film formed from 20 nm to 200 nm sputtered Au on

glass substrates show that the Ga concentrations is ~ 72 at. %. These data are taken far away from the Ga droplet. From application of the lever rule to the Au-Ga phase diagram (see Figure 2.5 and the example described in Section 2.2) one can estimate that 84 at. % of the material is solid AuGa_2 and 16 at. % is *Ga-rich liquid* (99 at. % Ga and 1 at. % Au).

X-ray diffraction (XRD) of Ga-Au samples was performed first at room temperature and then with the same samples cooled in liquid nitrogen. The samples were immediately transferred to an XRD sample holder. The spectra at room temperature correspond to that of AuGa_2 (Figure 3.8 black line). The cold sample shows additional peaks that belong to Ga. This demonstrates that the AuGa_2 crystallites are surrounded by crystalline Ga at low temperatures and Ga-rich liquid near room temperature (Figure 3.8 red line). These results confirm that the spreading film includes a mixture of AuGa_2 and liquid Ga at room temperature.

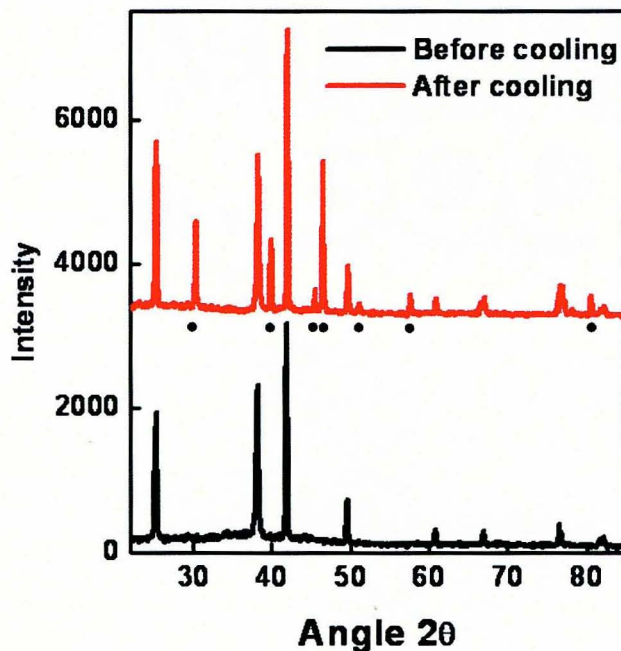


Figure 3.8. XRD of Ga-Au film before and after cooling the sample well below the Ga melting point. Black dots indicates the additional Ga peaks that appear after cooling the sample.

TEM images at room temperature also show that an amorphous region surrounds crystalline structures in the spreading film. Figure 3.9 shows low resolution and high resolution TEM images of a Ga-Au film. Figure 3.9a shows a grain (dark contrast) in the surrounding material (bright contrast). The high resolution image (Figure 3.9b) is a close-up view of the area inside the rectangle in Figure 3.9a. The lines in the region of the grain indicates that it is crystalline, while the material between the grains does not appear to be crystalline and is assumed to be the Ga-rich liquid.

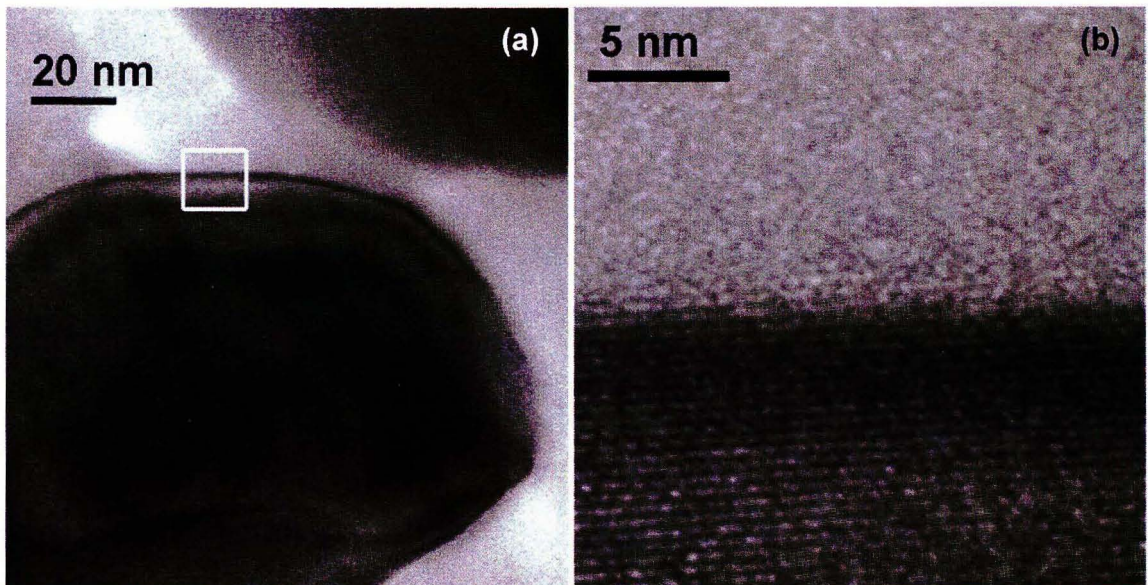


Figure 3.9. TEM images of an AuGa_2 grain in Ga-rich liquid. (a) Low resolution image, and (b) enlarged view of the rectangle in (a) which show that the grain is crystalline and it is surrounded by a non-crystalline material.

The composition of the reacted film formed at 26°C from 120 nm of Au is measured by EDS along the direction of spreading. Figure 3.10a shows resulting film after spreading for 5 hours. The remaining Ga droplet is visible at the left side of the image (Region 1) and the front has reached Region 4. The white line indicates the path where

EDS sampling was performed. Figure 3.10b shows the measured concentration of Ga along the path. Cr and Si contents is not reported since it is relatively constant across the EDS scan. At Region 1, the Ga concentration is 99 at. %. Over Regions 2 the Ga decreases to 74 at. %. Over Region 3 the Ga concentration decreases to 72 at. %. Region 4 is in the vicinity of the front. The fit (red line) shows a logarithmic decay between the Ga reservoir and the spreading layer. This fit will be used in Section 3.7 as part of a model of the spreading rate.

The inset is an expanded view of Region 4 that shows the transition in Ga concentration from the spreading front to the film. It changes from 72 at. % Ga to less than 1 at. % Ga (the limit of EDS detection). The distance l is referred to as the *transition width*. The transition width l together with the spreading velocity v , approximately represents the diffusion coefficient $D = vl$ [32]. Table 3.2 reports the transition width for Au films of various thicknesses at room temperature. Note that the ratio of the transition width to film thickness decreases from 4.7 down to 1.67 with increasing film thickness.

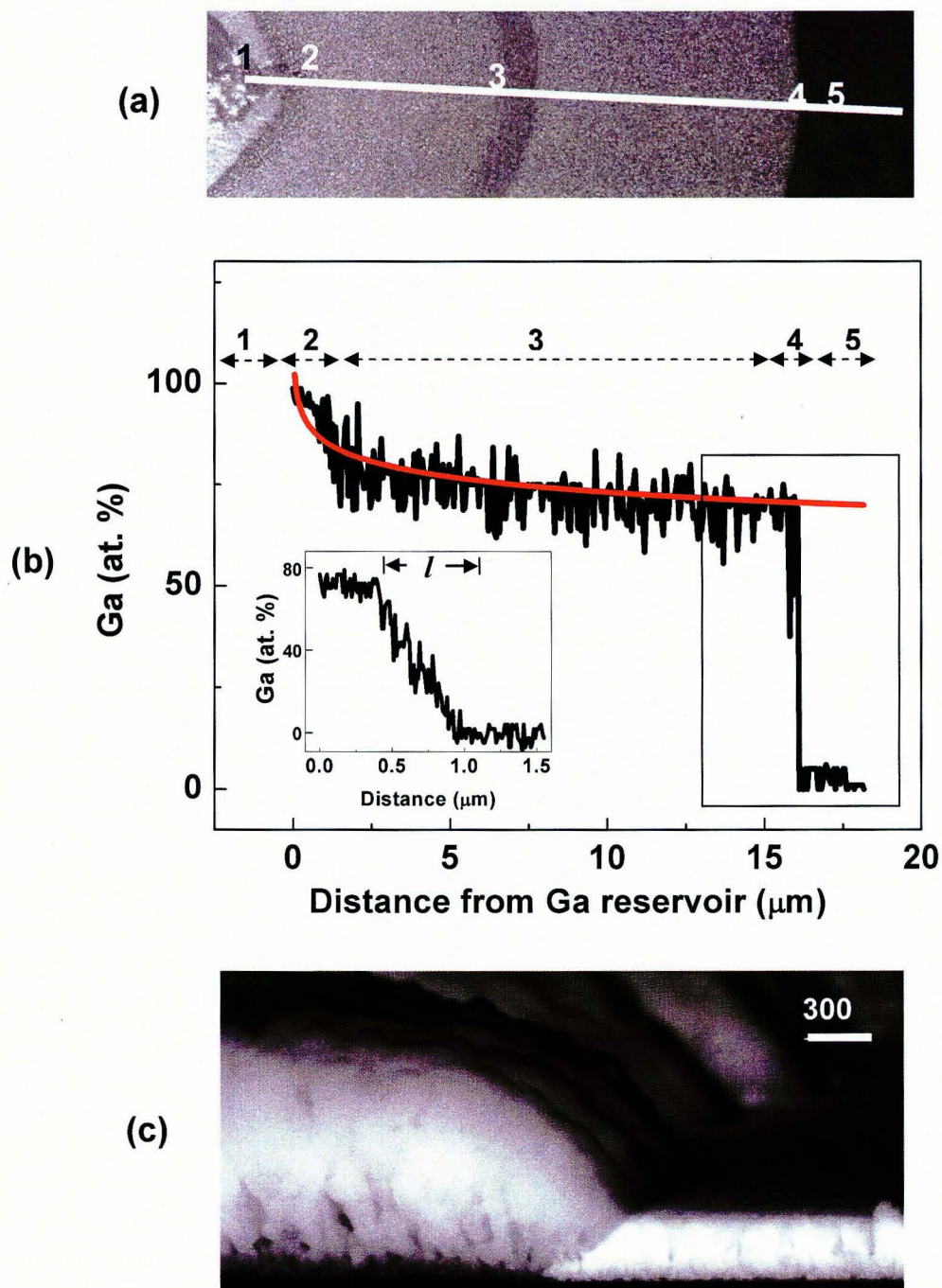


Figure 3.10. Composition changes from the Ga reservoir to the front on Au thin films. (a) Reacted Au on a 120 nm thick Au film. (b) Ga concentration along the white line in (a) as determined by EDS. The fit is $c = 0.99 - 0.83 \ln(x/0.05)$ (See Equation (3.3a) Section 3.7.2). (Inset) Transition in Ga concentration from the spreading front to the Au film. (c) Close-up of the side view of the spreading front on a 300 nm thick patterned line of Au.

While the transition widths are useful for modeling the diffusion and spreading rate, the actual front is not simply one-dimensional. Figure 3.10 shows the crosssection of a thick film along the direction of spreading. The front dissolves further into the Au at the air-Au interface than at the Au-substrate interface. It seems that the front reacts with the Au film over a finite distance. The junction between the Au film and front is not abrupt, giving rise to the slope of the Au/film interface seen in Figure 3.10c. At Region 5, more than 5 μm past the front, the Ga concentration becomes 0 at. %.

Table 3.2. Transition widths for various Au film thicknesses

Au film thickness t (nm)	Transition width l (nm)	l/t
30	140	4.7
50	175	3.5
125	210	1.6
300	500	1.7

Ga-Ag spreading films: Similar material characterization was performed for Ga-Ag spreading over different Ag films. EDS shows that the Ga concentrations is ~ 38 at. %. XRD studies of Ag-Ga films (Figure 3.11) reveals the existence of Ag_2Ga crystals. The transition width for different film thicknesses was measured and is reported in Table 3.3. The ratio of transition width to film thickness decreases from 3.3 to 1.6 with increasing thickness of the Ag.

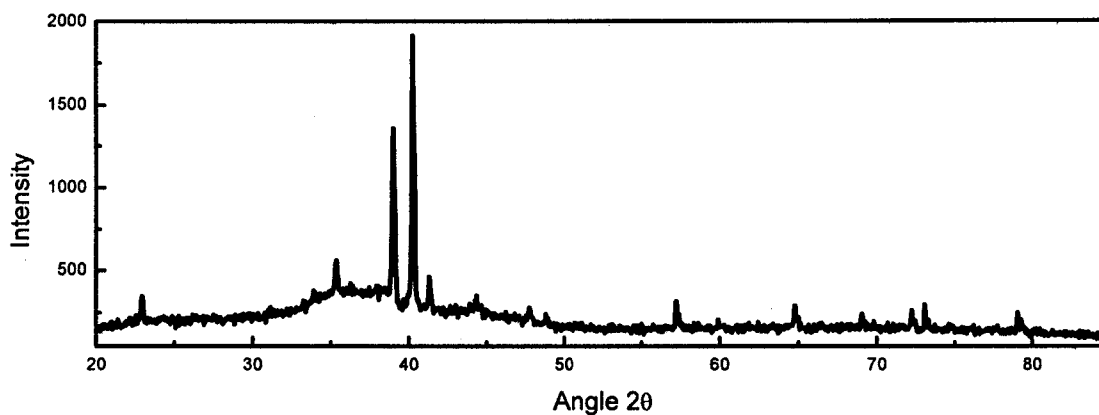


Figure 3.11. X- ray diffraction pattern of Ga-Ag. The spectrum corresponds to the ordered intermetallic ξ' phase of Ag_2Ga .

Table 3.3. Transition widths for various Ag film thicknesses

Ag film thickness t (nm)	Transition width l (nm)	l/t
70	230	3.3
120	270	2.3
175	425	2.4
202	450	2.2
300	480	1.6

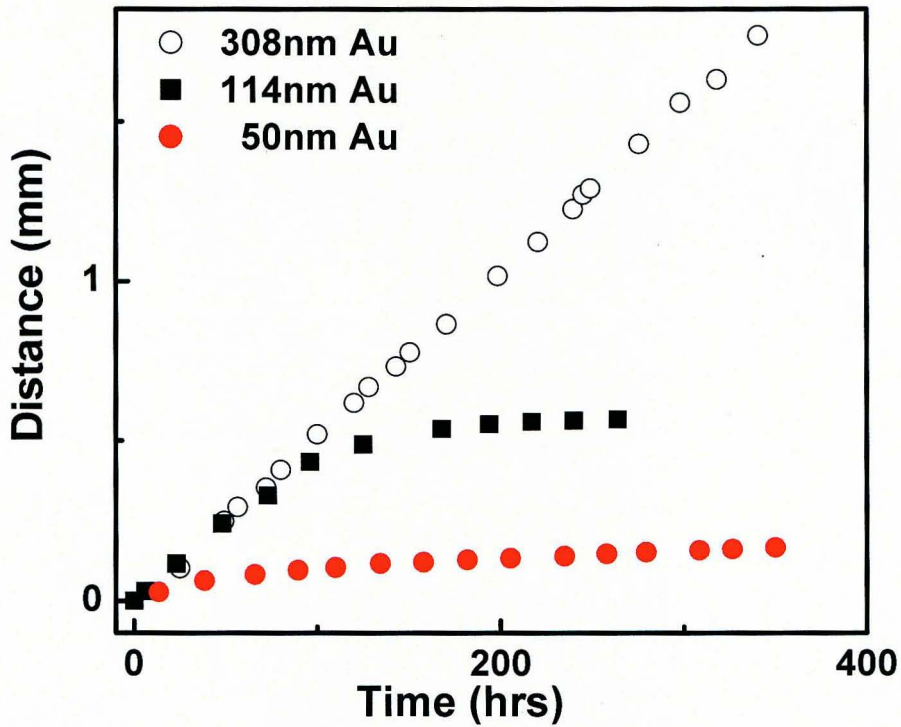
3.5 Spreading rates

Front velocity is observed to depend on temperature, film thickness and, in the case of Au, duration of the reaction. Velocity measurements were performed on 100 μm wide patterned traces of Au and Ag. Ga droplets of width much greater than that of the strips were placed at the end of each strip. The position of the front was monitored under a video microscope (in the Wyko NT2000 profilometer) for up to 1000 hours. During these experiments the droplet was never depleted of Ga, and depletion has not been considered as contributing to deceleration of the front. Measurements of front position were made as frequently as required by the spreading rates, but typically every 24 hours.

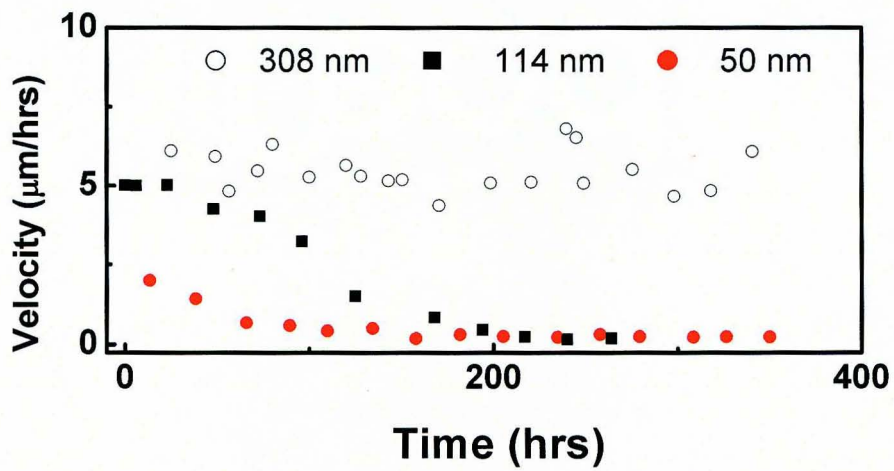
Each sample was maintained at a chosen temperature (within ± 2 °C) for the duration of the experiment, except for a 1 minute or less period when measurements of the front position were made under the Wyko.

Time dependence of spreading rates: The Au and Ag films were prepared as described in Section 3.1. The Au thicknesses were 50, 114 and 308 nm and the Ag thicknesses were 100 and 202 nm. Figures 3.12a and 3.13a plot the position of the front for different Au and Ag film thicknesses measured at room temperature. The velocity calculated from the data in these figures is plotted in Figure 3.12b and 3.13b.

The velocity is independent of time for Au thicknesses over 150 nm, but it decreases over time for film thickness under 150 nm. At the earliest time, the velocity appears to reach a maximum of 5-7 $\mu\text{m/hr}$.



(a)



(b)

Figure 3.12. Ga front (a) position and (b) velocity as a function of time for 50 nm, 114 nm and 308 nm thick Au films.

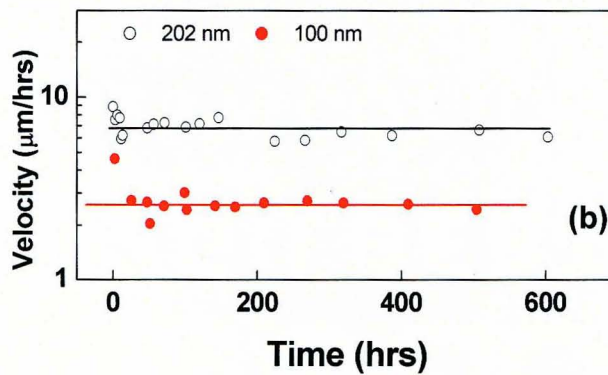
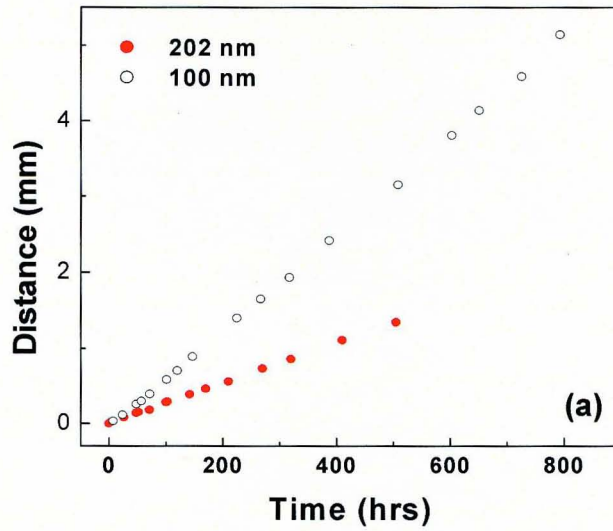


Figure 3.13. Ga front (a) position and (b) velocity on Ag thin films as a function of time. The linear fits for the velocity are $6.7 \mu\text{m/hr}$ for 202 nm film and $2.65 \mu\text{m/hr}$ for 100 nm film.

As proposed in the introduction to this chapter, the velocity decrease for thin Au films appears to be related to crystallites pinching off the flow of Ga. For thicker films for which a wetting layer follows the front, the velocity stays constant. Also for Ag, the grains do not pack tightly enough to pinch off the flow of Ga, and the spreading rate remains constant over times at all thicknesses.

Dependence of initial spreading rate on film thickness: Figure 3.14 plots the velocity as a function of film thickness of Au and Ag for the first few hours of spreading. The velocity reaches a maximum for Au films above 150 nm. For Ag films the velocity reaches a maximum above 100 nm. A more complex dependence is noted for Ag at 323 K. The velocity appears to overshoot and then decreases towards a constant value above 100 nm film thickness. In general, the spreading rate at higher temperatures is greater than at lower temperatures. This is to be expected if the reactive spreading is driven by diffusion of Ga into a second metal.

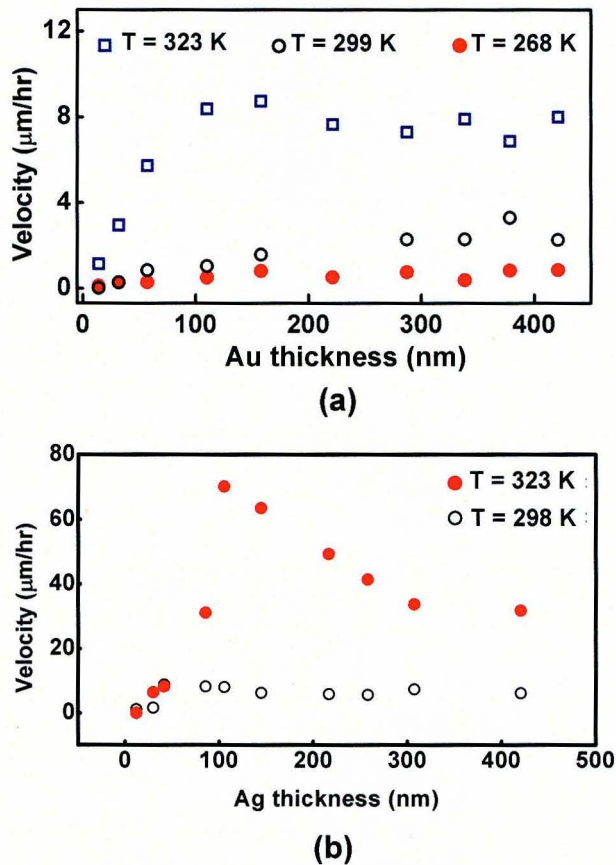


Figure 3.14. The velocity of the spreading front for (a) Au and (b) Ag films as a function of film thickness.

Temperature dependence of the initial spreading rate: The velocity of the front on 100 μm wide Au patterns was measured at various temperatures. To determine the initial spreading rate, velocity is determined from the time it took for the front to move only a few micrometers. Thus, for a temperature range between 250 K and 290 K, the front movement was measured within a few days after the Ga was placed on the sample. For the temperature range of 290 K to 320 K the front movement was measured within the first few hours. In the temperature range of 320 K to 400 K the movement was measured within an hour. For even higher temperatures the measurements were done over even shorter times, from a few seconds to a few minutes. Figure 3.15 shows a typical plot of spreading velocity versus temperature for a 35 nm thick Au film. The plot shows that the spreading rate is very sensitive to the temperature at which the spreading occurs. Model and numerical fits to this data are presented in the next section.

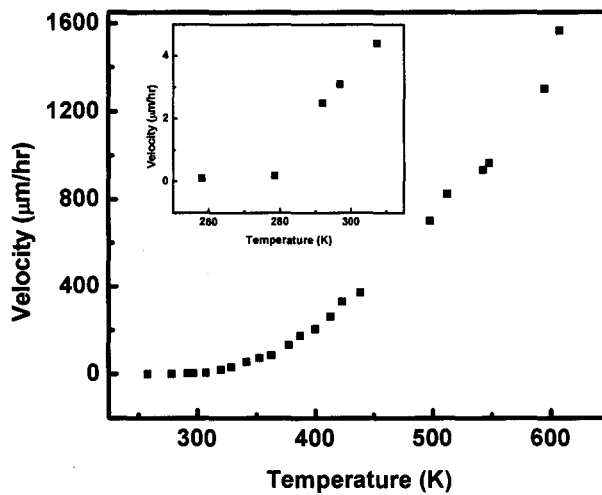


Figure 3.15 Temperature dependence of front velocity on Au thin films of 35 nm thickness. Inset shows an expanded range of the plot for temperatures less than 310 K.

3.6 Temperature dependence of Ga diffusion through Au

Diffusion is a thermally activated process that can be described by [32]

$$D = D_0 \exp\left(\frac{E_A}{RT}\right) \quad (3.1)$$

where E_A is the activation energy and D_0 is the diffusion constant at infinite temperature. A logarithmic plot of this as a function of $1/RT$, where T is the temperature and R is the universal gas constant, produces a straight line with a slope of E_A and a zero intercept of D_0 . The diffusion constant can be estimated from measurements of the spreading rate v and the length of the transition region l (reported in section 3.4) [32]. The model assumes a linear change in Ga concentration across the transition region ($\frac{\partial c}{\partial x} = -\frac{c}{l}$). This assumption is justified by the EDS data taken from the spreading front [Figure 3.10b (inset)]. Using Fick's first law ($J = -D \frac{\partial c}{\partial x}$) where $J = cv$ is the flux density of Ga, the diffusion constant is written as

$$D = vl \quad (3.2)$$

The values of D are plotted on a log scale against $1/RT$ in Figure 3.16. The value of D for the 300 nm Au film (Figure 3.16.a) is linear over the entire range of temperature with a slope of 7.07 kcal/mole. Previously, Gebenik and Tonokopryad have investigated the kinetics of Ga spreading on the surface of Au at temperatures between 350 and 670 K and reported the slope of the diffusion graph to be 7.00 kcal/mole [36].

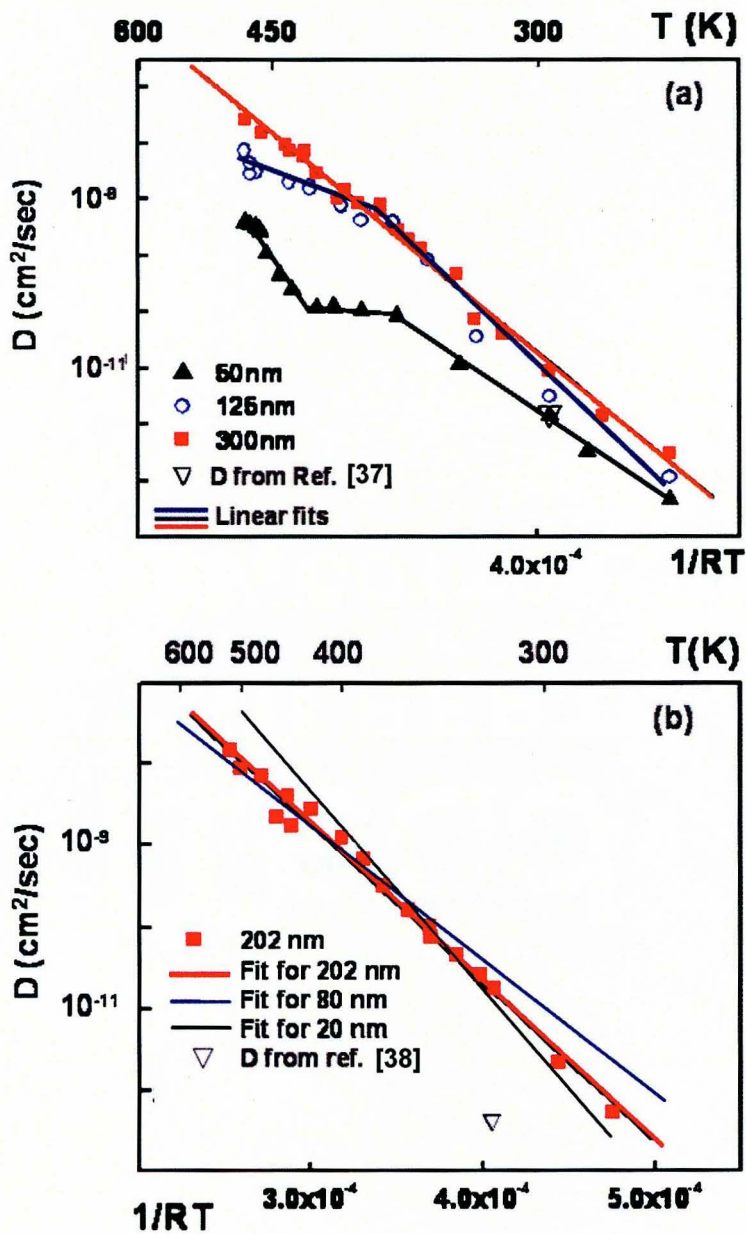


Figure 3.16. Ga diffusion constant at the early stage of the spreading process as a function of temperature for (a) 50, 125 and 300 nm Au films, and for (b) 20, 80, and 202 nm Ag films. To reduce clutter in (b) only the fits to the data are shown for the 20 nm and 80 nm films.

As described in section 3.2, for thick films of Au, Ga spreads as a wetting layer over the top of the reacted film. Thus, in addition to Ga flow between the grains, there is also transport of Ga through the wetting layer too. The excessive quantities of Ga close to the front suggest that the front velocity is only limited by the reaction rate of Ga with the Au film.

In 125 nm Au films, the fit is piecewise linear and has a kink at temperature about 385 K. For the temperature range lower than 385 K ($0.50T_m$, where $T_m = 770$ K is the melting point of AuGa₂) [26] the slope of the graph is 7.7 kcal/mole. This slope is nearly identical to the slope for 300 nm Au film. For temperatures between 385 K and 470 K (0.50 to $0.65T_m$) the slope of the graph is 3.9 kcal/mole. In this temperature range, intergrain diffusion may be a major contribution to the total flux. If this is true, then the slope in this range gives the activation energy of intergrain diffusion [39, 40]. Typically activation energies for intergrain diffusion are between 0.5 to 0.75 of the activation energy of the reaction [41].

For 50 nm Au thin films, the graph is more complicated. At lower temperatures, the slope of the graph is 6.9 kcal/mole, which again is close to the activation energy for the 300 nm film. For temperatures between 385 K and 445 K ($0.50 - 0.60T_m$) the slope decreases to 2.01 kcal/mole. For temperatures above 500 K ($0.65T_m$), the slope increases to 12.7 kcal/mole. This might be related to the formation of Au nanowire networks (reported in Chapter 4), although these networks have been shown to form at higher temperatures (580 K to 680 K) [30]. Another possibility is that at higher temperatures Ga may diffuse through the grains of AuGa₂ since the sample is heated above 0.65 of the

melting point of the grains. The above reported activation energies are summarized in Table 3.4.

Table 3.4. Activation energies for various Au film thicknesses and temperature ranges

Temperature range	Film Thickness		
	50 nm	125 nm	300 nm
260 K to 385 K	6.9 kcal/mole	7.7 kcal/mole	7.07 kcal/mole
385 K to 445 K	2.01 kcal/mole	3.9 kcal/mole	7.07 kcal/mole
445 K to 500 K	12.7 kcal/mole	3.9 kcal/mole	7.07 kcal/mole

Diffusion constants can be defined not only for atomic diffusion through a crystalline matrix, but also for flow between grains [32]. At temperatures between about 0.6 and 0.8 T_m , where T_m is the equilibrium melting temperature of the media, transport by grain boundary diffusion can greatly exceed atomic diffusion [32]. The competition between these two rates can in many systems lead to markedly different effective diffusion constants over different temperature ranges. This may be one source of the change in the slopes of the fits in Figure 3.16. Further consideration of time and temperature dependent diffusion constants is presented in Section 3.7.

Diffusion data for Ag-Ga for 20 nm, 80 nm and 202 nm Ag films is plotted in Figure 3.16b. Each graph is linear over the entire range of temperatures. The data for 202 nm Ag film are plotted in Figure 3.16b showing that the activation energy (slope of the graph) is 4.62 kcal/mole. The activation energies for Ag films are summarized in Table 3.5.

Linearity for the entire range of temperatures for all Ag film thicknesses suggest that the spreading is governed by a single types of diffusion at all temperatures. The differences between Figure 3.16a and b are believed to be related to the fact that Ga-Au forms close-packed grains (Figure 3.6) that limit intergrain diffusion, while Ga-Ag form

loosely packed grains (Figure 3.7) that enable significant area for the transport of Ga. Also Ga-Au supports a thick wetting layer, while Ga-Ag does not support a wetting layer.

Table 3.5. Activation energies for various Ag film thicknesses and temperature ranges

Temperature range	Film thickness		
	20 nm	80 nm	202 nm
260 to 500	4.9 kcal/mole	4.2 kcal/mole	4.62 kcal/mole

3.7 Model of the time dependent front velocity of reactive spreading of Ga on Au

In this section a model of the reactive spreading of Ga on Au is proposed that describes the decrease in the velocity with time. It is assumed that Ga is only transported through the channels between the grains and not through the grain themselves. This assumption is consistent with the higher melting temperature, and thus lowered diffusion rate through AuGa₂ grains. The velocity decreases with increasing distance between the Ga reservoir and the front, and also with the reduced area for Ga flow as the crystallites grow together. A model based on these assumptions is compared with the measured changes in spreading velocity. Fitting the data with the model gives the value for the intergrain diffusion constant D_{ig} . The diffusion constant calculated from this method is compared with the diffusion constant measured at the early stages of the spreading process (Figure 3.16).

More specifically, the model incorporates the following assumptions:

1. There is a gradient in the Ga concentration between the Ga reservoir and the spreading front. This concentration gradient brings Ga to the spreading front to react with the Au film.
2. Ga is transported through channels between the AuGa₂ grains. The fraction of the volume available for Ga transport between the grains is called the *open void fraction*. The open void fraction decreases over time as the grains grow together (as suggested by Figure 3.6).

The following equation for the Ga concentration gradient between the reservoir (Ga droplet) and the front is proposed (based on the EDS data in Figure 3.10),

$$\frac{\partial c}{\partial x} = -\frac{(c_0 - c_f)}{x} \quad (3.3)$$

which has the general solution of

$$c = c_0 - (c_0 - c_f) \ln\left(\frac{x}{x_0}\right) \quad (3.3a)$$

where c_0 and c_f are the respective concentrations of Ga-rich liquid (with respect to the total Ga in the liquid and AuGa₂) in the reservoir and in the reacted film. The value of x_0 is a small positive number corresponding to the location where the Ga concentration is c_0 .

The effective intergrain diffusion coefficient D_{eff} is defined as [42]

$$D_{eff} = \frac{\varepsilon}{k_t^2} D_{ig} \quad (3.4)$$

where ε is the open void fraction, D_{ig} is the diffusivity of liquid Ga in the intergrain region, and k_t is called the *tortuosity*. The value of k_t compensates for added path lengths due to channels being oriented in three dimensions, not just in the direction of front movement.

SEM study showed that the grains in the reacted film become larger and larger over time until they almost grow in diameter to the thickness of the film (Figure 3.6). From these observations the following relation for open void fraction as a function of time is proposed

$$\varepsilon = (1 - \varepsilon_f)e^{-t/\tau} + \varepsilon_f. \quad (3.5)$$

Equation (3.5) is configured so that the open void fraction of the film at $t = 0$ is unity, prior to the formation of any grains, and ε_f at $t = \infty$, with the steady state value of ε being reached within a time on the order of the characteristic time τ .

Substituting the equations (3.3) to (3.5) into Fick's first law, $J = -D_{ig} \frac{\partial c}{\partial x}$, yields

$$J = \left[\frac{(1 - \varepsilon_f)e^{-t/\tau} + \varepsilon_f}{k_t^2} \right] D_{ig} \frac{(c_0 - c_f)}{x} \quad (3.6)$$

where J is the flux of Ga per unit area, per unit time. For the front to advance an incremental distance of Δx in a incremental time of Δt , the flux of Ga at the front is

$$J = c_F \frac{\Delta x}{\Delta t} = c_F v \quad (3.7)$$

where v is the velocity of the front and c_F is the at. % of Ga with respect to the Au-Ga alloy (i.e. total percentage of Ga in the liquid and the AuGa₂) in the front. Over this short distance the concentration and flux can be approximated as independent of time (i.e. ignoring Fick's second law $\frac{\partial c}{\partial t} = -\frac{\partial J}{\partial x}$). This enables a simple model to be developed in which a limited set of measured concentrations can be used in place of time dependent concentration and fluxes, which would require a much more extensive set of measurements than it was possible to obtain. However this approximation does lead to a time-dependent velocity through the time dependence of the open void fraction ε .

Combining equation (3.6) and (3.7) and substituting velocity $v = \frac{dx}{dt}$ gives

$$c_F \frac{dx}{dt} = \left[\frac{(1 - \varepsilon_f) e^{-t/\tau} + \varepsilon_f}{k_i^2} \right] D_{ig} \frac{(c_0 - c_f)}{x} \quad (3.8)$$

Solving the above equation for $x(t)$ leads to

$$x(t) = \sqrt{2 \left(\frac{c_0 - c_f}{c_F} \right) \times \left[(1 - \varepsilon_f) \frac{D_{ig}}{k_i^2} \tau (1 - e^{-t/\tau}) + \varepsilon_f \frac{D_{ig}}{k_i^2} t \right]} \quad (3.9)$$

Taking the derivative of equation (3.9) with respect of time gives the velocity of the front as

$$v(t) = \left[(1 - \varepsilon_f) e^{-t/\tau} + \varepsilon_f \right] \sqrt{\frac{\left(\frac{c_0 - c_f}{c_F} \right) D_{ig}}{2k_i^2 (1 - \varepsilon_f) \tau (1 - e^{-t/\tau}) + \varepsilon_f t}} \quad (3.10)$$

In equation (3.9) note that considering $\varepsilon_f=1$, the first term becomes zero and the second term shows the standard dependence of diffusion on distance for the diffusion limited regime (i.e., $x \propto \sqrt{Dt}$). Setting $\varepsilon_f=0$ the velocity decreases to zero for time. This is the situation in which Ga flow is completely pinched off by the crystals.

3.7.1 Parameters for model

The experimental values needed for equation (3.10) are reported in this section and summarized in Table 3.6.

The value of Ga-rich liquid concentration in the Ga droplet c_0 is measured by EDS to be 0.99. The value of Ga-rich liquid concentration in the spreading film near the front is measured by EDS data and construction of level rule in Ga-Au phase diagrams to be 0.16. The total Ga concentration of the spreading film near the front c_F is measured by

EDS data to be 0.72. This value is included Ga-rich liquid as well as AuGa₂ crystals. The value of x_0 must be nonzero. Choosing it to be 0.05 μm produces the best fit that is plotted in Figure 3.10b.

The experimental value of k_t reported for different granular materials varies between 1.2 and 2.5 [42]. There are no reports of the experimental value for k_t for the system of Ga-Au. The average value of the reported data for the various material system of 1.85 was selected for the model.

The final open void fraction, ε_f is chosen to be 0.16 based on the percent volume calculation in Section 3.3, which based on the assumptions in this estimate gives $c_f = \varepsilon_f$.

The characteristic time τ is the time for grain size to asymptotically reach the thickness of the alloy film. Currently τ has not been measured. So instead it is used as a free parameter that is chosen by fitting the model with the experimental data.

Table 3.6. Experimental values used in the model.

Parameter	Concentration of Ga-rich liquid in droplet c_0	Concentration of Ga-rich liquid just behind the front c_f	Fraction of all Ga to all Ga and Au just behind the front c_F	Open void fraction ε_f	Tortuosity k_t
Experimental value	0.99	0.16	0.72	0.16	1.85
Measurement method	EDS data	EDS data and application of lever rule to the phase diagram	EDS data	$\varepsilon_f = c_f$	Average of reported data for different granular materials

Using these values in equation (3.10) leads to

$$v(t) = \left[0.84e^{-t/\tau} + 0.16 \right] \sqrt{\frac{2.36}{2.13\tau(1 - e^{-t/\tau}) + 0.16t}} D_{ig} \quad (3.11)$$

In equation (3.11) τ is a free parameter and D_{ig} is the parameter of interest. These parameters are determined by finding the values that best fit the model to the measured time-dependent velocity of the front.

Ga front velocities on Au were measured for four different samples as a function of time. Two samples were for circular spreading from a Ga droplet on unpatterned Au and two samples were for linear spreading on patterned lines of Au. Figure 3.17 shows the measured results for the two linear samples as well as the best fit curves to the equation (3.11).

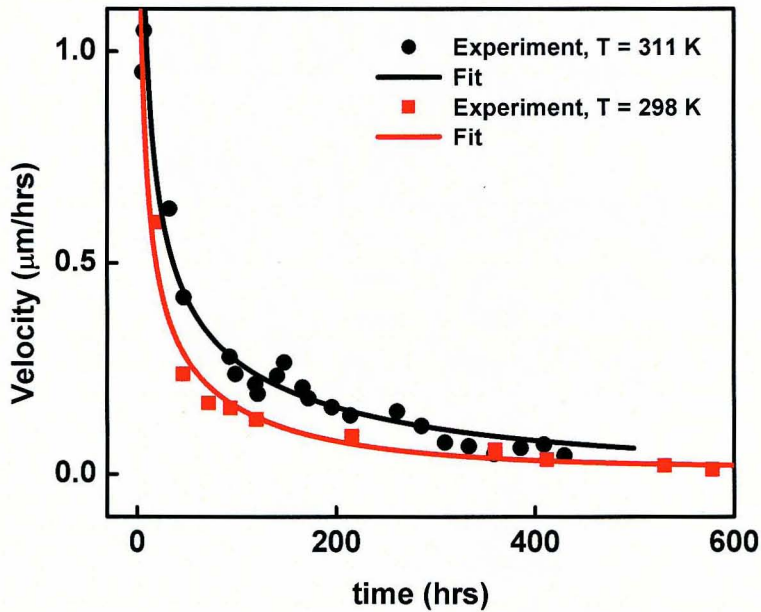


Figure 3.17. Time-dependent velocity of fronts on 125 nm thick patterned Au lines. Measured data and the best fits to equation 3.11. The fixed parameters used in the model are reported in Table 3.6 and the resulting parameters that give the best fit are reported in Table 3.7.

Table 3.7 lists the values of τ and D_{ig} that gives the best fits to the four sets of data. The diffusion coefficient, D_{ig} is between 0.88×10^{-10} and 0.95×10^{-10} at room temperature and it increases to 1.6×10^{-10} cm²/s at 311 K. The value of D_{ig} is almost two orders of magnitude larger than the reported value of 1.6×10^{-12} cm²/s for Ga diffusion inside the bulk Au at room temperature [37]. These results are in agreement with the fact that diffusion along the grain boundaries is much larger than Ga diffusion through the atomic lattice [41]. Although geometry of the spreading has not been considered in the model, the model can be well fit in both linear and circular geometries.

Table 3.7. Value resulting from the best fits to the model of reactive spreading of Ga on Au.

	Temperature (K)	Geometry of spreading	Time constant τ (hours)	Diffusion coefficient D_{ig} (m ² /sec)
1	298	Linear	192	0.95×10^{-10}
2	311	Linear	360	1.6×10^{-10}
3	298	Circular	168	0.88×10^{-10}
4	311	Circular	216	1.12×10^{-10}

Figure 3.18 plots the value of D_{ig} from Table 3.7 together with the data from Figure 3.16a. The two added data points fit the line corresponding to the higher temperature data. The slope of the line is 4.23 kcal/mole. This value can be considered to be the activation energy of diffusion of liquid Ga along the boundaries of the AuGa₂ crystals. Because the crystallites pinch off the flow, the effective diffusion constant appears lower than D_{ig} . This is even observed for less than 5 hours of spreading (open circles) and is very pronounced for 500 hours of spreading (triangles). Above 385 K, D and D_{ig} appear

to be the same. This is consistent with the increase in the value of τ with temperature. Apparently the time to pinch off increases with temperature (Table 3.7).

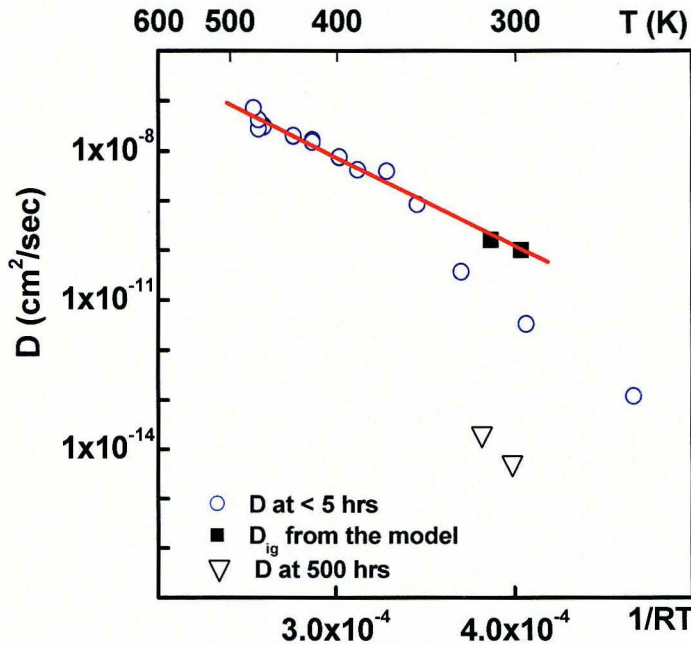


Figure 3.18. Ga diffusion constant as a function of temperature on 125 nm Au. The open circles are from Figure 3.16a for early measurements. The red line is the linear fit to the high temperature data.

This chapter has reported on the phenomena of Ga spreading on Au and Ag thin films. EDS, XRD and TEM studies of the film reveal the formation of a Ga-rich liquid with intermetallic crystallites of AuGa₂ and Ag₂Ga. SEM examination of crosssections of the films reveals that the packing fraction of the crystallites inside the Ga-Au reacted film is much higher than that of Ga-Ag. The time dependent velocity of the front over Au films of less than 150 nm decreases dramatically over time. However the velocity of the front on Au films of thicker than 150 nm and Ag films of all thicknesses studied does not

change with time. In the case of thick Au films, the velocity independence is due to wetting of the Au-Ga reacted film by Ga. In the case of Ag, the velocity independence is due to the low packing density of Ga-Ag crystallites. These observations suggested a model for the spreading of Ga based on transport of Ga between grains of crystallites that grow together over time.

CHAPTER 4

REACTIVE SPREADING OF GA: NON-PLANAR SPREADING

In Chapter 3, Ga was shown to spread through Au as a planar front leaving behind AuGa₂ crystallites that continue to grow as the Ga-rich liquid alloy spreads forward. In this chapter it is reported that over a range of temperatures and film thicknesses, a non-planar front develops and a more complex set of nanostructures arise, including networks of interconnected nanowires.

4.1. Sample preparation

A silicon substrate is first RF sputter-coated with a 5 - 10 nm Cr (300 W, 20 mtorr base pressure) followed by DC sputtering of a 10 to 100 nm Au thin film (350 W, 20 mtorr base pressure). Using a sharp tungsten tip, a droplet of Ga (10 to 150 μm in diameter) is placed on the Au film. The sample is then transferred to a hot plate and heated in air at temperatures between 310 and 400 °C for 5 to 10 minutes. It is also possible that first heat the substrate and then place the drop on the substrate. The sample is then cooled down to room temperature (20 to 25 °C) by placing it on a metal heat sink. Spreading reactions were observed for several thicknesses of Au at different temperatures. Also, the reaction was stopped by cooling, enabling the observation of structures formed at different times during the reaction. The resulting structures were

imaged on a LEO-1430 SEM, an optical microscope and an AFM. Compositional analysis was performed by energy dispersive spectroscopy (EDS) using an EDAX system that is attached to a JEOL 5310 SEM, and a JEOL 2000 TEM. The resolution of the EDS in these instruments is approximately 2 nm and 1 μm for the TEM and SEM respectively.

4.2. Experimental results

4.2.1 SEM observation

Figure 4.1 shows SEM images of the reaction area using a secondary electron (SE) detector [30]. There are bands or zones that exhibit six distinct morphologies labeled as Zone 0 to 5 in Figure 4.1b. Zone 0 is a planar spreading front (see Chapter 3). Zone 1 is a featureless area comprised of the bare Cr on the Si substrate. Zone 2 shows an extended nanowire network of length of about 3 μm with wire diameters from 30 to 300 nm. Zone 3 includes nanowires which are inter-connected between small islands. In Zone 4 there are Au islands that are smaller than the islands in Zone 3 and that are surrounded by a thin film. Zone 5 is a Au rich film that has reacted with Ga, and is as smooth and as thick as the unreacted Au beyond Zone 5 (the un-reacted Au film). The SEM contrast of Zone 5 is greater than the Au film but AFM studies show that there is no height difference between Zone 5 and the original Au film (see Section 4.2.4)

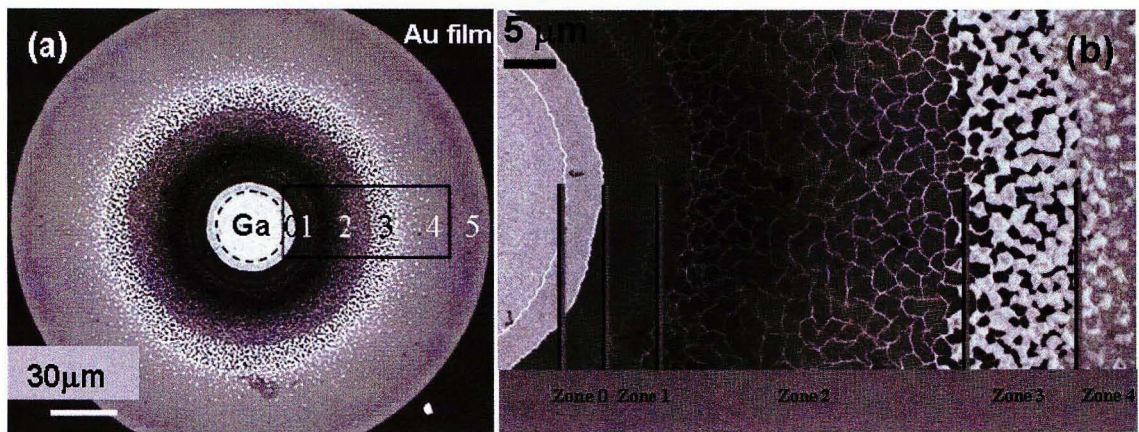


Figure 4.1. Pattern due to non-planar spreading of Ga on a 35 nm Au thin film at 360 °C for 5 minutes. (a) SEM image and (b) close-up.

Figure 4.2 shows an oblique view SEM (SE detector) of the boundary between Zone 3 and 4. The brighter areas are higher than the darker areas. The area between the islands (referred to as *background*) in Zones 3 and 4 are flat and uniform; however, the background in Zone 3 is darker than in Zone 4. This indicates that the background in Zone 4 corresponds to a thin film that is absent in Zone 3. It appears that the Au thin film has been removed from parts of Zone 3 (as well as Zone 1 and 2) and transferred to raised islands in Zone 3 and 4. Islands as high as 1 μm were observed in Zone 3, while the as-deposited Au film was only 15 nm thick. In Zone 4, which can be considered to be an earlier stage of the process in Zone 3, there are a few dark openings through the film and a few bright islands. It is quite remarkable that enough Ga can channel through the thin Au film to produce such massive and widely spaced islands. From the Ga-Au phase diagram (Fig 2.5) it can be seen that at temperatures between 300 °C to 400 °C, Ga-Au alloy with 23 at. % to 40 at. % can completely liquefy [26]. This may account for significant transport at the earlier stages of Ga infiltration into Zone 4.

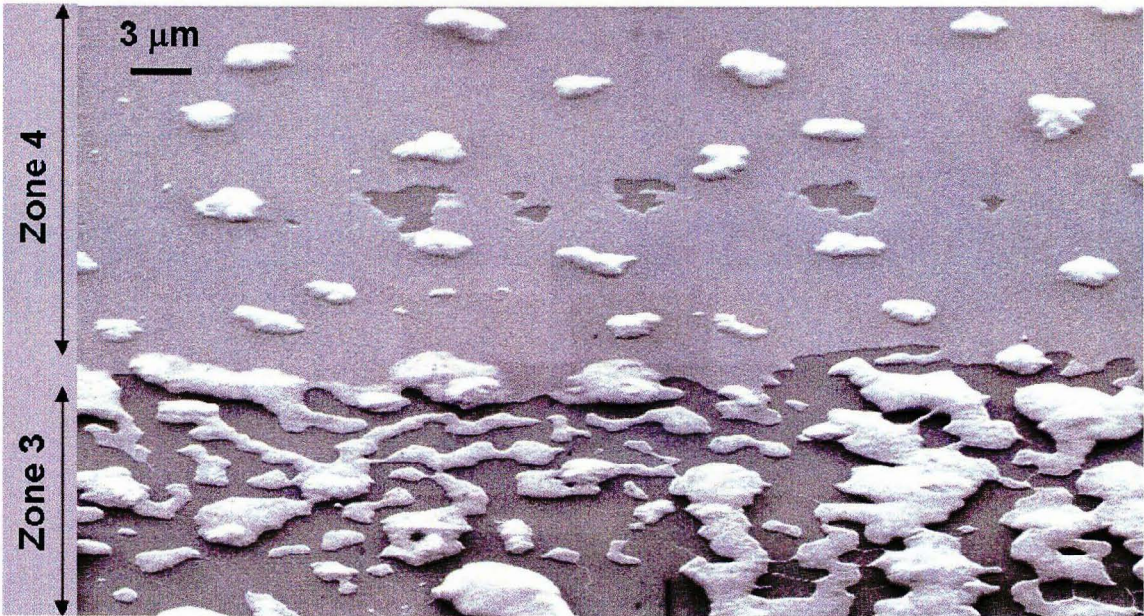


Figure 4.2. Oblique view of the boundary between Zone 3 and Zone 4 taken at 45° sample tilt. The sample was formed after a 7 minutes reaction at 370 °C from a 15 nm Au film.

Selective growth of nanowire networks: Nanowire networks can be formed selectively by performing the reaction on a micro patterned Au films. Figure 4.3 shows an SE detected SEM image of a Au nanowire network on a 30 nm thick Au line, thereby localizing the web to this line. The three varying contrast regions correspond to the thick Ga-Au nanostructures (highest contrast), the SiO₂ substrate (lower contrast), and the Cr adhesion layer (least contrast). The Cr layer is topographically higher than the SiO₂ substrate, but the SiO₂ layer has a brighter contrast due to electric charging of this insulator during SEM imaging.

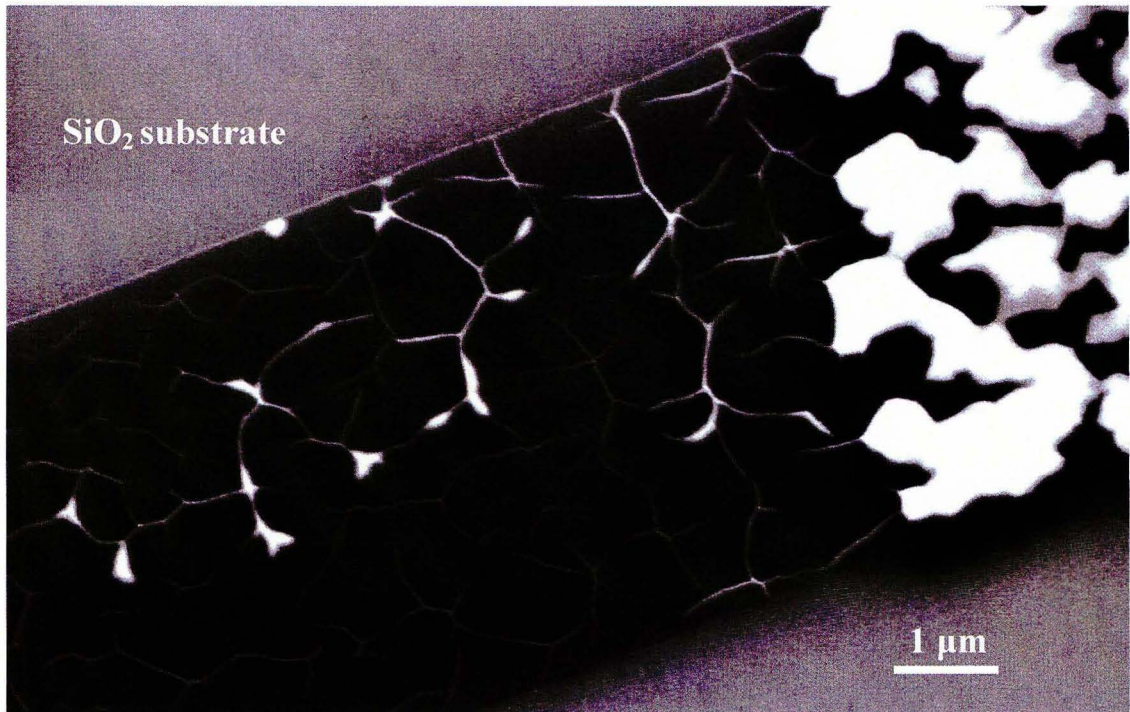


Figure 4.3. SE detector SEM image of a nanowire network and islands formed on a 5 μm wide Au line. The dark background is the Cr adhesion layer on which the 30 nm thick Au film had been deposited.

4.2.2 AFM dimensional measurements

The height differences between boundaries and also the morphology of the structures were measured using an M5 AFM (Park Scientific Instruments). Figure 4.4 summarizes these observations. From the start of Zone 4 onwards, the height of the background film is constant (10 nm) and unchanging. The nanowires are also approximately the thickness of the film with widths of a 15 to 100 nm and lengths of 2 to 6 μm .

While the background appears to be pure Cr, very low numbers of nanoparticles of 5 to 10 nm diameter are found in Zone 1, and also between the islands and wires in Zones 2 and 3.

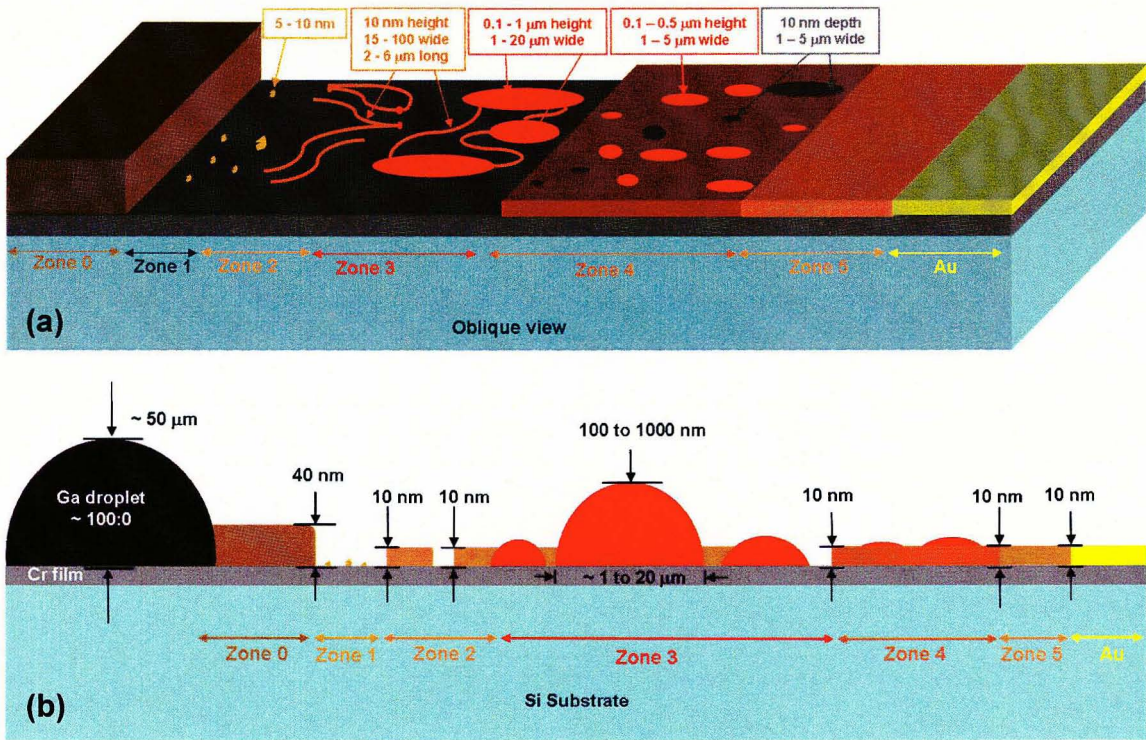


Figure 4.4. Typical dimensions observed after Ga spreading at 370 °C on a 10 nm Au thin film. (a) Oblique view, and (b) corresponding side view.

4.2.3 The effect of film thickness on non-planar spreading

A few Au films with different thicknesses were tested for growing nanowire networks. For film thicknesses less than 100 nm, non-planar spreading occurs and all of the different zone morphologies form. For Au films with more than 100 nm film thicknesses, only planar spreading (e.g. in Chapter 3) occurs that the front is $\sim 4\times$ thicker than the original Au film.

The Cr adhesion layer has an important role in the formation of different morphologies. Without the Cr layer, the Au is directly in contact with the Si substrate. For this situation, the reaction area expands only to a few microns (less than 10 μm), even after several minutes of observation. Without Cr the Si provides so little adhesion

that once the Au near the drop is dissolved, the droplet recedes due to poor wetting and separates from the Au film. The minimum required Cr film thickness to ensure non-planar spreading is somewhere in the range of 5 to 10 nm.

4.2.4 Effect of temperature range and reaction time

Chapter 3 showed that the spreading speed of the planar front Ga reactive spreading front increases exponentially with temperature. The spreading speed of the non-planar front also increases with temperature. The exact measurements are not available but the range of spreading varies between 1 $\mu\text{m/s}$ and 50 $\mu\text{m/s}$ when the temperature is changed between 300 °C and 400 °C.

The temperature range over which Au-Ga nanowires and islands form is narrow. Below 300 °C, only planar spreading is observed. In the range of 300 to 330 °C, Zones 2 and 5 form, but the islands (Zones 3 and 4) either do not exist or form in a very narrow band. In this range of temperatures a network of nanowires forms in Zone 2. The nanowires are between 10 nm and 100 nm in width and 10 nm height. In the range of 330 to 370 °C the width of Zones 3 and 4 increases, while the morphology of the nanowires network in Zone 2 remains the same as the lower temperature. At temperatures between 370 °C and 400 °C, the diameter of the wires in Zone 2 increases and the wires become shorter. The nanowire network is not continuous and the nanowires are separated from each other. The width of Zones 3 and 4 also increases.

For all range of temperatures, the amount of time that the sample is heated is also critical in the formation and expansion of different zones. In general, the expansion of the overall area of reaction increases with the duration of the reaction. For reaction times

between 5 to 10 minutes, the wires are thin (10 to 100 nm), and all Zones 1 through 5 develop. For such reaction times, the number of nanowires and nanowires-islands are maximized. For time periods between 10 to 30 minutes, the nanowires in Zone 2 and 3 and islands in Zone 3 become shorter and smaller. For times greater than 30 minutes, the wires evolve into nanoparticles of diameter 5 to 10 nm.

4.2.5 Observations of non-planar spreading under an optical microscope

Spreading at 350 °C was observed under an optical microscope and the time-lapse images were captured with a Pixelink A662 video camera (Figure 4.5). In these figures, the black region at the center of the rings is the original Ga droplet. The dark region around the Ga in Figure 4.5a (Zone 0) is the planar spreading front. It spreads to a limited radius and gradually fades from Figures 4.5a to f.

The rings in Zone 1-5 are observed to spread for 6 minutes, gradually slowing and appear to stop at ~ 20 minutes time. Note that the number of rings is fewer than for the SEM image (Figure 4.1). Comparison of the optical images with SEM images shows that in the optical images Zone 1 and 2, Zones 3 and 4, and Zones 5 and the unreacted Au each appear as a single zone (as marked in Figure 4.5c). These images show that the radius of the leading and trailing edge of the zones increases with time. This is shown most clearly in Figure 4.5g for combined Zones 3 and 4. Not only does radius increase with time, but the width of zones increase with time. Also the rate of increase in the radius decreases with time.

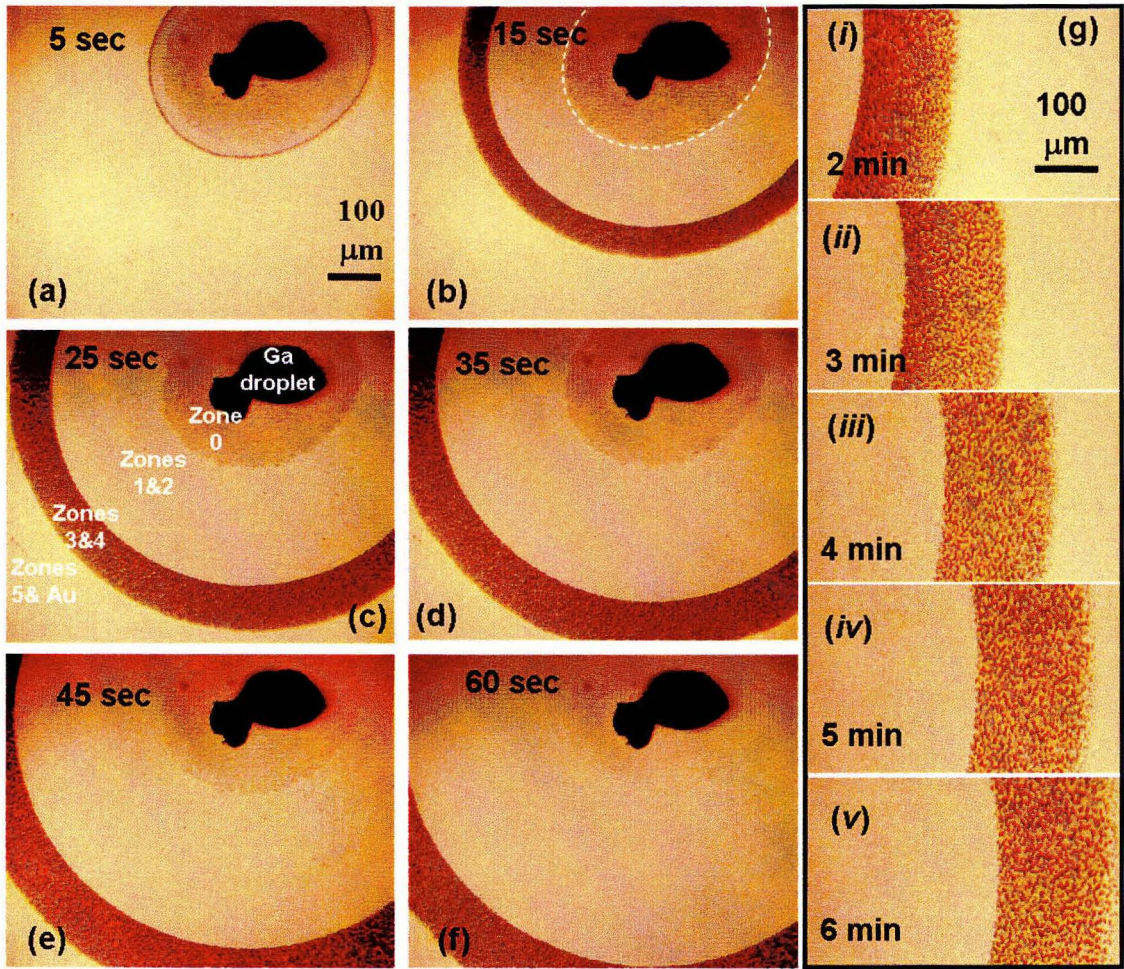


Figure 4.5. Time-lapse optical images of Ga spreading over a 35 nm Au thin film, after a 100 μm diameter Ga droplet is placed on the Au surface at 350 $^{\circ}\text{C}$. The dashed line in (b) shows the extent to which Zone 0 spreads. (g) shows the spreading of Zones 3 and 4.

4.2.6 Composition analysis

EDS composition analysis was performed in the SEM (for Zones 1, 4, 5) and in the TEM (for the nanowire networks and islands formed in Zones 2 and 3). The data is summarized in Table 4.1.

To prepare the TEM sample, the nanowire network is released from the Si surface (using the recipe in Chapter 6). The sample is then sonicated in acetone for 30 minutes. A

drop of the solution is then placed on a TEM grid. Nanowires that are interconnected to each other and connected to the island are found dispersed over the grid.

In Zone 1 mostly Cr is present with some Au and Ga. In Zones 2 and 3, there is mostly Au at the center of the islands and wires. At the peripheries of islands (5 to 50 nm) the Ga to Au ratio increases. In Zone 5 the Au concentration increases and Ga has the lowest concentration in comparison with the other regions. Thus, the relative concentration of Ga with respect to Au decreases from Zone 1 to Zone 5. It is noticed from Table 4.1 that the Cr underlayer cannot be detected in the EDS spectrum using SEM (in Zones 4 and 5) since the energy of the electron beam is only 20 kV, while it can be detected through the islands using TEM with 200 kV electron beam energy.

Due to the low resolution of JEOL 5310 SEM it was not possible to localize the EDS spectrum to the region between the islands and wires in Zones 2 and 3. The Supra 35 VP FE-SEM was not available during the time that this study was done. Further studies would be needed to completely characterize composition.

Table 4.1. EDS Composition analysis of non-planar spreading reaction.

Zone	Structure	Microscope	Cr (at. %)	Au (at. %)	Ga (at. %)	Au:Ga
0	Area average	SEM	0	28	72	28:72
1	Area Average	SEM	66	13.1	20.9	39:61
2,3	Interior of islands and wires	TEM	8.2	69.3	22.5	75:25
3	Periphery islands	TEM	53.3	26.8	19.8	47:53
4	Area average	SEM	0	55.9	44.1	56:44
5	Area average	SEM	0	85.0	15.0	85:15

The composition analysis enables further consideration of the role that Au-Ga phase diagram on the structures found in Zones 3 and 4. As mentioned before, the binary phase diagram of Au-Ga (Figure 2.5) suggests that in the range of temperatures between 310 and 400 °C a mixture of Ga and Au alloy, with 23 to 40 at.% Ga concentration, is in the liquid phase [26]. In Zone 5 at 300 to 400 °C there is clearly not enough Ga for the film to melt (at least under equilibrium conditions). However, in Zone 4 the average Ga concentration exceeds that required to melt the film. Therefore it is possible that Zone 4 contains melted regions and solid precipitates of Ga-Au of an amount predicted by tie-line constructions. More localized composition analysis would be helpful in determining the composition of the islands in Zone 4. In Zone 3 the center of the islands have much lower Ga concentrations than their peripheries. The Ga concentration on the periphery of islands is lower than in Zone 4, seems to indicate that the Ga is being drawn away from the islands as they grow and add into increasing the Ga concentration in Zone 5.

Figure 4.6 summarizes the measured composition data as well as locations that still require characterization. Selective area diffraction information would be also helpful in identifying which ordered phases from the phase diagram might be present.

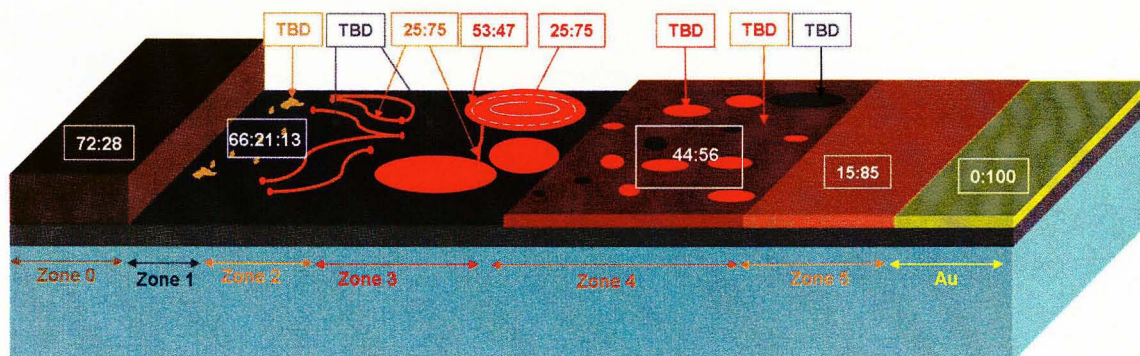


Figure 4.6. Composition of different zones of a typical sample. Compositions listed are Ga:Au or Cr:Ga:Au. Compositions inside boxes represents area averages, while arrows indicate composition localized to nanostructures or portions of nanostructures.

Figure 4.7 shows SEM images of the islands located at the boundary between Zones 2 and 3. Backscatter imaging (Figure 4.7b) indicates that the Au concentration (darker portion of image) is much higher at the center of the islands and wires than at their edges. The backscattered electron image provides further evidence that there is a composition gradient from the center towards the periphery of the islands and wires.

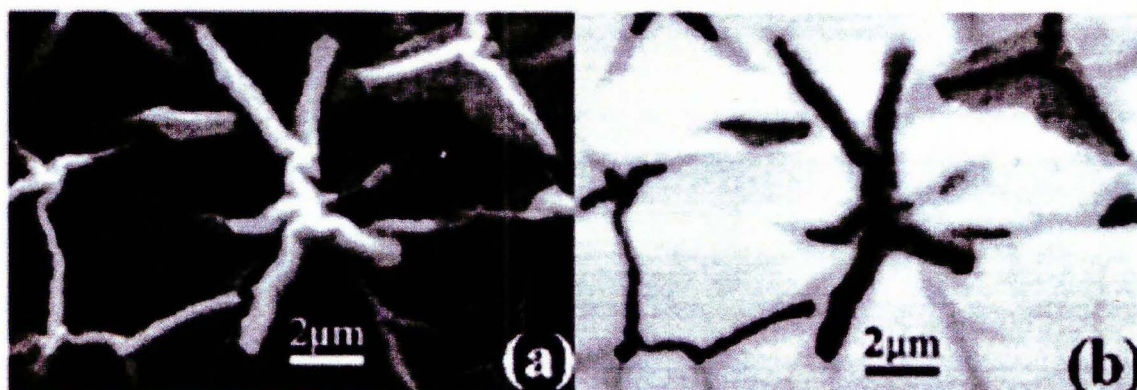


Figure 4.7. SEM images of the islands, located at the boundary between Zones 2 and 3. (a) Secondary electron image, and (b) corresponding backscatter electron images in which higher atomic number Au appears darker than lower atomic numbers Ga and Cr.

4.3. Discussion of nanostructure formations in non-planar spreading

Based on the observations reported above, the following qualitative model of non-planar Ga spreading is presented.

The moment that the Ga droplet is placed on the Au surface, planar spreading begins and Zone 0 forms (Figure 4.5a). Within a few seconds the planar spreading stops, but a thin layer of Ga continues to spread through the Au film. The zones further out in radius also can be considered to represent the film at earlier times of the reaction. Thus, when the Ga first leaves Zone 0, the film can be considered to be in the form of Zone 5 (Figure 4.8a). When the concentration of the Ga reaches above 23 at. % the film begins to dissolve and the region described as Zone 4 forms (Figure 4.8b). As time passes, islands form that are much thicker than the film. This might be due to a number of effects related to surface tension [43] or other interactions that cannot be determined without additional spatially and thermally resolved measurements and modeling. The islands continue to grow until most of the Ga and Au is removed from between the islands, resulting in a Zone 3 morphology (Figure 4.8c). These islands are also interconnected with wires of the same composition as the interior islands. Finally, due to the gradient of Ga concentration from Zone 3 to Zone 5, Ga-rich liquid on the islands in Zone 3 migrates outward towards Zones 4 and 5. This process erodes away the islands leaving a network of nanowires of the Zone 2 morphology (Figure 4.8d). In other words, the Au-rich alloy is segregated from the Ga-rich alloy. This type of segregation has been reported in several binary alloys during isothermal eutectic growth [44].

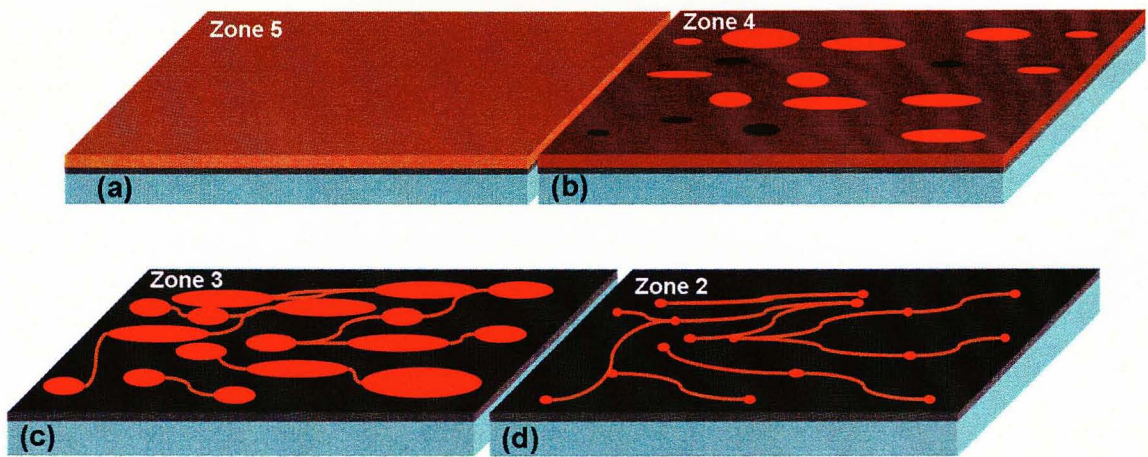


Figure 4.8. Schematic of the formation of the Au-Ga nanowire network. (a) Ga begins to infiltrate the Au. (b) The film is liquefied, which enhances the Ga transport leading to island formation. (c) The islands grow, the film disappears, and wires that interconnect the islands form. (d) The islands erode away leaving only a network of wires. Zone 1 (not shown here) results from additional transport that erodes away the nanowires leaving only nanoscale islands and particles.

In summary, Ga non-planar spreading on a Au thin film at 310 °C to 400 °C causes the self-assembly of nanostructures. A qualitative model was suggested based on observations with SEM, optical microscopy and AFM. In this model, the formation of the nanostructures begins with the formation of the islands from a liquid thin film of Ga-Au that solidifies through precipitation, becoming rich in Au. These islands then erode away leaving behind a network of nanowires. Additional spatially resolved composition analyses are required to begin modeling the material transport which is substantially more complex than room temperature spreading.

CHAPTER 5

SELECTIVE GROWTH OF INDIVIDUAL Ag_2Ga NANONEEDLES

5.1 Introduction

Figure 2.1 shows that a number of nanostructures spontaneously self-assemble from Ga-M reactions. This chapter focuses on using Ga-Ag reactions to produce individual needle-shaped nanostructures (Figure 2.1a and b) at selected locations and with selected orientations.

The ability to securely attach nanowires at desired locations has been quite limited and generally unsatisfactory for practical applications. One class of approaches has been to use mechanical manipulation [45] or microfluidics [46] to position a nanowire or nanotube near a surface followed by the application of an electric field or electron beam to attach the object. Chemical or thermal modification can be envisioned to increase the adhesion strength. A second class of approach is to selectively grow nanowires on chemically patterned surfaces. Nanowires can be grown selectively from catalyst nanoparticles by plasma enhanced chemical vapor deposition (PECVD) [47]. However, the required positioning of the nanoparticles at selected locations can be quite difficult due to the small size of the particles. Also, PECVD and other chemical vapor deposition (CVD) methods are usually performed at high temperatures that can damage the substrate material. The method of selective nanoneedle growth presented here, not only can be

performed at room temperature, but it produces strongly adhered needles that are positioned both at arbitrarily desired locations and at desired orientations.

This procedure for directed self-assembly of nanoneedles is illustrated in Figure 5.1, which will be explained in detail and compared with actual experiments in subsequent sections of this chapter. First however, the next section reports on the non-selective growth of Ag-Ga needles. These initial observations provide the basis for the proposal of the selective growth method.

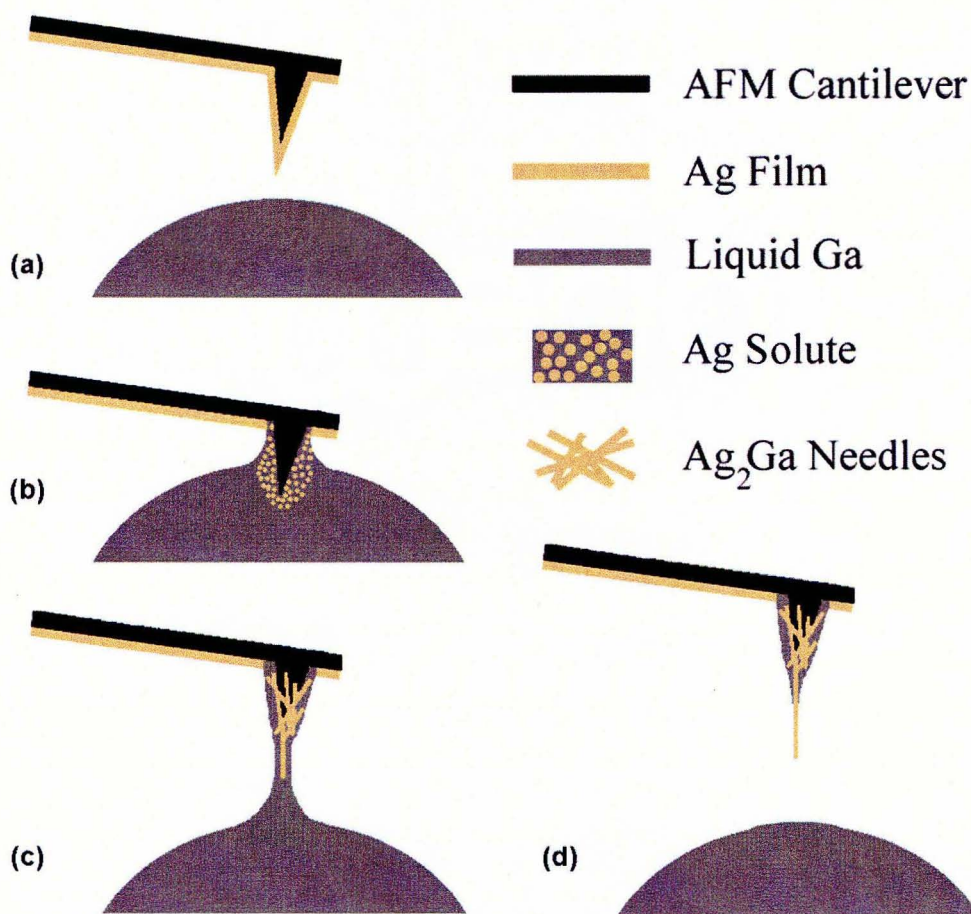


Figure 5.1. Schematic showing a method for pulling nanoneedles from a gallium droplet. (a) The silver coated tip is (a) positioned over a melted Ga droplet (b) dipped into the Ga. (c) pulled up to create a meniscus, and (d) after a few minutes either the cantilever is pulled back or the meniscus recedes leaving a single needle of Ag_2Ga .

5.2 Non-selective formation of Ag-Ga needles

5.2.1 Experimental procedures

Nanoneedles of Ag-Ga are self-assembled from a sputter-coated Ag thin film on a Si substrate. A thin film of Cr followed by a film of silver is sputter-coated on the Si substrate using a Technics sputtering system. Cr sputtering is performed using RF power of 300 W at 20 mbar operating pressure for 20 s to deposit ~ 10 nm of Cr. Different thicknesses of Ag sputtered film (between 15 nm and 350 nm) are coated using DC power of 350 W at 20 mbar operating pressure. When a drop of Ga is placed on a thin film of Ag, needle-like structures rapidly form underneath the drop. Figure 5.2a illustrates an approach for patterning Ga on the Ag film. A tungsten tip mounted on a micromanipulator is dipped into a pool of melted Ga until a small amount of Ga adheres to the tip. The hanging Ga droplet is brought towards the Ag film and dragged across the surface forming a Ga line from 10 to 100 μm wide and from 0.5 to 10 μm thick. In a few seconds, several alloy needles form parallel to the surface. Most of the needles nucleate near the edges and grow towards the center of the Ga line (Figure 5.2b).

This experiment is also performed with Ag foils. A droplet of Ga that is 1 to 2 mm wide and 50 - 200 μm thick is applied to a 125 μm Ag foil (99.9 % Ag foil from Alfa Aesar).

The samples are kept in ambient air for a few days (1 to 7 days) before they are imaged in an FE-SEM. Secondary electron (SE) detection and backscatter detection (BSD) are used to image the samples and study the effect of film thicknesses on the

morphology of the needle. SEM (including EDS), TEM (including EDS and SAD), and XRD are used to characterize the needles.

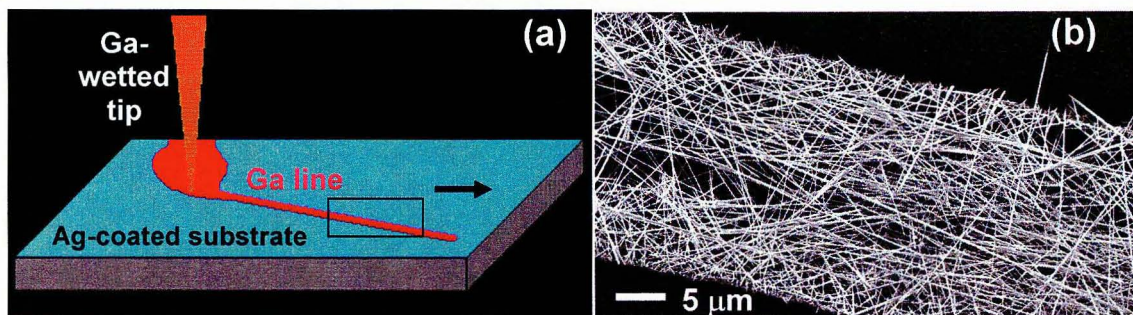


Figure 5.2. Patterning Ag_2Ga nanoneedles. (a) Schematic of patterning Ga on a thin film of Ag using a micromanipulator stylus. (b) SEM image of the nanoneedles formed in the patterned Ga. The excess Ga has been removed by reactive spreading of Ga through the Ag thin film on each side of the needles.

5.2.2 Experimental results

Formation of horizontal needles: Figure 5.3 shows SEM images of the needles forming on Ag films of thickness from 15 to 305 nm. All images were taken after a few days of Ga deposition on the film. In Figure 5.3a-c, which are the thinnest films, Ga remained visible around the needles even after several days. Apparently Ga dissolves the Ag so fast that the Ga droplet separates from the rest of the film, which stops it from spreading further. In thicker films, Ga reactively spreads through the surrounding Ag film, leaving behind nanoneedles that are free of Ga. The EDS spectrum of the darker areas in these images detects only Cr and Si which shows that all Ag has been alloyed with the Ga to form needles.

Figure 5.3 shows that the needle thickness and the number of needles per unit area is strongly correlated with the thickness of the Ag film. These observations are quantified in

Figure 5.4. The minimum diameter of the needles increases with the thickness of the film until the diameter saturates at around 100 nm (Figure 5.4a). Also the number of the needles per unit area increases linearly with the thickness of the needles. With more Ag available in the thicker films, more needles are created.

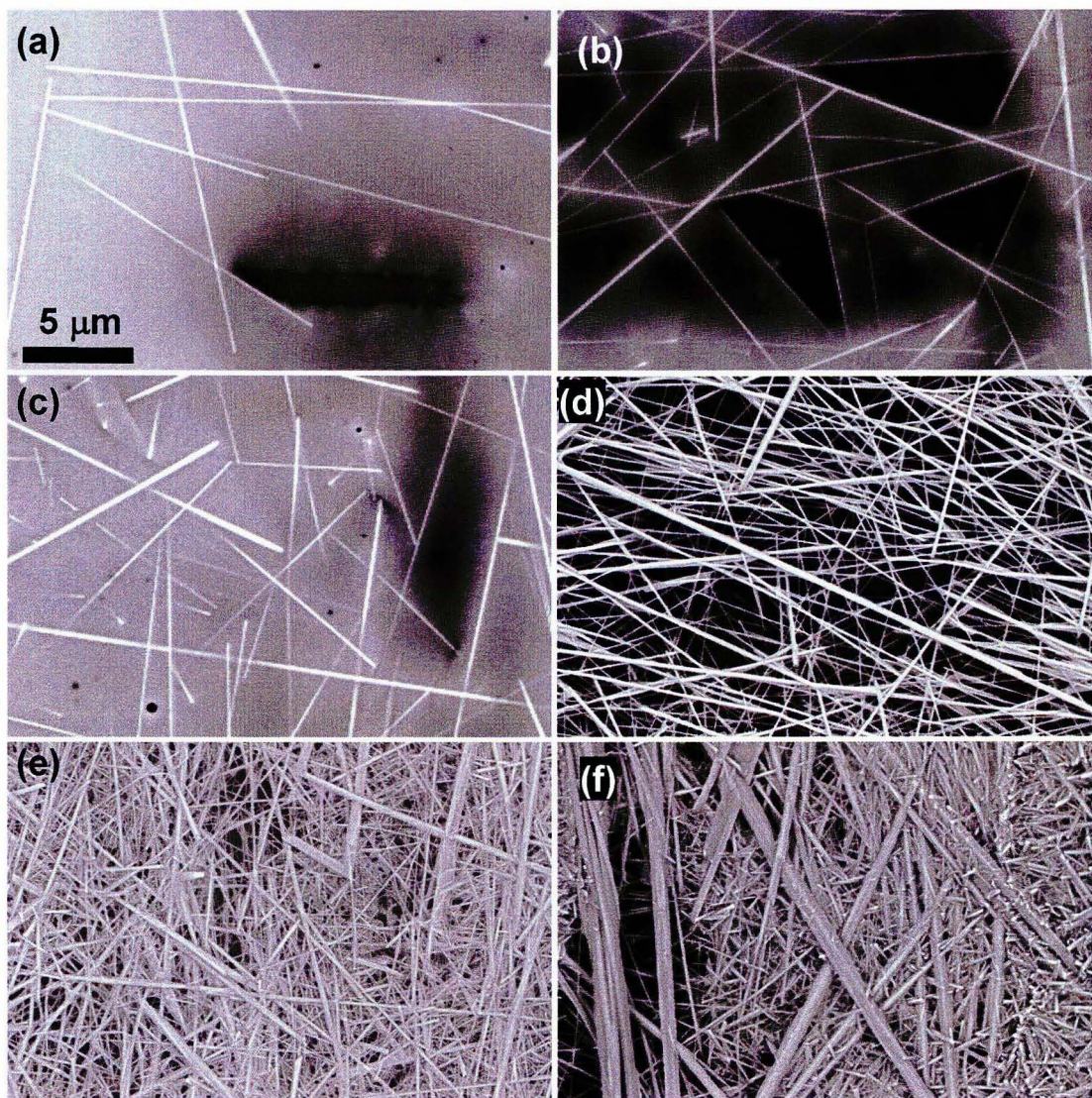


Figure 5.3 Nanoneedles formed by Ga reacting with Ag thin films. Resulting SEM images for Ag films of (a) 15 nm, (b) 30 nm, (c) 55 nm, (d) 127 nm, (e) 195 nm, (f) and 305 nm thickness.

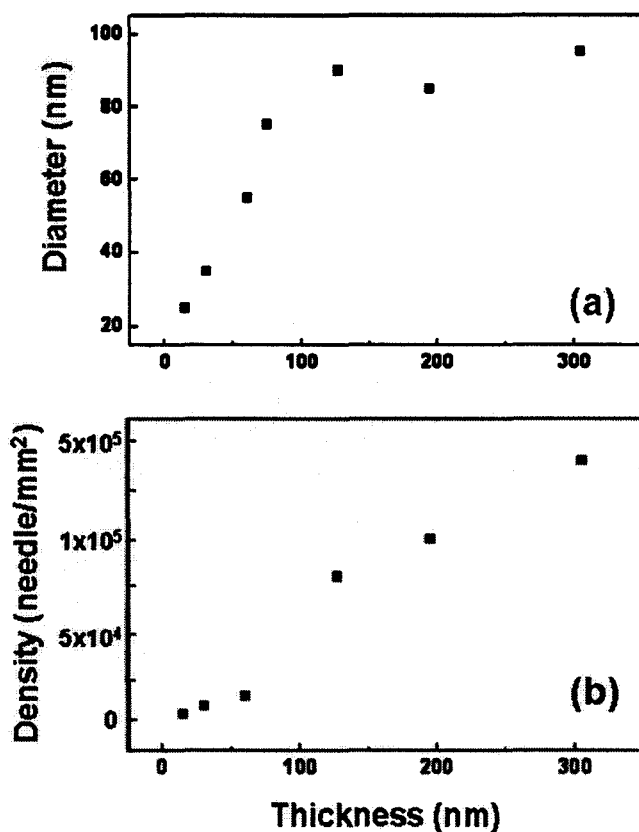


Figure.5.4. Dependence of needle (a) diameter and (b) quantity as a function of Ag film thickness.

Removal of excess Ga: The extra Ga surrounding the needles was removed by applying 1 N HCl at a temperature between 25 °C and 60 °C. Most of the Ga is removed without damaging the needle after a 20 minutes etch, for the sample shown in Figure 5.5. Ga can be completely removed by etching the sample for a longer time, or for the same time but a higher temperature. However extended etching does attack the needle (see Chapter 7). The best etching condition to ensure smooth needles is at room temperature for no longer than 30 minutes.

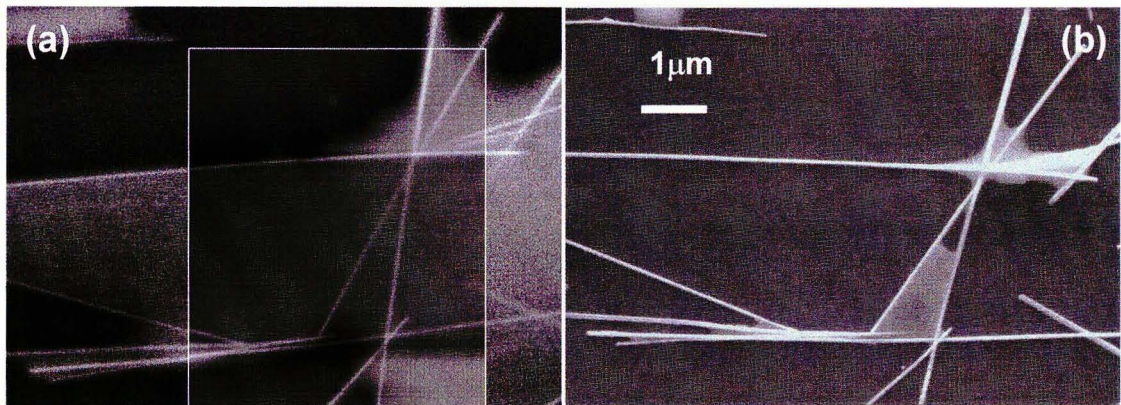


Figure 5.5. Selective removal of excess Ga. SEM images of needles formed in 30 nm Ag film (a) before and (b) after etching the sample in HCl for 20 minutes at room temperature.

Formation of vertical needles: When melted Ga is applied to a 125 μm silver foil, vertically oriented needles form. The Ga reaction can take 2 to 7 days before all of the Ga is depleted and the structures shown in Figure 5.6a are produced. The close-up of the central region (Figure 5.6b) shows that the needles grew in a vertical direction with respect to the foil surface. It appears that Ga transport direction is primarily into the foil, rather than laterally, which suggests that needle growth is oriented with the direction of Ga flow.

Repeating this experiment at a higher temperature (240 $^{\circ}\text{C}$) results in the formation of thicker and shorter needles (Figure 2.1a).

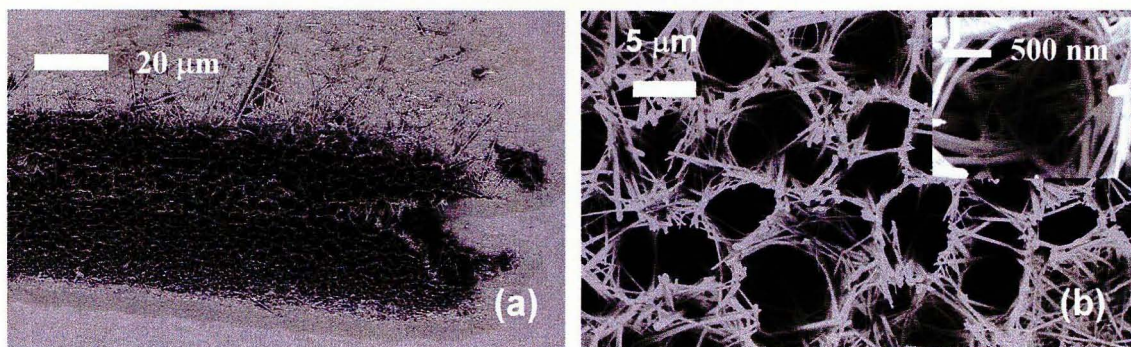


Figure 5.6. Region of Ag foil after reaction with Ga. (a) central region consist of nearly vertical wires. (b) Close-up views of the central region.

SEM In-situ observation of needle growth: Since the reaction occurs at room temperature, and Ga does not evaporate, even at pressures of 1×10^{-5} torr, needle growth can be observed under the vacuum condition in SEM. A droplet of Ga is deposited on a Ag foil using the micromanipulator arm. Then a sequence of images is recorded. Figure 5.7 shows the backscatter-detected images of the formation of needles inside the Ga droplet. These images show that the needles grow longitudinally, but only from one end. The diameter of the needle, once it forms, does not appear to change, but the growing end tapers (*i*) as it lengthens. Note at (*ii*) in Figure 5.7 the needle re-grows from the tapered part and the diameter of the needle increases to its original size. Also note in (*iii*) of Figure 5.7 that a needle of smaller diameter than earlier in the experiment starts to grow from the end of the needle that previously exhibited no growth.

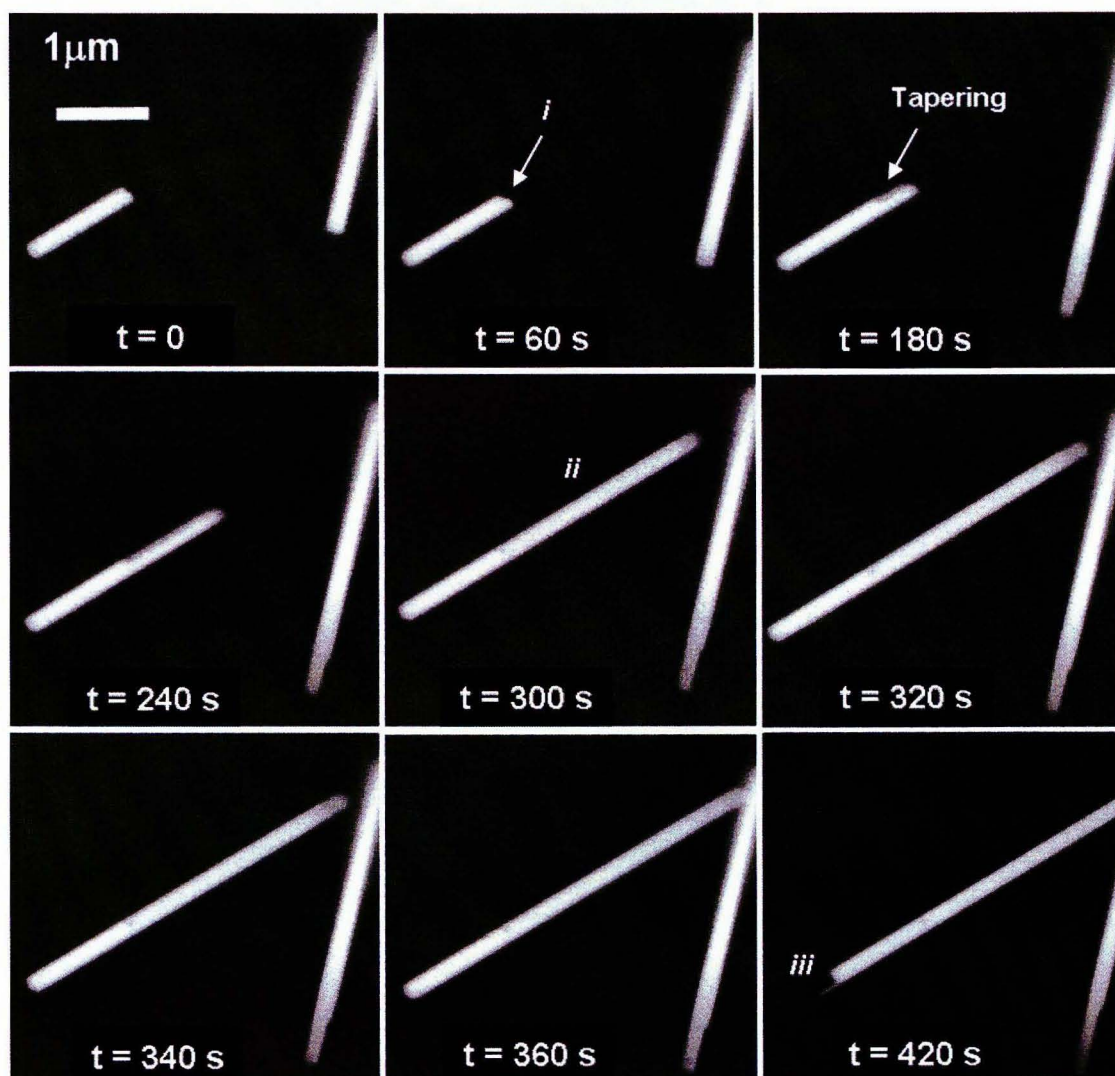


Figure.5.7. Time-lapse SEM images of needle formation inside a Ga droplet. (i) The needle tapers. (ii) The tapered portion grows to the diameter of the left end of the needle. (iii) A smaller diameter needle starts to grow on the left end of the needle.

Material characterization: XRD analysis with the Cu $K\alpha$ line ($\lambda=1.54 \text{ \AA}$) (Figure 5.8a) of the needles grown in similar conditions to those in Figure 5.3 shows that the crystalline structures are the ordered ζ' phase of the Ag-Ga binary phase diagram (Figure 2.4), which is known to be hexagonal close-packed (HCP) structures with a space group

of $p\bar{6}2m$. Simic and Marinkovic [48] reported a similar formation of ζ' phase when Ga was evaporated on a Ag film at room temperature. From XRD analysis, the calculated lattice parameters a and c are 7.75 and 2.87 Å, respectively. These closely match the lattice parameters of 0.77709 nm and 0.28788 nm for a and c respectively, reported by Gunnaes *et. al.* [49] for Ag_2Ga grown from a melt.

Figure 5.8b shows BSD image of needles that were formed when Ga was applied to the Ag foil at 240 °C. The needles are larger in diameter and shorter in length. The cross-sections of the needle are hexagonal which is in agreement with the HCP structure of the needles.

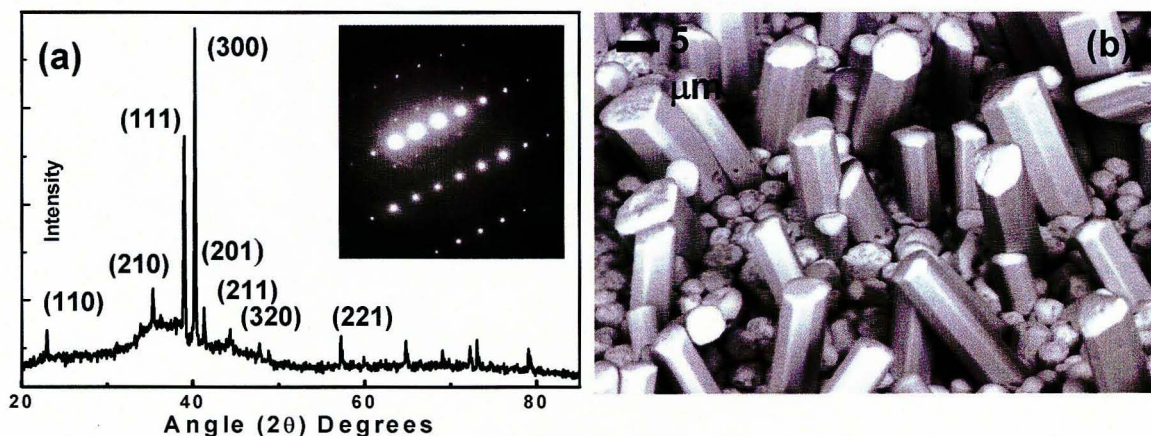


Figure 5.8. Measurements of the composition and structure of the Ga-Ag needles. (a) XRD pattern from the bulk material. (Inset) SAD pattern from a single 200 nm diameter needle. (b) SEM image of the thicker needles formed on a Ag foil at 240 °C.

Selected area diffraction (SAD) of the needles dispersed on TEM grids shows that the needles are highly crystalline [Figure 5.8 (inset)]. Energy dispersive spectroscopy (EDS) in an FE-SEM was performed on several single, freestanding nanoneedles and the ratio of

Ga:Ag was found to be 1:2, although the Ga-Ag binary phase diagram (Figure 2.4) shows that the ζ' has a broad value between 1:3.3 and 1:2 Ga:Ag.

5.3 Selective growth of single needles

The observation of needle growth from the liquid-Ag boundary within the liquid Ga (Figure 5.2b) and vertical growth in the direction of Ga flow (Figure 5.6) suggested the possibility of obtaining oriented single-needle growth. This led to the arrangement in Figure 5.1 in which the growth is localized to a thin meniscus of Ga. The meniscus is created by pulling the AFM tip away from the Ga droplet. This method will be referred to as the *pulling technique*.

5.3.1 Experimental procedures

Tip preparation: The AFM tips are sputter-coated with ~ 10 nm Cr film followed by a Ag film. The thickness of Ag films is usually between 50 to 200 nm with a preferred thickness of 100 nm.

Ga droplet preparation: Small Ga spherical droplets are made on a Si substrate. First, a small amount of Ga (less than 1 mm diameter) is placed on the Si surface using a tungsten tip. Then the tip is scratched on the Si substrate until several micron wide lines of Ga are formed. Next the sample is dipped in 1 N HCl at 60 °C for 1 minute. The sample is then blown dry with nitrogen and immediately transferred into a SEM chamber. The droplets, used to pull the needles, are usually smaller than 20 μm in diameter.

Manipulation: The AFM tips are manipulated using a Zyvex nanomanipulator inside the FE-SEM. Coarse mode manipulation is used while moving the cantilever close to the

Ga droplet and fine mode (5 nm resolution) is used while dipping the tip inside the droplet. The silver coated AFM tip is dipped into the liquid Ga droplet and partially retracted from the droplet forming a meniscus between the cantilever and the droplet (Figure 5.1b). Ga reacts with and dissolves the silver film, and nanoneedles form. Before the needle formation is complete, the cantilever is pulled further to narrow the meniscus (Figure 5.1c). The needles continue to grow within the meniscus and towards the center of the Ga droplet with a single needle eventually extending past the others. As shown in Figure 5.1d, the cantilever is completely retracted and separated from the droplet and a freshly grown needle is found attached to the cantilever. The total time of needle formation on the AFM tip ranges from 5 seconds to 10 minutes. The temperature inside the SEM chamber is usually room temperature. While this is below the melting point of Ga, the melted Ga remains in a liquid state during the process. The pressure inside the chamber is between 1×10^{-5} torr to 5×10^{-5} torr.

It is not necessary to make the needles inside the SEM chamber. The needles have also been grown in ambient air using a M5 AFM in contact mode. In this set up, a Ag-coated cantilever is positioned over a small Ga droplet. After engaging in contact mode, the cantilever is then (using the z axis step motor) pushed into the Ga droplet $\sim 1 \mu\text{m}$ and pulled back $\sim 1 \mu\text{m}$ to make the meniscus. The tip is held in this position for 2 to 10 minutes. Then it is pulled back and completely separated from the Ga droplet.

5.3.2 Results of selective growth of needles by the pulling technique

Figure 5.9 shows time-lapse SEM images of the selective formation of a single needle. An AFM tip coated with 100 nm Ag is brought close to a Ga spherical droplet of $\sim 20 \mu\text{m}$ diameter. The tip is then dipped in the Ga droplet and pulled back and held for 5 seconds. Then it is separated from the droplet to form a single needle at the end of AFM tip.

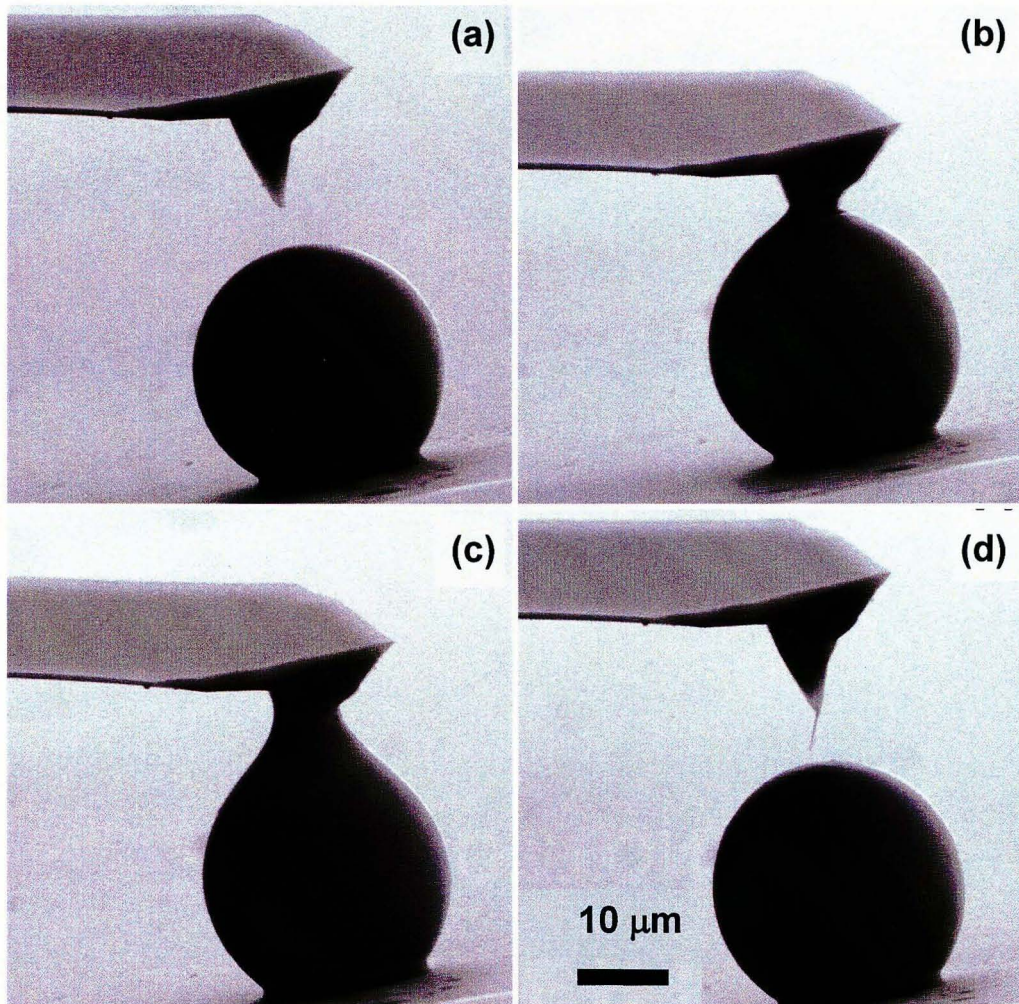


Figure 5.9. Time-lapse images of freestanding needle fabrication inside the SEM. (a) An AFM tip (coated with 100 nm of Ag) is positioned above the Ga droplet. (b) The tip is dipped inside the Ga droplet, (c) immediately pulled back and held for 5 seconds, and (d) the cantilever is retracted further to free the needle and cantilever from the Ga droplet.

Several samples were made using this technique. Four of these are shown in Figure 5.10. A needle as small as 55 nm is shown in Figure 5.10d. The smallest diameter that has been obtained is 25 nm.

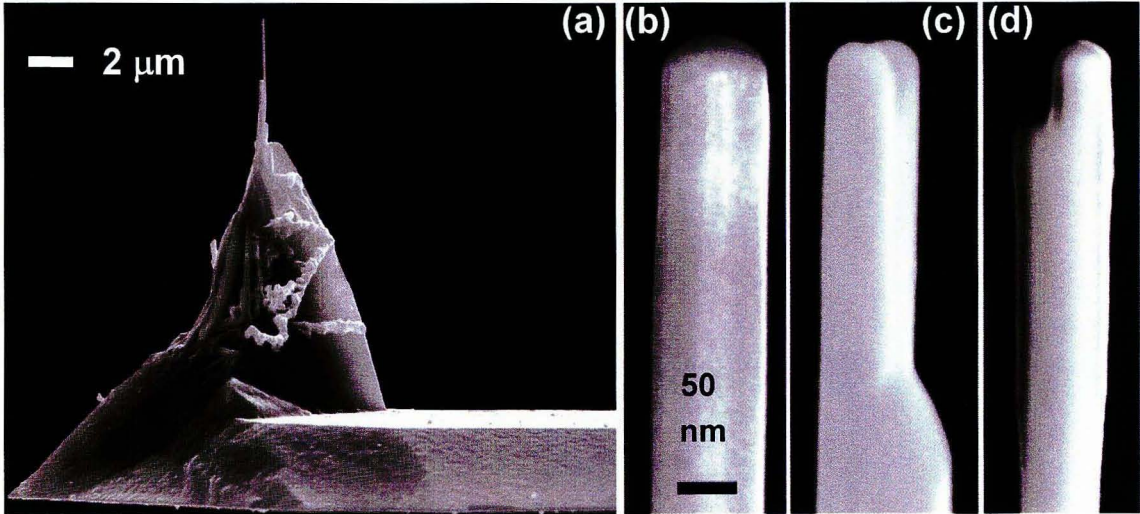


Figure 5.10. Nanoneedles formed on AFM tips by the pulling technique. (a) Close-up view of an AFM cantilever with an attached needle. (b-d) Close-up views of singles needles formed on AFM tips. The scale bar in (b) also applies to (c) and (d).

Figure 5.11 shows SEM images of two AFM tips with vertical needles that have been grown in air at standard temperature and pressure, using the AFM as a manipulator. A large amount of Ga adhered to the AFM tip resulting in a fused bundle of needles forming a base that supports a single freestanding needle. Using an AFM to pull needles, 15 % to 20 % of the attempts are successful, while using a nanomanipulator in the SEM increases the success rate to 85 %.

The tip of the cantilever is not required to selectively grow the needles. This is demonstrated in Figure 5.12a-c in which a 55 nm diameter needle is formed on a tipless cantilever (Veeco Ultralever with 90 nm Ag coating). One difference compared with

Figure 5.9 is that Ga drop rather than being spherical, here it has an irregular shape. HCl treatment of the Ga droplet at 60 °C was used in the earlier case, but not in the experiment reported here. Also note in Figure 5.12b the strong adhesion of the Ga to the Ag causes the cantilever to bend. The close-up view of the base of the needle shows that most of the Ag around it has been dissolved (Figure 5.12d,e). Beyond the dissolved region, Ga reactive spreading through the Ag is evident (Figure 5.12d).

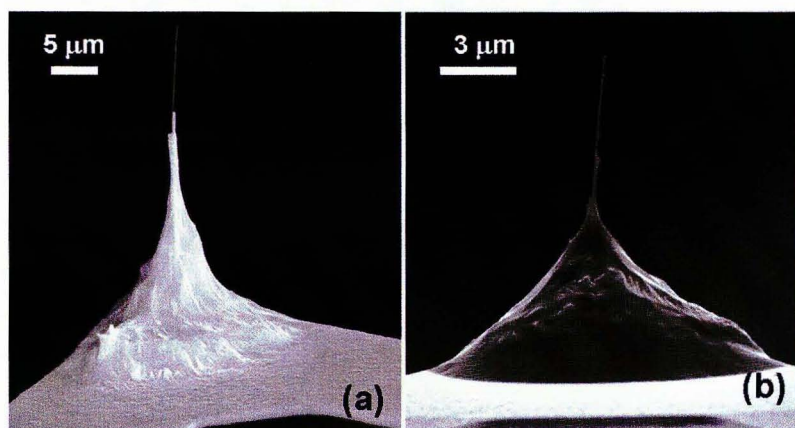


Figure 5.11. SEM images of two selectively grown needles by AFM manipulation.

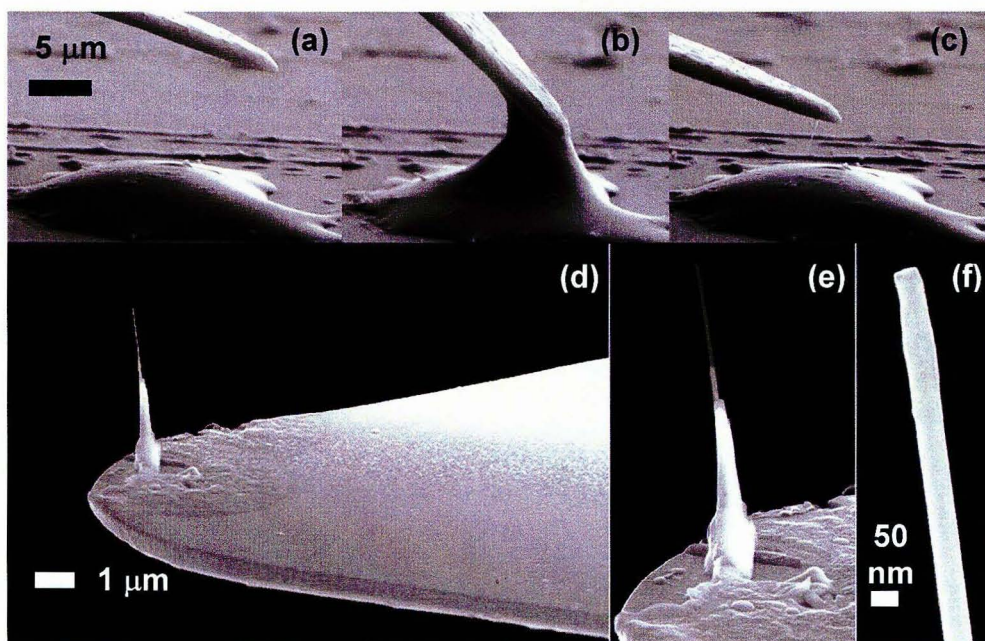


Figure 5.12. Needle fabrication on a tipless cantilever. (a-c) Time-lapse SEM images of the fabrication. (d-f) Close-up views of the needle and cantilever from (c).

Control over orientation and length: The orientation of the needles can be controlled by appropriately orienting the cantilever with respect to the Ga droplet. As shown in Figures 5.12 and 5.13, needles have been grown in various orientations from parallel to perpendicular to the substrate surface. The orientation of the needle is along the axis of the meniscus and the meniscus orients along the direction at which the substrate is retracted from the Ga. Figure 5.14 shows time-lapse images of the formation a meniscus and a needle. The non-normal orientation is a result of retracting the cantilever at an oblique angle from the surface of the Ga droplet. In a set of 15 identically prepared cantilevers 11 needles were grown in a direction of $12^\circ \pm 3^\circ$ with respect to the normal to the apex of the tip.

The length of the freestanding needles can be also controlled by varying the time that the cantilever is immersed in the Ga droplet. The short needles shown in Figures 5.9 and 5.10a are made in a few seconds while the longer needles shown in Figure 5.11, 5.13d and 5.14 result when the end of the needles is kept inside the Ga droplet for several minutes (between 2 and 10 minutes). For example, the needle shown in Figure 5.13d was held for 2 minutes. The cantilever was further retracted to expose $10\ \mu\text{m}$ of the needle, leaving an additional length submerged in the Ga droplet. The needle was completely removed from the droplet after another 8 minutes, resulting a $33\ \mu\text{m}$ long needle. In another example, the needle shown in Figure 5.14 was made in ~ 5 minutes resulting in a $20\ \mu\text{m}$ long needle.

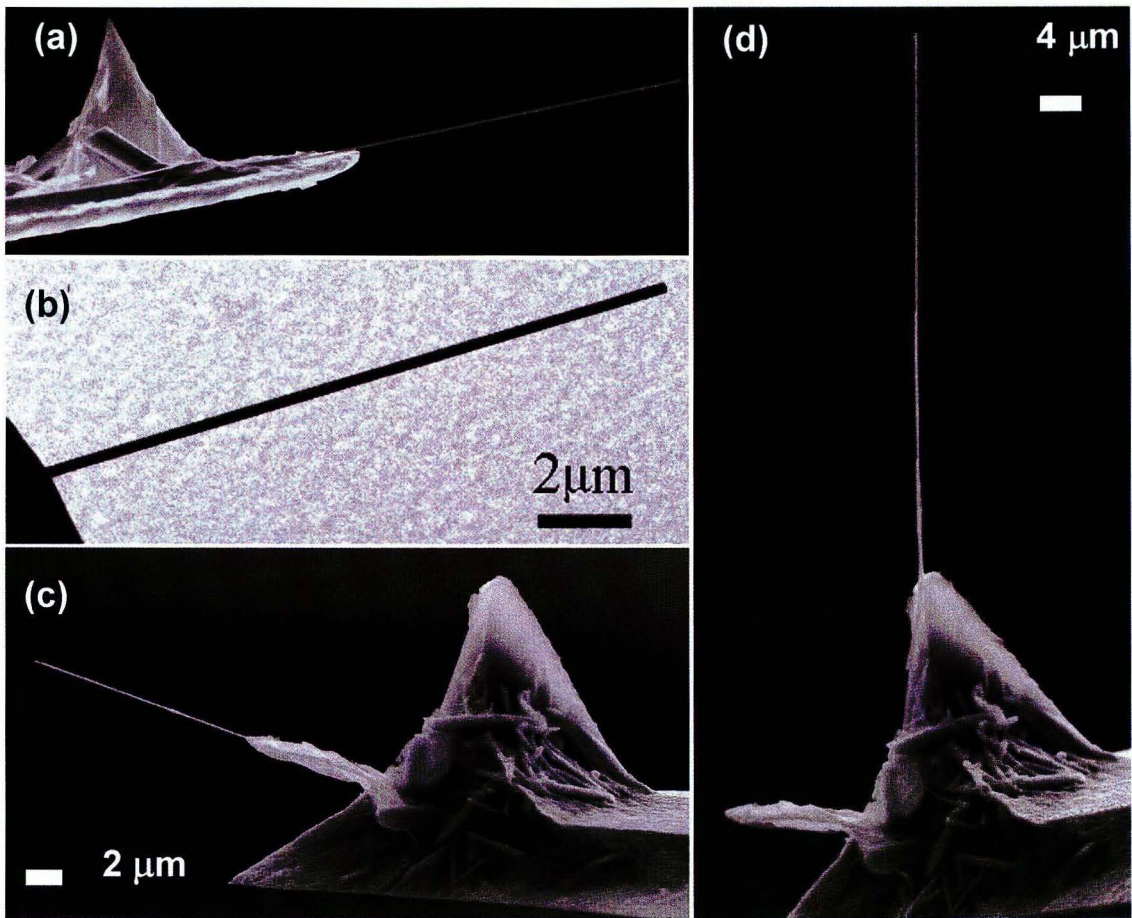


Figure 5.13. Needles of custom orientation and length. (a) SEM image of a needle with 250 nm diameter and 14 μm length that was grown by the parallel retraction of the cantilever from the Ga droplet. (b) TEM image of (a) which shows the needle to be essentially uniform in diameter throughout its length. (c) SEM image of a needle with 120 nm diameter and 12 μm length. (d) A 33 μm long vertical needle that was grown after the needle in (c) was broken off the cantilever.

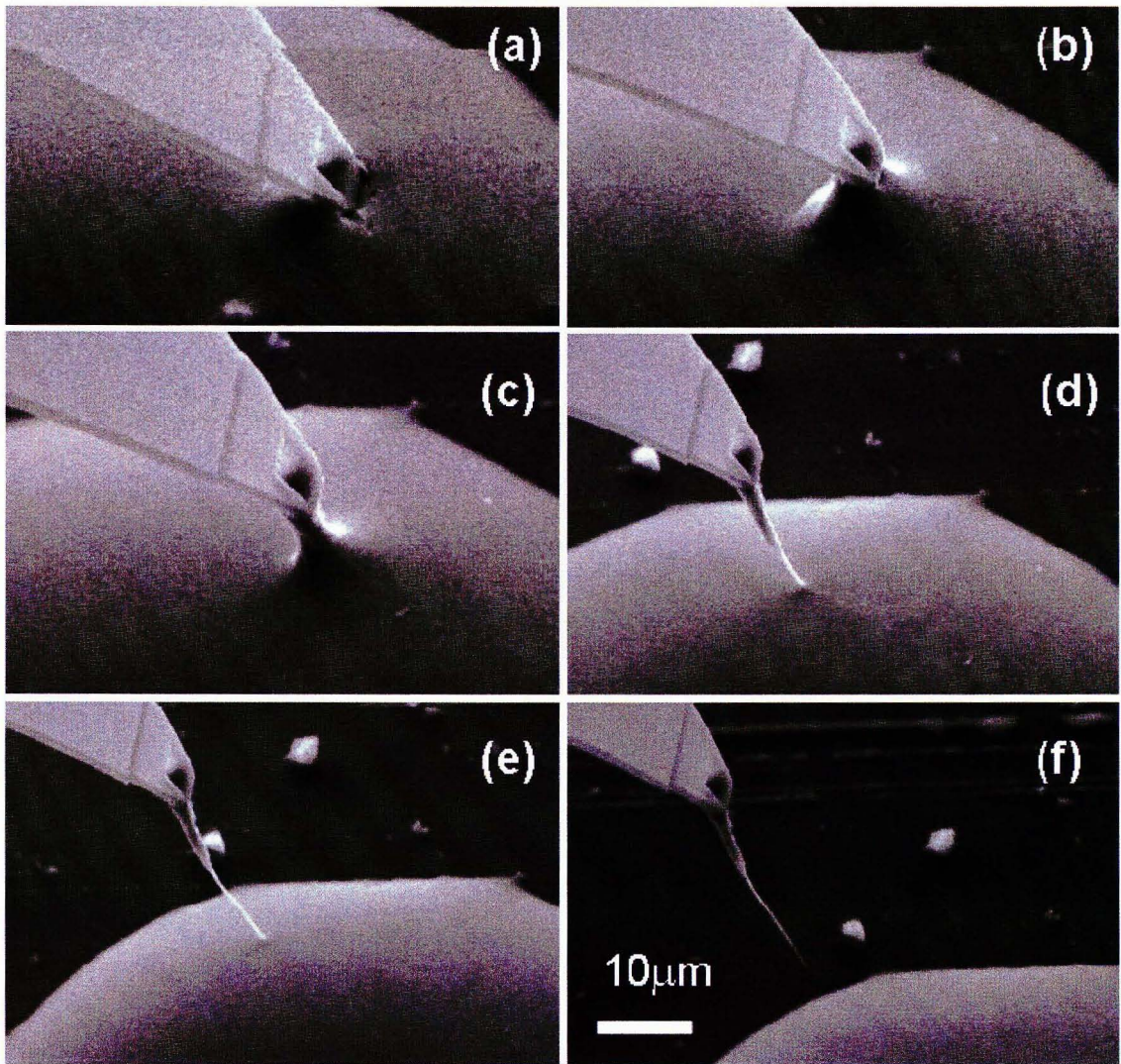


Figure 5.14. Time-lapse SEM images of the formation of the meniscus and a nanoneedle at an oblique orientation to the AFM tip. The meniscus is flexible to some extent and it laterally displaces with respect to the Ga droplet during pulling. The images (a) to (f) were recorded over 5 minutes.

The effect of voltage on needle formation: A preliminary investigation of the effect of electric potential on the needle growth was performed. Voltages of +10 V and -10 V are applied from the nanomanipulator through the cantilever to the grounded Ga droplet. Preliminary observations show that with both positive and negative potential, the

Ga more strongly wets the cantilever. Also, it is not necessary to push the tip inside the droplet. Instead, moving the AFM tip toward the Ga droplet attracts the Ga to the tip and also makes the meniscus more reproducibly attach to the cantilever. In addition, it has been found that the needles become thicker in diameter when using the voltage. Thus applying the voltage at the beginning of the process (for a few seconds) and rapidly decreasing it to zero could potentially be an approach to taper the needles. Also, applying voltage and measuring the current may provide a way to monitor the process without the need for visual observation by SEM.

5.4 Discussion of the growth process

The qualitative observations of Ag₂Ga needle growth are explained using standard descriptive models of alloy solidification [50-52]. Several experimental observations are related to the standard models, though further studies will be required to develop a quantitative model of the growth process of single freestanding needles.

5.4.1 Nucleation

Spontaneous alloy solidification typically begins upon the formation of a nucleus that exceeds a critical diameter. Consider the formation of a spherical nucleus in a liquid environment (Figure 5.15a). The Gibbs free energy of the system decreases because the volume free energy of the nucleus decreases with increasing radius. This is counteracted to a degree by the interfacial energy which increases the free energy with increasing radius of the nucleus. Thus for a sphere with radius r , the change in the free energy ΔG_r^{hom} is expressed as [50]

$$\Delta G_r^{\text{hom}} = -\frac{4}{3}\pi r^3 \Delta G_V + 4\pi r^2 \gamma_{SL} \quad (5.1)$$

where γ_{SL} is the solid-liquid interfacial energy and $\Delta G_V = G_V^L - G_V^S$ where G_V^L and G_V^S are the free energies per unit volume of liquid and solid respectively. This expression is plotted in Figure 5.15b. Differentiation of equation (5.1) with respect to r and setting the derivative equal to zero gives the solution for the critical radius r^* . For a nucleus with radius greater than r^* , the free energy decreases with radius, leading to spontaneous alloy solidification. The activation energy barrier to homogenous nucleation at r^* is [50]

$$\Delta G_{\text{hom}}^* = \frac{16\pi\gamma_{SL}^3}{3(\Delta G_V)^2} \quad (5.2)$$

This energy barrier can be lowered through heterogeneous nucleation. A planar surface, e.g. a mold wall can provide a site for heterogeneous nucleation. (Figure 5.15c). Using the same analysis as for homogeneous nucleation, the activation energy barrier to heterogeneous nucleation is given by [50]

$$\Delta G_{\text{het}}^* = \frac{16\pi\gamma_{SL}^3}{3(\Delta G_V)^2} S(\theta) \quad (5.3)$$

where $S(\theta)$ has a numerical value ≤ 1 that depends only on the contact angle θ . Therefore the energy barrier for heterogeneous nucleation is smaller than the activation energy barrier for homogenous nucleation by a factor of $S(\theta)$. This lower energy means that nuclei on a mold wall are more likely than nuclei on a homogeneous solution to exceed the energy barrier and start growing spontaneously.

Both types of nucleation can be described by the general equation [50]

$$\Delta G^* = \frac{1}{2} V^* \Delta G_V \quad (5.4)$$

where V^* is the volume of the nucleus at critical radius. This also describes nuclei of any shape. If a nucleus forms at the root of a small crack or crevice, the critical volume will be smaller than that of nucleation on a planar surface, which leads to an even lower energy barrier to nucleation (Figure 5.15b).

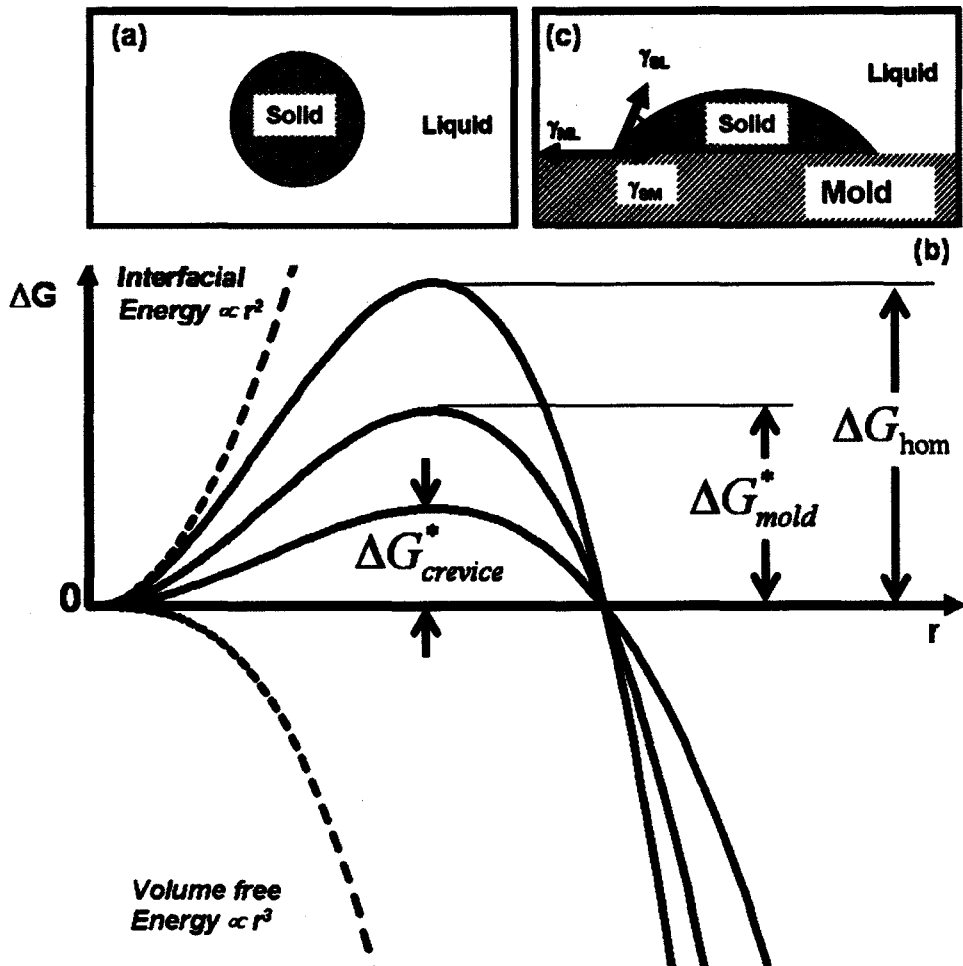


Figure 5.15. Nucleation and growth (a) Homogeneous nucleation: A spherical nucleus grows in a liquid of an identical composition (b) The free energy changes for homogenous and heterogeneous nucleation (planar and crevice) as a function of radius of curvature r . (c) Heterogeneous nucleation: A nucleus with a spherical cap grows in contact with a planar surface [53].

The above concepts are useful in considering of the mechanism of Ag_2Ga needle growth. Several observations of the tip region during the needle formation appear to fit the sketch in Figure 5.16. Immediately after dipping the tip inside the Ga droplet, the Ag film completely dissolves away from the point of the tip up to the air/Ga/Ag triple point [Figure 5.16(a and d)]. The retraction of the tip forms a crevice shaped region between the Cr-Ga interface on one side, and the Ga-air interface on the other side, with Ag at the apex of the crevice. Since a crevice lowers the energy barrier to nucleation, the needles (from a few to many) originate from the apex [Figure 5.16(b and d)]. It should be noted that several images taken of needle growth on the AFM tip, as well as on the Ag film support the hypothesis that the needles originate from the edge of Ag film. As the needles lengthen, they can grow into each other forming a bundle (Figure 5.16c and d, also see Figure 5.14). Then the bundle tapers down to a single needle that continues to grow toward the center of the Ga droplet. More details in the lengthening of needles are presented in the following section.

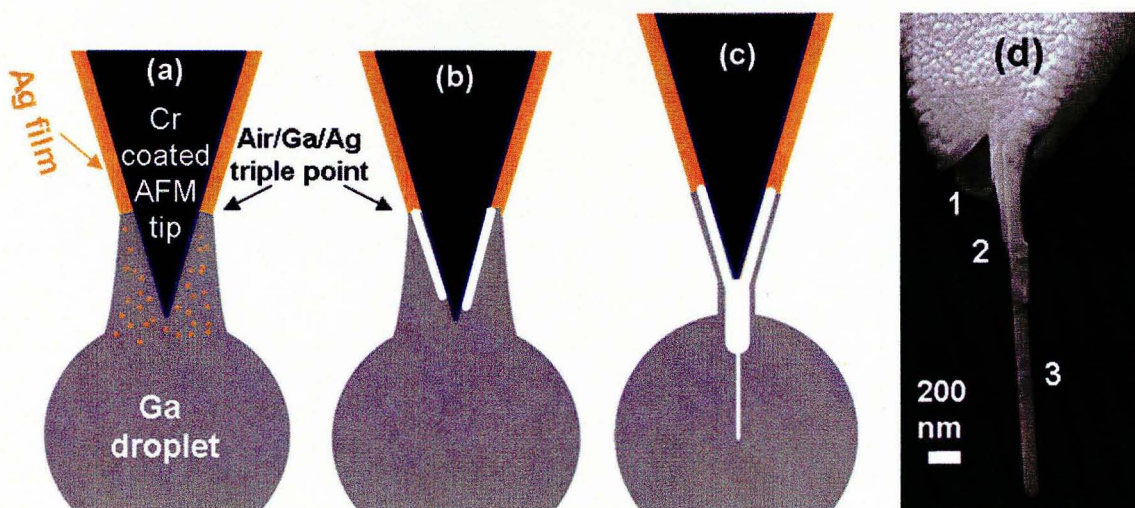


Figure 5.16. Proposed model of the nucleation of the needles. (a) Ag dissolves away up to triple point. (b) Needles nucleate and grow from the crevice at the triple point. (c) The needles lengthen and grow into each other, and a single needle grows longer and past the bundle. (d) SEM image of a tipped AFM shows that (1) Ag film has been dissolved away (2) two needles have originated from the Ag film and have grown into each other, and (3) one of them has grown longer than the others.

5.4.2 Lengthening and tapering of the needles

Most of the needle ends have a cylindrically curved incoherent edge as shown in Figure 5.10b. The longitudinal growth of these needles is modeled based on a capillary effect called the Gibbs-Thomson effect [54]. Due to this effect, free energy increases at the end of the needle and creates a concentration gradient of Ag solute along the axis of the needle that sustains the lengthening of the needle.

In most of the experiments with AFM tips [Figure 5.10 (a and d), 5.11, 5.12, 5.16d] as well as with needle formation on Ag foil and thin films, tapering is seen. Tapering could be related to the reduction of available solute and the instability of the system in

maintaining the planar fronts. In other words, more Ag will diffuse into a sharper surface, enhancing the growth rate of a single needle versus a flat bundle.

The growth of the needles has many features similar to the standard models of alloy solidification and growth [50-52]. In these models the growth is strongly dependent on temperature and temperature gradient, and thus further studies are required to optimize the needle growth process.

This chapter has demonstrated that Ag_2Ga needles can be directed to self-assemble at desired locations and with desired orientations. They appear to grow by a nucleation process. Future studies on temperature control and voltage control would be useful to develop a more detailed understanding of the growth mechanism, as well as an improved control of the length, diameter, and taper of the needles.

PART III
APPLIED PROCESSES

CHAPTER 6

SUSPENDED GOLD NANOWIRE NETWORKS

Self-assembly can be the first step in a series of steps used to fabricate devices. This chapter and the next illustrate these possibilities. As explained in Chapter 4, the non-planar reactive spreading of gallium through Au, produces nanowires that are connected to islands (Zone 3 in Figure 4.1). Due to their size, which is larger than the nanowires, the islands might serve as anchors enabling the wires to be undercut and released without completely undercutting the islands. Using common microfabrication etchants, it is possible to suspend Au nanowires between the large islands (Figure 6.1).

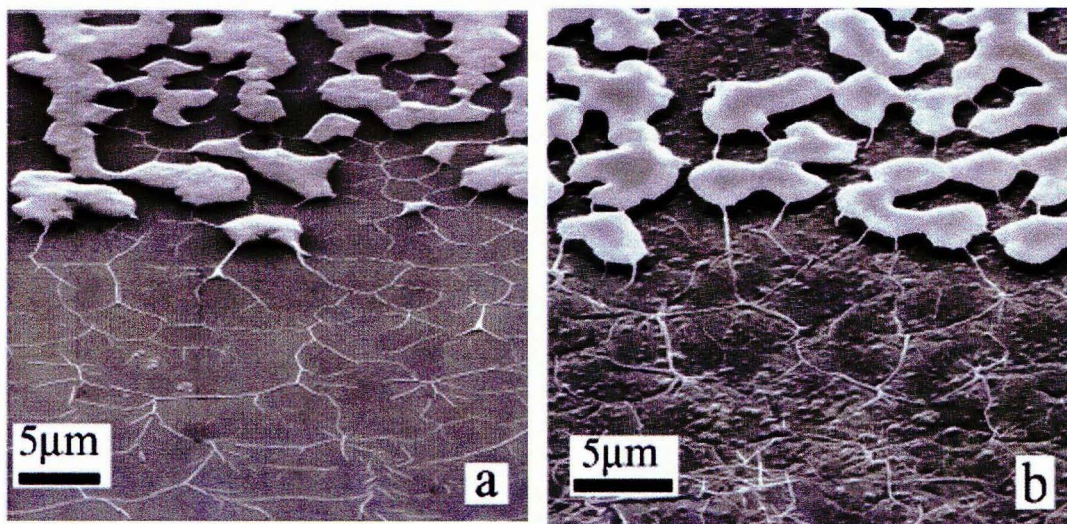


Figure 6.1. Au-Ga structures (a) before and (b) after etching. After etching the wires are released and are found suspended between the islands. Away from the islands, networks of nanowires are adhered to the substrate. The sample in (b) is not from the sample in (a), but from an identically prepared sample.

6.1 Sample preparation

A sample is prepared by the procedures of chapter 4. The substrate has a 20 nm Au film with 5 nm of Cr underlayer on a Si (110) wafer. The reaction is performed at 370 °C for 7 minutes resulting in the formation of Zone 2 and 3 structures in Figure 6.1a. The process to release the wires is as follows: First the substrate is etched for 15 minutes at room temperature in chromium etchant (Microchrome Technology Inc. Reno, NV) to remove the Cr adhesion layer. Then the sample is etched for 2 minutes in a dilute hydrochloric acid (100:1 H₂O:HF) to remove any possible native oxide layer. Next, the silicon is etched at 80 °C for 1 min in tetramethyl-ammonium hydroxide (TMAH) at 45 wt.% H₂O (from Alfa Aesar) that is diluted to 83% TMAH to 17% Isopropanol by volume. Finally the sample is immersed in 80 °C water for 1 minute and dried in air. A Tousimis SAMDRI-PVT critical point drier (CPD) has also been used for drying some of the samples. To use CPD, the sample is transferred from TMAH into acetone. The CPD chamber is also filled with acetone. The sample is then transferred quickly to the acetone before it dries. Liquid CO₂ then flows into the CPD chamber and eventually forces out the acetone and fills the entire chamber at a low pressure. A heater then raises the chamber temperature, but the CO₂ remains liquid until it reaches the critical point (1070 psi at 31 °C). At this point CO₂ is allowed to evaporate. At the critical point there is no well defined gas or liquid phase, and surface tension and capillary forces that could otherwise damage the nanostructures, vanish. After this the CO₂ is vented and the sample is removed.

6.2 Results

Figure 6.1b shows an SEM image of the structures after performing the release procedure [30]. Multiple wires are shown suspended between the islands. In regions where there are no islands, all the nanowires are adhered to the Si substrate and interconnected to each other.

Figure 6.2 shows close-up views of the suspended wires in Figure 6.1b after the etching processes. Diameters as small as 35 nm are observed with values ranging from 35 to 130 nm. Figure 6.2a shows three interconnected wires that are suspended from 3 anchors. Figure 6.2b includes a two point suspended wire and a single ended wire that is supported by the double ended wire. Suspended Au nanowires as long as 6 μm and as narrow as 35 nm are produced by this method.

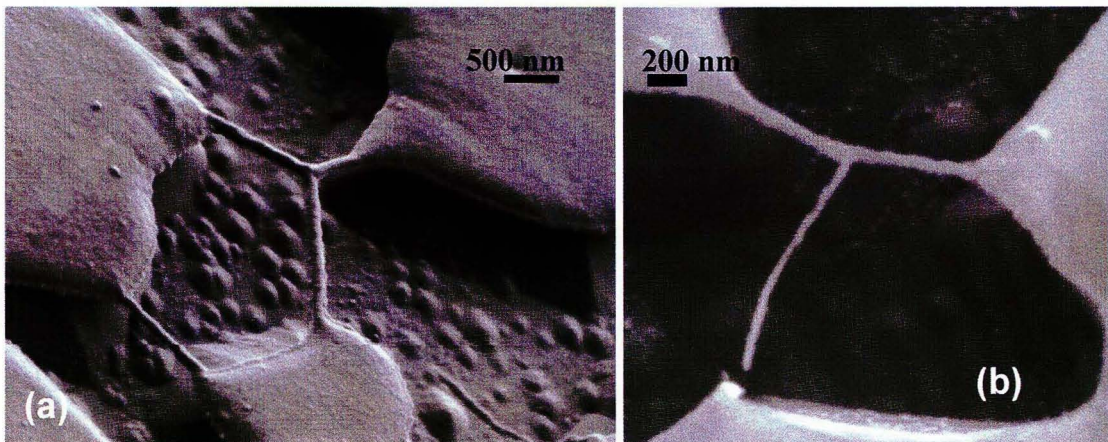


Figure 6.2. Close-ups of suspended nanowires from Figure 6.1b. (a) A double-suspended and triple-suspended wires with a range of widths of 100 to 130 nm. (b) A triple supported nanowire that has been detached at one end resulting in a single supported wire (~ 35 nm diameter) attached to a double supported wire.

EDS composition analysis shows that etching removes Ga from the wires. Prior to the etching the wires have a 3:1 Au:Ga atomic ratio and after etching the wires have a 6:1 Au:Ga composition. In a related observation, it was found that excess Ga on the substrate balls up and detaches from the substrate during the TMAH etching step.

In summary, this chapter demonstrates how a single subsequent processing step can be used to make suspended nanowires from the self-assembled nanostructures reported in Chapter 4. The resulting structures may be useful for studies of nanomechanics, nanoelectronics and biochemical systems.

CHAPTER 7

POROUS MATERIALS MADE BY CHEMICAL MODIFICATION OF SELF-ASSEMBLED GA-M ALLOY NANOSTRUCTURES

Materials that are permeated by nanoscale pores have greatly increased surface areas that can increase chemical reactivity [55,56], gas sensing [57], and effectiveness in catalysis [58,59]. Ga reactions on metal thin films forms nanocrystals and nanostructures (as described in Chapters 2, 3 and 4). It follows that other structures may be possible using additional processes. Perhaps networks similar to the nanowire network in Chapter 6 could be made with greater density, resulting in a porous network. In fact, this does occur when Ga reacts with Au at room temperature, followed by preferential etching of Ga.

The process described here for fabricating the superporous metal can be considered to be *dealloying* in which an alloy decomposes (using etching or an electrochemical process) into a pure metal. Dealloying has been used in several systems including Al-Cu [60,61] and Ag-Au, [62-64] for the fabrication of superporous metals. In this chapter, dealloying of Ga-Au and Ga-Pt thin films to produce superporous metal is reported.

7.1 Formation of superporous Au

7.1.1 Sample preparation

A thin film of Cr adhesion layer (~ 10 nm) is sputter-coated (RF, 300 W, 20 mtorr) on a SiO₂ substrate. Then, Au films between 10 nm and 150 nm thickness are sputter-coated (DC, 350 W, 20 mtorr) on the sample. Ga deposition and dealloying are performed using two different recipes as follows.

Recipe #1: Ga reactive spreading is performed on Au films as described in Chapter 3 at (25 °C to 50 °C). The sample is then dealloyed for 60 to 90 minutes in 1 N Hydrochloric acid (HCl) at 60 °C. Then, it is immersed in deionized (DI) water at 60° C and dried in the air.

Recipe #2: A 3 to 5 μm layer of Ga is thermally evaporated on the Au films. The evaporation is done using a Veeco thermal evaporator. A 55 to 60 A electric current is passed through a tungsten boat filled with Ga, at 5 mtorr pressure. The deposition rate is ~ 2 μm/min. The sample is then annealed at 50 °C for 3 hours and etched in 1 N HCl at 60 °C for 25 to 35 minutes. Then it is immersed in DI water at 60 °C and dried in the air. This recipe permits large areas to react in parallel as opposed to the slow serial spreading in Recipe #1.

7.1.2 The Resulting superporous Au

Results for Recipe #1: Figure 7.1a shows an SEM image of a film formed after the Ga has spread over a 30 nm Au micropattern. Figure 7.1b shows the same film after HCl etching for 90 minutes. Numerous open structures of nanometer scale are observed.

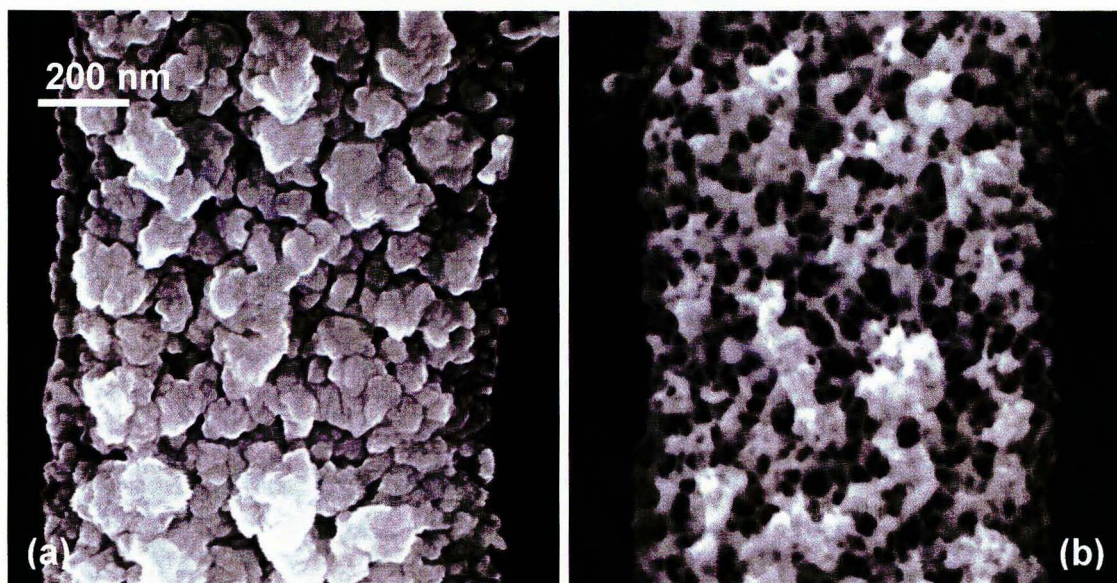


Figure 7.1. SEM images of Au-Ga alloy film (a) before and (b) after the etching step using Recipe #1. The Ga: Au composition of the film is 72:28 before and 15:85 after etching. The scale bar in (a) also applies to (b)

The morphology of superporous gold depends on the film thickness of the original gold thin film. Figure 7.2 shows SEM images of two samples made from 30 nm (Figure 7.2a) and 150 nm (Figure 7.2b) films of Au. The thicker film has several porous layers, while the thinner film has a single web-like layer. In both films, filaments that define the pore walls as small as 5 nm and pores as small as 10 nm are observed.

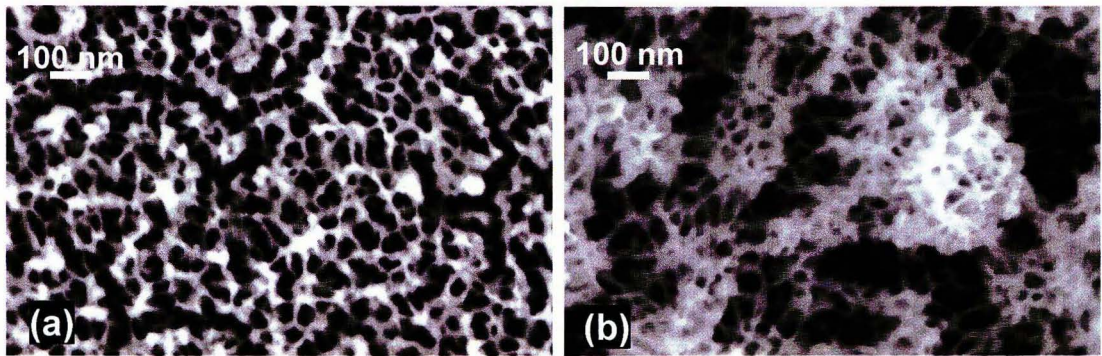


Figure 7.2. Superporous Au, made from (a) 30 nm and (b) 150 nm Au thin films.

In the peeled up film in Figure 7.3 the film is porous down to the substrate. These SEM images also show a slight difference in the morphology of the front and the back of the film. This might be due to oxidation of the front side of the Ga film, while the back side was protected against exposure to air prior to HCl etching.

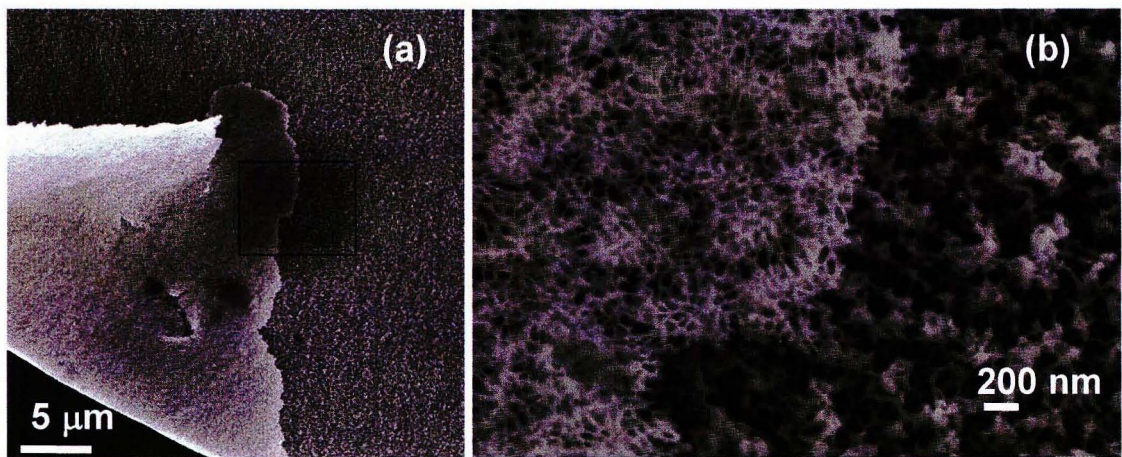


Figure 7.3. SE detector SEM images of both sides of the porous film. (a) The sample and (b) close-up view of the area in the rectangle in (a). These images demonstrate that the film is porous down to the substrate.

Results for Recipe #2:

Figure 7.4 shows the top view SEM images of the Au/Ga film before (a) and after (b) HCl etching. Since the Ga evaporation rate is high, the Ga coated layer is very rough. Droplets of Ga as large as a few microns are seen in Figure 7.4a. In Figure 7.4b, most of the Ga has been etched away and the film consists of several submicron grains that are packed together. Each individual grain is filled with pores of a few nanometers size. The superporous film appears brown under white light.

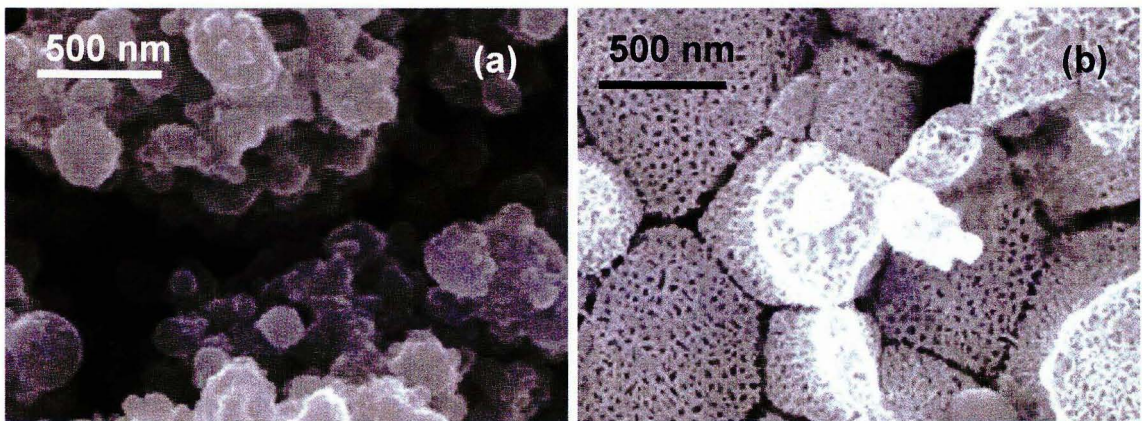


Figure 7.4. Superporous Au prepared by Recipe #2. (a) SEM image of the 4 μm layer of Ga evaporated on a 150 nm film Au. (b) The resulting porous film after etching in 1 N HCl for 25 minutes.

7.1.3 Characterization of the dealloying step

Following Recipe #2 a 100 nm Au film is coated with Ga and then etched with HCl for various durations. At each time, the composition of the sample is characterized by EDS. Images of the resulting film are shown in Figure 7.5a-e. The porosity of the film appears to increase with increasing etching time. Figure 7.5f shows a graph of Au

composition as a function of etching duration. The concentration of Au increases with etching time to as much as 99 at. % within 35 minutes.

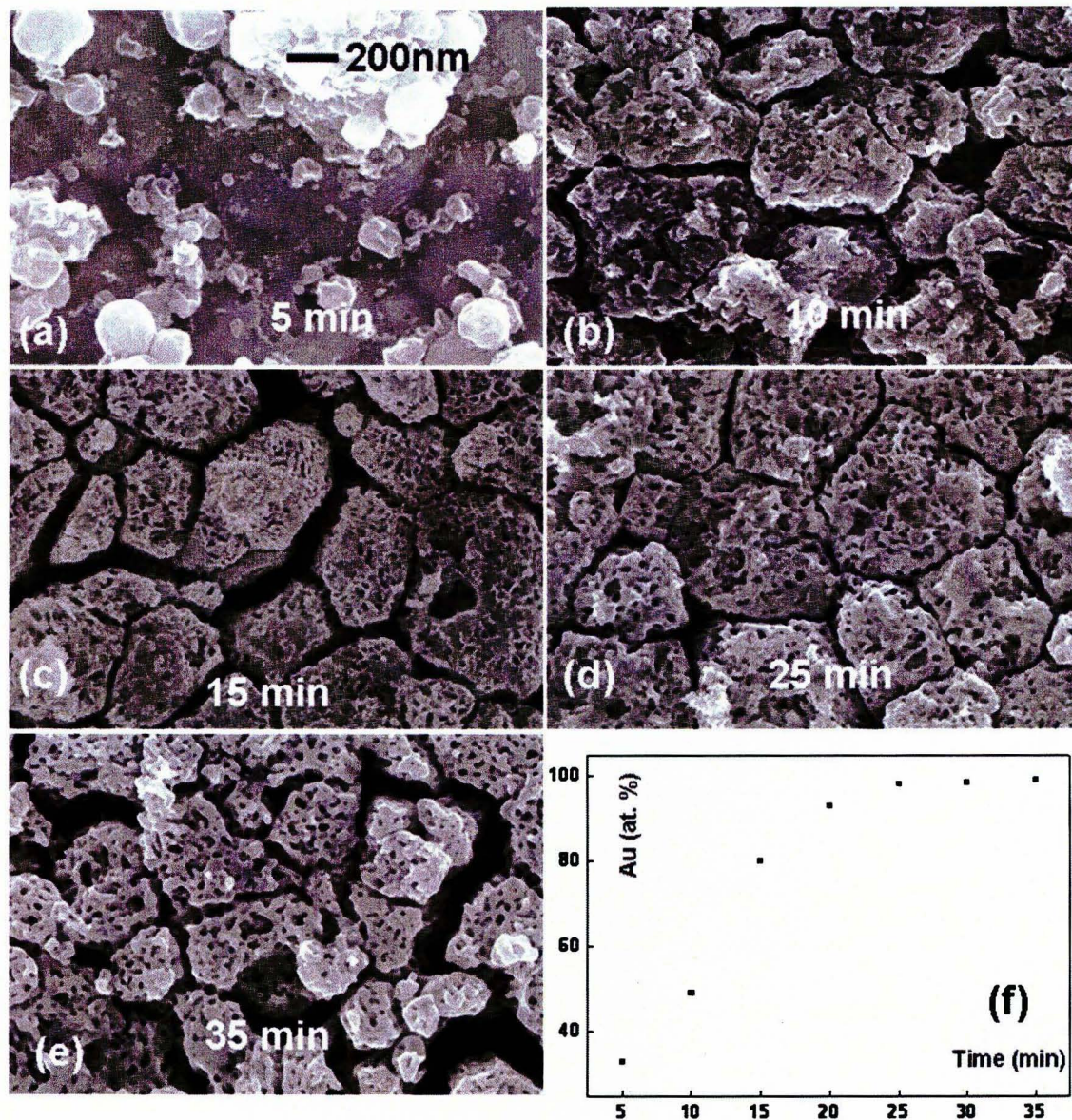


Figure 7.5. The effect of HCl etching on porosity and Au purity. SEM image of etched sample after (a) 5 min (b) 10 min (c) 15 min (d) 25 min (e) 35 min. (f) EDS data of Au purity as a function of etching time, showing the gradual removal of Ga.

Similar experiments with the samples prepared by Recipe #1 show that the concentration of Au does not increase to more than 85% even after 90 minutes of HCl etching. This might be due to the formation of Ga₂O₃ as discussed in Section 7.1.2.

7.2 Formation of superporous crystals of Pt

7.2.1 Sample preparation

Superporous Pt can be made by the same procedures used to make superporous Au. Silicon or SiO₂ substrates are sputter-deposited with Cr (~ 10 nm thick) followed by a layer of Pt (50 to 150 nm thick). Ga is deposited on Pt by placing a drop of melted Ga on the substrate or by evaporating Ga under the same conditions as in Section 7.1.1. The displacement of the Ga droplet on metal thin film is achieved by dipping a tungsten tip inside a melted Ga droplet, and then scanning it across the metal film, leaving a line or droplet of liquid Ga nominally 50 to 500 μm wide and 5 to 10 μm in height. The sample is then aged at room temperature for 2 to 8 hours. For the samples on which Ga was deposited by evaporation, the sample is annealed on a hotplate at 200 to 300 °C for 8 hours. The dealloying is done in two steps. First the sample is etched in 1 N HCl for 10 to 30 minutes at 60 °C, followed by etching in 40:1 H₂O:HF for 1 hour, at room temperature. Then the sample is rinsed with DI water and dried in the air.

7.2.2 Results of superporous Pt formation

Figure 7.6 follows the dealloying process for a Ga drop placed on a 150 nm Pt film. After HCl etching for 30 minutes, several Ga/Pt crystals of micron and nanometer scale are exposed (Figure 7.6a). Examination at higher magnifications does not show evidence

of pore formation. However, after the second step of etching pores are evident in the crystals (Figure 7.6b). Unreacted sputtered Pt film is also seen in this image. Superporous crystals with pore sizes as small as 5 nm are seen in Figure 7.6c,d.

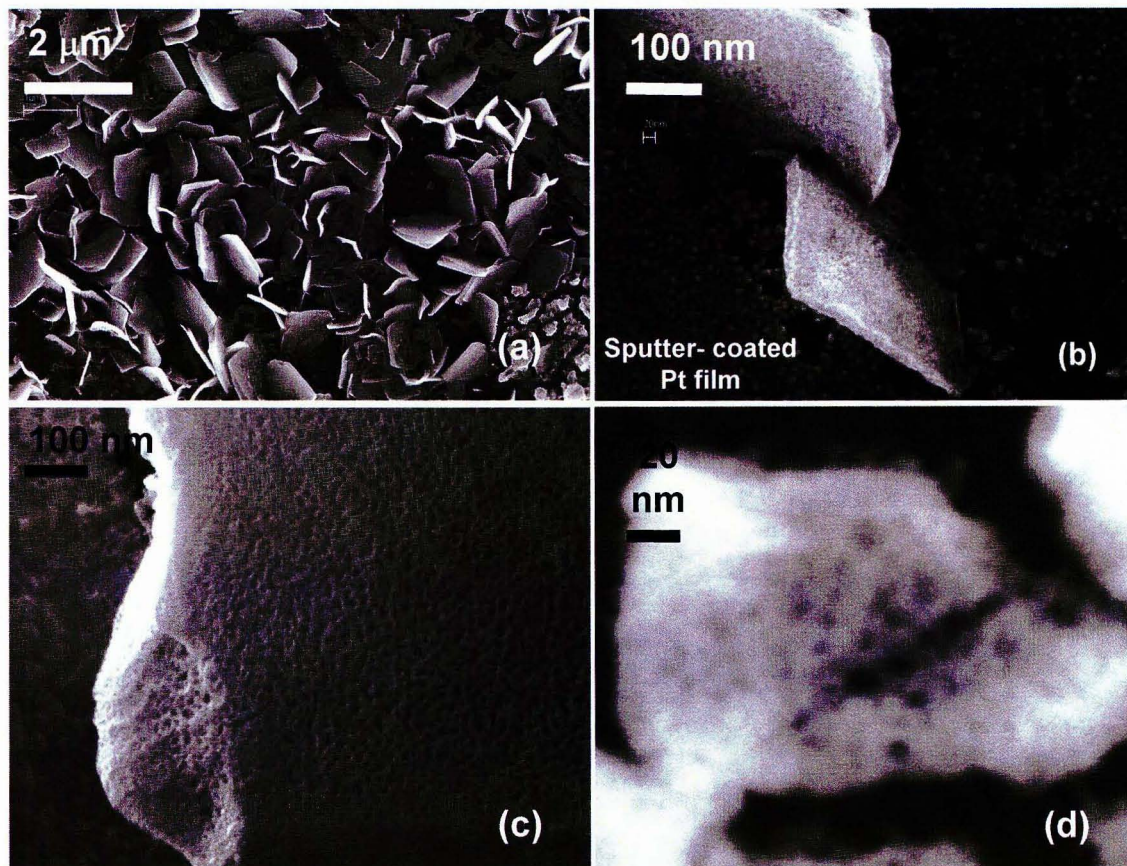


Figure 7.6. Alloying of Pt with Ga, followed by dealloying. (a) Plate-like crystals are exposed after removing excess Ga with HCl. (b) After HF etching pores develop in the crystal. (c) Normal incidence view of pores on a micron scale crystal. (d) Nanometer scale porous crystal with pores as small as 5 nm.

7.2.3 Material composition and structure

The concentration of Ga/Pt crystals, before and after etching was evaluated for two samples. The first sample was etched for only 10 minutes in 1 N HCl to remove the non-reacted Ga, and the second sample was etched in HCl followed by HF as described in

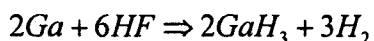
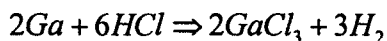
Section 7.2.1. The samples were separately sonicated for 30 minutes in acetone. The resulting solutions were then applied to the Si substrates to disperse the individual crystal. The EDS analysis of 9 different crystals shows that the average Ga:Pt atomic ratio for the first sample is 85:15, while this ratio for dealloyed sample is as low as 17:83.

The Ga-Pt phase diagram (See Figure 2.3) shows that Ga₆Pt, Ga₇Pt₃, Ga₂Pt, Ga₃Pt₂, GaPt, Ga₃Pt₅, GaPt₂ and GaPt₃, are the thermodynamically stable intermetallic compounds that can form from Ga and Pt [26]. EDS data shows that the ratio of atomic concentration of Ga-Pt crystals is about 85:15 (~6:1) before etching. In addition, most of the crystals are formed in rectangular plates (see Figure 2.1c,d) that are consistent with the orthorhombic crystalline structures [26] of Ga₆Pt. These observations reveal that the crystals are most likely Ga₆Pt. X-ray diffraction studies are needed to complete the material characterization.

7.3 Discussion

7.3.1 Chemistry of the etching (oxidation) process

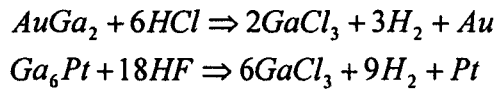
In Ga-M alloys, intermetallic compounds (here AuGa₂ and Ga₆Pt) as well as pure Ga coexist. During etching, HF and HCl etch (oxidize) the Ga into salt according by the reactions [65]



After etching, EDS analysis shows a significant reduction in the Ga concentration with the ratio of Ga:Au becoming 1:99 and Ga:Pt becoming 17:83.

HCl and HF do not oxidize the noble metals such as Au and Pt since the reduction potentials for Au and Pt are higher than that of Ga. (Reduction potential is the tendency

of an element to acquire electrons. An element with a more positive reduction potential has less tendency to be oxidized, or a greater tendency to gain electrons). The reduction potential of Ga^{3+} is -0.45 V, while the reduction potential for Au^{3+} is 1.5 V and for Pt^{+2} is 1.2 V [66]. Thus the tendency of Ga to oxidize is much higher than that of Au leading to the selective dissolution of Ga from Ga-Pt and Ga-Au alloys. This consideration leads to the presumed chemical reaction of acids with $AuGa_2$ and Ga_6Pt of



7.3.2 Estimate of the porosity

The open void fraction of the superporous crystals made from $AuGa_2$ and Ga_6Pt is estimated by calculating the volume of Ga that is removed during etching as a fraction of the volume of the intermetallic crystals. It is assumed that the crystals do not shrink or swell during the etching process, and keep their original crystalline geometry. Possible volume change due to interactions and packing of the atoms in the crystals are ignored for this rough estimate.

First, the atomic volume of the intermetallic compound is calculated. Then the atomic volume of the Ga removed by etching is calculated from the measured stoichiometry of the etched crystal. The atomic volume is calculated as

$$\text{Atomic volume in cm}^3/\text{molecule} = \frac{\text{atomic weight in gm/mole}}{(\text{density in gm/cm}^3)(\text{Avogadro's number in molecule/mole})}$$

The density of the Ga and Pt is 5.9 gm/cm³ and 21.4 gm/cm³, respectively. The atomic weight of Ga and Pt are 69.9 gm/mole and 195 gm/mole respectively. Thus the atomic volume of Ga is 1.96×10^{-23} cm³ and the atomic volume of Pt is 1.51×10^{-23} cm³.

For simple addition of the atomic volume, the atomic volume of the Ga₆Pt crystals would be $\sim 12.27 \times 10^{-23} \text{ cm}^3$.

After dealloying, the ratio of Ga:Pt concentration reduces to 17:83. This is equivalent to removing 5.795 of each 6 atoms of Ga from each Ga₆Pt molecule. Thus the open void fraction is calculated by subtracting the atomic volume of the Ga₆Pt crystal from the final volume of the Ga_{0.205}Pt alloy and then dividing by the atomic volume of the Ga₆Pt. This gives an estimated open void fraction of 85 %. A similar calculation for AuGa₂ etched to 99 % purity gives an open void fraction of 70%.

7.3.3 Possible theory for pore formation during dealloying

In this section, a theory for the formation of the porous thin film is considered. Self-assembly of nanoscale features (i.e. the nanowire web in Figure 7.2) from dealloying might be attributed to spinodal decomposition [67,68] in which the remaining metals (here, Pt and Au) are driven to accumulate into two-dimensional clusters by a phase separation process at the solid-liquid interface. The following argument has been used by Erlebacher *et. al.* [62] to explain the formation of nanoscale features during dealloying. To relate his theory to this study, the argument is stated for the specific Ga-Au system studied herein.

Consider a Ga-Metal crystal in an etchant (i.e. HCl). Initially, Ga will be dissolved from the top surface of the crystal. Gold atoms should accumulate on the surface and locally protect the crystal from further dissolution. But as shown in the experiments (Section 7.1.2), the films are porous down to the substrate. These results suggest the following qualitative description of porous formation. Consider that a single Ga atom is

removed from the surface, which leaves behind a terrace vacancy. The Ga atoms surrounding this vacancy have fewer neighbors than others and thus have a greater tendency for dissolution. As a result the entire terrace is removed leaving behind Au atoms with no lateral coordination; these atoms are called *adatoms*. Before the second layer is attacked, the Au adatoms with local site occupancy are far from thermodynamic equilibrium. Thus there is a strong driving force for Au adatoms to aggregate, forming small islands. Regions of the surface that have a uniformly high concentration of Au adatoms have free energy $G(c)$ (where c is the gold concentration) that has a negative curvature (i.e. $d^2G/dc^2 < 0$) which is the condition for spinodal decomposition. Within the spinodal, an arbitrary small fluctuation in composition leads to a lower overall free energy for the system and causes atomic diffusion against the concentration gradient. The system then becomes unstable causing the spontaneous formation of the islands (in this case networks of Au wires that define the pore). As a result, rather than a uniform Au layer over the top layer of the crystal, the surface consists of two distinct regions: pure Au regions that are locally passivated at the surface and unreacted areas that are exposed to the acid. In the early stages the Au clusters are mounds that are Au-rich at their peaks and are Ga-rich at their bases. These mounds get undercut, resulting in the formation of superporous Au.

While the theory seems to describe all qualitative features of the porous material it should be noted that further studies would be required to evaluate the actual free energy conditions needed to obtain spinodal decomposition.

This chapter has shown superporous Pt and Au can be formed by selectively etching Ga from Ga-M intermetallic compounds. Superporous Pt and Au with open void fractions as high as 85% and feature sizes as small as 5 nm were produced using this method. Nanostructure formation caused by the etching is attributed to spinodal decomposition.

This method of making porous metals has a number of desirable features. First, using low melting point Ga as one of the elements in the binary alloy is advantageous since Ga is a very reactive metal at room temperature and it can be completely removed from the Ga-M alloy with even a weak acid (e.g. dilute HCl). This results in the formation of nearly pure superporous metal. Second, the surface of a pre-existing electrode on a device can be made porous (see Chapter 11) by direct Ga deposition on the electrode at or near room temperature, followed by etching. Third, the reaction of Ga with metal films creates micro and nano crystals of Ga-M can be quite thick, as shown in Figures 7.6, providing a large surface area.

PART IV
APPLICATIONS

CHAPTER 8

MECHANICAL PROPERTIES OF Ag₂Ga NEEDLES

8.1 Introduction

Because long Ag₂Ga nanoneedles can be grown directly on AFM cantilevers, or any other micromechanical platform, it is possible to directly measure their mechanical properties. As demonstrated in this chapter, a number of measurements can be performed reliably, as is shown by the consistency between the various measurements.

From these measurements it is possible to determine Young's modulus E of Ag₂Ga materials, the Hamaker constant A between Ag₂Ga and the Si, the frictional coefficient μ_k between Ag₂Ga and Si, the mechanical resonance frequency f_n , quality factor Q , and spring constant k of the needles. Table 8.1 lists the key equations and definitions of the constants that are used in this chapter. These expressions are all from classical mechanics. Additional explanations of the equations are presented as they are described in the chapter.

Table 8.1. List of the key equations and definitions of the constants used in this chapter.

Eq. #	Formula	Description	Variable definitions
(8.2)	$E = \frac{k_n L^3}{3I}$	E from k_n	k_n = Spring constant of a beam when the force is applied perpendicular to the longitudinal axis
(8.3)	$f_n = \frac{\left(\frac{\beta_n^2}{2\pi}\right)\left(\frac{EI}{\rho}\right)^{1/2}}{L^2}$	n^{th} resonance frequency f_n of a clamped-free beam	E = Young's modulus I = Moment of inertia L = Length $\beta_1 = 1.875, \beta_2 = 4.964$, etc. ρ = density
(8.4)	$I = \frac{1}{4}\pi R^4$	Moment of inertia of a cylindrical beam about its longitudinal axis	R = Beam radius
(8.5)	$E = \frac{16\pi^2 f_n^2 L^4 \rho}{\beta_n^4 R^2}$	E for cylindrical fixed-free beam at f_n	
(8.6)	$Q_n = \frac{f_n}{B_n}$	Quality factor Q_n of the n^{th} resonance	B_n = FWHM of the resonance peak around f_n
(8.13)	$k_{ch} = 4.08 \frac{\pi^2 EI}{L^3}$	Spring constant of a buckled clamped-hinged beam in its 1 st mode	k_{ch} = Spring constant of a clamped-hinged beam when it is compressed along its longitudinal axis
(8.14)	$k_s = 11.79 \frac{\pi^2 EI}{L^3}$	Spring constant of a buckled clamped-hinged beam in its 2 nd mode	k_s = Spring constant of "S shaped" buckle
(8.26)	$W(D) = -\frac{AR}{6D} \quad D \ll R$	Interaction potential W between a sphere and a flat surface	A = Hamaker constant D = The distance between flat surface and a sphere
(8.29)	$D^* = \sqrt[3]{\frac{AR}{3k_n}}$	The distance at which sphere snaps into the surface	
(8.39)	$\mu_k = \left(\frac{k_r - k_e}{k_r + k_e}\right) \cot(\theta)$	Sliding friction coefficient μ_k between Si surface and tip of the needle	$k_r = k$ during retraction $k_e = k$ during extension α = the angle between the needle and the surface
(8.45)	$M_{\min} \approx 0.24m \left(\frac{2}{Q-2}\right)$	Minimum detectable mass as a function of Q of the needle	m = mass of the needle

8.2 General background on the mechanical systems studied

This section presents background on the mechanical systems studied. It specifically formulates equations for the evaluation of material and system properties e.g. Young's modulus and spring constant.

Young's modulus: Young's modulus describes the elastic properties of a material. If a material is either stretched or compressed as illustrated in Figure 8.1a, the ratio of the stress $\sigma = F/A$ to the strain $\varepsilon = \Delta L/L$ is the *Young's modulus*.

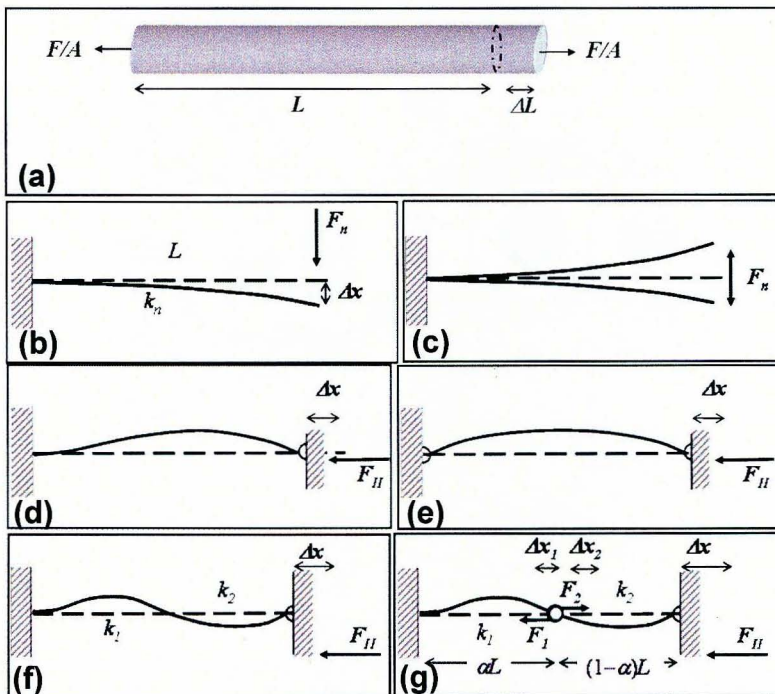


Figure 8.1. Mechanical elements used to model bending and buckling of the nanoneedles. (a) Schematic drawing of elastic deformation of a beam used in defining Young's modulus. (b) Static bending, and (c) vibration of a clamped-free beam by applying a force, perpendicular to the orientation of the beam. Buckling of (d) clamped-hinged, and (e) hinged-hinged beam when the beam is compressed along its length. (f) Second buckling mode or "S shaped" of a clamped-hinged beam. (g) Free-body diagram of buckling of a clamped-hinged beam. The inflection point is considered to be hinged.

In this chapter the Young's modulus of Ag₂Ga will be calculated by bending the needles as illustrated in Figure 8.1b. In some references this is called the *bending modulus* E_b [69].

Beam bending: A cantilevered beam is defined to have one end rigidly fixed or *clamped* and the other end free (i.e. a clamped-free beam). If the force F_n is applied at the free end of a beam normal to the longitudinal axis, the end deflects a distance Δx , (Figure 8.1b). In this situation the spring constant of the beam is

$$k_n = \frac{F_n}{\Delta x} \quad (8.1)$$

From k_n For a beam of length L and cross-sectional moment of inertia I , Young's modulus E is [70]

$$E = \frac{k_n L^3}{3I} \quad (8.2)$$

Beam vibration: A sinusoidal force $F(t) \sim \sin(2\pi f_n t)$ of frequency of f_n is applied to the end of a cantilever as illustrated in Figure 8.1c. The maximum displacement is found at the resonance frequencies f_n . For a clamped-free beam the resonance frequencies are [71]

$$f_n = \frac{\left(\frac{\beta_n^2}{2\pi}\right)\left(\frac{EI}{\rho}\right)^{1/2}}{L^2} \quad n=0, 1, 2, \dots \quad (8.3)$$

where ρ is the density of the material and β_n is a coefficient that is different for each mode of vibration. For the first resonance frequency $\beta_1= 1.875$, and for the second, $\beta_2= 4.694$. Note that in beam vibration problems the resonance frequencies are not harmonically related. For a cylindrical beam, the cross-sectional moment of inertia is

$$I = \frac{1}{4} \pi R^4 \quad (8.4)$$

where R is the radius of the beam. Combining equations (8.3) and (8.4) Young's modulus can be expressed in terms of known and/or measured parameters as

$$E = \frac{16\pi^2 f_n^2 L^4 \rho}{B_n^4 R^2} \quad (8.5)$$

The sharpness of the resonance peak is often described by the *quality factor* Q_n that is defined as

$$Q_n = \frac{f_n}{B_n} \quad (8.6)$$

where B_n is the bandwidth full width at half maximum (FWHM) of the passband of the n^{th} resonance peak. Q_n describes the sharpness of the resonance peak. The higher the Q , the more closely to a single frequency or pure tone the structure vibrates. Unless stated otherwise Q will represent Q_0 , the Q of the fundamental resonance frequency.

Beam buckling: If a force F_{II} is applied along the longitudinal axis of a beam, as illustrated in Figure 8.1.d it can buckle. Depending on the boundary condition of the beam support, the critical force F_c at which the beam becomes unstable and buckles varies. For various clamping condition, the equation for critical force takes the general form of

$$F_c = K \frac{\pi^2 EI}{L^2} \quad (8.7)$$

The value of K corresponds to the specific end conditions; i.e., for the first buckling mode of a hinged-hinged beam K is 1 and for a clamped-hinged beam K is 2.04 [72].

Note that the value of K increases for higher order of buckling. This indicates that buckling a beam can be found in a stable mode until the next value of F_c is applied.

It is objective to this discussion to approximate the spring constant of a clamped-hinged beam in the second order buckling mode (i.e. Figure 8.1f). Higher buckling modes can be represented in term of the first buckling mode by a standard procedure that is referred to as, *the effective length method* [72,73]. The approach considers the beam to be composed of two beams joined together at their inflection point that are each in the first order buckling modes. Figure 8.1g shows the free body diagram for each of the two point of the compound of the beam. The left section (*Beam 1*) with a length of αL is modeled as a clamped-hinged beam and the right section (*Beam 2*) with a length of $(1-\alpha)L$ is similar to a hinged-hinged beam. The fractional distance from the fixed end to the inflection point is $0 < \alpha < 1$. The respective critical forces F_{c1} and F_{c2} at which each Beam 1 and Beam 2 become unstable are

$$F_{c1} = 2.04 \frac{\pi^2 EI}{(\alpha L)^2} \quad (8.8)$$

$$F_{c2} = \frac{\pi^2 EI}{[(1-\alpha)L]^2} \quad (8.9)$$

Since the two compound are connected in series, then

$$F_{c1} = F_{c2} \quad (8.10)$$

Solving equations (8.8) to (8.10) for α , gives $\alpha = 0.588$ and the critical force F_{cS} for a second order buckling mode that is referred to as "*S*" shaped buckling is

$$F_{cS} = 5.9 \frac{\pi^2 EI}{L^2} \quad (8.11)$$

From the critical force in Figure 8.7 one can roughly estimate the spring constant of a beam for force slightly larger than F_c and small changes in length L . This is done by taking the first derivative of the critical force with respect to L , considering change in the length is the same as the change in distance between the two ends of the beam. This assumption leads to

$$k = \frac{2}{L} F_c \quad (8.12)$$

For values of $K = 2.04$ and 5.9 described above, the corresponding spring constant are

$$k_{ch} = 4.08 \frac{\pi^2 EI}{L^3} \quad (8.13)$$

$$k_S = 11.8 \frac{\pi^2 EI}{L^3} \quad (8.14)$$

where k_{ch} is that of a clamped-hinged beam (Figure 8.1e) and k_S is the spring constant of the second buckling mode (“S shaped” buckling, Figure 8.1h). From equations (8.13) and (8.14), the spring constant of the second buckling mode of a clamped-hinged beam is estimated to be 2.88 times larger than that of the first mode.

8.3 Overview of the experimental procedures

The elastic properties of the needles are studied by observing the deflection of individual needles attached to AFM cantilevers. Several measurements methods are used and the results are compared against each other to demonstrate the accuracy of the data. SEM together with a nanomanipulator and AFM are the principal instruments used in these measurements.

8.3.1 Electrostatic deflection of needles

Deflections of the needles are viewed inside the SEM. An AC voltage is applied between the needle and an electrode connected to a nanomanipulator arm. The electrode is brought close to the free end of the needle. The frequency of the AC voltage is then varied until the deflection of the needle is maximum. This frequency is considered to be the resonance frequency of the needle. From the resonance frequency and information about the length and diameter of the needle, and the density of the material, Young's modulus of the material is calculated by equation (8.5).

8.3.2 AFM Force microscopy

The needle-tipped cantilevers are mounted in an AFM. The needles are pressed against a hard, negligible deforming surface such as silicon. The AFM records the deflection of the cantilever as a function of applied force. The resulting plot is referred to as a *force-distance* (F-D) curve. In these studies force and torque from a needle produces cantilever deflections that are recorded as force in the F-D curve.

The F-D curves provide data from which can be determined spring constant, Young's modulus of Ag₂Ga, Hamaker constant between Ag₂Ga and Si in air, the frictional constant of Ag₂Ga, and the spring constants of needles in specific buckling modes.

8.3.3 Visual observation of deflection

SEM observations of bending, buckling and sliding of needles are used to provide visual confirmation of the type of deflection that corresponds to the AFM F-D curves.

8.4 Measurement of E and Q by electrostatic deflection

8.4.1 Experimental procedure

Nanoneedles are grown on AFM tips by the method developed in Chapter 5. They are electrostatically deflected over a range of frequencies to produce a spectrum of the displacements. The data is then used to evaluate Q and E . This method has been used by Poncharal *et. al.* [69, 74]. The needle is directly imaged in the SEM as it is deflected. An AFM cantilever with an attached Ag_2Ga needle is mounted on a Zyvex nanomanipulator inside the FE-SEM. The pressure inside the chamber is between 1×10^{-5} and 5×10^{-5} torr. The needle is brought close to an electrode that is connected to a second nanomanipulator arm. The free end of the needle is positioned between 500 nm to 5 μm above the electrode (Figure 8.2a). In this arrangement the needle is directly under the SEM lens where it can be imaged. A fixed AC voltage between 1 and 10 V is swept from 20 kHz to 10 MHz.

The resonance frequency of the needle corresponds to the frequency at which the deflection of the needle is maximized and the bandwidth B corresponds to the FWHM of the resonance. Q is determined using B and f_0 in equation (8.6). E is determined using f_0 together with material and dimensional parameters in equation 8.5.

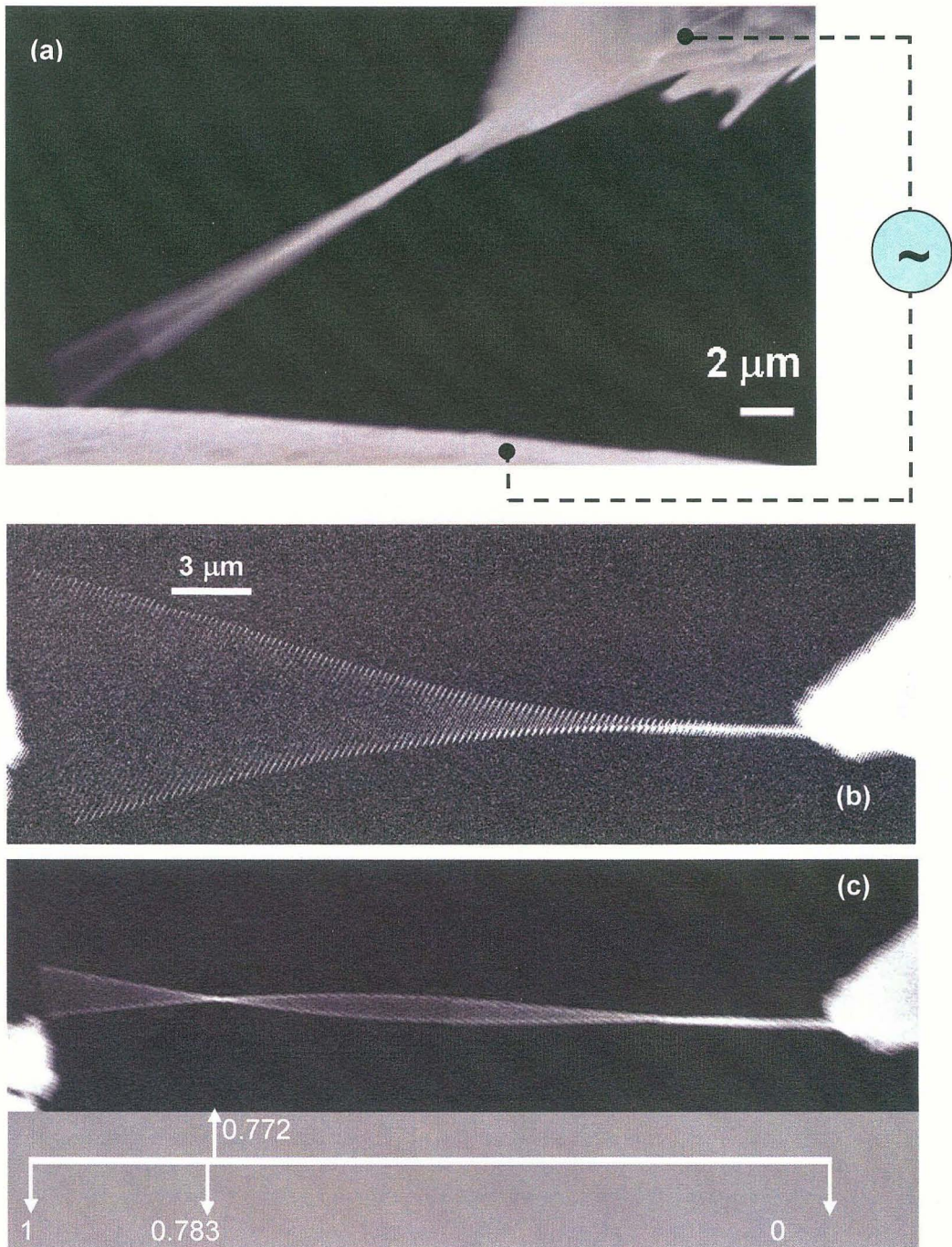


Figure 8.2. AC voltage excitation of a nanoneedle. (a) Experimental setup (b) SEM image of the first mode occurring at 76.6 kHz, and (c) the second mode at 675 kHz. The white spot in the left hand side of the image is the electrode. A scale bar in the figure shows measured (0.772) and theoretical (0.783) locations of the node.

8.4.2 Experimental results and discussion

Figure 8.2a is an SEM image of an excited needle with schematic drawing of the electrical contacts between the AFM tip and a second electrode that is a tungsten wire. SEM images of another needle excited in its first and second harmonic modes is shown in Figure 8.2(b,c). The first resonance (Figure 8.2b) occurs at 76.6 kHz and the second one (Figure 8.2c) occurs at 675 kHz. The ratio of the resonance frequencies is 8.8. In theory [75] the ratio between first and second natural frequency of a uniform beam is 6.26. A closer correspondence is found in the location of the stationary point or *node*. The node as annotated on Figure 8.2c is at $0.772L$ from the clamped end. The theory for a uniform diameter beam with one end clamped indicates that the node would be at $0.783L$ [76].

The resonance frequencies of 21 nanoneedles have been measured and are reported in Appendix A. Calculated values of E using equation (8.5) are also reported in Appendix A and presented as a histogram in Figure 8.3. The value of E varies between 17 and 96 GPa with an average of 42.6 GPa and a standard deviation of 22.4 GPa. The most frequent measurement was the 28.5 to 31.5 GPa bin of the histogram. Various non-ideal properties of the needle could contribute to the observed variations; e.g., the non-circular cross-section and tapering of the needles.

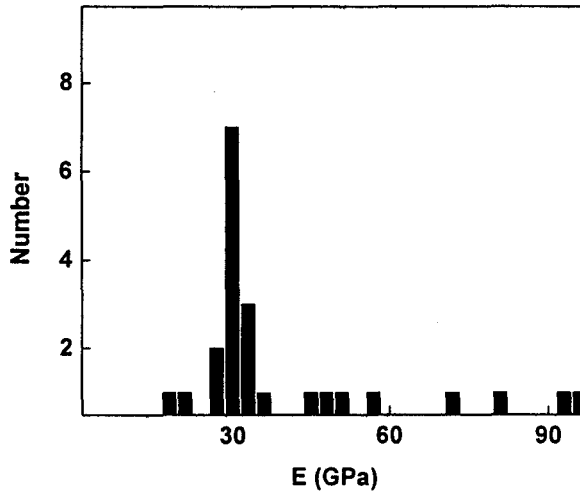


Figure 8.3. Histogram of Young's modulus of 21 nanoneedles. These needles vary in length from 3 to 30 μm and in diameter from 100 to 500 nm. The width of the bins is 3 GPa. A table listing the exact values for each needle is presented in Appendix A.

The Q in the fundamental mode was evaluated for seven needles. A typical deflection versus frequency response is shown in Figure 8.4. The Q varies between 600 and 3300. In similarly performed measurements, Q of carbon nanotubes was reported to be between 300 and 2000 [77].

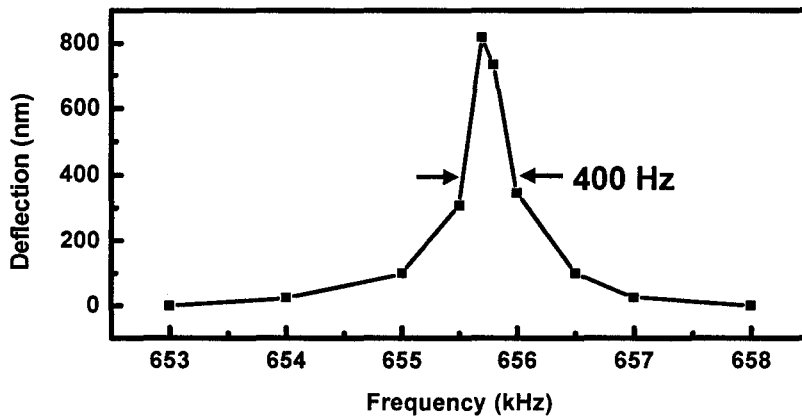


Figure 8.4. Deflection as a function of frequency of a needle around its fundamental mode. The

needle is 8.35 μm long and 85 nm in diameter. $Q \cong \frac{655000}{400} \cong 1700$ (Needle 16 in Appendix A)

8.5 Spring constant of cantilevered needles by force microscopy

In this section the spring constant a needle configured as in Figure 8.1b is determined. Since the needle is connected to an AFM cantilever, the effect of the cantilever mechanical properties and the geometry of the system of cantilever and needle need to be accounted for. This subsection and the next account for these effects, enabling determination of the spring constant of the cantilevered needle.

The spring constant of the AFM cantilever is measured before growing the needle. It is found by measuring the frequency spectrum of the cantilever caused by collision of the air molecules with the cantilever (i.e. Brownian motion). In the frequency spectrum the power spectral density of the cantilever fluctuation gives the spring constant of the cantilever by [78]

$$k = \frac{k_B T}{P} \quad (8.15)$$

where k_B is the Boltzmann's constant, T is the temperature and P is the integrated power spectrum underneath the resonance passband of the cantilever fluctuation. The Asylum AFM measures this spectrum from the intensity fluctuation of the AFM laser on the quadrant photodetector (Figure 8.5a). Once k is known, the cantilever deflection is directly interpreted as force. The cantilever is brought in contact with the surface (Figure 8.5b) and the F-D curve is measured from the cantilever deflection which gives force as a function of the piezo extension. The piezo extension corresponds to the distance on the curve.

The F-D curve of a system of a Ag_2Ga needle on a cantilever is made by pressing the free end of the needle against the rigid surface and monitoring the subsequent deflection of the AFM cantilever. In this experiment, the slope of the F-D curve gives the spring

constant of the system of the needle and cantilever k_T . From this data and the spring constant of the cantilever, the spring constant of the needle k_n is extracted.

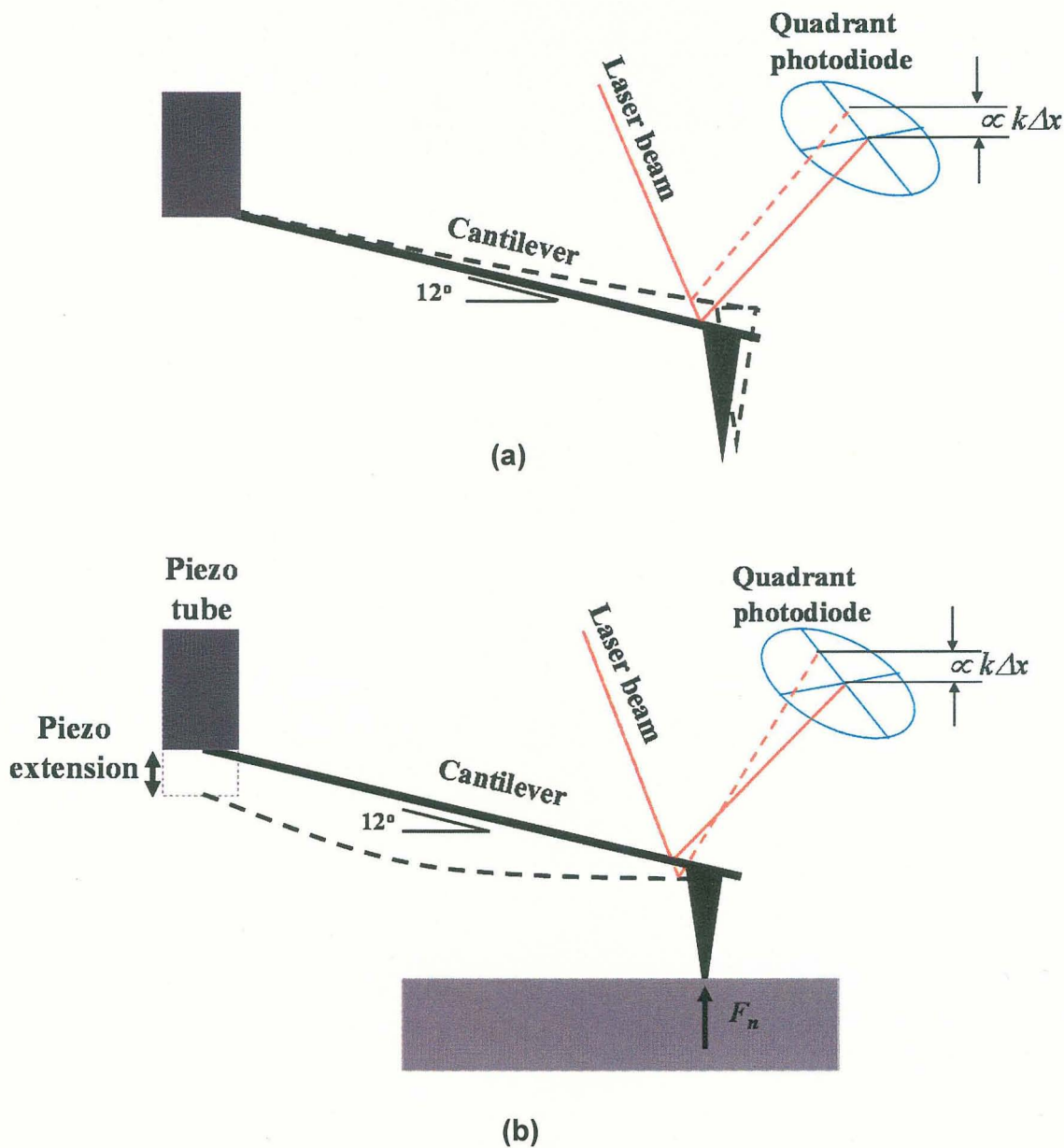


Figure 8.5. Schematic of F-D experiment with an AFM cantilever. (a) Calibration of the cantilever: Thermal fluctuation of the cantilever is detected from the intensity fluctuation of the laser on the photodetector. (b) Measurement of the F-D curve: Bending of the cantilever is measured by the photodetector as a function of piezo extension.

8.5.1 Mechanics of the double cantilever system

Figure 8.6a shows a schematic of a system of needle and cantilever in the F-D experiment and Figure 8.7 shows the actual system. The angle between the cantilever and the needle α is less than 10° and the angle between the cantilever and the surface is 12° . The angle between the needle and the surface is $\theta = \alpha + 12^\circ$. As shown in Figure 8.6b, the needle can be bent enough that the AFM tip and needle can simultaneously contact the surface. This condition makes it possible to measure the spring constant of the needle and the cantilever from a single force curve. A model for this mechanical system is presented to explain some of the features of the experimental F-D curves.

There are two situations illustrated in Figure 8.6: 1) where the needle touches the surface but the cantilever does not contact the surface (Figure 8.6a,c), and 2) where both the cantilever and needle contact the surface (Figure 8.6b).

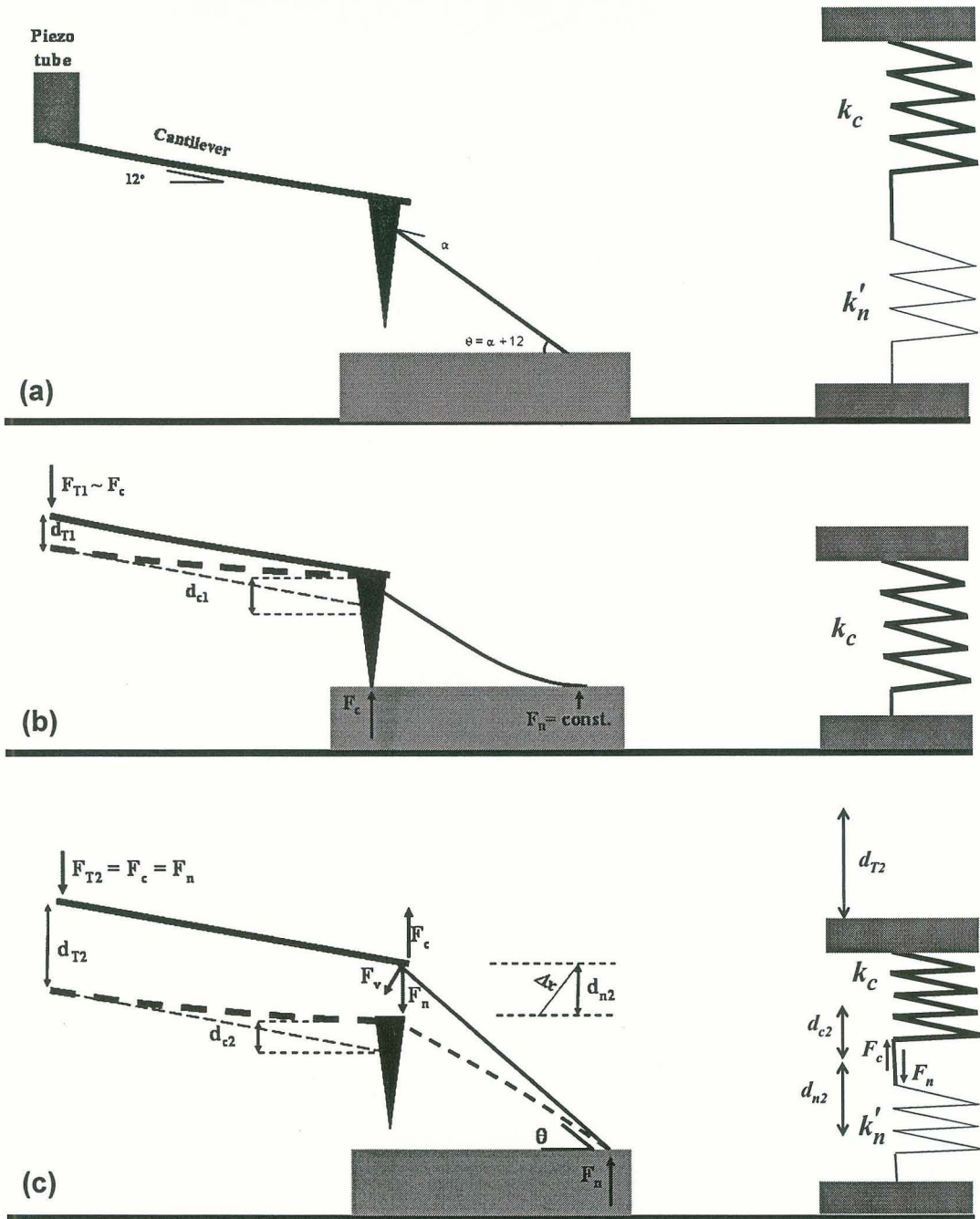


Figure 8.6. Schematic of the two cantilever system that consists of needle attached to the side of an AFM tip. (a) Diagram of the system when only the needle contacts the surface. Free body diagram of the system when (b) the needle and AFM tip contact the surface and (c) only the needle contacts the surface. The drawings to the right of each schematic show equivalent one-dimensional springs used to model the system.

When the needle and cantilever are both in contact with the surface, the total applied force from the piezo tube F_{T1} to the system is equal to the combined force of reaction from the surface to the needle F_n and cantilever F_c or

$$F_{T1} = F_n + F_c \quad (8.16)$$

However, since the cantilever is much stiffer than the needle, then $F_n \ll F_c$ even with small extensions beyond initial contact of the cantilever with the surface. Therefore upon contact the spring constant of the system will be approximately identical to the spring constant of the cantilever

$$k_{T1} \cong k_c \quad (8.17)$$

as in Figure 8.5. The small force of the needle also allows one to ignore torques of the needle on the cantilever due to the small cantilever bending when in contact with the surface.

In Figure 8.6c only the needle contacts the surface. The spring constant of the system can be modeled as two springs in series. It is assumed that the end of the needle does not slip. The system of two one dimensional springs in series experiences a displacement of d_{T2} for a force of F_{T2} . The force on each spring is

$$F_{T2} = F_c = F_n \quad (8.18)$$

The displacements of the springs are

$$d_{c2} = \frac{F_c}{k_c} \quad (8.19)$$

$$d_{n2} = \frac{F_n}{k_n} \quad (8.20)$$

$$d_{T2} = \frac{F_{T2}}{k_{T2}} \quad (8.21)$$

where k_n' and k_c are the spring constant of the needle and cantilever respectively, d_{c2} and d_{n2} are the displacement of the cantilever and the needle respectively and k_{T2} is the stiffness of the system of cantilever and the needle. Substituting equation (8.18) into (8.19) to (8.21) gives

$$k_{T2} = \frac{k_n' k_c}{k_n' + k_c} \quad (8.22)$$

Note that the needle is not in the same orientation as was used for equation (8.2) to determine the Young modulus from the spring constant k_n . For this reason the effective spring constant for the tilted needle is written as k_n' . The spring constant k_n' can be related to k_n through the geometry differences between the parallel and tilted orientations.

The bending of the needle is essentially due to a force F_v that is perpendicular to the axis of the needle

$$F_v = F_n \cos \theta = F_c \cos \theta = k_n \Delta x = \frac{k_n}{\cos \theta} d_{c2} \quad (8.23a)$$

With the specific result of interest being

$$F_n = \frac{k_n}{\cos^2 \theta} d_{c2} \quad (8.23b)$$

Combination of equation (8.20) and (8.23) and substituting the result into (8.22) gives

$$k_n = \frac{k_c k_{T2}}{k_c - k_{T2}} \cos^2 \theta \quad (8.24)$$

If the spring constant of the needle is much smaller than the cantilever, then equation (8.23) can be simplified to

$$k_n \cong k_{T2} \cos^2 \theta \quad (8.25)$$

The value of k_{T2} is interpreted on the F-D curve as the slope when only the needle is in contact with the surface.

8.5.2 Experimental details

Figure 8.7 shows an SEM image of a needle grown on the side of an AFM tip. For convenience it is called *Sample 1*. The needle is grown as described in Chapter 5. Table 8.2 shows mechanical properties and geometrical parameters for the needle and cantilever before and after growing the needle.

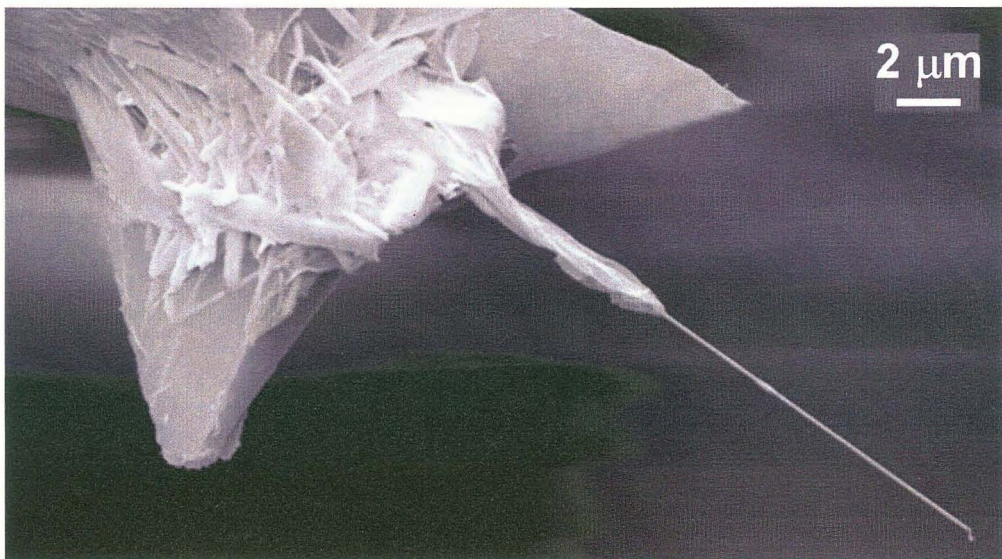


Figure 8.7. SEM image of a nearly-parallel grown nanoneedle on the side an AFM cantilever.

F-D measurements are made using an Asylum Research AFM. Initially the tip is positioned 1 μm from the surface and the piezoelectric tube extension range is limited to 200 nm. If the tip does not make contact with the surface, the tip is lowered slightly and the process is repeated until the needle touches the surface and a reasonable force curve is observed. The scan is repeated until the force curve can be retraced several times. Then

the curve is recorded. SEM images before and after the measurement confirm that the needle is unchanged by the AFM experiment.

Table. 8.2. The mechanical parameters of Sample 1 before and after the adding the needle.

Parameters	Symbol	Sample 1	
		Before adding needle	After adding needle
Nanoneedle length (μm)	L	-	11.86
Average nanoneedle radius (nm)	R	-	75
Resonance frequency of the nanoneedle (kHz)	f_0	-	421.0
Angle between the needle and the surface (Degrees)		-	20
Model of AFM cantilever		Budget sensor BS-Tap 300	-
Resonance frequency of the AFM cantilever (kHz)	f_{0c}	293.27	293.2
Spring constant of cantilever after Ag sputtering (N/m)	k_c	10	9.83
Spring constant of needle and cantilever when both are in contact with the surface (N/m)	k_{T1}	-	9.83
Spring constant of needle and cantilever when only needle is in contact with the surface (mN/m)	k_{T2}	-	37
The spring constant of the needle (mN/m)	k_n	-	33
Young's modulus of the needle (GPa)	E	-	71.2

8.5.3 Results and discussion

Figure 8.8 is the F-D curve for Sample 1. In Location 1 the needle snaps onto the surface due to van der Waals (vdW) force [79]. The force increases faster than the restraining force of the needle leading to the unstable snap-down within a few nanometers of the surface. At Location 2 over almost 40 nm of extension of the piezotube, the needle and cantilever produce a linear F-D curve with a slope of 37 mN/m.

At Location 3, the AFM tip approaches the surface. This instability does not appear to be due to vdW force because the snap down distance is almost 5 times larger than snap down distance based on theory [See section 8.6.1]. If the instability was due to vdW force, a snap-off would be expected in the retraction curve rather than the gradual recovery observed in Figure 8.8. For these reasons a mechanical instability, torsional instability, or slipping is a more likely explanation.

At Location 4, once the AFM tip is in contact with the surface, the slope increases to 9.83 N/m.

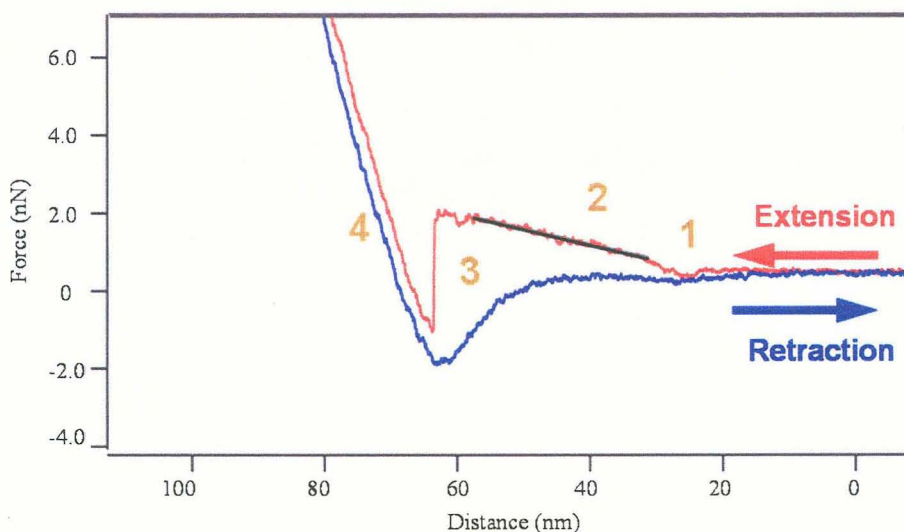


Figure 8.8. F-D curve of the needle-cantilever system (Sample 1).

Using the slope for Location 2 in the curve, the spring constant of the system of the needle and cantilever is 37 mN/m. Using the slope of Location 4 the spring constant of the system is 9.83 N/m which is essentially the spring constant of the cantilever. Using a 20° as the angle between the needle and the surface (Table 8.2), the spring constant of the needle is calculated from equation (8.24) to be 33 mN/m. It should be noted that the

spring constant of the cantilever before growing the needle was thermally measured to be 10 N/m. The small shift might be due to extra Ga that spread over the cantilever.

The spring constant of a second needle (Sample 2) was measured with this method. The spring constant of the cantilever is 1.41 N/m, and the total spring constant of the system is 105 mN/m the angle between the surface and the needle is 30°. Using equation (8.23) the spring constant of the needle is calculated to be 85 mN/m. Further studies using Sample 2 are reported in section 8.7.

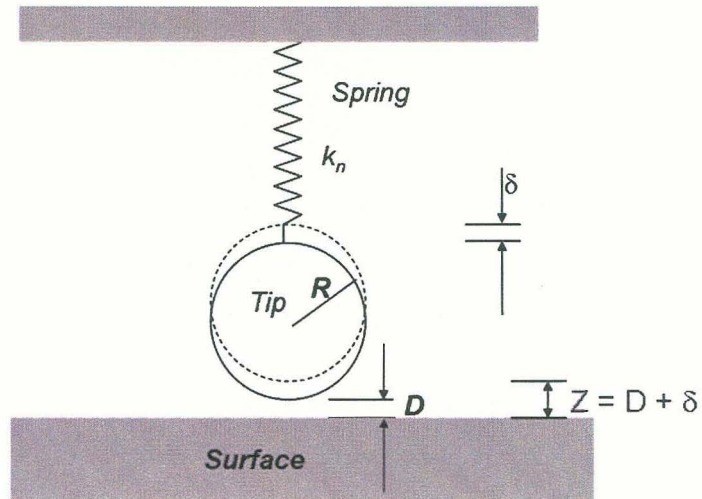
8.6 Measurement of vdW force between Ag₂Ga and Si

8.6.1 Theory

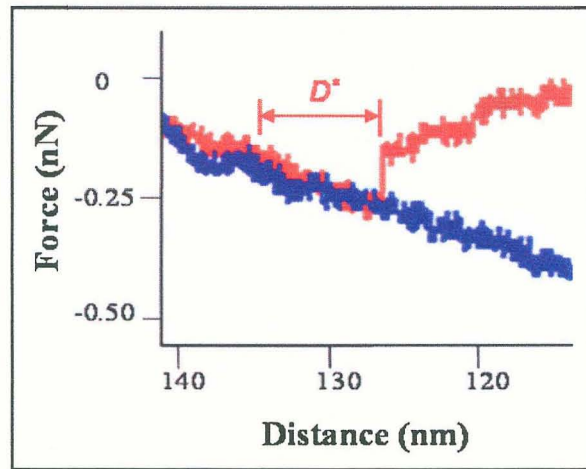
F-D curves can be used to calculate the vdW force between the needle and the surface. As the tip of the nanoneedle approaches to the sample, the needle deflects due to vdW force. The end of the needle is modeled as a sphere of radius R that is connected to a spring of stiffness k_n (Figure 8.9). The vdW potential energy between two surfaces depends on their geometries. For a sphere and a planar surface, when their separation is much smaller than the diameter of the sphere, the potential is approximated as [78,79]

$$W(D) = -\frac{AR}{6D}, \quad D \ll R \quad (8.26)$$

where D is the distance between the plane and the sphere and A is Hamaker constant, which has units of energy. The constant A was named after H. C. Hamaker (1937), who performed many of the early studies on forces between macroscopic bodies.



(a)



(b)

Figure 8.9. van der Waal force between the tip of a needle positioned close to a planar substrate. (a) Idealized geometry for the tip of a needle positioned close to the surface [80]. (b) Close-up view of the snap-down event on the from F-D curve in Figure 8.8. This range is used to measure the distance D^* at which the system becomes unstable and snaps-down.

Figure 8.9a presents an idealized geometry that represents a spherically tipped needle in close proximity to the surface. The total potential energy of the system of the spring and vdW attraction is written as

$$U(\delta) = -\frac{AR}{6(Z-\delta)} + \frac{1}{2}k_n\delta^2 \quad (8.27)$$

where $Z=D+\delta$ is the distance between the surface and the un-deflected spring, and δ is deflection from the rest position due to vdW force. In a stable situation, the potential energy is minimized. The minimum energy is found by setting the derivative of U in equation (8.26) with respect to δ equal to zero. The resulting equation is

$$\frac{AR}{6(Z-\delta)^2} = k_n\delta \quad (8.28)$$

For stability it is also required that the energy function has a positive curvature. If the curvature is negative, the vdW force grows faster with δ than does the spring restraining force, which produces the leading to unstable snap down. The transition between stability and instability corresponds to a curvature of zero. This corresponds to an undeflected separation of Z^* . Any closer separation results in snap down. Taking the second derivative of energy $U(\delta)$ and setting it to zero gives the value of D^* and Z^*

$$D^* = \left(\frac{AR}{3k_n} \right)^{\frac{1}{3}} = \frac{2}{3}Z^* \quad (8.29)$$

Since the cantilever or the needle during an F-D measurement bends increasingly as the tip approaches the surface, the cantilever snaps down to the surface from a height of D^* . The value of D^* is then determined from the F-D measurement by extending the piezo until the cantilever is at the same force (or is identically bent) as it was just prior to the snap-down. The distance that the piezo extends from the snap-down position to the position of equal force is interpreted as D^* . In Figure 8.9b the value of D^* is 85 Å.

8.6.2 Results

F-D data for Sample 1 (Location 1 in Figure 8.8), is evaluated for the Hamaker constant of the Si-air-Ag₂Ga system. In this experiment, the distance at which the system becomes unstable is measured to be $D^* = 47 \text{ \AA}$. The radius at the tip of the needle is 65 nm. The spring constant of the needle is 33 mN/m. From equation (8.29), A is calculated to be $1.58 \times 10^{-19} \text{ J}$. In a similar experiment with another needle (referred to as Sample 3), $D^* = 85 \text{ \AA}$, the radius of the needle is 49 nm and the spring constant of the needle is 5.42 mN/m. Thus, the Hamaker constant is calculated to be $2.03 \times 10^{-19} \text{ J}$. For metals such as Au, Ag, and Cu the Hamaker constant of two identical media through the air is 3 to $5 \times 10^{-19} \text{ J}$ [81].

The Hamaker constant of a system of Si-air-Si is also measured using a commercial Si tip with a spring constant of 0.1 N/m and tip radius of 60 nm. The snap-down distance is 35 \AA . Thus the Hamaker coefficient for the Si-air-Si system is $2.14 \times 10^{-19} \text{ J}$. The Hamaker constant of Si-Si interaction through air is reported to be $1.865 \times 10^{-19} \text{ J}$ [82].

The resulting measurements are compared with the theory (equation 8.28) in Figure 8.11 for both Ag₂Ga and Si tips. The experimental value of D^* and k (k_n for needle and k_c for the cantilever) are combined with the value of $D^*k^{1/3}$ which is found in equation 8.28 and which is a function of Hamaker constant A and variable R . For Si, the Hamaker constant of $1.865 \times 10^{-19} \text{ J}$ is used [82]. For Ag₂Ga, the Hamaker constant is chosen to be $2.03 \times 10^{-19} \text{ J}$ that is calculated from F-D evaluation of Sample 3. Therefore, the curve and data point match perfectly. The other data point from Sample 1 differs only by 8% of the theoretical value.

The third data point (black square) from Si tip is found to only differ by 4% from the theoretical value. This data point is also repeated in the inset of Figure 8.10 and compared with the data taken from Location 3 in Figure 8.8.

If this instability is assumed to be due to the snap-down of Si cantilever, then considering the radius of the AFM tip $R = 750$ nm (Figure 8.7), $D^* = 73$ Å (Figure 8.8), and $k_c = 9.83$ N/m (Section 8.5.3), the value of $D^* k^{1/3} = 1.56 \times 10^{-8}$ (Jm) $^{1/3}$. This value is ~ 5 times larger than required by the model. Some other instability; e.g., elastic or torsional buckling is a more likely cause of the instability in Location 3 in Figure 8.8.

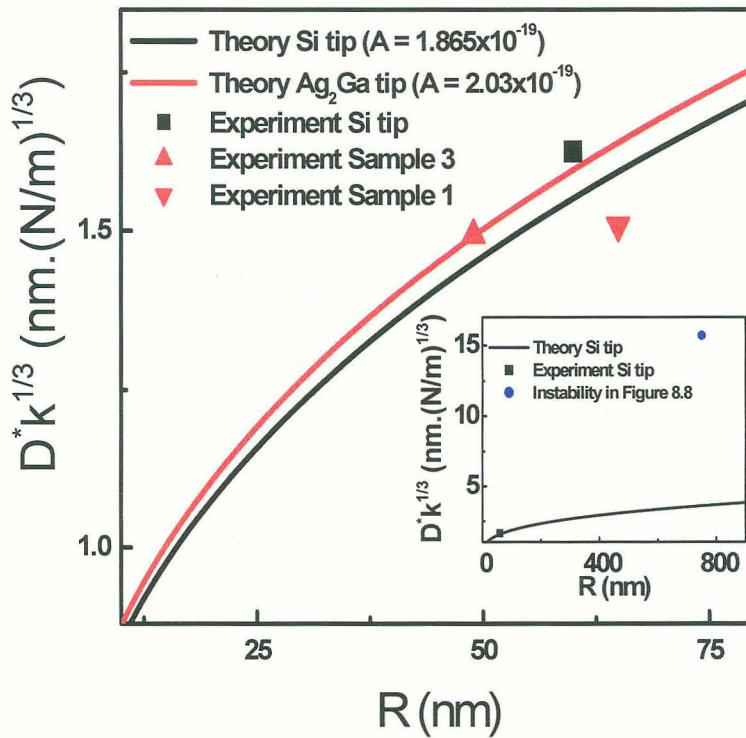


Figure 8.10. Comparison of theory of vdW snap-down [equation (8.29)] with measured value of snap-down. Inset shows that the snap-down at Location 3 in Figure 8.8 is not modeled as vdW attraction.

8.7 Frictional properties of Ag₂Ga needles

8.7.1 Mechanical model

When enough force is applied along the longitudinal axis of a beam, rod or column it can either buckle or slip. At normal incidence to the surface, buckling is favored. As the beam is tilted away from normal, the force transferred to the horizontal direction increases, favoring slipping over buckling. When a needle slides, the reaction to sliding or frictional force is imparted to the AFM cantilever and is evident in the F-D curves. This section considers frictional properties.

The classical description of frictional properties of materials is

$$\begin{aligned} f_k &= \mu_k N \\ f_s &= \mu_s N \end{aligned} \quad (8.30)$$

where N is the normal force applied to the object, μ_k is the kinetic or sliding frictional coefficient, and μ_s is the static frictional coefficient. Since μ_s is usually larger than μ_k , this relationship leads to stick-slip motion where f_s must be reached before the object slips.

A simple model is proposed to explain the main features observed in AFM F-D curves of needles slipping. Figure 8.11 shows a geometry in which a needle with an oblique angle to the surface slides. The needle is treated as being freely hinged at the AFM cantilever. One end of the needle slides along a vertical frictionless surface and the other end of the needle slides with friction over the horizontal substrate. In this configuration, the vertical force is measured from the deflection of the cantilever in F-D experiments. For this model it is assumed that

- 1) The movements during the slipping are *quasi-static*, i.e. the velocity is constant.
- 2) The needle is essentially a rigid rod; i.e., it does not bend or buckle any significant amount while slipping.

- 3) The end of the needle attached to the cantilever is restrained to move in only the vertical direction.
- 4) The end of the needle in contact with the substrate only moves parallel to the surface.
- 5) The change in the angle between the needle and the surface during slipping is negligible; i.e., the angle is assumed constant.
- 6) The mass of the needle is negligible; i.e., gravitational effects are not considered.

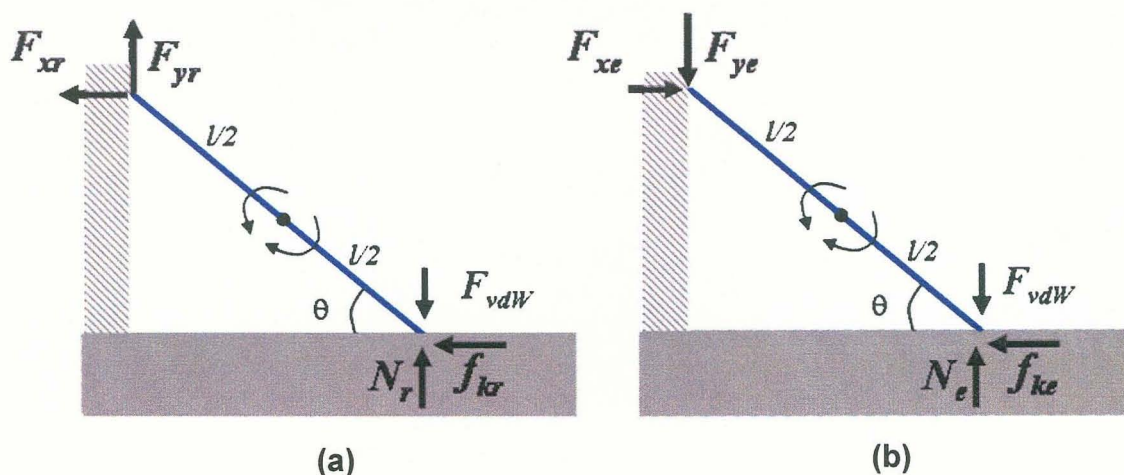


Figure 8.11. Free body diagram of a rigid rod sliding during (a) extension and (b) retraction of an actuator.

Figure 8.11a,b details the forces applied to the needle during extension and retraction. F_x and F_y are the respective x and y components of the applied force from the cantilever to the needle. Where the needle touches the substrate there is a reaction force N on the needle that is the summation of the vdW force F_{vdW} and the normal force (F_{ye} during the extension and $-F_{yr}$ during the retraction) from the cantilever. Also a sliding friction

produces a force f_k at the end of the needle that is parallel to the surface. Note the differences in the free body diagrams for extension (Figure 8.11a) and retraction (Figure 8.11b). In particular, note that the frictional force always opposes the motion of the needle, while the vdW force is always downward. For the quasi-static assumption, the summation of all forces in both x and y directions must be zero, and the sum of all rotational moments must be zero. During extension, the force balance equations

$$\begin{aligned} F_{xe} &= f_{ke} \\ N_e &= F_{vdW} + F_{ye} \end{aligned} \quad (8.31)$$

and the total moment around the centroid of the rod is

$$\frac{l}{2} [(N_e - F_{vdW}) + F_{ye}] \cos \theta - \frac{l}{2} (F_{xe} + f_{ke}) \sin \theta = 0 \quad (8.32)$$

Eliminating N and F_x gives

$$F_{ye} = f_{ke} \tan \theta = \mu_k (F_{vdW} + F_{ye}) \tan(\theta) \quad (8.33)$$

where the last equation followed from eliminating f_{ke} by using N_e from equation 8.31 in equation 8.30.

Note the addition of the subscripts “e” and “r”, which are used to distinguish the variables during extension from the variables during retraction. Duplicating the derivation for the retraction (Figure 8.11b) gives the force and moment balance equations

$$\begin{aligned} F_{xr} &= f_{kr} \\ N_r &= F_{vdW} - F_{yr} \end{aligned} \quad (8.34)$$

$$\frac{l}{2} [(F_{yr} + F_{vdW}) - N_r] \cos \theta - \frac{l}{2} (F_{xr} + f_{kr}) \sin \theta = 0 \quad (8.35)$$

Following the steps to obtain equation 8.32, retraction force can be written as

$$F_{yr} = \mu_k (F_{vdW} - F_{yr}) \tan \theta. \quad (8.36)$$

Equations (8.33) and (8.36) can be combined to eliminate F_{vdW} to give

$$(F_{ye} - F_{yr})\cos\theta = \mu_k(F_{ye} + F_{yr})\sin\theta \quad (8.37)$$

Note that F_{vdW} does not need to be known. Therefore any adhesive force will produce the same result. F_{ye} and F_{yr} can be directly related to the spring constant of extension k_e and retraction k_r of the F-D curve. Specifically note that

$$\begin{aligned} F_{yr} &= k_r \Delta y \\ F_{ye} &= k_e \Delta y \end{aligned} \quad (8.38)$$

And that Δy divides out of equation 8.37 resulting in

$$\mu_k = \left(\frac{k_r - k_e}{k_r + k_e} \right) \cot(\theta) \quad (8.39)$$

8.7.2 Experimental details

The experimental setup is similar to the one in Section 8.4.2. An SEM image of the needle-cantilever is shown in Figure 8.12a. This device is referred to as *Sample 2*. The properties of the sample are listed in Table 8.3. The angle between the needle and the surface is 30° . This angle is smaller than shown in Figure 8.12a due to the 12° tilt of the cantilever in the AFM cantilever holder.

Table 8.3. Mechanical properties of Sample 2

Parameter	Sample 2	
	with needle	After breaking needle
Type of cantilever	Veeco ULCM-B	Veeco ULCM-B
Needle length (μm)	13.1	-
Needle diameter (nm)	484	-
Resonance frequency of the needle kHz	726	-
Angle between the needle and the surface (degrees)	30	-
Resonance frequency of the AFM cantilever (kHz)	45.00	45.011
Spring constant of needle and cantilever (N/m)	0.105	1.41

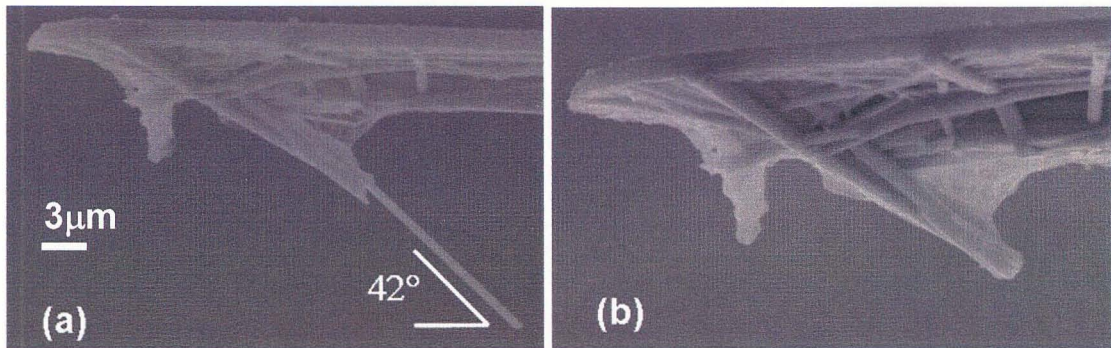


Figure 8.12. SEM images of Sample 2 (a) before and (b) after breaking off the needle.

8.7.3 Results

Figure 8.13 shows the F-D curves of the needle and cantilever system, as well as the cantilever by itself, after the needle is broken off. The slope of F-D curve in Figure 8.13a gives a cantilever spring constant of 1.41 N/m. The F-D curve of the system of needle and the cantilever is more complicated (Figure 8.13b). Four different slopes are indicated as Locations 1 to 4 in Figure 8.13b. Extension of the piezoelectric tube brings the needle close to the surface, and at a certain distance it snaps into contact with the silicon surface. With further extension the needle and cantilever flex together over a short distance

(Location 1). Thus the slope in Location 1 gives the spring constant for the flexing of a needle attached to a cantilever that is 105 mN/m. Using equation (8.25) and considering the spring constant of the cantilever $k_c = 1.41$ N/m, the spring constant of the needle is $k_n = 85$ mN/m. The needle spring constant predicts Young's modulus of $E = 23.8$ GPa by equation (8.2). This value is consistent with $E = 29.9$ GPa determined by the resonance frequency method (Section 8.4).

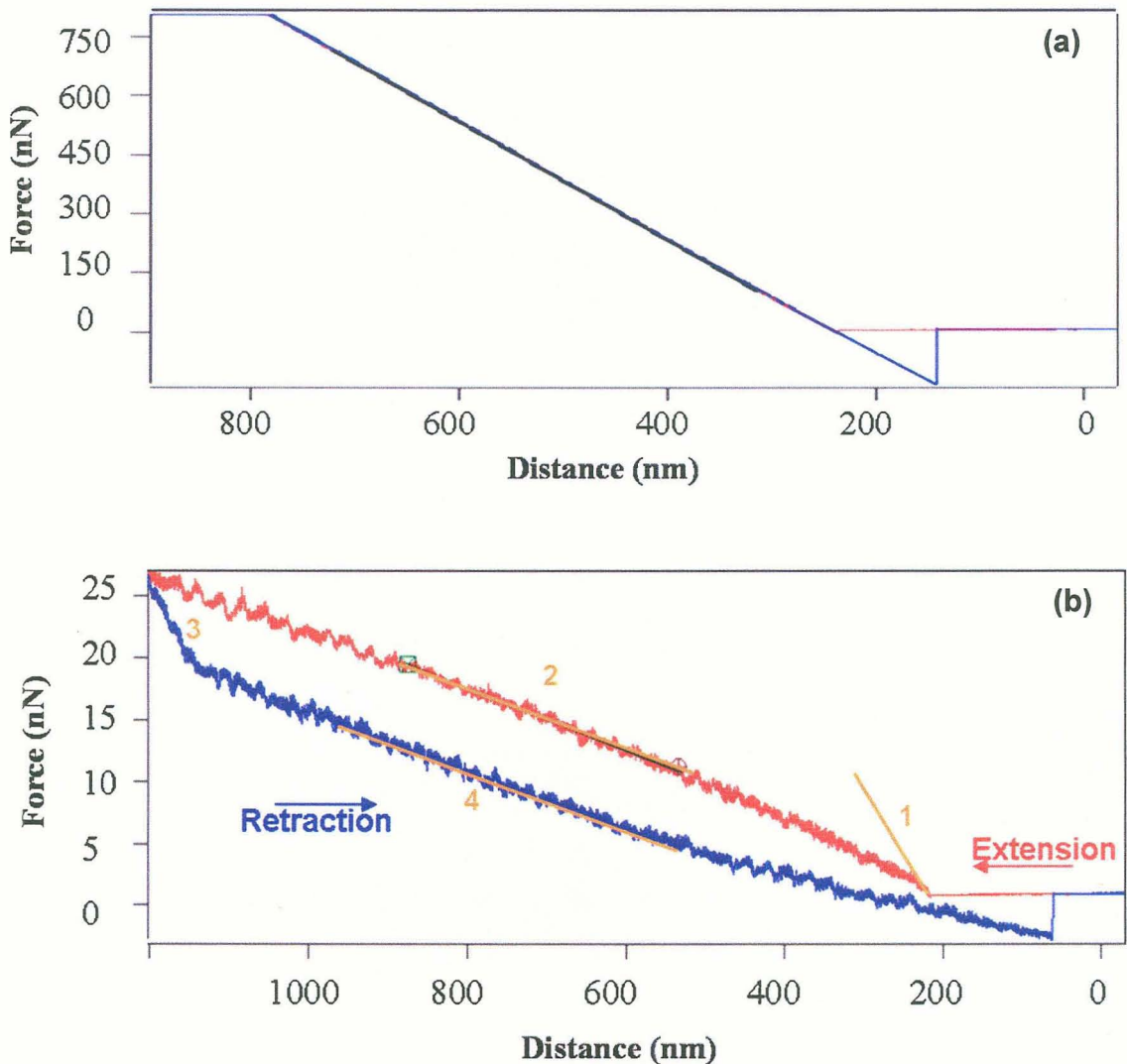


Figure 8.13. F-D response of a cantilever (a) after and (b) before breaking off the needle.

Due to the low angle between the needle and the surface, further extension of the piezoelectric tube, causes the needle to slip. This situation is shown at Location 2. The stick-slip motion is evident on the curve. When the direction of applied force changes from extension to retraction (Location 3), the needle releases from its flexed state. With further retraction (Location 4) slipping with stick-slip motion is again observed. The spring constants corresponding to Locations 1-4 are listed in Table 8.4. The spring constant k_e and k_r at Locations 2 and 4 when inserted in equation (8.39) gives a sliding friction coefficient μ_k of 0.168.

Table. 8.4. Measured spring constant of the needle-cantilever system at locations 1 to 4.

Location No.	Symbol	Spring constant of the system of needle and cantilever system (mN/m)
1	k_{T2}	105
2	k_e	27
3	k_3	433
4	k_r	22

8.8 Buckling in long needles

8.8.1 Modification of the buckling in semi-vertical needles

The buckling equations (8.12) to (8.14) that are presented in Section 8.2 should be slightly modified since the needles, grown on AFM tips, are not exactly vertical to the surface (Figure 8.14). A similar modification that was presented in Section 8.5.1 leads to

$$k_{||} = \frac{k_c k_{T2}}{k_c - k_{T2}} \sin^{-2}(\theta) \approx k_{T2} / \sin^2 \theta \quad (8.40)$$

where $k_{||}$ is the needle spring constant when a force is applied along the longitudinal axis of the needle, k_c is the spring constant of the cantilever, k_T is the spring constant of

the system that is measured from the slope of the F-D curve, and θ is the angle between the needle and the surface.

8.8.2 Experimental details

A 14 μm long nanoneedle with an average diameter of 98 nm (Figure 8.14) was grown on a Veeco ULCM-B cantilever by the method of Chapter 5. This sample is referred to as *Sample 3*. Some parameters of this needle were reported in Section 8.6.2. Using AC voltage excitation, the resonance frequency of the needle was measured to be 255 kHz. Considering an angle of 12° between the AFM chip carrier and the sample surface, the final angle between the tip and the silicon surface is 68 degrees. The characteristics of the cantilever without the needle are a resonance frequency of 26.999 kHz and spring constant of 1.54 N/m.

The F-D curves of buckling (as shown in Figure 8.15), can be quite complicated. To help interpret the curves, the same needle is imaged inside an SEM undergoing the same deflections as under the AFM.

8.8.3 Results and discussion

Figure 8.14 shows a sequence of images of Sample 3 approaching a surface, being compressed and being released. In Figure 8.14a at some distance from the surface the needle is straight. As it is brought closer to the surface, the needle bends through vdW attraction and snaps down in Figure 8.14b. The shape of the needle resembles the fundamental buckling mode. Depressing the cantilever further bends the needle until the needle becomes unstable and slips over the silicon surface toward the right (Figure

8.14c). The needle also has a slight “S” shape, suggesting that it might be in the second buckling mode.

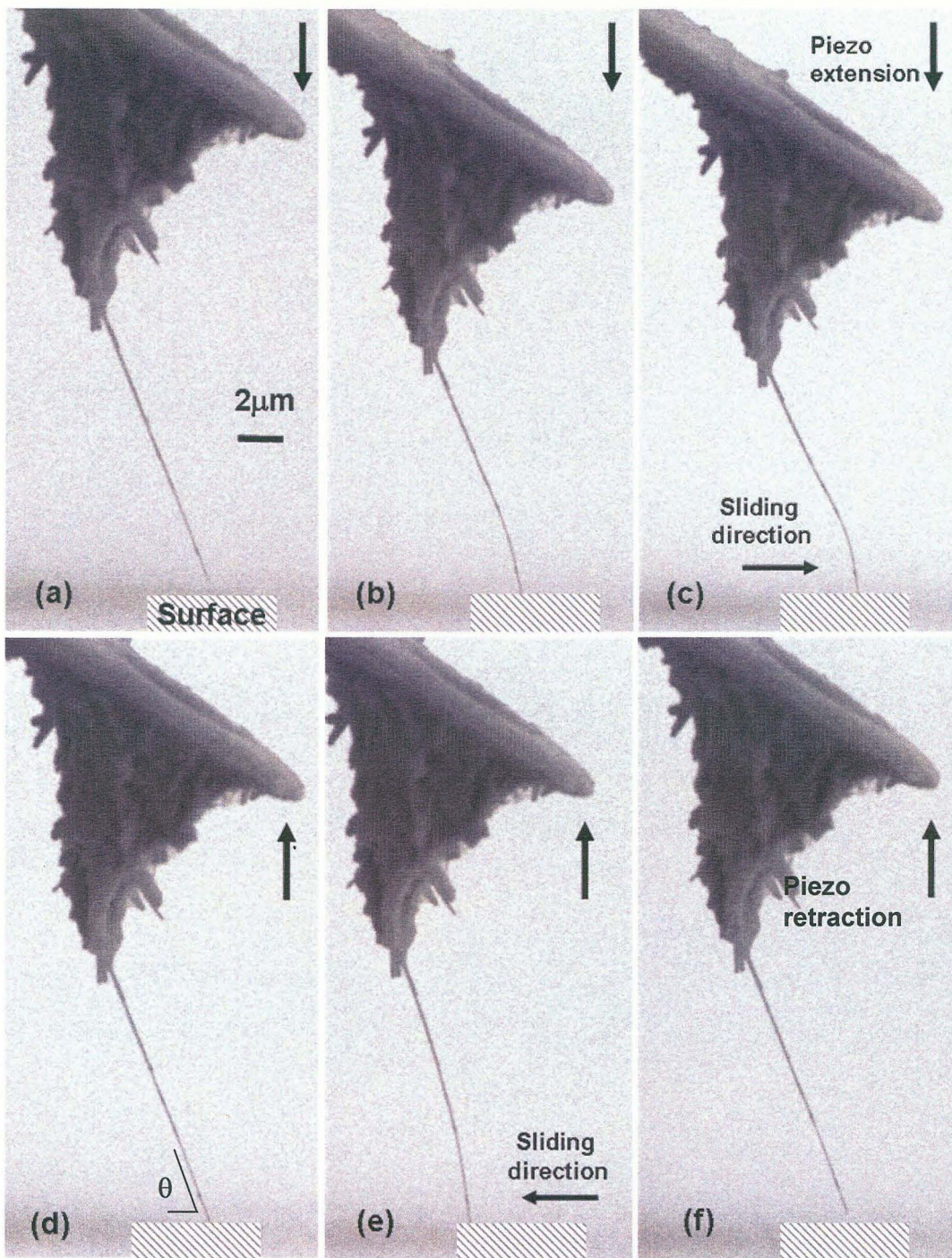


Figure 8.14. Time-lapse SEM images of Sample 3 during compression and release. The cross-hatching is added to make the surface easier to see.

Retracting the needle causes it to straighten in Figure 8.14d. Further retraction would separate the needle from the surface, except for vdW force which bends the needle and pulls it to the left (Figure 8.14e). Further retraction causes the needle to release from the surface and becomes straight again (Figure 8.14f).

Sample 3 is similarly deflected in an AFM while measuring the F-D response. Figure 8.15 shows three F-D curves of Sample 3 with different ranges of piezotube extension. In Figure 8.15a the needle is brought close to the surface causing it to bend closer towards the surface (Location 1 in the curve). With further extension the vdW force snaps the needle into the surface (Location 2). An expanded view of Location 2 used to determine D^* is shown in Figure 8.9b. The needle and cantilever flex together as the piezo tube continues to extend (Location 3). The retraction and extension curves have the same slope. The force required to separate the needle from the surface is 0.85 nN, which is much greater than the vdW snap-down force at Location 2. The slope of the graph at Location 3 is 4.65 mN/m, which is the spring constant of the needle and cantilever system just after snap-down. Using equation (8.38) the spring constant of the needle during buckling is $k_{II} = 5.42$ mN/m.

Figure 8.15b shows the force curve of the sample over a 500 nm extension distance. For this range which is larger than in Figure 8.15a, the nonlinearity of the force curve is apparent around Location 4 and 5. The slope of the curve immediately after the snap-down point (Location 2) corresponds to a linear spring constant of 4.65 mN/m, while the slope at Location 5 decreases to 1.54 mN/m.

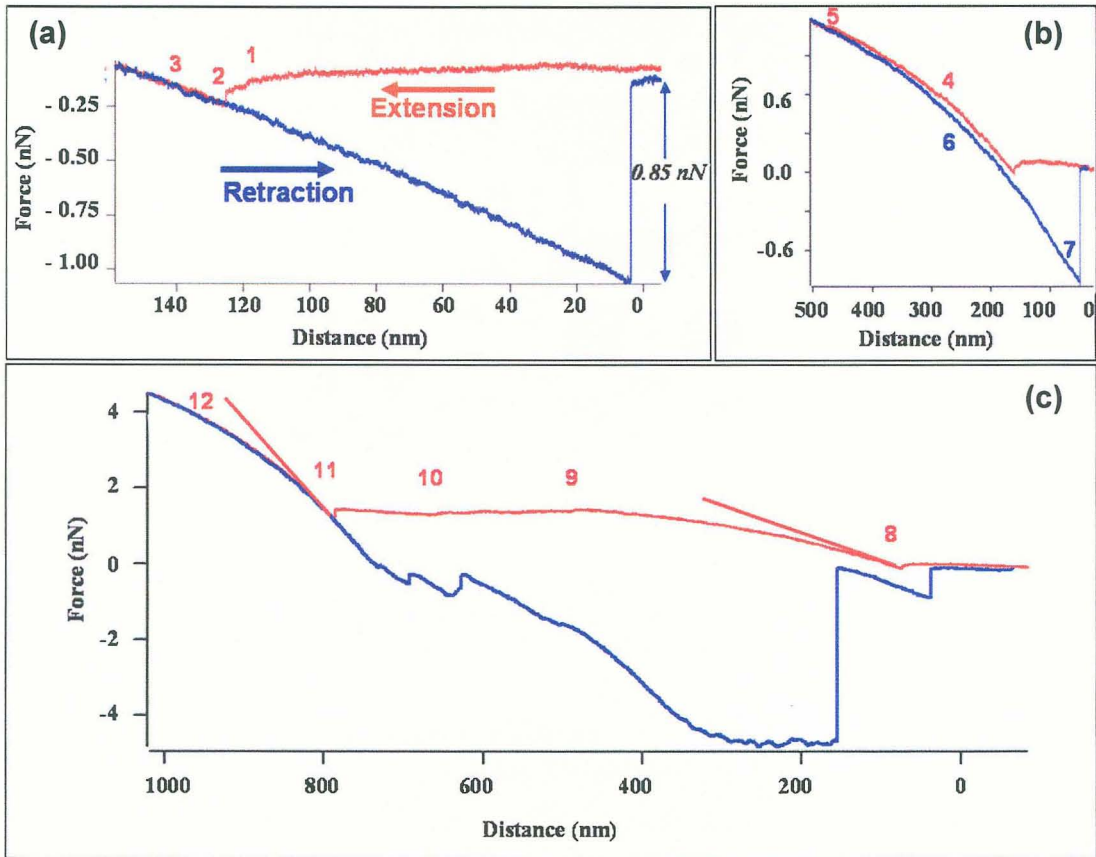


Figure 8.15. F-D curves of Sample 3 for a (a) 160 nm, (b) 500 nm, and (c) 1100 nm piezo extension range. The straight lines in (c) are the slopes at Location 8 and 11.

At Locations 4 through 6 some sliding occurs that leads to hysteresis between the extension and retraction curves (Location 6). At Location 7 sudden release from the surface occurs and the needle recovers to its unbent position.

Figure 8.15c, shows the F-D curve for an extension range of 1.1 μm . The needle snaps down to the surface at Location 8. Then the needle and cantilever flex together as the piezo extends. During compression, the end of the needle slides at Locations 9 and

10. At Location 11 the needle deflection changes from the first to the second buckling mode which stiffens the needle as described by equation (8.14). The slope at Location 12 is 18.50 mN/m which is the spring constant of the system of cantilever and needle in the second buckling mode. Using equation (8.40) and considering $k_c = 1.54$ N/m, the spring constant of the needle in the second buckling mode is $k_S = 21.50$ mN/m. The ratio between k_S and k_{II} as measured is 3.98. However, according to equation (8.13) and (8.14) the ratio between the first and the second buckling mode should be 2.88. Despite these numerical differences, many expected features are seen in the F-D curve. This includes stiffening due to higher order buckling and a near zero or negative slope (Location 4 to 11) corresponding to an instability region between the two buckling modes. Of course, the model ignores additional factors of sliding and bending due to vdW force. Additionally the spring constant model is only a crude approximation compared to the substantially more complex solution or simulations of the defining partial differential equations.

8.9 Summary of results obtained from elastic deformation experiments

Table 8.5 summarizes the mechanical parameters obtained from electrostatic deflection and F-D experiments of the four needles. The Young's modulus of the material, except for Sample 1, is calculated to be $E \sim 30$ GPa. For Sample 1, from F-D data E is calculated to be 72.1 GPa, while from resonance frequency it is calculated to be 877 GPa. This large discrepancy might be due to an insecure connection of the needle to the cantilever (See Figure 8.7). It appears that the thick rod that the needle connects to also deflects with the applied electric field.

The Hamaker constant obtained from two experiments also is listed in table 8.5. Resonance frequency, quality factor and spring constant (calculated from resonance frequency and AFM experiments, are also tabulated.

Table 8.5. Needle spring constant, Young's modulus, Quality factor and Hamaker constant.

Sample	L (μm)	R (nm)	f_0 (kHz)	Q	k (mN/m)		E from f_0 (GPa)	E from F-D (GPa)		Hamaker constant (A) $\times 10^{-19}$ J
					Electrostatic deflection	F-D curve		Bending	Buckling	
1	11.9	75	421	1700	3.8	33	71.2	877		1.58
2	11.06	242	726	1500	108	102	29.9	28.5		
3	14	49	255	2200	10	4.6	29.7	35.7	37	2.76
4	2.15	50	5600	3300	90.1		45.3			

8.10 Potential application of freestanding needles as a mass balance

The resonance frequency of the Ag_2Ga nanoneedles made to date should be detectably sensed with mass loading as small as 10^{-20} kg. For a needle with a uniform diameter and a total mass of m , the first resonance frequency is [83]

$$f_0 = \frac{1}{2\pi} \sqrt{\frac{k_n}{0.243m}} \quad (8.41)$$

With a load of mass M at the end of the needle, the equation becomes [83]

$$f_M = \frac{1}{2\pi} \sqrt{\frac{k_n}{0.243m + M}} \quad (8.42)$$

The minimum detectable shift in the resonance frequency is considered to be the bandwidth B of the resonance

$$B = \frac{f_0}{Q} = f_0 - f_M \quad (8.43)$$

Using equation (8.42) to eliminate f_M from equation (8.43) gives a minimum detectable mass of

$$M_{\min} = \frac{0.243m \left[\frac{2}{Q} - \frac{1}{Q^2} \right]}{\left[1 - \frac{2}{Q} + \frac{1}{Q^2} \right]} \quad (8.44)$$

For $Q \gg 1$ the term $1/Q^2$ can be neglected and the minimum detectable mass will be

$$M_{\min} \approx 0.243m \left(\frac{2}{Q-2} \right) \quad (8.45)$$

This equation shows that decreasing the mass of the needle, and increasing the Q increases sensitivity.

To date the highest Q measured for the Ag_2Ga needles is 3300 for Sample 4 from Table 8.5. For a density of 8960 kg/m^3 [84] the needle would have a mass of $1.51 \times 10^{-16} \text{ kg}$. For Sample 4, equation (8.43) give a mass sensitivity of $2.2 \times 10^{-20} \text{ kg}$. In a similar work Nishio *et. al.* [77] reported 10^{-22} kg sensitivity, using multiwall carbon nanotubes. However, they claimed a 10 Hz resolution in measuring the resonance frequency shift for a nanotube that had $B = 688 \text{ kHz}$ and $Q = 1500$. In the formula presented here, their value of $f_0 - f_M = 688000/1500$ which would lead to a value of M_{\min} that is 688/15 larger than they reported, or $M_{\min} = 0.5 \times 10^{-20}$. The needle sensitivity depends on its use on a vacuum. At standard pressure air damping can dramatically lower the Q , thereby reducing sensitivity [85].

8.11 Plastic deformation

This section reports on initial observations of plastic deformation of the needles.

8.11.1 Plastic deformation during bending

Simple bending of a needle can be used to determine ultimate tensile strength of a needle. A needle with diameter d and Young's modulus E is bent into a loop of radius r .

The strain ε at the surface of the needle is [86]

$$\varepsilon = \frac{d}{2r} \quad (8.46)$$

The maximum stress σ at the surface of the needle is

$$\sigma = E\varepsilon = \frac{Ed}{2r} \quad (8.47)$$

Decreasing the radius of the loop to a critical radius r_c produces kinking or fracture at the elastic limit. Using the critical radius in the equation (8.46) and (8.47) gives the ultimate tensile strain ε_c and tensile strength σ_c . While the value for E is strain-dependent, for initial estimates the value of $E = 30$ GPa from the elastic measurements in Section 8.4 will be used in equation (8.47).

Ultimate tensile strain and strength were estimated from images of needles being bent inside the SEM by the nanomanipulator. In Figure 8.16, a 29 μm long needle with 130 nm diameter is pushed against a solid Ga droplet (Figure 8.16a) and then released (Figure. 8.16b) to a nearly unbent position. This elastic property was observed several times without plastic deformation of the needle. Figure 8.16c shows a bending radius of ~ 3 μm was achieved without fracture of the needle. However, plastic deformation did occur when the bending radius was decreased slightly below this value. Considering 3

μm as the critical radius, the value of ε_c is 0.022 and the ultimate tensile strength σ_c is 0.66 GPa. Tensile stress for commercial metal and alloys are reported to be as small as 0.042 GPa (for solder) and as high as 1.855 GPa (for zirconium) [87].

The plastic deformation resulted in kinking and breaking off of a $4.4 \mu\text{m}$ length of the needle. The broken section is shown in Figure 8.16d, which was separated from a $33 \mu\text{m}$ long needle. Three broken pieces were found after the experiment with lengths of 800 nm, 1600 nm, and 2000 nm. In future SEM observations it may be possible to measure the curvature where elastic failure of the material just becomes apparent

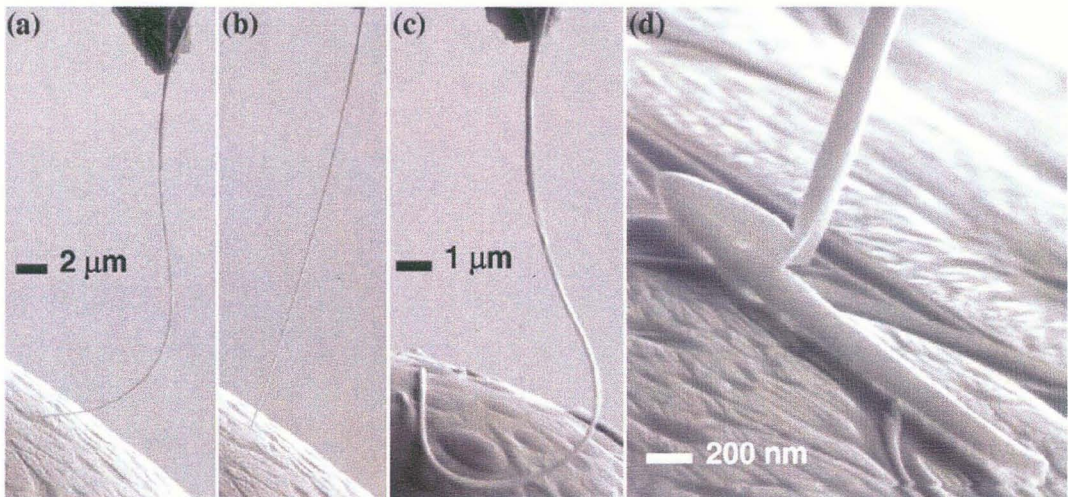


Figure 8.16. SEM images of elastic and plastic deformation of a long needle. (a-c) show the $29 \mu\text{m}$ needle being flexed in the elastic regime. The original length of the needle was $33 \mu\text{m}$ prior to elastic failure which results in the breaking off of $4.4 \mu\text{m}$ of the needle shown in (d). Also note in (c) that the needle is buckled and twisted out of a single plane. This mode of buckling is referred to as torsional buckling.

8.11.2 Plastic deformation during collision

It was observed that a needle would sharpen while it was electrostatically deflected, as in Figure 8.2a, and allowed to lightly tap the counter electrode. The experimental setup is similar to that in Section 8.4.2. The needle used is 10.13 μm length and 323 nm average diameter. Considering the density of the needle to be 8960 kg/m^3 [84], the mass of the needle is 9.44×10^{-15} kg. The needle is brought close to a tungsten electrode. An AC voltage is applied between the electrode and the needle. The frequency of the AC voltage is then swept to find the resonance frequency of the needle. This frequency is measured to be about 772 kHz and the deflection amplitude is ~ 1 μm . While the needle is resonating, the electrode is brought closer to the electrode. The needle is allowed to strike the electrode for a few seconds. During these few seconds the needle strikes the surface of the electrode a few million times. This procedure results in the flattening of the side of the needle, as well as sharpening the tip of the needle. Figure 8.17 shows the SEM images of a needle (a) before and (b) after striking the tungsten tip. The flattened area of the needle is 2.25×10^{-14} m^2 . The ability to sharpen a needle is of practical usefulness. However, it is of great interest to understand and model the cause of the flattening. There are several physical effects that might contribute individually or together to reshape the tip. Distinguishing these effects appears to require additional experiments. Therefore in the remaining of this section, these possible effects will be discussed.

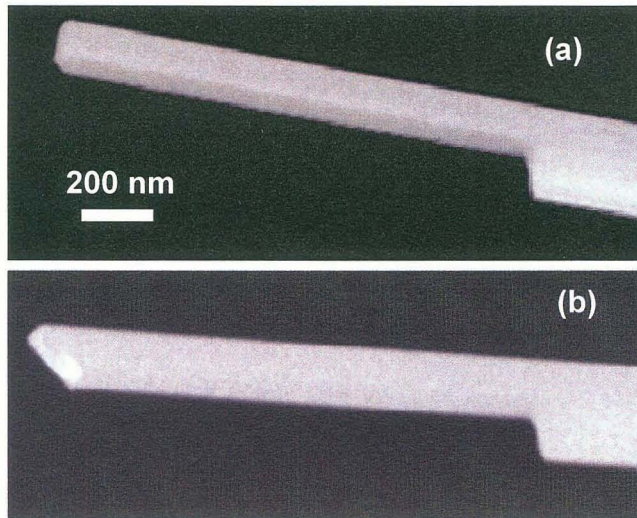


Figure 8.17. Sharpening of a needle by electrostatic deflection. (a) Before and (b) after sharpening of the tip. Figure 8.2a shows the needle in vibration as it was sharpened.

The tip could be changed by momentum transfer from the needle to the electrode leading to plastic deformation. For a yield strength of 0.66 GPa (from Sec. 8.10.1) a force of 1.5×10^{-5} N would lead to the measured flattened area of 2.25×10^{-14} m². This amount of force might be produced by the momentum of the normally oscillating needle as it strikes the surface. However, at the limits of its excursion, the needle velocity is nearly zero. More likely is that the electrostatic force produced by the electrode produces an elastic instability in the needle, causing it to snap down towards the electrode. The velocity of the needle during an unstable event is difficult to predict, which makes it difficult to determine the momentum transfer on impact. Furthermore, when the needle comes close enough for dielectric breakdown, field emission or tunneling, the electric field begins to short out, reducing the electrostatic force, and releasing the needle (assuming that the needle restraining force exceeds vdW and other adhesion forces.)

Striking the surface can lead to heating of the needle through dissipation in Young's modulus (the imaginary component of E) and ohmic heating. In fact, ohmic heating can arise prior to contact, due to both field emission and cyclic charge accumulation and decay at the tip as the electric field oscillates. Heating can soften, melt or possibly even vaporize the needle. Localized melting seems most likely on the first impact, when there can be an enormous current density through the initially sharp tip.

Rather than develop a speculative model at this point, various experiments can be imagined that would help separate these possible effects. Transient electrical measurements could be measured of a needle striking an electrode. The electrode could be coated with a thin insulator to eliminate current from the source. The needle could be mechanically deformed with a known force in the nanomanipulator or AFM, followed by observation in the SEM. Including temperature controlled stages could also be used to both reduce and enhance the effects of heating. These planned experiments should provide sufficient information to be able to explain the reshaping of the tips during electrostatically driven collision of a needle with an electrode.

This chapter has evaluated several mechanical properties of Ag_2Ga needles. Electrostatic deflection of the needles as well as direct deformation of the needles by F-D measurements were used to measure the Young's modulus E of Ag_2Ga . E , obtained from both methods, is calculated to be ~ 30 GPa. F-D curves lead to additional information such as the Hamaker constant and the friction coefficient of the needles with Si.

CHAPTER 9

AFM PROFILING AND NANOLITHOGRAPHY WITH NEEDLE-TIPPED CANTILEVERS

Since Ag_2Ga nanoneedles can be directly grown on (or even in place of) the tips on AFM cantilevers using the pulling technique (in Chapter 5), it would be potentially useful to demonstrate if these needles can be used in AFM profiling and lithography. Current needles are somewhat larger in tip radius than typical silicon AFM tips (10 to 20 nm radius), but these and other tips, usually become blunt on first contact with the surface. High aspect ratio tips (e.g. the nanoneedles tips) would likely maintain their radius as the needle wears down. For AFM nanolithography [88], thin films that are coated on tips to make them conductive often wear off due to mechanical abrasion and electrochemical reactions [89] when high currents are passed through them. Compared to a thin film coating, a solid metal needle tip should last indefinitely. In this chapter AFM profiling and lithography with Ag_2Ga tips made by the selective needle growth method in Chapter 5 is evaluated and demonstrated. The specific tips used in this chapter are listed in Table 9.1.

Table 9.1. List of the needle-tipped cantilevers used for AFM topography and lithography

Tip #	Cantilever model	Cantilever resonance frequency (kHz)	Spring constant (N/m)	Needle diameter (nm)	Needle length (μm)
#1	Veeco ULNM-D	354.7	50	120	5
#2	Veeco ULCM-NTNM-B	78	1.1	200	4
#3	Veeco ULCM-NTNM-B	78.1	1.1	120	2
#4	Veeco ULCM-NTNM-D	155	5	60	2
#5	Veeco ULNM-B	78	3.2	N/A	N/A
#6	Budget Sensor BA-Tab300	315	45	90	5

9.1 Non-contact AFM topography with needle-tipped cantilevers

9.1.1 Experimental details

The needle-tipped cantilevers are made by self-assembling Ag_2Ga on tipped and tipless cantilevers. The thinner and shorter needles (less than 200 nm in diameter and 1 to 5 μm in length) are chosen for AFM non-contact mode height profiling. Tip #1 is used for non-contact AFM of a 50 nm sputter coated Au thin film. The Au thin film is prepared using a Technics 4604 sputterer system (DC target, 350 W, 20 mtorr). A CP Park Scientific Instrument AFM (5 μm scanner) is used to profile the film. The sample is scanned at 0.5 $\mu\text{m}/\text{sec}$. A field emission scanning electron microscope (FE-SEM), with 2 nm resolution, is also used to image a similar area of the same Au thin film. The

resolution of the AFM image is compared with the FE-SEM image by a correlation method described below.

9.1.2 AFM topography results

To test the resolution of Tip 1, a $1 \times 1 \mu\text{m}^2$ AFM topography image in tapping-mode is taken from the Au film (Figure 9.1a) and compared with an FE-SEM image of a similar area of the same sample (Figure 9.1b). The FE-SEM has a resolution of 2 nm, which makes SEM images a good resolution standard to compare with the AFM images.

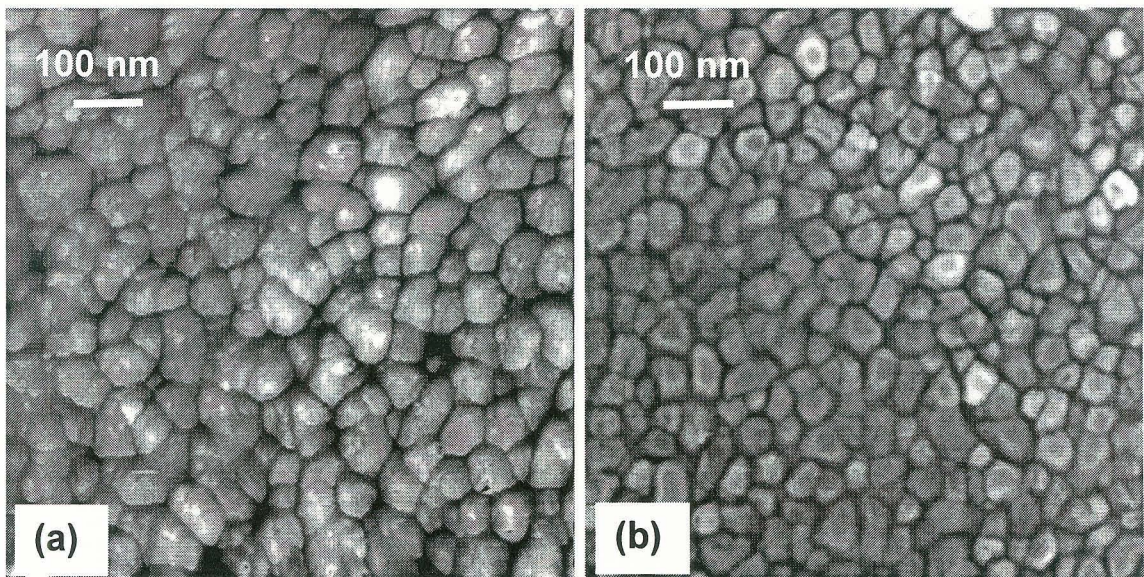


Figure 9.1. Images for evaluating the resolution of the needle-tipped cantilever (tip #1) (Images taken by S. Harfenist) (a) AFM topography image of a thin sputtered Au film using a needle-tipped cantilever with 120 nm in diameter and 4 μm in length. The vertical roughness of the grains is ~ 1 nm (b) SEM image of a similar area of the same film [90].

Autocorrelation functions of the AFM height profile and the grayscale SEM image are calculated to estimate the grain size of the sample. From this information the loss of resolution due to the diameter of the needle is calculated. The grain size is quoted as $\sqrt{2} \times \text{FWHM}$ (full width at half maximum of the autocorrelation peak). The average diameter of the grain in the AFM image is ~ 28 nm and the average diameter in the SEM image is 21 nm. Gaussian functions with different FWHM were convolved with the autocorrelation function of the SEM image until the resulting function closely fits the AFM autocorrelation function. A Gaussian function with $\sqrt{2} \times \text{FWHM}$ corresponding to a 14 nm is the closest fit to the AFM image, so the loss of the resolution due to the tip diameter is considered to be 14 nm. This resolution ultimately depends on the slope or vertical roughness of the sample; i.e., higher sloped samples would report greater loss in resolution.

9.2 Durability of needle-tipped cantilevers in contact and non-contact modes

It is important that the needles are securely attached and last for reasonable time during AFM profiling [91]. Extended-duration scans are performed on the Ag_2Ga tipped cantilevers in both contact and non-contact mode to determine their durability.

9.2.1 Experimental details

Tip #2 is used for the durability testing, first in non-contact and then in contact mode. An Asylum Research MFP-3D AFM is used for taking AFM topography images in both non-contact and contact mode. For the non-contact mode, a Au thin film (40 nm) that is reactively spread with Ga is used as a sample for AFM imaging. A $2 \times 2 \mu\text{m}^2$ region is

continuously scanned for 14 hours at a 1 $\mu\text{m}/\text{sec}$ scan rate. For the contact mode, the images are taken from a $20 \times 20 \mu\text{m}^2$ region of a standard calibration sample (a silicon substrate with $5 \times 5 \mu\text{m}^2$ and 200 nm depth square features shown in Figure 9.3). The scanning is continuously performed for 14 hours at 6.6 $\mu\text{m}/\text{sec}$ tip velocity.

9.2.2 Results of durability testing of needle-tipped cantilevers

Figure 9.2 shows the resulting non-contact scans and Figure 9.3 shows the resulting contact scans at 2 hours, 7 hours and 14 hours. The differences between the image after scanning 2 hours and after 14 hours in both figures are minimal. Also, SEM study of the end of the tips before and after AFM have shown minor changes even after about 336 mm of total tip translation in contact mode.

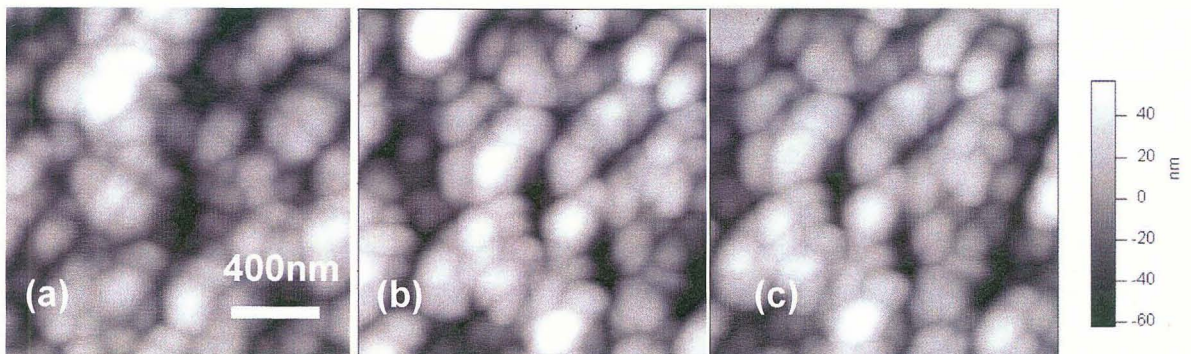


Figure 9.2. Time-lapse non-contact mode AFM topography with a needle-tipped cantilever. The images are taken at (a) 2, (b) 7, and (c) 14 hours of continuous scanning. The images show almost no change even after about 25 mm of total tip translation.

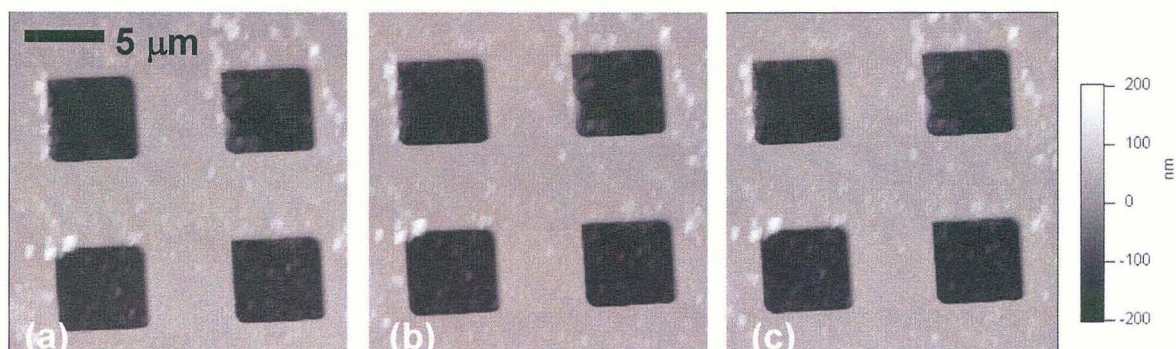


Figure 9.3. Time-lapse contact mode AFM topography images with the same needle-tipped cantilever as used for Figure 9.2. The images are taken at (a) 2, (b) 7, and (c) 14 hours of continuous scanning. The images show almost no change even after about 336 mm of total tip translation.

9.3 Nanolithography with needle-tipped cantilevers on polymer substrates

Needle-tipped cantilevers are used for voltage lithography through a polymer e-beam resist surface and compared with regular AFM tips. Applied voltage that drives current through the polymer breaks the polymer chains into fragments that are dissolved preferentially by a developer such as methyl isobutyl ketone (MIBK) [92].

9.3.1 Experimental details

A silicon wafer (500 μm thick, 1 to 10 Ωcm resistivity) is sputter-coated with 5 nm of Cr and 20 nm of Au. The metal layer is used to ensure that the substrate is highly conductive. Then PMMA, (4% wt. polymethyl methacrylate in chlorobenzene solvent, MicroChem Corp., Newton, MA) which is an electron-beam resist, is spin coated to a thickness of 123 nm onto the substrate. Finally, the sample is prebaked for 5 minutes in a convection oven at 150 $^{\circ}$ C.

The needle-tipped cantilevers are mounted in a Park M5 AFM and evaluated for voltage nanolithography of the PMMA sample. Tips #3 and #4 from Table 9.1 are used for the results reported in this section. The tips are used in tapping mode with 300 nm/s scan speed at a 12 nm distance from the polymer surface. For comparison, a regular AFM tip (tip #5), is also evaluated for nanolithography. This tip is sputter coated with a 10 nm Cr layer and 20 nm Au layer.

A Keithley 6430 Sub-Femtoamp Remote SourceMeter is used to set the current passing through the nanoneedle between 150 and 200 pA. The voltage reported by Keithley varies between 1 and 8 V during the lithography experiment. The exposed pattern is then developed in a 2:1 MIBK:isopropanol solution for 90 seconds. The patterns are then imaged with AFM using Budget Sensors BA-Tap300 probes (51 N/m spring constant, 319 kHz resonance frequency).

9.3.2 Results of lithography on PMMA

AFM topography images of the developed polymers are shown in Figure 9.4. Tip #3 has been used to write the pattern shown in Figure 9.4a. The trenches are as deep as 35 nm and the width is as narrow as 80 nm. Tip #4 has been used to generate the parallel lines shown in Figure 9.4b. The pattern includes 25 lines, each line 10 μm in length. The pitch is 400 nm. As seen in the Figure 9.4b, the width of the trenches is very uniform and are about 60 nm wide and 34 nm deep. The needle-tipped cantilevers have written for over 1 hour with no change in resolution. The initial writing voltage (at 150 pA constant current) was 1 V and the voltage was essentially constant over a 10 minutes time period.

The applied voltage varied from 1 to about 4 volts after 650 μm of writing. Tip 5 (the metal coated AFM tip) was used to generate the lines shown in Figure 9.4c. The average of the width of the trenches is about 150 nm and they are about 20 nm deep. With the metallized silicon tip cantilever the initial voltage (at 150 pA constant current) was 1 V and the voltage rose to 8 V within 10 minutes after only 200 μm of writing.

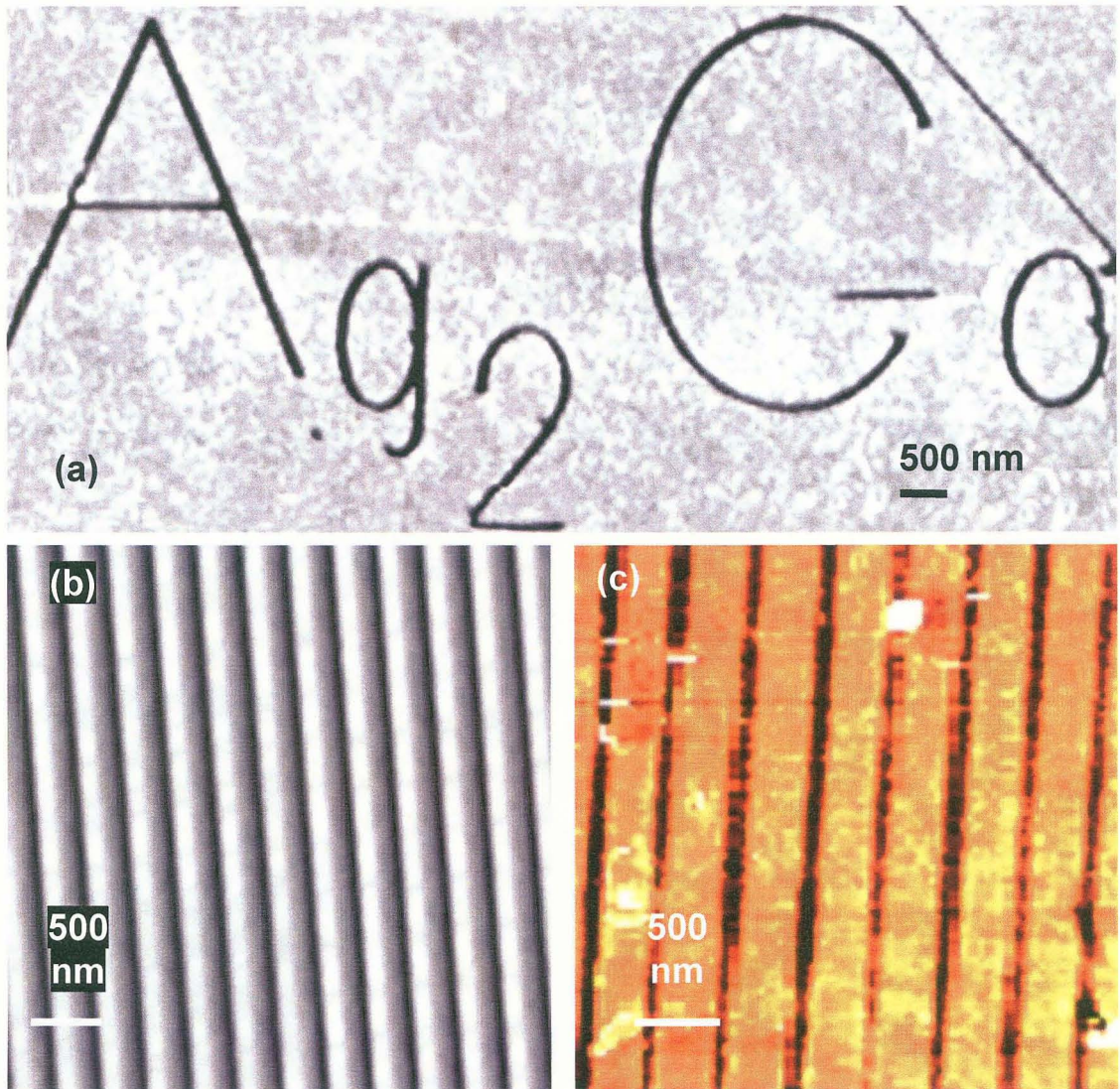


Figure 9.4. Voltage nanolithography results of PMMA with needle-tipped and conventional AFM tips (a) AFM image of pattern written with a needle-tipped cantilever. AFM image of pattern written with (b) a needle-tipped cantilever and (c) a conventional metal-coated AFM tip (The lithography and AFM imaging performed by A. Safir) [90].

Comparing Figure 9.4b written with needle and Figure 9.4c written with metal coated AFM tip shows that the lines are more uniform in width for the needles.

9.4 Voltage nanolithography results on silicon substrates

The needle-tipped AFM probes were also evaluated for voltage nanolithography on silicon surfaces. In this case, voltage is used to locally oxidize the silicon surface [89].

9.4.1 Experimental details

(110) oriented Silicon with 1 to 10 Ωcm resistivity and 300 μm thickness is etched in a 100:1 Water:1N HF solution for 2 minutes to remove the native oxide from the silicon surface. The sample is used immediately after the HF etch step. Ag_2Ga nanoneedles were grown on several AFM tips and tipless cantilevers, and evaluated in a Veeco Dimension 3100 (Nanoman II) SPM for voltage nanolithography. Tip #6 in Table 9.1 is used here. The diameter of the needle is about 90 nm with a curve at the end of the tip that reduces the tip radius to 40nm. The tip is then used in tapping mode and scanned in the [-1,1,-2] crystalline direction of the substrate at a tip velocity of 1 $\mu\text{m}/\text{sec}$, a set point of 1V, and a 0 nm distance from the silicon surface. An internal voltage source applies voltage between the tip and the silicon surface. In six different experiments the internal voltage applied to the substrate are 1, 2, 4, 6, 7 and 8 volts. The sample is then anisotropically etched for 20 seconds at 80 $^\circ\text{C}$ in 83:17 tetramethylammonium hydroxide (TMAH):isopropanol.

9.4.2 Results

SEM images (Figure 8.5 and 8.6) show the results of voltage nanolithography with Tip # 6 after etching. Six sets of parallel lines were written, but as indicated by the arrows in Figure 9.5, only three complete sets and a part of the fourth developed. The applied voltage for each set is shown in Figure 9.5. For voltages of 4 volts and less the oxide layers were too thin and could not withstand the etching process. But for voltages of 6, 7 and 8 volts the oxide layers are thick enough to survive the etching process. The average line width is about 30 nm (Figure 9.6), and the average height of the structures is about 70 nm.

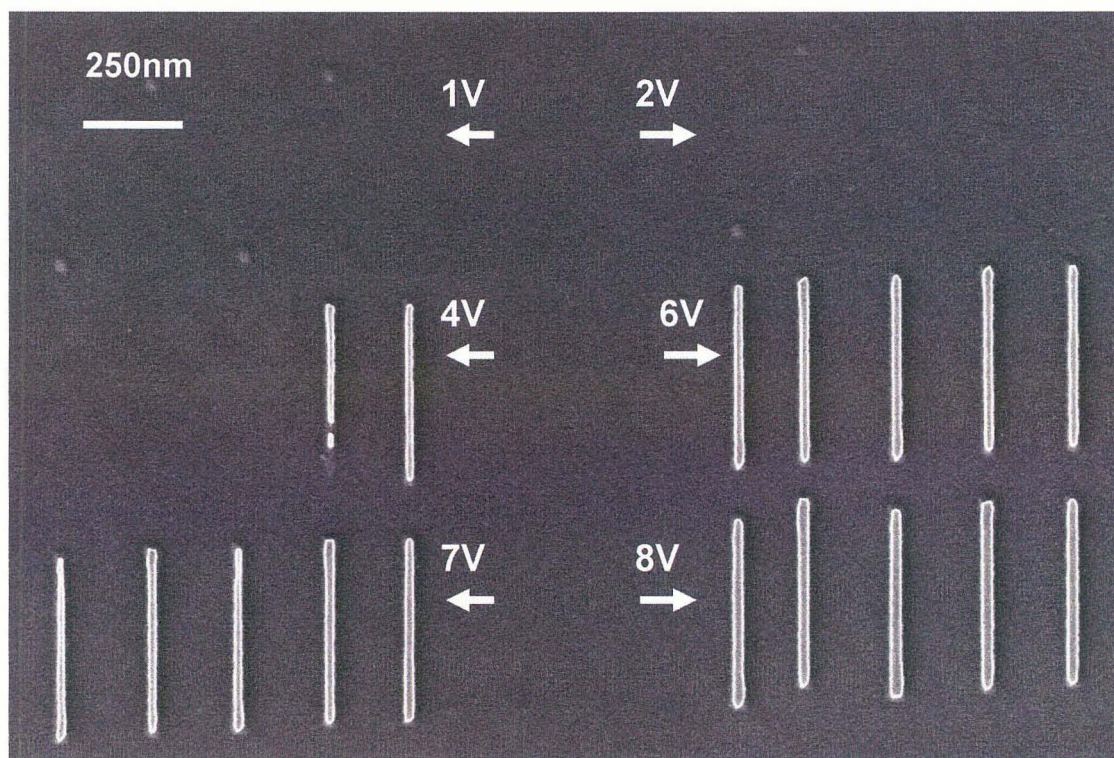


Figure 9.5. Voltage lithography results on silicon using Ag_2Ga nanoneedles. Regions where each voltage was applied are marked on the SEM image. In only three areas (6, 7, 8 V) did the patterns survive the etching process [93].

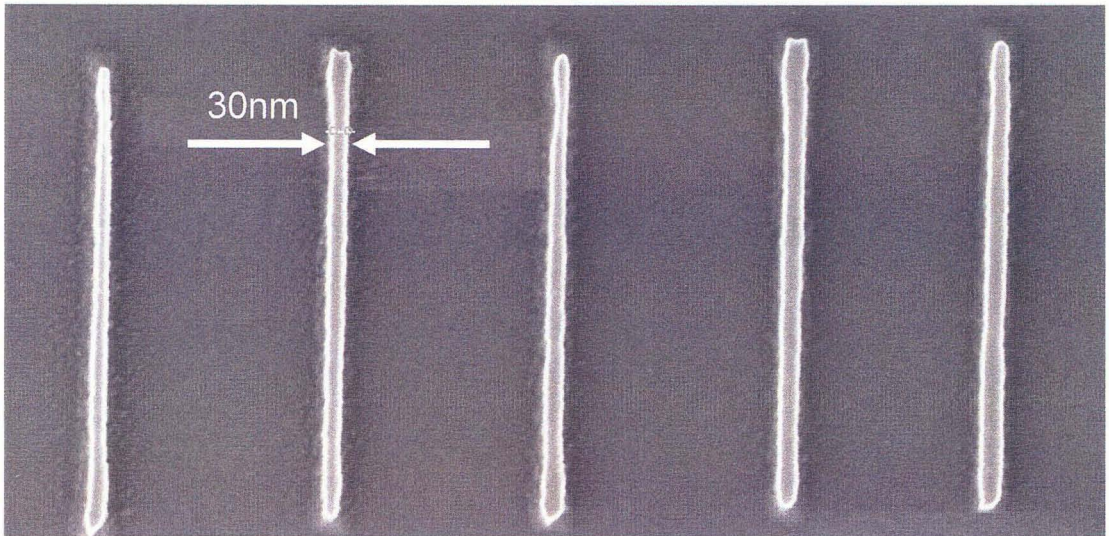


Figure 9.6. Close-up view of voltage lithography results from the 7 V region of Figure 9.5. Lines as thin as 30 nm have been written with nanoneedles (Voltage lithography performed by A. Safir).

Figure 9.7 shows SEM images of the needle probe before and after voltage lithography. Some reshaping of the end of the tip has occurred, but there is no major change to the needle even after 20 minutes of applying voltage. This shows that the needles are robust even with a high current density of $\sim 110 \text{ A/m}^2$ flowing through the needle.

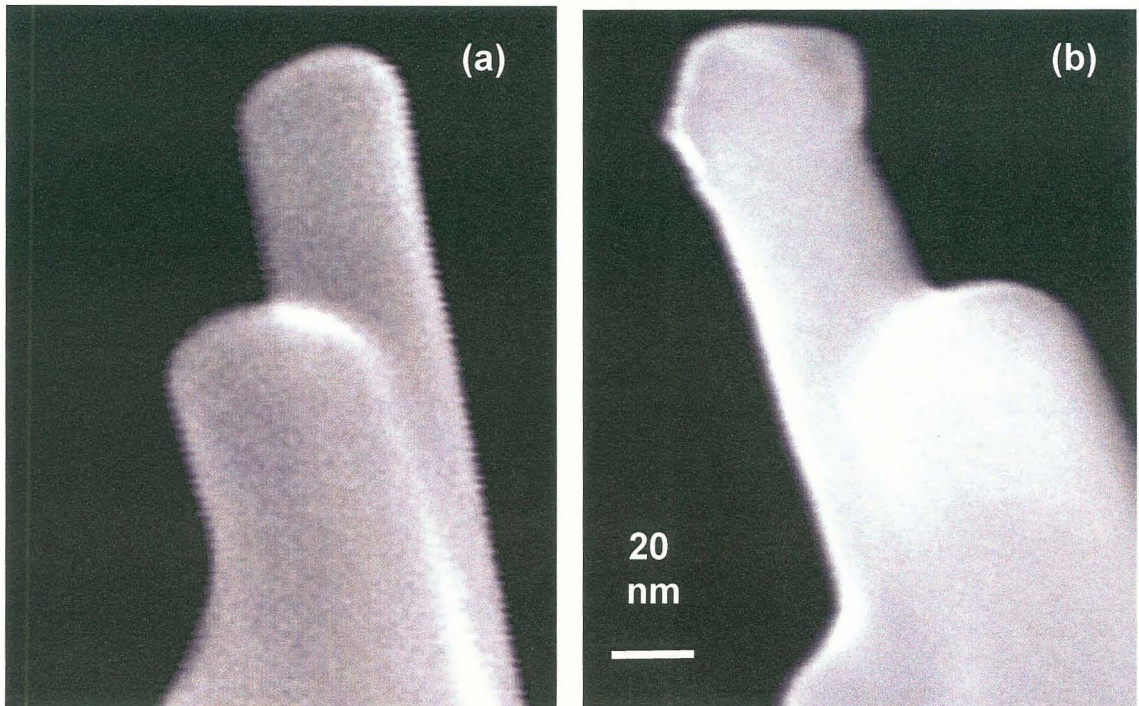


Figure 9.7. SEM images of the end of a Ag_2Ga needle-tipped AFM probe (a) before and (b) after 20 minutes of voltage nanolithography with continuous application of 150 pA of current.

9.5 Advantage of using needle-tipped cantilevers for AFM lithography

One of the most promising results of using the needle-tipped cantilevers is improved voltage stability compared to metal thin-film-coated AFM tips. The problem with the metal coated AFM tips is that the metal becomes separated from the end of the tip during writing, resulting in an insulating path between tip and the substrate. In contrast, breaking off a part of the needle does not change the diameter of the tip (since the needles are constant in diameter over a long length), nor does it change the resistance appreciably.

In this chapter initial investigations show that the needles can be used for AFM topography profiling in both contact and non-contact mode. In non-contact mode a 14 nm

resolution has been achieved. In contact mode, a wear test was done for 14 hours, and change in the AFM resolution was slight even after traveling about 336 mm. The needles were used for voltage nanolithography on both PMMA and silicon, and uniform width lines as narrow as 30 nm have been patterned using these tips.

CHAPTER 10
GALLIUM SPREADING USED TO STUDY CONTACT RESISTANCE OF
CARBON NANOTUBES

10.1 Introduction

Ga reactively spreads through metal thin films at moderate rates near room temperature. This spreading provides a way to study the electric contact to nanostructures in real-time. This is demonstrated by studying the change in contact resistance as the spreading front contacts carbon nanotubes that bridge across two Au thin film electrodes. The experimental method is similar in principle to that of Frank *et. al.* [94], who dipped multiwall carbon nanotubes (MWNT) into liquid Ga and Hg while measuring the nanotube conductance. The main result of their investigation was to verify that the nanotubes are single channel conductors with conductance value of $2e^2/h$ (corresponding to a resistance of 12.85 k Ω) for which the resistance is only due to the contacts, and is independent of the length of the conductor [95]. Thus Frank observed that conductance increases in a step-like manner when the nanotube contacts the liquid metal, and stays constant with increasing immersion into the liquid and reduction in the conductor length.

In this study, the experiment is performed on a planar substrate, and the Ga spreading is used to replace the tedious operation of selectively attaching a nanotube to a metal tip and then dipping the tip into a liquid using a nanomanipulator. In addition to illustrating

the fundamental properties of nanotubes, the experimental arrangement would be useful for making better and more stable contacts to nanotube and nanostructures. This is a recognized problem [96] and, in practice, the conductance of nanotubes is frequently found to be less than $2e^2/h$. A way to consistently choose solid state contact material to eliminate this problem is not currently known. Thus, varying the contact materials in real-time might help to provide the understanding needed to resolve this problem.

10.2 Experimental Details

The experimental apparatus for studying the contact resistance of nanotubes is shown in Figure 10.1. The Ga reactive spreading front [97] (as described in Chapter 3) spreads to and passes the ends of carbon nanotubes (CNT's) that are resting on Au electrodes. At the same time the conductance of the CNT is continuously measured.

The experimental apparatus is fabricated by sputter coating 20 nm Cr and 70 nm Au on the surface of a 400 nm thick silicon oxide layer. The film is then patterned using photolithography. Pairs of leads are patterned with a 1 μm separation. Each lead is 50 μm long and 10 μm wide and are interconnected to a pad of 100 μm by 200 μm . A DMF (dimethyl formamide) solution containing multiwall nanotubes is dispersed on the substrate resulting in a few nanotubes randomly bridging the gap between the Au leads. The nanotubes were produced by the arc-discharge method [98] and are 20 to 30 nm in diameter and 3 to 6 μm in length. The chip is inspected using a scanning electron microscope (SEM) and the positions of nanotubes that span the gap are identified. Gaps with only one or two nanotubes are selected for investigation.

A Ga drop ($\sim 50 \mu\text{m}$ diameter) is deposited on each of the larger pads using a micromanipulator under a video microscope (part of a Wyko interferometer). The sample is then placed in a probe-station chamber under the vacuum ($\sim 10^{-3}$ mtorr) at $320 \text{ }^\circ\text{K}$. Tungsten tips on the microprobe arms provide electrical connections between the device and the conductivity test measurement instruments.

The reaction front spreads along the Au leads at a rate of $\sim 7.5 \mu\text{m/h}$. Figure 10.1 shows a schematic drawing of the apparatus together with SEM images of the device before and after Ga spreading. Note that the front passes by the CNT without displacing the position of CNT.

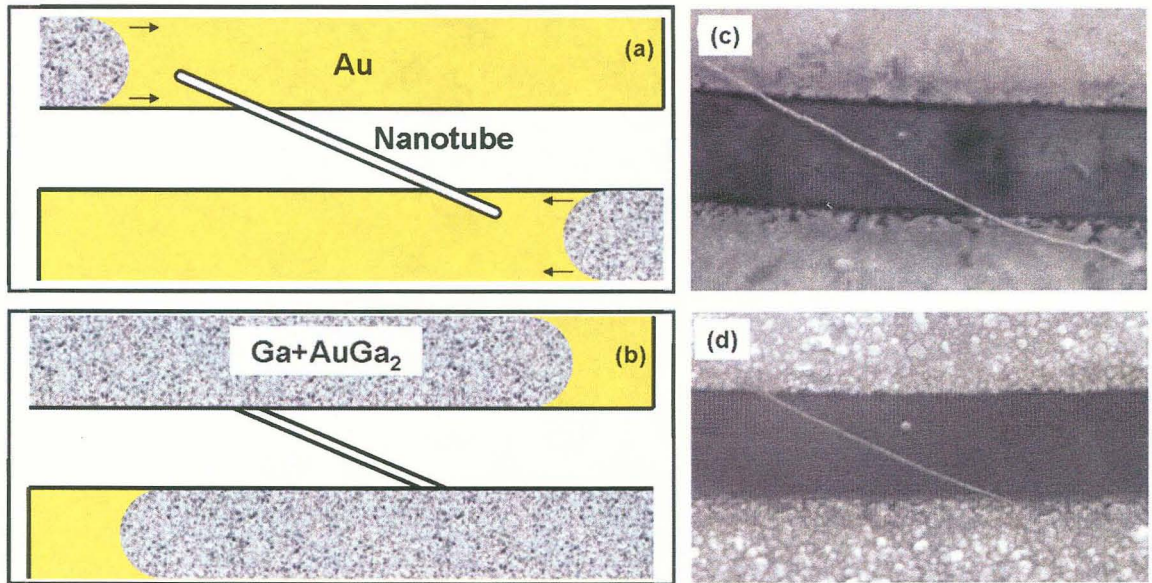


Figure 10.1 Apparatus for observing contact resistance changes in a CNT. Schematic drawing of the apparatus (a) as the spreading front approaches and (b) passes the end of the nanotube. SEM image of the CNT (c) before and (d) after the passage of the front. The distance between two leads is $\sim 1 \mu\text{m}$.

The *Zero bias differential conductance* is the differential change in current ΔI for a differential change in voltage ΔV with no applied DC bias. This measure of conductance

is measured for several of the experimental devices. The device is connected through microprobe arms to a lock-in amplifier which enables low noise measurements of a narrowband AC signal. A sinusoidal reference (1 mV, 13 Hz) is applied to the device and the current is monitored by the lock-in amplifier that is connected to a 7561 Yokogawa multimeter. Multimeter measurements are taken at 1 second intervals for up to 48 hours and recorded to a computer using a general purposes interface board (GPIB) card.

10.3 Results and discussion

The typical zero bias conductance behavior of a single MWNT is shown in Figure 10.2a. Before the spreading front reaches the nanotube, the conductance of the device is about $0.3e^2/h$ (86 k Ω). As the spreading front comes in contact with one end of the nanotube, there is a stepwise change in conductance to $0.9 e^2/h$. When the spreading front contacts the other end of the nanotube, there is a second step in the conductance that raises the conductance to $1.2 e^2/h$.

Figure 10.2b shows the result of this experiment for a device on which two nanotubes were placed across the Au leads. In this case there are 4 distinct steps in conductance. Each step occurs as the spreading front contacts a nanotube.

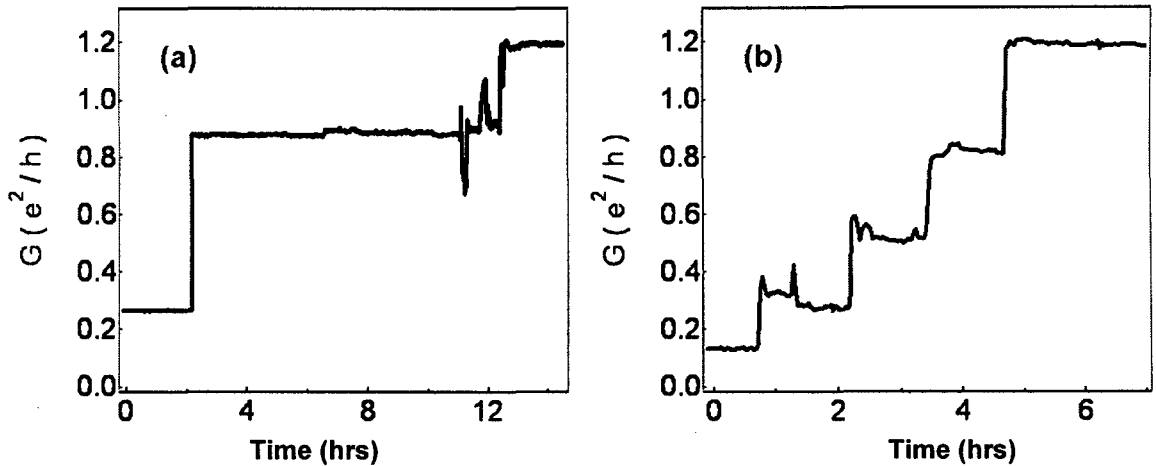


Figure 10.2. Zero bias differential conductance of MWNTs at 320 °K as the front spreads along the Au electrodes. A step in conductance is observed each time the spreading front contacts a nanotube. Conductance when (a) a single MWNT and (b) two MWNTs bridge span the gap between the electrodes [99].

The conductance steps are consistent with the concept of ballistic transport in that the resistance does not decrease as more of the nanotube length is covered. However, the steps are inconsistent with the CNT being an ideal single channel conductor since the conductance of $2e^2/h$ is not realized with this contact material.

Temperature and bias dependence of a device with one MWNT was also studied. These studies show that the increase in device conductance is caused by change in the contact resistance, rather than changes in the electrical transport properties of nanotube.

For the bias dependence studies, the device was cooled to 77 K under the vacuum inside the probe station. The conductance of the device was measured as a function of applied DC bias, using a 7651 Yokogawa DC programmable power supply source, first before and then, after gallium spreading. These results are plotted in Figure 10.3a. The conductance of the Ga-contacted nanotube is five times greater than the Au-contacted

nanotube. In both cases the minimum conductance is found at ~ 0 V (0.005 V for the Au-contacted nanotube and 0.01 V for the Ga-contacted nanotube). Also the conductance in both cases increases 4 % to 5 % of their minimum value as the bias increases to 100 mV. In case of the Au-contacted nanotube, the conductance increases from $0.185 e^2/h$ at zero bias to $0.193 e^2/h$ at 100 mV bias. In case of the Ga contacted nanotube, the conductance increases from $0.894 e^2/h$ to $0.934 e^2/h$.

The temperature dependence of device conductance was also measured during the cooling process. Figure 10.3b shows the temperature dependence of conductance before and after Ga contacts the CNT. In both cases the conductance G increases with increasing temperature, and follows a power law equation [96]

$$G = aT^\alpha \quad (10.1)$$

where a and α are constant.

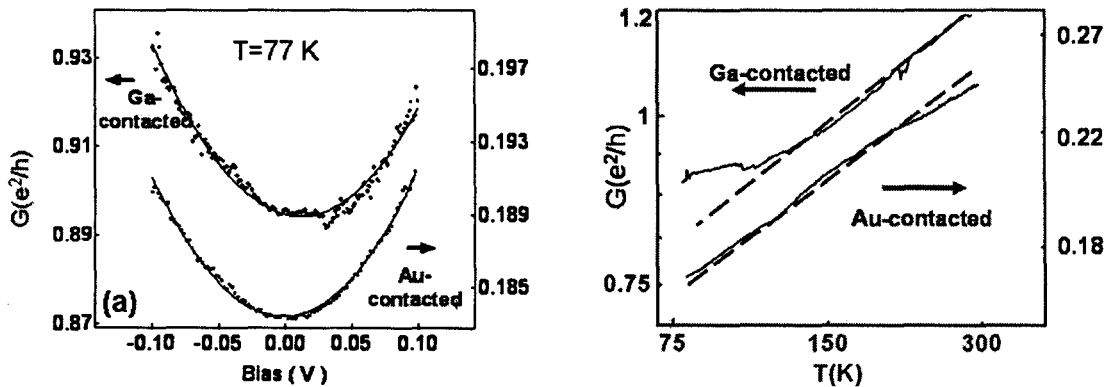


Figure 10.3. Temperature and bias dependence of a single channel nanotube before and after Ga spreading. (a) Differential conductance as a function of bias. (b) Zero bias conductance as a function of temperature. Note the logarithmic scaling of the axes in (b) [99].

The power law dependence of the conductance on temperature has been used as evidence that electrons within MWNTs form a Luttinger liquid [101,102]. Fitting the graphs in Figure 10.3b, the parameter a for the Au contacted nanotube is 0.29 and for the Ga-contacted nanotube a is 0.97. However, the exponent ($\alpha = 0.28$) is identical for both curves. These fits in Figure 10.3b indicate that both Au and Ga contacts are tunneling contacts rather than Schottky contacts [103]. For Schottky contacts the conductance has a $G \propto \exp(-qV/kT)$ temperature dependence, while the temperature dependence of tunneling contacts follows the equation (10.1).

The alloy contact provides additional opportunities to vary the contact condition. One example is the observation of irreversible changes to the contact resistance following the application of high voltage biases. The measurements of low bias voltage are stable and repeatable (Figure 10.3). However, after applying biases of 1 V or greater across the MWNT, the contacts become more conductive [104]. This is shown for a single MWNT in Figure 10.4.

Using a 7651 Yokogawa DC source, the bias voltage is decreased at a rate of 10 mV/sec to -4 V and then swept between -4 V and +4 V at 10 mV/sec. At the same rate the voltage is then decreased to -6 V and swept between -6 V to +6 V. Then the voltage is decreased to -11 V and swept between -11 to +11 V. During each sweep the conductance is measured simultaneously. The sweep for each of these curves is repeated a few times before moving to the next curve, which confirms that the data is repeatable.

For each time that the sweep range is expanded, the conductance increases further until a maximum conductance of $1.9 e^2/h$ was observed (at a bias of -6 V). For a MWNT with a 20 nm diameter, this corresponds to a current density of 2×10^8 A/cm². This

significant current density may cause heating which could locally melt Ga, cause further growth in the size of AuGa₂ grains, and change the wetting of the Ga to the MWNT.

Thus, kinetic changes and phase transformations in alloy contacts may provide a large range of variables with which to explore the fundamentals of contacts. Not only electrical but also magnetic contacts could be varied both by front spreading and by thermally induced transformations of the contacts.

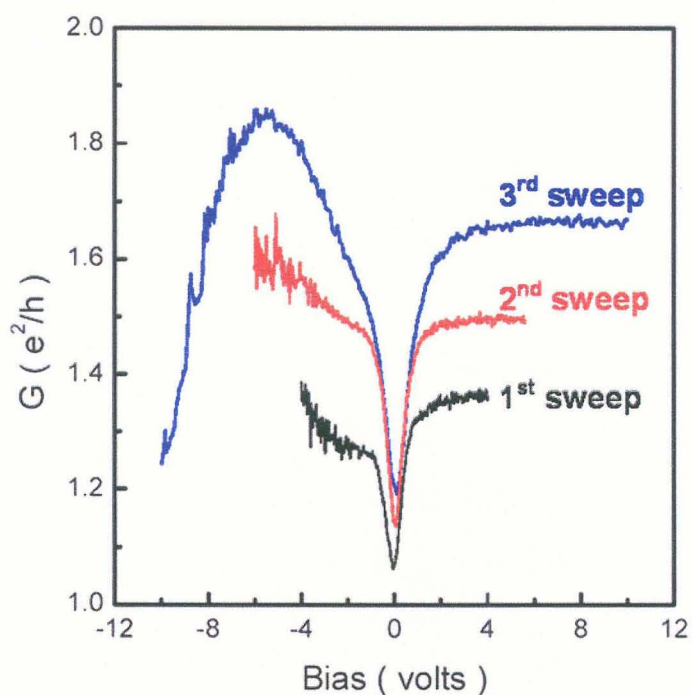


Figure 10.4 Differential conductance of a Ga-contacted MWNT as a function of bias at 175 K [104].

CHAPTER 11

ELECTROCHEMICAL SENSING WITH SUPERPOROUS Pt

Superporous materials can have enhanced catalytic [105] and electrochemical [106,107] properties over nonporous materials due to their increased surface area and through the Gibbs-Thomson effect [15] an increased diffusion rate of reactants to the small features of the superporous materials, and porosity which enables reactants to be pumped through the material.

As shown in Chapter 7, Ga-M films can be dealloyed to produce porous materials on nearly pure elemental metals. In this chapter films of superporous Pt (as described in Chapter 7) are evaluated and compared against non-porous films for electrochemical detection. This study is an extension to an earlier study of the performance of Pt microelectrodes (Figure 11.1) at detecting H_2O_2 [108,109]. Any improvement in sensitivity that might result from using superporous electrodes can be used to design smaller microelectrodes that would be useful for biomedical implants.

11.1 Sample preparation

A set of ceramic-based multisite microelectrodes (from Quanteon, L.L.C., Denver CO) have been used in this study. In each sample there are four $50 \times 150 \mu m^2$ Pt recording

sites with a film thickness of ~ 100 nm (Figure 11.1). Except for the recording sites, the rest of the ceramic surface is covered with polyimide.

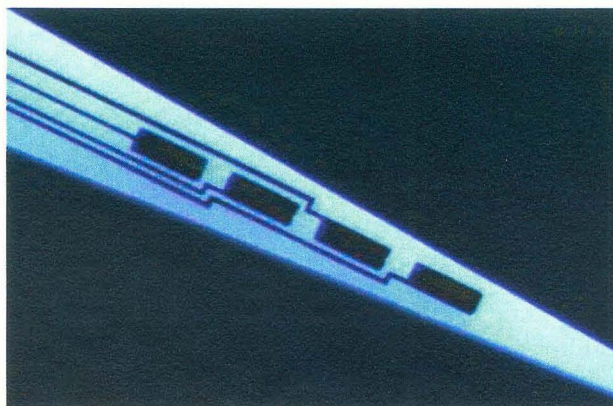


Figure 11.1. A micrograph of a ceramic microelectrode array (Quanteon, L.C.C., Denver CO). The dark regions are the Pt electrodes.

Using a Veeco thermal evaporator, a Ga layer about $2\ \mu\text{m}$ thick was evaporated (at 60 A from a tungsten boat for 2 minutes at 5 mbar) over the entire sample. The resulting sample is shown in Figure 11.2a. This sample was annealed with a hot plate at 280°C for 8 hours and then etched with 1 N HCl at 60°C for 30 minutes followed by 40:1 $\text{H}_2\text{O}:\text{HF}$ at room temperature for 90 minutes producing porous Pt as shown in Figure 11.2(b-d). During the HCl etching, pure Ga is quickly removed (in under 10 minutes) from the polyimide surface. With ~ 30 minutes of etching, the Ga is removed from over the recording sites uncovering the Ga_6Pt crystals. Further etching of the sample in HF removes most of the Ga from Ga_6Pt compounds (see Chapter 7). The close-up view (Figure 10.2c) of the area with darker regions in Figure 10.2b shows that inside the crack there are tightly packed Ga_6Pt crystals. A close-up view of these crystals (Figure 10.2d) shows that there is a dense network of pores permeating the structures. In agreement with Chapter 7, the concentration of Pt is about 83 at. % after dealloying.

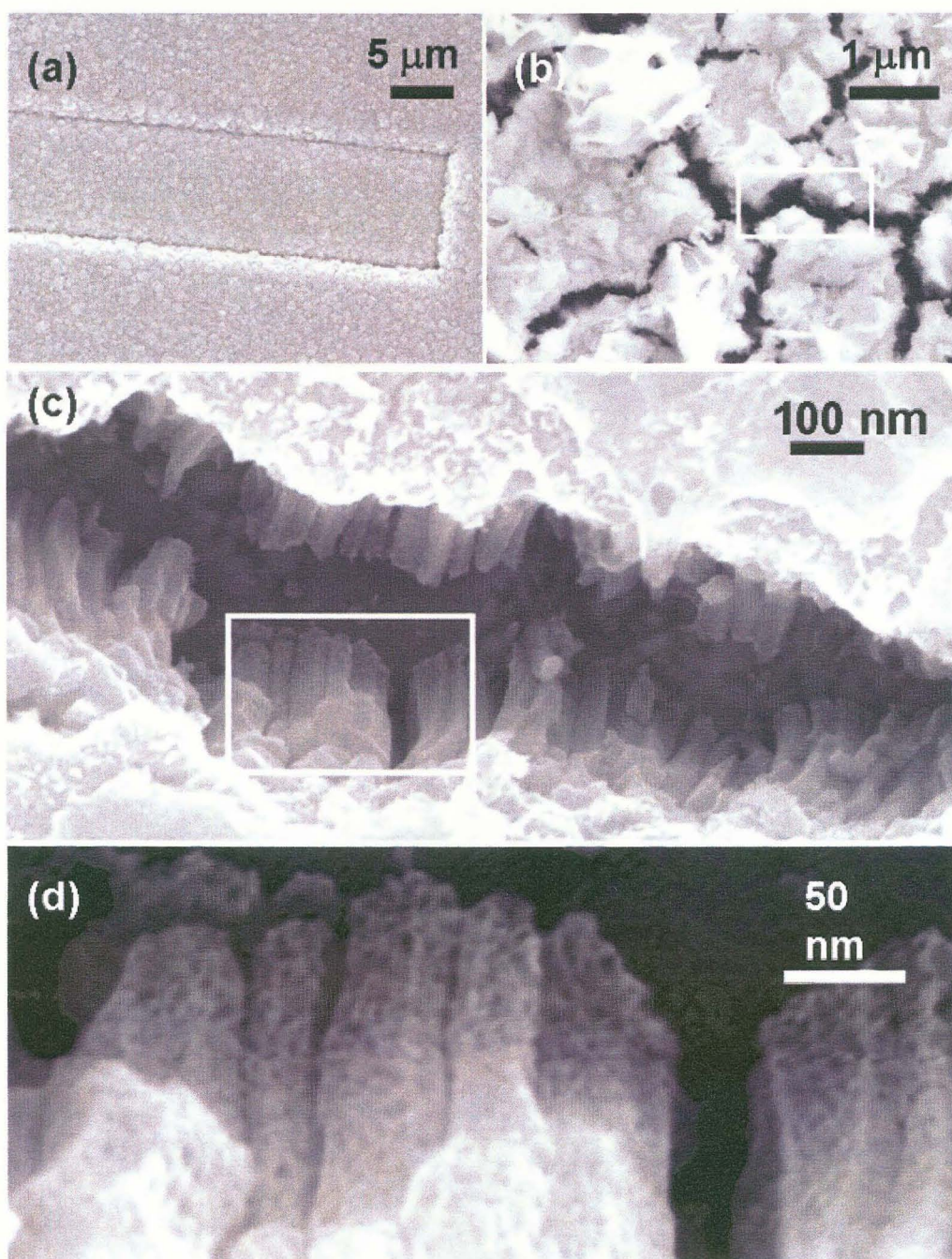


Figure 11.2. Images of the transformation of a Pt microelectrode into a superporous film. (a) A microelectrode after Ga ($2\ \mu\text{m}$ thickness) was evaporated on top of the electrodes. (b) The surface of the microelectrode after etching for 30 minutes in HCl and 90 minutes in HF. (c) Close-up of rectangle in (b) shows very dense arrays of nanometer scale pores. (d) Further close-up of rectangle in (c) that shows a very high density of pores.

11.2 setup for evaluation sensing performance

Porous and non-porous electrodes were evaluated by constant voltage amperometry using a Quanteon L.L.C, FAST-12 high speed electrochemistry instrument. Fast Analytical Sensor Technology (FAST) software, written for simultaneous four channel recording, was used to collect the data. The microelectrodes were placed in a 50 ml beaker containing 40 ml of 0.05 M phosphate buffer solution (PBS), pH 7.4. The beaker was at room temperature and slowly stirred without creating a vortex. A potential of +0.7V with respect to the Ag/AgCl reference electrode was applied to the Pt electrodes. Hydrogen peroxide (40 μ L, 8.8 mM) was added to the buffer to provide a final concentration of 8.8 μ M H₂O₂.

11.3 Sensing performance

Table 11.1 reports limit of detection (LOD), sensitivity, and linearity for each site of the four electrodes before and after the porosity treatment. The LOD is defined as the concentration that corresponds to a signal-to-noise level of 3. Root-mean-squared noise levels are calculated using 10 sample points. The sensitivity of each electrode is described as the slope of the current versus concentration plot in units of pA/ μ m. The goodness of fit to linear response of each electrode is described by the Pearson correlation coefficient (R^2).

Table 11.1. Limit of detection and sensitivity of the microelectrodes before and after being made porous.

	LOD (μM)		Sensitivity ($\text{pA}/\mu\text{M}$)		Sensitivity LOD ($\text{pA}/\mu\text{M}^2$)		Linearity (R^2)	
	Before	After	Before	After	Before	After	Before	After
Ch. 1	0.062	0.141	0.025	0.137	0.571	0.972	0.997	0.982
Ch. 2	0.050	0.154	0.041	0.147	0.822	0.954	0.9986	0.992
Ch. 3	0.080	0.279	0.029	0.158	0.358	0.568	0.9959	0.996
Ch. 4	0.079	0.182	0.036	0.178	0.452	0.982	0.9959	0.996

The sensitivity of the channels 1 to 4 has been increased by factors of 6, 3.5, 5.5 and 5 respectively, although the limit of detection has also been increased due to the increased noise level in the current measurement. The ratio of sensitivity to the limit of detection increases by an average factor of 1.7 (averaged over 1.7, 1.16, 1.58 and 2.17 from channel 1 to 4 respectively) after the treatment.

These modest increases in the ratio of sensitivity to limit of detection for these preliminary experiments are promising. Further experiments are planned on other superporous metals and different chemicals that can be sensed. Also methods of removing oxide and any remaining Ga should be explored as a way to enhance performance.

CHAPTER 12

PATTERNING OF GALLIUM

The results in this chapter represent the first studies performed by the author on Au-Ga systems. The studies were originally undertaken with the goal of patterning Ga so that nanowires could be selectively grown at Ga locations by a CVD process [110,111]. Ga was found to not adhere well to silicon and glass substrates. At first Au appeared to be a good wetting layer; however, the issues of spreading and alloying were immediately noted, and have since been extended into the major focus of this dissertation. In light of these findings, Ga patterning may still serve useful purposes. For instance, patterning Ga on a metal film can be used to pattern regions of crystallites. These crystallites also can serve as seed particles for the growth of crystals of the same, or even different materials. These original AFM and mold delamination studies also provide information on the adhesion of Ga to Au. It is clear from the growth of nanowires in Chapter 5 that the adhesion forces change as the Ga-M reaction proceeds. While this was not recognized at the time of this study on patterning, it is clear that these studies could be extended to time-resolved evaluation and application of Ga-M adhesion. Even without these recently developed recognitions, the experiments presented here show a number of surprising properties of liquid Ga near its melting temperature related to its adhesion, viscous flow, and patterned line width.

12.1 Texturing of gallium

Ga can be transferred from solid phase to liquid phase with a few degrees change in temperature around 30 °C. Taking advantage of this property, hillocks of Ga are pulled from a liquid layer of Ga using the AFM and then the sample is cooled to solidify the hillocks.

A uniform layer of Ga is prepared by placing a droplet of liquid gallium on a silicon wafer that has been heated to ~ 40 °C. Using another silicon wafer, the droplet is compressed and flattened out between the two silicon wafers. Then the sample is immersed in liquid nitrogen to freeze the gallium. The wafers are separated by pulling nearly normal to the surface from a point at the edge, leaving Ga adhered to one of the substrates. The sample is then transferred to a thermoelectric heater with a range of temperature from 25 °C to 35 °C, and both are placed on the stage of an M5 AFM. The Ga is then heated to ~ 35 °C and liquefied. A non-contact mode Ultralever D AFM tip sputter-coated with a 10 nm Cr adhesion layer and a 20 nm gold thin film is brought close the surface of the liquid Ga. The tip is then dipped ~ 3 μm into the liquid Ga and after few seconds pulled out of the liquid. The tip is translated horizontally using the AFM stage and the process is repeated. After pulling is done, the Ga is solidified at 25 °C. Using a new AFM tip the sample is imaged in contact mode.

Figure 12.1 shows an AFM image of an array of Ga hillocks made by this method. With this technique gallium dots from 400 nm to 4 μm in diameter and from 200 nm to 1.3 μm in height having a typical aspect ratio of 0.3 and maximum aspect ratio of 0.5 have been made. One hundred Ga hillocks were formed in a 100 μm by 100 μm array.

One of the most surprising aspects is that the hillocks do not collapse but retain their shape and size for the extended period of this experiment (~ 30 minutes) before the Ga is solidified. It is possible that the thin oxide layer may provide rigidity that resists the collapse of the liquid Ga.

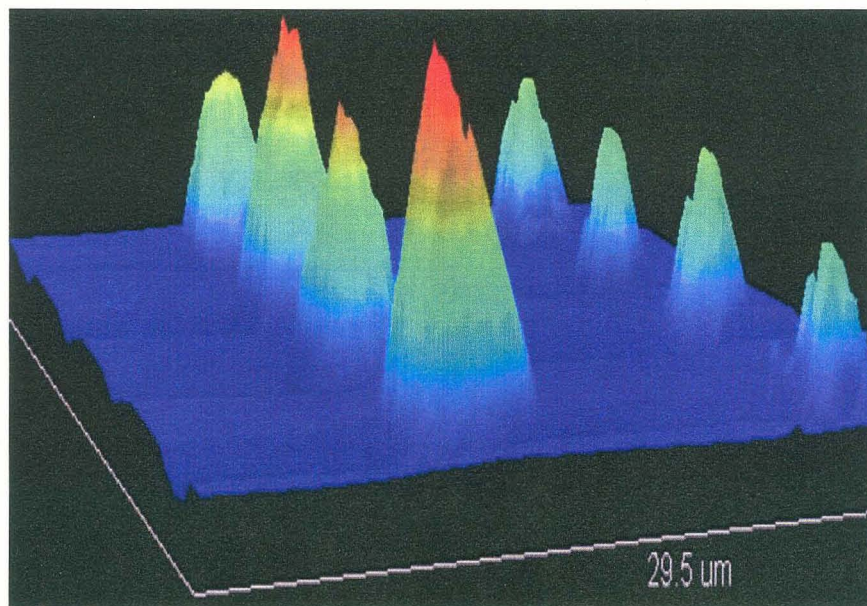


Figure. 12.1. Array of gallium dots pulled with AFM from a liquid Ga bath. Maximum height is about $1.4 \mu\text{m}$. The waviness of the substrate is an artifact in the AFM image processing software.

Further understanding of hillock formation can be obtained from AFM force vs. distance (F-D) responses for dipping a gold-coated AFM tip into liquid gallium.

The experiment is done with an M5 AFM. The AFM cantilever used is a contact mode Ultralever D AFM tip with a 2.1 N/m spring constant. It is sputter-coated with a 10 nm Cr layer and a 20 nm gold thin film. F-D is done over a range of $\sim 2 \mu\text{m}$ distance (between $-1 \mu\text{m}$ and $+1 \mu\text{m}$) with a retraction and extension speed of 100 nm/sec . It should be noted that the contact mode AFM tips are more sensitive thus they are used for F-D measurement and the non-contact mode are more rigid, thus they are used for

pulling. Figure 12.2 shows F-D results at four different temperatures (above and below the melting point of Ga) for extension into the Ga (Figure 12.5a) and retraction from the Ga (Figure 12.2b).

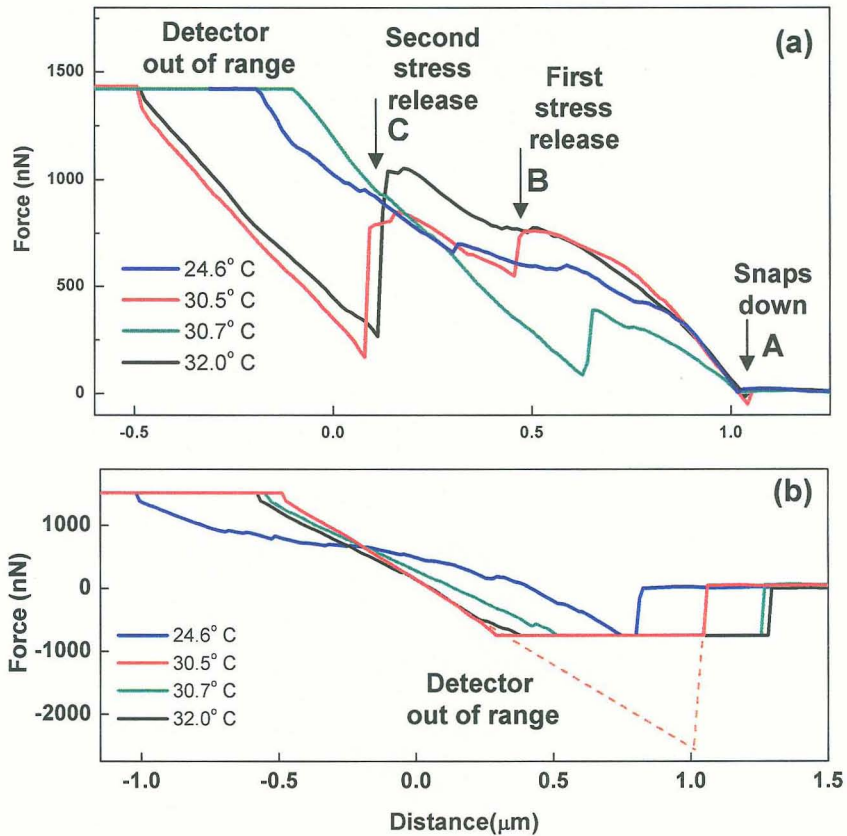


Figure 12.2. F-D curves for (a) extension into and (b) retraction from Ga.

The most interesting curve is for 30.5 °C. At point A in Figure 12.2a, the tip snaps down to the surface. After extending about 500 nm, the applied force approaches to about 870 nN (difference between point A and point B), the surface (probably native gallium oxide) is broken and the Ga releases stress by wetting up the tip. This is shown with a sudden decrease in the force. With further extension, the applied force reaches about 1000 nN, the stress is released again probably due to oxide of a greater diameter breaking, or an enhancement in the wetting between the Au and Ga. At this point, the

cantilever appears to be in hard contact with the substrate. For the 24.0 °C experiment, some nonlinear behavior is noted in the F-D curve, but there is no sudden release of force as in the three other curves.

The retraction curves (Figure 12.2b) show an additional feature of interest. The linear part of the graph (30.5 °C, 30.7 °C, and 32.0 °C) essentially reflects the spring constant of the cantilever. Note that the retraction force exceeds the range of the graph (2.1 μN). Extrapolating from the slope, it is seen that the force required to pull the tip out of the Ga is $\sim 2.5 \mu\text{N}$. This feature is interpreted as the force required to form a hillock.

It should be noted that the force experiments was repeated for a few times until it becomes stable then the data was collected. Then by changing the temperature the experiment was repeated at the same location. Repeating this experiment in a different location gave different force curves. More experiments need to be performed to complete this study. Different metal coated tips (Ga-reactive metals, such as Ag, Pt, Co, etc, and non-reactive metals such as Ti or Cr) can give more in-depth information.

12.2 Dip pen nanolithography with Ga

Dip pen nanolithography [112] (DPN) was done using AFM tips as a pen. In most of the cases the tip was an Ultralever A or B at an applied force of 16 and 20 nN respectively. The substrate is heated between 30 and 33 °C. First the AFM tip is dipped in a large droplet of gallium and the adhered gallium is placed near the region to be patterned. This serves to blot excess gallium off the tip and allows the smaller blotted excess to be used as a reservoir that can be returned to when the tip runs dry. Figure 12.3 shows an example of writing gallium patterns on silicon. Lines as narrow as 14 nm and as

high as 2 nm (Aspect ratio of 0.15) were written on the silicon. However it was frequently observed that Ga did not adhere well to the Si substrate.

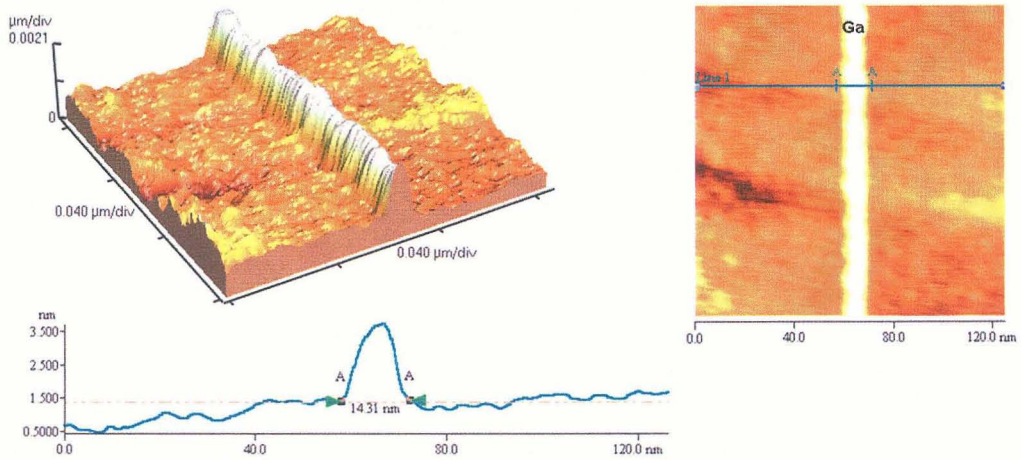


Figure 12.3. Line of gallium written from an AFM tip to a silicon substrate. The line is 14 nm wide at its base and ~2 nm high.

Different substrates including mica glass and sputtered gold film were tested. Ga was found to most strongly adhere to Au. Figure 12.4 shows examples of writing gallium patterns on a 20 nm sputtered gold thin film. The line width on Figure 12.4a is 87 nm, and the line height is 25 nm with aspect ratio of 0.29. In Figure 12.4b the line segments taper from 300 nm wide and 140 nm height (at the highest part of the line segment) down to 100 nm wide and 25 nm height before the line breaks up. The writing speed was 7 $\mu\text{m}/\text{sec}$ and 20 $\mu\text{m}/\text{sec}$ for the samples shown in Figures 12.4a and b respectively. Writing on gold was much easier and more reproducible. However as described in chapter 3, it was also observed that, within a few hours time, Ga spreads some distance beyond its original location.

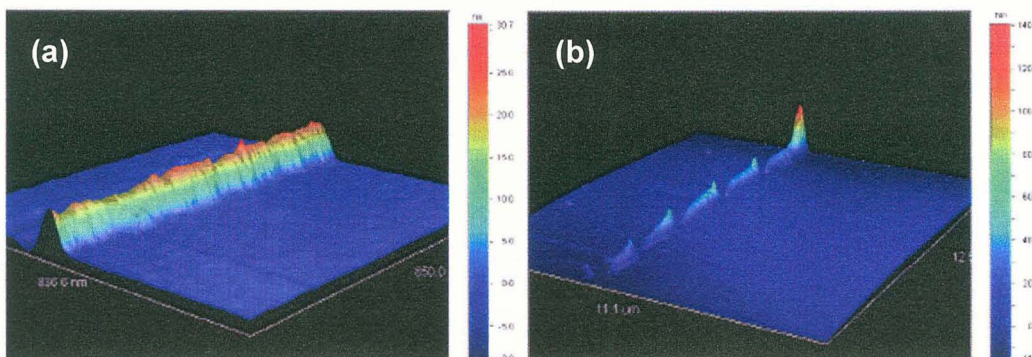


Figure 12.4. Lines of gallium written from an AFM tip to a gold-coated silicon substrate. (a) The line is 87 nm wide at its base and ~25 nm high. (b) A single line scan of the tip produces a segmented and non-uniform height gallium line, indicating discontinuous flow of Ga between the tip and the substrate. The writing direction was from upper right to lower left [113].

A significant advantage of using Ga as a media for dip pen lithography is the aspect ratio of the created structures. As it is reported here, the writing results have aspect ratios between 0.21 and 0.46. Such a high aspect ratio is seldom if ever produced by DPN with organic molecules or by voltage lithography.

12.3 Nanoimprint lithography (NIL) [114] with Ga

The melting point of Ga is well below that of polymers such as PMMA, so even a polymer mold can be used as a master for molding gallium, as reported here (Figures 12.5). These replicas were made by melting gallium onto a silicon substrate heated to 80 °C. The gallium leaves a drop of 10 mm diameter by 0.5 mm high. The master (a PMMA pattern on silicon, Figure 12.5d) is placed in contact with the gallium. The pattern is then transferred using an Obducat nanoimprinter, which is set to apply 20 to 40 bar pressure at 85 to 115 °C. The upper limit of 115 °C is set by the onset of deformation of the PMMA.

Then using liquid nitrogen, the sample is cooled and separated from the mold. The cooling step is crucial to decrease the surface tension between the mold and gallium and ease the separation.

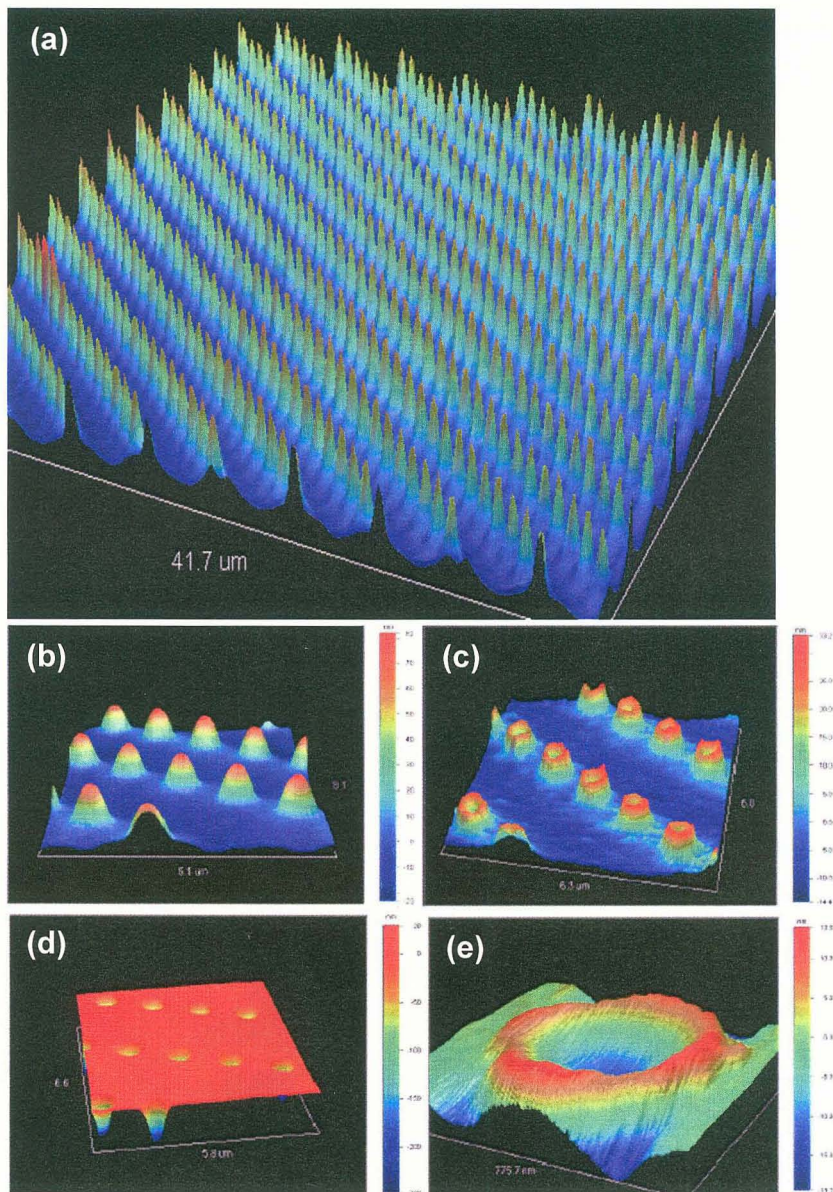


Figure 12.5. Nanoimprinting lithography (NIL) of Ga at 85 °C using a PMMA mold. (a-c) AFM topography images of NIL results with Ga on a silicon substrate. (d) AFM image of PMMA mold on silicon substrate. Note that the depth of the master as measured by AFM (>250 nm) is much greater than 20 to 100 nm height of the dots in (a-c). (e) Close-up of the shorter dots in (c) shows a 4 to 5 nm raised rim and a depressed center [113].

Note that different shapes and different surface heights were observed in different regions of the same imprint. In Figure 12.5b dots have a hillock shape. Also the depth of the holes in the master are much greater than the height of the dots in the replica. In other regions of the sample (Figure 12.5c,e) the dots are very short and have raised rims and depressed centers. The mold is not perfectly flat, which leads to incomplete filling on some regions of the mold. The rim shape is indicative of wetting a short distance into the mold.

To summarize, taking advantage of the low melting temperature of Ga, Ga hillocks were pulled from the liquid surface prior to freezing. Preliminary study of the F-D curves of hillock formation was done at different temperatures. Ga was also evaluated for nanopatterning using dip pen lithography and nanoimprint lithography. Several aspects of the wetting and adhesion of Ga to Au, Si and PMMA were observed in these patterning experiments.

PART V
CONCLUSIONS AND RECOMMENDATIONS

CHAPTER 13

CONCLUSIONS AND FUTURE PLANS

The premise of this research investigation and dissertation has been that thermodynamic and kinetic transformations in metal alloy systems can be viewed as self-assembly, in part because interesting structures can form automatically with limited user intervention, but also because these types of processes do appear potentially useful for the fabrication of practical devices. The studies were mostly limited to Ga-M alloys, which at room temperature were shown to form several nanostructures (needles, rods, plates) out of several elemental metals that are notable for their conductive (Ag, Au), electrochemical (Pt) and magnetic (Co) properties. A number of other Ga-M systems were identified that appear likely to form alloy crystals at room temperature and the number of possible metal nanostructured alloys can be extended by using other low melting temperature metals in place of Ga.

Applicability of the processes of self-assembly was demonstrated by using the reactive spreading front of Ga on Au to change the contact resistance of a nanotube in real-time. Applicability of the self-assembled nanostructures was demonstrated by the applications of the nanoneedles in mechanical and electromechanical properties

measurements, and in voltage nanolithography, as well as the application of the porous metal films to electrochemical sensing.

Given the numerous results developed over a short period and the many additional promising avenues that became apparent, it appears that the applications of metal alloy self-assembly can be quite extensive.

Some apparent extensions to the methods presented here include growing arrays of alloy needles in parallel, building advanced devices out of freestanding nanostructures with additional fabrication processing steps, constructing electromechanically-actuated devices out of freestanding nanostructures. In fact, each of these concepts already has been demonstrated in recent preliminary experiments. Continued investigations should lead to increasingly advanced concept devices and applications. Investigations such as these will continue as long as the methods of self-assembly of metal alloys point toward simpler ways to make useful devices.

REFERENCES

1. S. Saxena A. S. Warner, "*The Science and Design of Engineering Material*", 2nd ed., McGraw-Hill Pg. 269-277. (1999)
2. D. A. Porter and K. E. Easterling, "*Phase Transformations in Metals and Alloys*" 2nd ed., CRC Press Pg. 186-223. (2001)
3. J. J. Hickman, D. Ofer, P. E. Laibinis, G. M. Whitesides, and M. S. Wrighton, "Molecular self-assembly of two-terminal, voltammetric microsensors with internal references" *Science*, 252(5006), Pg. 688-691. (1991)
4. G. M. Whitesides, J. P. Mathias, C. T. Seto, "Molecular self-assembly and nanochemistry: A chemical strategy for the synthesis of nanostructures" *Science*, 254(5036), pg. 2312-1319. (1991)
5. G. M. Whitesides and B. Grzybowski "Self-assembly at all scales" *Science*, 295(2418), Pg. 2418-2421. (2002)
6. K.E. Drexler, "*Nanosystems, Molecular Machinery, Manufacturing and computation*" 1st ed., John Wiley & sons Inc. (1992)
7. R. P. Feynman, "There is plenty of room at the bottom" *Engineering and Science*, 23, Pg. 23-26. (1960).
8. P. Gordon, "*Principles of Physics Diagrams in Materials Systems*", 2nd ed., McGraw-Hill, (1983)
9. D. A. Porter and K. E. Easterling, "*Phase Transformations in Metals and Alloys*" 2nd ed., CRC Press (2001)
10. S. Saxena A. S. Warner, "*The Science and Design of Engineering Material*", 2nd ed., McGraw-Hill, Pg. 269. (1999)
11. R. W. Balluffi, S. M. Allen, W. C. Carter, "*Kinetics of Materials*", 1st ed., Wiley-Interscience, (2005)
12. P. Gordon, "*Principles of Physics Diagrams in Materials Systems*", 2nd ed., McGraw-Hill, Pg. 29-38. (1983)

13. S. Saxena A. S. Warner, "*The Science and Design of Engineering Material*", 2nd ed., McGraw-Hill, Pg. 249-257. (1999)
14. D. A. Porter and K. E. Easterling, "*Phase Transformations in Metals and Alloys*" 2nd ed., CRC Press, Pg. 60-106. (2001)
15. D. A. Porter and K. E. Easterling, "*Phase Transformations in Metals and Alloys*" 2nd ed., CRC Press, Pg. 44-52. (2001)
16. B. W. Mangum and D. D Thornton, "*Gallium Melting Point Standard*" 1st ed., U.S. Govt. Print. Off (1977)
17. I. A. Sheka, I. S. Chaus and T. T. Mityureva, "*The Chemistry of Gallium, (Topics in Inorganic and General Chemistry)*" Elsevier Pub. Co., Pg. 2-20. (1966)
18. G. Bhimarasetti, M. Sunkara, U. Graham, B. Davis, C. Suh, K. Rajan, "Morphological control of tapered and multi-junctional carbon tubular structure" *Adv. Mater.*, 15(19), Pg. 1629. (2003)
19. P.E. Lecoq de Boisbaudran, "Discovery of gallium" *Annales de Chimie* 5(10), Pg. 100-141. (1877)
20. <http://dbhs.wvus.k12.ca.us/webdocs/Chem-History/Disc-of-Gallium.html>
21. <http://en.wikipedia.org/wiki/Gallium>
22. Lyman J. Briggs, "Gallium thermal conductivity: supercooling: negative pressure" *J. Chem. Phys.*, 26(4), Pg. 784. (1957)
23. O. V. Vershkovskaya, V.S. Krasnova, V. S. Saltykova and A. E. Pervukhina, "*Gallium*" Academy of Science press, Pg. 3. (1960)
24. S. Saxena A. S. Warner, "*The Science and Design of Engineering Material*", 2nd ed., McGraw-Hill Pg. 110-140. (1999)
25. S. Saxena A. S. Warner, "*The Science and Design of Engineering Material*", 2nd ed., McGraw-Hill Pg. 258. (1999)
26. B. Predel, "Phase equilibria of binary alloys", CD-ROM, edited by O. Madelung, Springer, (2003) [CD Compilation of B. Predel, O. Madelung "*Phase Equilibria, Crystallographic Data and Values of Thermodynamic Properties of Binary Alloys*" (Landolt-Bornstein - Numerical Data and Functional Relationships in Science and Technology, vol. 5) Springer, (1996)]
27. S. Saxena A. S. Warner, "*The Science and Design of Engineering Material*", 2nd ed., McGraw-Hill Pg. 236-260. (1999)

28. S. Saxena A. S. Warner, "*The Science and Design of Engineering Material*", 2nd ed., McGraw-Hill Pg. 795. (1999)
29. A. E. Gunnaes, O. B. Karlsen and P. T. Zagierski, "Phase relations and crystal structures in the Ag–Ga system" *J. Alloy Comp.* 297, Pg. 144-155. (2000)
30. Mehdi M. Yazdanpanah S. A. Harfenist, and R.W. Cohn, "Gallium driven assembly of gold nanowire networks" *Appl. Phys. Lett.*, 85(9), Pg. 1592-1984. (2004)
31. R. Williams "The advancing front of liquid spreading" *Nature*, 266(5598), Pg. 153-4. (1977)
32. D. A. Porter and K. E. Easterling, "*Phase Transformations in Metals and Alloys*" 2nd ed., CRC Press, Pg. 60-110. (2001)
33. A. A. Nepomnyashchy "*Interfacial phenomena and convection*" Chapman & Hall/CRC, (2001)
34. The higher contrast in backscatter detector images relates to the higher atomic weight of the material being imaged.
35. G.Gao, "*Nanostructures and nanomaterials*", Imperial College Press, Pg. 17-26. (2003)
36. S. Nakahara and E. Kinsbron, "Room temperature inter-diffusion study of Au/Ga thin film couples", *Thin solid films*, 113, Pg. 15-26. (1984)
37. Z. Marinkovic and V. Simic, "Kinetics and mechanism of reaction at room temperature in thin Au/metal couples", *Thin Solid Films*, 156, Pg. 105-115. (1988)
38. Z. Marinkovic and V. Simic "Comparative analysis of interdiffusion in some thin film metal couples at room temperature", *Thin Solid Films*, 217(1-2), Pg. 26-30. (1992)
39. D. A. Porter and K. E. Easterling, "*Phase Transformations in Metals and Alloys*" 2nd ed., CRC Press, Pg. 101. (2001)
40. D. S. Willkinson, "*Mass Transport in Solid and Fluids*" 1st ed., Cambridge University Press, Pg. 35- 39. (2000)
41. D. A. Porter and K. E. Easterling, "*Phase Transformations in Metals and Alloys*" 2nd ed., CRC Press, Pg. 98-103. (2001)
42. C. J. Geankoplis, "*Mass Transport Phenomena*" Holt Rinehart and Winston, Inc., Pg. 149-151. (1972)

43. F. Liu "Self-assembly of three-dimensional metal islands: nonstrained versus strained islands", *Phys. Rev. Lett.* 89(24), Pg. 246105-1-4. (2002)
44. F. Drolet, K. R. Elder, M. Grant, and J. M. Kosterlitz, "Phase-field modeling of eutectic growth", *Phys. Rev. E*, 61, Pg. 6705-6720. (2000)
45. T. Fukuda, F. Arai, and L. Dong, "Assembly of nanodevices with carbon nanotubes through nanorobotic manipulations" *proceedings of the IEEE*, 91(11), Pg. 1803-1818. (2003)
46. J. Tang, G. Yang, Q. Zhang, A. Parhat, B. Maynor, J. Liu, Q. Lu-Chang, O. Zhou, "Rapid and reproducible fabrication of carbon nanotube AFM probes by dielectrophoresis" *Nano Letters*, 5(1) Pg. 11-14 (2005)
47. H. Cui, S. V. Kalinin, X. Yang, D. H. Lowndes, "Growth of carbon nanofibers on tipless cantilevers for high resolution topography and magnetic force imaging", *Nano Letters*, 4(11), Pg. 2157-61. (2004)
48. V. Simic and Z. Marinkovic, "Stability of compounds in thin film metal couples in the course of long ageing at room temperature" *Thin Solid Films*. 209(2), Pg. 181-187. (1992)
49. A. E. Gunnaes, O. B. Karlsen and P. T. Zagierski, "Phase relations and crystal structures in the Ag-Ga system" *J. Alloy Comp.* 297, Pg. 144-155. (2000)
50. D. A. Porter and K. E. Easterling, "*Phase transformations in metals and alloys*" 2nd ed., pg. 185-197, CRC PRESS (2001)
51. D. A. Porter and K. E. Easterling, "*Phase transformations in metals and alloys*" 2nd ed., Pg. 283-285. CRC PRESS (2001)
52. D. A. Porter and K. E. Easterling, "*Phase transformations in metals and alloys*" 2nd ed., Pg. 214-221. CRC PRESS (2001).
53. Modified by M.M. Yazdanpanah from D. A. Porter and K. E. Easterling, "*Phase transformations in metals and alloys*" 2nd ed., Pg. 187. CRC PRESS (2001).
54. D. A. Porter and K. E. Easterling, "*Phase transformations in metals and alloys*" 2nd Pg. 1-56. CRC PRESS (2001)
55. M. Beltowaska-Brzezinska, T. Luczak, M. Mączka, H. Baltruschat, and U. Muller "Ethyne oxidation and hydrogenation on porous Pt electrode in acidic solution" *J. Electroanal. Chem.* 519, Pg. 101-110. (2002)
56. R. Noroozi-Esfahani and G. J. Maclay "Electrical properties, stability, and applications of ultra thin porous Pt films on SiO₂" *J. Vac. Sci. Technol, A*, 8(4), Pg. 3591 (1990)

57. Z. Gaburro, P. Bettotti, M. Saiani, L. Pavesi, L. Pancheri, C. J. Oton, and N. Capuj, "Role of microstructure in porous silicon gas sensors for NO₂", *Appl. Phys. Lett.* 85(4) Pg. 555-557. (2004)
58. A. Desforges, R. Backov, H. Deleuze, O. Mondain-Monval, "Generation of palladium nanoparticles within macrocellular polymeric supports: Application to heterogeneous catalysis of the Suzuki-Miyaura coupling reaction", *Adv. Func. Mat.*, 15(10), Pg. 1689-1695 (2005)
59. G. Wu, J. Wang, J. Shen, Q. Zhang, B. Zhou, Z. Deng, B. Fan, D. Zhou, F. Zhang, "Strengthening mechanism of porous silica films derived by two-step catalysis" *J. Phys. D (Applied Physics)*, 34(9), Pg. 1301-1307. (2001)
60. D. E. Williams, R. C. Newman, Q. Song, and R. G. Kelly, "Passivity breakdown and pitting corrosion of binary alloys". *Nature*, 350, Pg. 216-219. (1991)
61. R. C. Newman, and K. Sieradzki, "Metallic Corrosion". *Science*, 263, Pg. 1708-1709. (1994).
62. J. Erlebacher, M. J. Aziz, Al. Karma, N. Dimitrov and K. Sieradzki "Evolution of nanoporosity in dealloying" *Nature* Vol. 410, No. 22, page 450 (2001)
63. C. Ji and P. C. Searson "Synthesis and characterization of nanoporous gold nanowires" *J. Phys. Chem. B*, 107, Pg. 4494-4499. (2003)
64. C. Ji, G. Oskam, Y. Ding, J. D. Erlebacher, A. J. Wagner, P. C. Searson, "Deposition of Au_xAg_{1-x}/Au_yAg_{1-y} multilayers and multisegment nanowires" *J. Electrochemical Society*, 150(8), Pg. C523-528. (2003)
65. <http://www.scescape.net/~woods/elements/gallium.html>
66. M. Slowinski, E. J. Slowinski, "Chemical Bonding" 1st ed., W. B. Saunders Company, Pg. 565- 594. (1973)
67. J.W. Cahn, and J. E. Hilliard, "Free energy of a nonuniform system III. Nucleation in a two-component incompressible fluid", *J. Chem. Phys.* 31, Pg. 688- 699 (1958).
68. J. E. Hilliard, "Solidification" American Society for Metals, Metals Park, Ohio, Pg. 497- 560 (1971).
69. P. Poncharal, Z. L. Wang, D. Ugrate, W. A. de Heer, "Electrostatic deflection and electromechanical resonance of carbon nanotubes" *Science*, 283, Pg. 1513-1516. (1999)
70. T. Hsu "MEMS and Micro system design and Manufacture" Pg. 166. McGraw-Hill (2002)

71. L. Meirovich, "*Elements of Vibration Analysis*", 2nd ed., page 223-227. McGraw-Hill (1986).
72. D. O. Brush, B. O. Almorth, "*Buckling of Bars, Plates, and Shells*" McGraw-Hill, Pg. 21-28. (1975)
73. L.D. Landau and E. M. Lifshitz, "*Theory of Elasticity*" Page 98 2nd ed., vol. 2 Pg. 98. (1970)
74. Z. L. Wang, R. P. Gao, P. Poncharal, W. A. de Heer, Z. R. Dai and Z. W. Pan, "Mechanical and electrostatic properties of carbon nanotubes and nanowires" *Matt. Sci. Eng., C* 16, Pg. 3-10. (2001)
75. W. C. Young and R. G. Budynas, "*Roark's Formulas for Stress and Strain*", 7th ed., Pg. 765-768. McGraw-Hill, (2002)
76. C. M. Harris, "*Shock and Vibration Handbook*" 4th ed., Pg. 7.17. McGraw-Hill (1996)
77. M. Nishio, S. Sawaya, S. Akita Y. Nakayama "Carbon nanotube oscillators toward zeptogram detection" *Appl. Phys. Lett.*, 86, Pg. 133111-3. (2005)
78. J. L. Hutter and J. Bechhoefer, "calibration of atomic-force microscope tips", *Rev. Sci. Instrum.*, 64(7), Pg. 1868-1872. (1993)
79. N. Israelachvili, "*Intermolecular and Surface Forces*" 2nd ed., Pg. 152-192. Academic Press (1991)
80. Modified form J. L. Hutter and J. Bechhoefer, "calibration of atomic-force microscope tips", *Rev. Sci. Instrum.*, 64(7), Pg. 1868-1872. (1993)
81. N. Israelachvili, "*Intermolecular and surface forces*" 2nd ed., Academic Press pg. 186-187. (1991)
82. R. Perez , M. C. Payne, I. Stich and K. Terakura "Role of Covalent Tip-Surface Interactions in Noncontact Atomic Force Microscopy on Reactive Surfaces" *Phys. Rev. Lett.* 78, Pg. 678–681. (1997)
83. C. M. Harris, "*Shock and Vibration Handbook*" 4th ed., Pg. 7.5. McGraw-Hill (1996)
84. The density of Ag₂Ga crystals is approximately calculated by average of density of Ag (10.5 g/cm³) and Ga (5.9 g/cm³)
85. Y. Xu, J.-T. Lin, B. W. Alphenaar and R. S. Keynton, "Viscous damping of microresonators for gas composition analysis" *Appl. Phys. Lett.*, 88, Pg. 143513 (2006)

86. A. P. Levitt "*Whisker Technology*", John Wiley & sons, Pg. 136. (1970)
87. D. R. Lide "*Hand Book of Chemistry and Physics*" 3rd ed., Pg. 12-232. CRC PRESS, (2002)
88. J. A. Dagata, J. Schneir, H. H. Harary, J. Bennett, W. Tseng, "Pattern generation on semiconductor surfaces by a scanning tunneling microscope operating in air" *J. Vac. Sci. & Tech. B*, 9(2), Pg. 1384-1388. (1991)
89. S. A. Harfenist, M. M. Yazdanpanah and R.W. Cohn, "High Aspect Ratio Etching of AFM-Patterned Nitrided Silicon", *J. Vac. Sci. Technol. B*, 21(3), Pg. 1176-1180. (2003)
90. Mehdi M. Yazdanpanah S. A. Harfenist, A. Safir and R.W. Cohn, "Selective self-assembly at room temperature of individual freestanding Ag₂Ga alloy nanoneedles" *J. App. Phys.* 98, 073510-1-7 (2005)
91. H. W. Lee, S. H. Kim, Y. K. Kwak, C. S. H., "Nanoscale fabrication of a single multiwalled carbon nanotube attached atomic force microscope tip using an electric field" *Rev. Sci. Instrum.*, 76(4), Pg. 46108-1-5. (2005)
92. J. S. Greeneich, "Time evolution of developed contours in poly-(methyl methacrylate) electron resist" *J. Appl. Phys.*, 45(12), Pg. 5264-5268. (1974)
93. M. M. Yazdanpanah, S. A. Harfenist, A. Safir, and R. W. Cohn. "Room Temperature, Selectively Self-Assembled, Freestanding Alloy Nanoneedles of Ag₂Ga", *2005 Physical Electronics Conferences*, Madison, WI, June 20-22, (2005)
94. S. Frank, P. Poncharal, Z.L.Wang, W.A. de Heer, "Carbon Nanotube Quantum Resistors", *Science*, 280, Pg. 1744-1746. (1998)
95. S. Datta, "*Quantum Transport Atom to Transistor*" 1st ed., Cambridge University Press, (2005).
96. A. Javey, J. Guo, Q. Wang; M. Lundstrom, H. Dai, "Ballistic carbon nanotube field-effect transistors", *Nature*, 424(6949), Pg. 654-657. (2003)
97. See Chapter 3, Pg. 23-50
98. Y. Ando, S. Iijima, "Preparation of carbon nanotubes by arc-discharge evaporation" *Jpn. J. Appl. Phys.*, Part 2, 32(1), Pg. 107-109. (1993)
99. M.M. Yazdanpanah, S. Chakraborty, S. A. Harfenist, R. W. Cohn, and Bruce Alphenaar, "Formation of highly transmissive liquid contact to carbon nanotubes" *Appl. Phys. Lett.* 85(16), Pg. 3564-3566. (2004)

100. R. Egger and A. O. Gogolin, "Bulk and boundary zero-bias anomaly in multiwall carbon nanotubes", *Phys. Rev. Lett.* 87, Pg. 066401/1-4. (2001)
101. A. Bachtold, M. de Jonge, K. Grove-Rasmussen, P.L. McEuen, M. Buitelaar, and C. Schönberger, "Suppression of tunneling into multiwall carbon nanotubes", *Phys. Rev. Lett.* 87, Pg. 166801/1-4. (2001).
102. Luttinger liquid, is a theoretical model describing interacting electrons or other fermions in a one-dimensional conductor such as carbon nanotubes.
103. Z. Yao, C. L. Kane, and C. Dekker, "High-field electrical transport in single-wall carbon nanotubes" *Phys. Rev. Lett.* 84, Pg. 2941-4. (2000)
104. M. M. Yazdanpanah, S. Chakraborty, S. A. Harfenist, R. W. Cohn, and B. Alphenaar, "Direct Measurement of Nanotube Conductance during Contact Formation" *American Physical Society March meeting*, Montreal, Canada, March 24, (2004).
105. F. Scheffler, A. Zampieri, W. Schwieger, J. Zeschky, M. Scheffler, P. Greil, "Zeolite covered polymer derived ceramic foams: novel hierarchical pore systems for sorption and catalysis" *Advances in Applied Ceramics*, 104(1), Pg. 43-48. (2005)
106. R. Noroozi-Esfahani and G. Jordan Maclay "Electrical properties, stability, and applications of ultra thin porous Pt films on SiO₂" *J. Vac. Sci. Technol, A*, 8(4), Pg. 3591 (1990)
107. V. de Silva, A. Chamberlain, S. Kortikar, M. M. Yazdanpanah, R. Cohn, P. Huettl, F. Pomerleau, G.A. Gerhardt, J.T. Hastings, "Nano-structured Microelectrode Arrays with Enhanced Sensitivity and Limit of Detection for in vivo Enzymatic Sensing" *Neuroscience Annual Society meeting*, Washington, DC, November 12 –16, (2005).
108. M. Beltowaska-Brzezinska, T.Luczak, M.Mączka, H.Baltruschat, U.Muller "Ethyne oxidation and hydrogenation on porous Pt electrode in acidic solution" *J. Electroanal. Chem.* 519, Pg. 101-110. (2002)
109. J. J. Burmeister, K Moxon, and G. A. Gerhardt "Ceramic-Based Multisite Microelectrodes for Electrochemical Recordings" *Anal. Chem.* 72, Pg. 187-192 (2000)
110. M.K. Sunkara, S. Sharma, R. Miranda, G. Lian and E. C. Dickey, "Bulk Synthesis of silicon nanowires using a low-temperature vapor-liquid-solid method," *Appl. Phys. Lett.* 79(10), Pg. 1546-1548. (2001)
111. B. Zheng, Y. Wu, P. Yang, J. Liu, "Synthesis of Ultralong and Highly-Oriented Silicon Oxide Nanowires from Liquid Alloy," *Adv. Mater.* 14(2), 122-144. (2002)

112. Richard D. Piner, Jin Zhu, Feng Xu, Seunghun Hong, Chad A. Mirkin “Dip-pen nanolithography” *Science*, 283(5402) Pg. 661-663. (1999)
113. M. M. Yazdanpanah, S. A. Harfenist, and R. W. Cohn, “Nanoimprint and dip pen lithography of gallium”, *The 1st International Conference on Nanoimprint and Nanoimprint Lithography*, San Francisco, CA, 11-13, December (2002)
114. S. Y. Chou, P. R. Krauss, P. J. Renstrom, “Imprint lithography with 25-nanometer resolution” *Science*, 272(5258), Pg. 85-87. (1996)

BIBLIOGRAPHY OF THE UNREFERENCED ARTICLES

SELF-ASSEMBLY

115. Hosokawa, I. Shimoyama, and H. Miura, "Two-dimensional micro-self-assembly using the surface tension of water," *Sensors and Actuators*, 57, Pg. 117-125. (1996)
116. T. Takigawa, H. Wada, Y. Yoshikawa, I. Mori, and T. Abe, "Advanced e-beam lithography" *J. Vac. Sci. Technol. B*, 9(8), Pg. 2981-2985. (1991)
117. F. E. Osterloh, "Stringing up the Pearls: Self-Assembly, Optical and Electronic Properties of CdSe- and Au-LiMo₃Se₃ Nanoparticle-Nanowire Composites" *Nano Lett.* 3(2), Pg. 125-128. (2003)
118. M. C. McAlpine, et. al., " High-Performance Nanowire Electronics and Photonics on Glass and Plastic Substrates" *Nano Lett.* 3(11), Pg. 1531-1534. (2003)
119. C. Young-Min, R. Hyun-Ku "Pt-Pd bimetallic nanoparticles encapsulated in dendrimer nanoreactor" *Catalysis Letters*, 85(3-4), Pg.159-164. (2003)
120. N. Garcia, E. V. Ponizovskaya, H. Zhu, J. Q. Xiao, and A. Pons "Wide photonic band gaps at the visible in metallic nanowire arrays embedded in a dielectric matrix" *Appl. Phys. Lett.*, 82(19), Pg. 3147-3149. (2003)
121. F. Qian, Y. Li, S. Gradecak, D. Wang, C. J. Barrelet, and C. M. Lieber, "Gallium Nitride-Based Nanowire Radial Heterostructures for Nanophotonics", *Nano Lett.*, 4(10), Pg.1975-1978. (2004)
122. F. Patolsky, Y. Weizmann and I. Willner, "Actin-based metallic nanowires as bio-nanotransporters" *Nature Materials*, 3, Pg. 692-695. (2004)
123. T. Hassenkam, K. Moth-Poulsen, N. Stuhr-Hansen, K. Norgaard, M. S. Kabir, and T. Bjornholm, "Self-Assembly and Conductive Properties of Molecularly Linked Gold Nanowires" *Nano Lett.*, 4(1), Pg. 19-22. (2004)
124. H. Fukuda, R. Zohnishi, S. Nomura, "Highly sensitive metal-insulator-semiconductor field-effect transistor sensors for detecting carbon monoxide gas

- using porous platinum and tungsten oxide thin films” *Jpn. J. Appl. Phys. Part 1*, 40(4B), Pg. 2782-6. (2001)
125. D. Walsh, L. Arcelli, T. Ikoma, J Tanaka and S. Mann, “Dextran templating for the synthesis of metallic and metal oxide sponges, Nature materials” *Nature Materials*, 2, Pg. 386–390. (2003)
 126. Taleb Mokari, Eli Rothenberg, Inna Popov, Ronny Costi, Uri Banin¹, “Selective Growth of Metal Tips onto Semiconductor Quantum Rods and Tetrapods” *Science*, 304, Pg. 1878-9 (2004)
 127. Hongyou Fan, Kai Yang, Daniel M. Boye, Thomas Sigmon, Kevin J. Malloy, Huifang Xu, Gabriel P. Lo’pez, C. Jeffrey Brinker “Self-Assembly of Ordered, Robust, Three-Dimensional Gold Nanocrystal/Silica Arrays” *Science* 304, Pg. 567, (2004)
 128. <http://www.sandia.gov/news-center/news-releases/2004/micro-nano/nanotoolcase.ht>
 129. M. Fleischer and H. Meixner “Gallium oxide thin films: a new material for high-temperature oxygen sensors” *Sensors and Actuators B (Chemical)*, B4(3-4), Pg. 437-41. (1991)
 130. R. Torees et. al. “Performance of single use purifiers vs. regenerable purifiers for growth of high brightness gallium nitride LEDs”, *Journal of Crystal Growth*, 261(2-3), Pg. 231-235. (2004)
 131. D. Ravi Shankaran, K. Iimura, T. Kato “A novel metal immobilized self-assembled surface for electrochemical sensing”, *Sensors and Actuators B*, 96 Pg. 523–526. (2003)
 132. A. Taleb, A.O. Gusev, F. Silly, F. Charra, M.P. Pileni, “Local photon emission of self-assembled metal nanoparticles ”, *Appl. Surf. Sci.* 162–163 Pg. 553–558. (2000)
 133. C. Teichert and M. G. Lagally “Self-organization in growth of quantum dot superlattices” *phys. rev. lett.*, 76(10), Pg. 1675 (1996)
 134. J. A. Floro “Novel SiGe island coarsening kinetics: Ostwald ripening and elastic interactions ” *phys. rev. lett.*, 84(4), Pg. 701 (2000)
 135. O. M. Magnussen, B. M. Ocko, M. Deutsch, M. J. Regan, P. S. Pershan, D. Abernathy, G. Grübel and J. Legrand, “Self-assembly of organic films on a liquid metal”, *Nature*, 384, Pg. 250 – 252, (1996)
 136. Z. R. Tian, J. Liu, J. A. Voigt, H. Xu, and M. J. Mcdermott “Dendritic growth of cubically ordered nanoporous materials through self-assembly” *Nano Lett.* 3(1) Pg. 89 – 92. (2003)

137. T. Qiu, X.L. Wu, Y.F. Mei, P.K. Chu and G.G. Siu “Self-organized synthesis of silver dendritic nanostructures via an electroless metal deposition method” *Appl. Phys. A* 81, Pg. 669–671. (2005)

CRYSTAL GROWTH

138. A.E. Gunnas, A. Olsen and H. Hero, “Dental gallium alloy composites studied by SEM and TEM”, *J. of Microscopy* 185, Pg. 188 – 198. (1997).
139. E. A. Stach, P. J. Pauzauskie, T. Kuykendall, J. Goldberger, R. He, and P. Yang “Watching GaN Nanowires Grows” *Nano Lett.*, 3(6), Pg. 867-869. (2003)
140. Z. H. Wu, X. Mei, D. Kim, M. Blumin, H.F. Ruda, J.Q. Liu, K.L. Kavanagh, “Growth, branching, and kinking of molecular-beam epitaxial <110> GaAs nanowires” *Appl. Phys. Lett.*, 83, Pg. 3368-70. (2003)
141. S. C. Lyu, Y. Zhang, H. Ruh, H. J. Lee, and C. J. Lee “Synthesis of high-purity GaP nanowires using a vapor deposition method” *Chem. Phys. Lett.*, 367, Pg. 717-22. (2003)
142. R. Jalilian, M. M. Yazdanpanah and Gamini Sumanasekera “*Synthesis of Gallium oxide nanowire and nanocrystals*” APS march meeting, LA. CA. (2005)
143. C. Wetzel, T. Salagaj, T. Detchprohm, P. Li, and J. S. Nelson, “GaInN/GaN growth optimization for high-power green light-emitting diodes” *App. Phys. Lett.* 85, Pg. 866-8. (2004)

PLANAR SPREADING

144. A. I. Bykhovskii and A. G. Tonkopyrad, “Equilibrium of liquid gallium thin film on Ag” *The physics of Metal and Metallography*, 52, Pg. 100-105. (1981)
145. V.M. Andronov, I.P. Grebennik, and S.V. Dukarov. “Features of gallium spreading over surfaces of Ag - Au - Ga thin films”, *Functional materials*, 4(3), Pg. 387-391. (1997)
146. A.I. Bykhovski and A. G. Tonkopyrad “Equilibrium of liquid gallium on Ag film” *The physic of Metal and Metallurgy*, 52, Pg. 100-105. (1981) [Translated from Russian To English by Bohdana Sherehi and M. M. Yazdanpanah]
147. Z. Marinkovic and V. Simic, “Kinetics and mechanism of reaction at room temperature in thin Au/metal couples”, *Thin solid films*, 156, Pg. 105-115. (1988)

148. Z. Marinkovic and V. Simic, "Room temperature formation and stability of compounds in metal couples of bulk-film type", *Thin solid films*, 249, Pg. 168-173. (1994)
149. V. Simic, and Z. Marinkovic, "Thin film interdiffusion of Au and Ga at room temperature", *Thin solid films*, 34, Pg. 179-183, (1976)
150. S. Nakahara and E. Kinsbron "Room temperature interdiffusion study of Au/Ga thin film couples", *Thin solid films*, 113, Pg. 15-26. (1984)
151. Z. Marinkovic and V. Simic, "Comparative analysis of interdiffusion in some thin film metal couples at room temperature" *Thin solid films*, 217 Pg. 26-30. (1992)

NON-PLANAR SPREADING

152. R. Adelung, L. Kipp, J. Brandt, L. Tarcak, M. Traving, C. Kreis, and M. Skibowski "Nanowire network on perfectly flat surfaces", *Appl. Phys. Lett.* 74(20), Pg. 3053-3055. (1999)
153. U.M. Graham , S. Sharma , M.K. Sunkara , B.H. Davis, "Nanoweb formation: 2D self-assembly of semiconductor gallium oxide nanowires/nanotubes" *Advanced Functional Materials*, 13(7), Pg. 576-581. (2003)
154. F. Liu "Self-assembly of three-dimensional metal islands: nonstrained versus strained islands", *phys. rev. lett.*, 89(24), Pg. 246105, (2002)

NANOWIRE SELECTIVE GROWTH

155. H. Dai, J. H. Hafner, A. G. Rinzler, D. T. Colbert, and R. E. Smalley, "Nanotubes as nanoprobe in scanning probe microscopy", *Nature*, 384, Pg. 147, (1996).
156. C. V. Nguyen, K. J. Chao, R. M. D. Stevens, L. Delzeit, A. Cassell, J. Han, and M. Meyyappan, "Carbon nanotube tip probes: stability and lateral resolution in scanning probe microscopy and application to surface science in semiconductors" *Nanotechnology* 12, Pg. 363, (2001)
157. R. Stevens, C. Nguyen, A. Cassell, L. Delzeit, M. Meyyappan, and J. Han, "Improved fabrication approach for carbon nanotube probe devices" *Appl. Phys. Lett.* 77, Pg. 3453, (2000)
158. N. de Jonge, Y. Lamy, and M. Kaiser, "Controlled mounting of individual multi-walled carbon nanotubes on support tips" *Nano Lett.*, 3, Pg. 1621, (2003).

159. A. B. H. Tay and J. T. L. Thong, "High-resolution nanowire atomic force microscope probe grown by a field-emission induced process" *Appl. Phys. Lett.*, 84, 5207 (2004).

SUPERPOROUS

160. R.S. Keynton *et. al.* "Design and development of microfabricated capillary electrophoresis devices with electrochemical detection" *Analytica Chimica Acta* 507, Pg. 95–105. (2004)
161. R. Noroozi-Esfahani and G. J. Maclay "Electrical properties, stability, and applications of ultra thin porous Pt films on SiO₂" *J. Vac. Sci. Technol, A*, 8(4), Pg. 3591, (1990)
162. Maria Beltowaska *et. al.* "Ethyne oxidation and hydrogenation on porous Pt electrode in acidic solution" *J. Electroanal. Chem.* 519, Pg. 101-110. (2002)
163. I. Rong Li and K. sieradzki "Ductile-Brittle Transition in Random Porous Au" *Phys. Rev. Lett.* 68, 1168 (1992)

NANOMECHANICS

164. L. Jeffery and J. Bechhoefer, "Calibration of atomic-force microscope tips", *Rev. Sci. Instrum.* 64(7), Pg. 1868, (1993)
165. C. Argento and R. H. French Parametric tip model and force–distance relation for Hamaker constant determination from atomic force microscopy *J. Appl. Phys.*, 80(11), Pg. 6081, (1996)
166. Yuan-Wei Zheng, Yong-Feng Lu, Zhi-Hong Mai and Wen-Dong Song "Removing Spherical Silica Particles from Si, Ge and NiP Substrates by KrF Excimer Laser", *Jpn. J. Appl. Phys.*, 39, Pg. 5894-5898. (2000)
167. L. Jeffery Hutter and J. Bechhoefer, measurement and manipulation of van der Waals forces in atomic –force microscopy, *J.Vac. Sci. Technol. B* 12(3), Pg. 2251, (1994)
168. A. Gupta, D. Akin, and R. Bashir, "Single virus particle mass detection using microresonators with nanoscale thickness", 84(11), Pg. 1976-1978. (2004)

APPENDIX A

YOUNG'S MODULUS, QUALITY FACTOR AND EFFECTIVE MASS OF THE NEEDLE DETERMINED BY ELECTROSTATIC DEFLECTION METHOD. IT ALSO INCLUDES THE SPRING CONSTANT OF THE NEEDLES FROM BOTH ELECTROSTATIC AND FORCE MICROSCOPY METHODS

	Length (μm)	Radius (nm)	Resonance Frequency (kHz) f_0	Quality factor Q	Young's modulus (Gpa) E	Spring constant from resonance frequency (pN/nm) k_n	Spring constant from F-D curves (pN/nm) k_n	Spring constant from snap-in data (pN/nm) k_n	Min mass sensitivity 10^{-19}Kg
1	27.9	137	86		27.1	1.05			
2	24.9	117	170		93.7	2.66			
3	42.3	274	95.5		44.4	7.77			
4	11.1	168	525		17.1	23.3			
5	49.7	400	68		20.2	9.9			
6	42	188	55.8		31.5	1.24			
7	11.9	75	421	1700	71.2	3.18	36		6.06
8	7	52	967		94.9	4.76			
9	10.1	166	780		26.2	45.6			
10	10.1	190	999		32.9	97.9			
11	6.13	133	2970		80.4	257			
12	14	98	255	1500	29.7	2.35	4.65	4.75	4.94
13	6.24	71	1290		57.2	14.1			
14	13.8	220	767		50.2	106			
15	29.5	130	76.6	601	30	0.78			
16	8.35	85	656	1700	33	6.96			
17	50	100	20.5		30	0.06			
18	9.6	78	485		37.4	3.69			
19	13.1	242	726	2200	29.9	108	114		2.44
20	5.3	91.6	2090	1400	46.9	52.3			
21	2.15	50	5600	3300	45.2	90.1			

CURRICULUM VITAE

NAME: Mehdi Mohammad Yazdanpanah

ADDRESS: 2210 South Brooks St.
Room 253, Belknap Research Building
University of Louisville
Louisville, KY 40208

DOB: Birjand, Iran - March 21, 1975

EDUCATION & TRAINING:

B.S., Applied physics,
Sharif University of Technology,
Tehran, Iran
1993-98

M.S., Applied physics,
University of Beheshti
Tehran, Iran
1998-2001

Ph.D., Electrical Engineering
University of Louisville
2002-2006

AWARDS:

Outstanding graduate student for Electrical and Computer Engineering
in year 2005

Second place winner of Promotional/Poster Section at the 2004
International Material Nanotechnology Workshop in September 2004,
Lexington, Kentucky

Honorable mention fifth Iranian Physics Olympiad 1992

PROFESSIONAL

SOCIETIES: American Physical Society

PUBLICATIONS:

REFEREED JOURNALS:

R. Jalilian, M. M. Yazdanpanah, B. K. Pradhan, and G. Sumanasekera
“Crystalline nano-ribbons of Ga₂O₃ with herringbone structures”
Chemical Physics Letters 426 Pg. 393–397. (2006)

M. M. Yazdanpanah S. A. Harfenist, A. Safir and R. W. Cohn,
“Selective self-assembly at room temperature of individual freestanding
Ag₂Ga alloy nanoneedles” J. App. Phys. 98, 073510-1-7 (2005)

M. M. Yazdanpanah S. A. Harfenist, and R. W. Cohn, “Gallium Driven
Assembly of Gold Nanowire Networks” App. Phys. Lett., 85, Pg. 1592-
1594. (2004)

M. M. Yazdanpanah, S. Chakraborty, S. A. Harfenist, R. W. Cohn and
B W Alphenaar, “Formation of Highly Transmissive Liquid Metal
Contact to Carbon Nanotubes” App. Phys. Lett., 85, Pg. 3564-3566.
(2004)

S. A. Harfenist, M. M. Yazdanpanah and R. W. Cohn, "High Aspect
Ratio Etching of AFM-Patterned Nitrided Silicon", J. Vac. Sci.
Technol. B, 21(3), Pg. 1176-1180. (2003)

SELECTED CONFERENCE

PAPERS & PRESENTATIONS:

M. M. Yazdanpanah, A. Safir, S. Pabba, F. P. Zamborini, and R. W.
Cohn, “Nanostructure self-assembly by gallium-metal reactions at room
temperature” Gordon Conference on Nanostructure Fabrication, Tilton
NH, (16-21 July 2006)

A. Safir, M. M. Yazdanpanah S. Pabba, S. Cambron, R. S. Keynton,
and R. W. Cohn, “Fabrication of an insulated probe on a self-assembled
metallic nanowire for electrochemical probing in cells”, Proceeding of
the IEEE Nano-2006, Cincinnati, OH, (16-21 July 2006)

S. Pabba, S. Berry, M. M. Yazdanpanah, S. Cambron, R. S. Keynton,
and R. W. Cohn, “Nanotube suspension bridges directly fabricated
from nanotube-polymer suspensions by manual brushing”, Proceeding
of the IEEE Nano-2006, Cincinnati, OH, (16-21 July 2006)

V. de Silva, A. Chamberlain, S. Kortikar, M. M. Yazdanpanah, R.
Cohn, P. Huettl, F. Pomerleau, G. A. Gerhardt, J. T. Hastings, “Nano-
structured Microelectrode Arrays with Enhanced Sensitivity and Limit
of Detection for in vivo Enzymatic Sensing” Neuroscience annual
Society meeting, Washington, DC, November 12 – 16, 2005

M. M. Yazdanpanah, S. A. Harfenist, A. Safir and R. W. Cohn, "Room Temperature, Selectively Self-Assembled, Freestanding Alloy Nanoneedles of Ag₂Ga" Physical Electronics Conferences, Madison, WI, June 20, 2005

M. M. Yazdanpanah, S. A. Harfenist, A. Safir and R. W. Cohn "Room temperature in-situ growth of individual Ag₂Ga nanoneedle as AFM tips" American Physical Society March 2005 meeting, Los Angeles, CA, March 23, 2005

J. Hadizadeh, D. L. Goldsby, M. M. Yazdanpanah, A. I. Konkachloev, T. E. Tullis, N. Beeler "Some Mechanical Implications of the Development and Evolution of Y shears in Simulated Granite Gouge" American Geographical Union, Dec. 2004 meeting, San-Francisco, CA Dec 11, 2004

K. Hagg, M. M. Yazdanpanah S. A. Harfenist. M. Otto, J. Hadizadeh "A Microstructural Study of small-Displacement Fault in Aztec Sandstone" American Geographical Union, Dec. 2004 meeting, San-Francisco, CA Dec 11, 2004

S. A. Harfenist, M. M. Yazdanpanah, A. Safir, T. Olaleye, P. Gopinath, S. Chakraborty, S. M. Berry, S. D. Cambron, E. A. Nelson, R. S. Keynton, B. W. Alphenaar and R.W. Cohn "Directed and self-assembled nanowire formation at room temperature for rapid nanoprototyping," International Workshop in Nanomaterials, Lexington, KY. (20 September 2004)

M. M. Yazdanpanah, S. A. Harfenist, A. Safir and R. W. Cohn "Directed self-assembly of surface-oriented and freestanding Ag₂Ga alloy nanoneedles," International Workshop in Nanomaterials, Lexington, KY. (20 September 2004)

R. W. Cohn, S. A. Harfenist, M. M. Yazdanpanah, A. Safir, T. Olaleye, P. Gopinath, S. Chakraborty, S. M. Berry, S. D. Cambron, E. A. Nelson, R. S. Keynton, B. W. Alphenaar, "Directed and Self-Assembled Nanowire Formation at Room Temperature For Rapid Nanoprototyping" Gordon Conference on Nanostructure Fabrication, Tilton NH, (18-23 July 2004)

P. Gopinath, M.M. Yazdanpanah, S. Chakraborty, S. A. Harfenist, R.W. Cohn and B W Alphenaar, "Evidence for Ballistic Electron Transport Through Carbon Nanotubes using Liquid Metal Contacts" 10th Annual Kentucky EPSCoR conference, Lexington, KY, May 13, 2004

M. M. Yazdanpanah, S. Chakraborty, S. A. Harfenist, R.W. Cohn and B W Alphenaar, "Direct Measurement of Nanotube Conductance during Contact Formation." American Physical Society March 2004 meeting, Montreal, Canada, March 24, 2004

M. M. Yazdanpanah, S. A. Harfenist, and R. W. Cohn, "Nanoimprint and Dip Pen Lithography of Gallium" First International Conference on Nanoimprint and Nanoimprint Lithography, San Francisco, CA, 11-13 December 2002

M. M. Yazdanpanah: "Design and Fabrication a High Resolution Scanning Tunneling Microscope" Iranian physical society July 2001
Tehran Iran